Vers la compréhension des réponses de l'environnement côtier aux évènements extrêmes dans un contexte de changement climatique

Coline Poppeschi

COLLEGE SCIENCES DOCTORAL DE LA MER BRETAGNE ET DU LITTORAL

Université de Bretagne Occidentale

THESE DE DOCTORAT DE

L'UNIVERSITE
DE BRETAGNE OCCIDENTALE

ECOLE DOCTORALE N° 598
Sciences de la Mer et du Littoral
Spécialité : *Océanographie physique et environnement*

Par

Coline POPPESCHI

Vers la compréhension des réponses de l'environnement côtier aux évènements extrêmes dans un contexte de changement climatique

Thèse présentée et soutenue à Plouzané, le 13 octobre 2023
Unité de recherche : Laboratoire d'Océanographie Physique et Spatiale (LOPS)

Rapporteurs avant soutenance :

Michael FETTWEIS	Professeur, RBINS, Bruxelles - Belgique
Rodney FORSTER	Directeur de recherche, Université de Hull - Angleterre

Composition du Jury :

Président :	Anne-Marie TREGUIER	Directrice de recherche au CNRS, IUEM, LOPS, Brest
Examinateurs :	Michael FETTWEIS	Professeur, RBINS, Bruxelles - Belgique
	Rodney FORSTER	Directeur de recherche, Université de Hull - Angleterre
	Nicolas SAVOYE	Physicien CNAP, EPOC, Bordeaux
Dir. de thèse :	Guillaume CHARRIA	Chercheur Ifremer, LOPS/OC, Brest
Co-dir. de thèse :	Romaric VERNEY	Chercheur Ifremer, DYNECO/DHYSED, Brest

Invité(s)

Co-enc. de thèse : Anne DANIEL	Ingénieure Ifremer, DYNECO/PELAGOS, Brest

En prélude, voici une citation pour rappeler que le changement global est bien là:

« Le problème, ce n'est pas qu'on aille dans le mur ou pas. On va dans le mur !
Le problème, c'est à quelle vitesse on y va, à 50 km/h ou à 5 km/h ? »

Jean-Marc Jancovici

Table des matières

Table des Figures *5*

Table des tableaux *7*

Glossaire *8*

Chapitre 1 Introduction *9*

1.1 Contexte **9**

1.2 Objectifs de la thèse **20**

1.3 Plan de thèse **21**

Chapitre 2 Matériels et méthodes *23*

2.1 Matériel **23**

2.2 Méthodes de détection des évènements extrêmes **31**

2.3 Régions étudiées **43**

Chapitre 3 Les vagues marines de chaleur et de froid en Atlantique Nord-Est *45*

3.1 Résumé **45**

3.2 Article : Coastal and regional marine heatwaves and cold-spells in the Northeast Atlantic **47**

Chapitre 4 Dessalures extrêmes hivernales en rade de Brest *64*

4.1 Résumé **64**

4.2 Article : Unraveling Salinity Extreme Events in Coastal Environments: A Winter Focus on the Bay of Brest **66**

Chapitre 5 La réponse des matières en suspension aux forçages extrêmes *80*

5.1 Résumé **80**

5.2 Article : Suspended particulate matter response to extreme forcings in the Bay of Seine **82**

Chapitre 6 Évolution de l'initiation de la période productive du phytoplancton en zone côtière face aux évènements extrêmes *116*

6.1 Résumé **116**

6.2 Article : Interannual variability of the initiation of the phytoplankton growing period in two French coastal ecosystems **118**

Chapitre 7 Conclusions *139*

7.1 Identifier les évènements extrêmes **139**

7.2 Caractériser les évènements extrêmes **140**

7.3 Comprendre les évènements extrêmes **141**

7.4 Les évènements extrêmes, un enjeu scientifique en pleine évolution **142**

Chapitre 8 Perspectives *144*

8.1 Vers des indicateurs d'évènements extrêmes en milieu côtier **144**

8.2 Phénomènes d'hypoxie en baie de Vilaine 146
8.3 Mesures des EE en milieu côtier 150
8.4 Evolution des EE côtiers et points d'inflexion 151
Bibliographie 152
Annexes 169
Annexe 1 169
Annexe 2.....216

Table des Figures

Figure 1-1 Localisation des EE les plus importants de 1998 à 2017 (IPCC, SROCC, 2019) . 10

Figure 1-2 Schéma présentant les deux façons d'étudier un évènement extrême 1) à partir de la réponse aux extrêmes dans l'environnement côtier vers les forçages extrêmes et 2) à partir des forçages extrêmes vers la réponse aux extrêmes dans l'environnement côtier..... 11

Figure 1-3 Évolution des phénomènes extrêmes selon la distribution d'un paramètre ici la température comme exemple. (a) Décalage de la distribution (b) Augmentation de la variabilité (c) Modification de la forme de la distribution (SREX, IPCC, 2023)..... 13

Figure 1-4 (a) Augmentation des jours chauds dans l'atmosphère selon plusieurs scénarios de l'IPCC au niveau mondial (Domeisen et al., 2023) (b) Augmentation du record des précipitations annuelles au niveau mondial (Lehmann et al., 2015) 14

Figure 1-5 Photos de conséquences sur l'environnement côtier français face aux EE. (a) Mortalité de masse de poissons suite à un phénomène d'anoxie en baie de Vilaine (Chapelle et al., 1994) (b) Mortalité de masse de coraux dans la mer Méditerranée par la présence de MHW (Garrabou et al., 2022) (c) Efflorescence algale de Lingulodinium polyedra - algue toxique en baie de Vilaine liée à un phénomène d'hypoxie (Mertens et al., 2023) 15

Figure 1-6 Schéma conceptuel reliant les évènements extrêmes dans le milieu côtier 20

Figure 2-1 Localisation des stations de mesures utilisées dans cette thèse à haute fréquence du réseau COAST-HF (ronds rouges), du Met Office (ronds roses), du Western Channel Observatory (rond violet), de Puertos del Estado (ronds marrons) et à basse fréquence du réseau SOMLIT (étoile verte) et du réseau REPHY (étoile bleue)..... 15

Figure 2-2 Illustration du produit OISST dans l'Atlantique Nord-Est avec une carte de SST pour le 28 juin 2020..... 27

Figure 2-3 Illustration des régimes de temps dominant la variabilité de la pression atmosphérique en Atlantique Nord en mètres géopotentiels (mgp ; Cassou et al., 2011) 28

Figure 2-4 Présentation des deux principales méthodes statistiques de détection d'extrêmes avec les seuils (lignes rouge) et les évènements extrêmes (cercles rouges) 31

Figure 2-5 Distribution statistique des paramètres environnementaux tels que (a) le débit, (b) la turbidité, (c) la fluorescence, (d) la salinité, (e) la température et (f) l'oxygène dissous 35

Figure 2-6 Séries temporelles enregistrées à la bouée Marel-Iroise en rade de Brest et pour la rivière Aulne de 2000 à 2022. (a) Les percentiles 80, 85, 90, 95 et 99 fixes sont testés sur le débit représentant le groupe A et (b) Les percentiles 1, 5, 10, 15 et 20 fixes sont testé sur la concentration en oxygène dissous représentant le groupe B..... 36

Figure 2-7 Percentile 90 fixé ou variable par saison ou par mois calculé pour (a) la turbidité et (b) l'oxygène dissous en rade de Brest de 2000 à 2022..... 38

Figure 2-8 Influence de la lumière sur la variation du signal de fluorescence chlorophylienne selon les heures de la journée (Poppeschi et al., 2021).....39

Figure 2-9 Influence de la marée sur la taille des matières en suspension – Climatologie intratidale de D50opt-acc (diamètre médian des matières en suspension) calculée sur la période 2015-2022 par rapport à l'amplitude de marée des conditions de faibles vagues (HsP90=[0.5-1]m) (Verney et al., à soumettre, 2023).....39

Figure 2-10 Exemple de la validation de données de concentration de matières en suspension issues de simulations numériques et comparées à des données *in situ* (Poppeschi et al., 2023) 40

Figure 2-11 Caractéristiques majeures d'un évènement extrême.....42

Figure 2-12 Carte avec les sites d'études de la thèse pour les cinq paramètres clés de l'environnement côtier reliés aux extrêmes 44

Figure 8-1 Carte de présentation de la baie de Vilaine avec la bouée MOLIT (rond violet), les mastodons déployés (ronds rouges) et les points de grille du modèle associés (étoiles noires) 147

Figure 8-2 Oxygène dissous de fond enregistré par les mastodons (a) de 2021 à 2022 aux stations St Jacques, Loscolo et Normande et (b) de 2020 à 2022 aux stations Dumets, Les Mats et Kervoyal.....148

Table des tableaux

Tableau 2-1 Valeurs de seuil déterminées par le percentile 90 fixe calculé sur des périodes de 10, 15, 20, 30, 40 et 50 ans de données consécutives pour la turbidité (NTU), le débit (m^3 s^{-1}), la température (°C), la salinité (PSU), l'oxygène dissous (mg L^{-1}) et la fluorescence (FFU).. 37

Tableau 8-1 Caractéristiques interannuelles des désoxygénations détectées à la bouée Molit de 2020 à 2022 148

Tableau 8-2 Caractéristiques principales des trois cas d'étude de désoxygénation enregistrés par les Mastodons en baie de Vilaine. 149

Glossaire

EE Évènement extrême

EEC Évènement extrême composé

IPCC Groupe d'experts Intergouvernemental sur l'Evolution du Climat (GIEC)

IPGP Initiation de la période productive du phytoplancton

MCS Vague marine de froid (Marine Cold Spell)

MES Matières En Suspension

MHW Vague marine de chaleur (Marine Heat Waves)

NAO Oscillation nord Atlantique (North Atlantic Oscillation)

SPM Matières en suspension (Suspended Particulate Matter)

SREX Rapport spécial de l'IPCC sur les extrêmes

SST Température de surface de la mer (Sea Surface Temperature)

Chapitre 1 Introduction

1.1 Contexte

1.1.1 Les zones côtières face au changement global

A l'heure de l'anthropocène, l'océan est sous l'influence du changement global (Cook et al., 2022) qui regroupe les évolutions à long terme liées à l'activité humaine, en particulier depuis les années 1900, avec une accentuation en période post-industrielle et les évolutions naturelles du climat, constituant le changement climatique. La forte contribution de l'Homme dans les émissions de gaz à effet de serre fait que la planète se réchauffe plus rapidement et plus intensément ces 200 dernières années (IPCC, 2023 - groupe d'experts intergouvernemental sur l'évolution du climat). Le réchauffement de l'océan au niveau mondial est plus intense en surface qu'au fond, et montre des variations régionales marquées. De nombreux changements sont engendrés par ce réchauffement océanique comme par exemple, la montée du niveau de la mer et l'évolution de la circulation thermohaline. Le niveau de la mer global relatif a augmenté en moyenne de 3.6 mm an^{-1} de 1994 à 2018 mais cette hausse reste variable autour du globe. Cette hausse est liée à la dilatation des molécules d'eau, la fonte des glaciers et la fonte des calottes du Groenland et de l'Antarctique, la circulation de l'océan et de l'atmosphère ainsi qu'aux élévations terrestres. La circulation thermohaline, qui redistribue les masses d'eaux dans l'océan global, est aussi touchée par l'augmentation de la température de surface de l'océan (SST) ainsi que par la baisse de salinité dans les eaux de surface provoquée par la fonte des calottes glaciaires. L'augmentation de la stratification des eaux provoquée par ces deux phénomènes conduit à un affaiblissement de la circulation thermohaline. Ces évolutions à grandes échelles vont avoir des incidences sur la circulation des masses d'eaux proches de côtes.

L'océan côtier est une partie de l'océan particulièrement touchée par le changement global (Losada et al., 2020) et le sera d'autant plus dans le futur (Najjar et al., 2000). Par exemple, l'élévation du niveau de la mer à la côte est responsable en partie de l'érosion du littoral de plus en plus importante. Cette région, déjà impactée par les activités anthropiques, est fragilisée par le changement global car elle renferme des services écosystémiques largement plus importants que ceux de l'océan ouvert (Mateos et al., 2023). C'est un espace maritime complexe aux enjeux très forts avec près de 60 % de la population mondiale vivant à moins de 150 kilomètres des côtes (UICN, 2023).

Ces évolutions climatiques et anthropiques induisent des modifications des échanges entre l'atmosphère et l'océan qui engendrent des évènements hydro-météorologiques plus intenses. Ces évènements impliquent des évènements extrêmes (EE) et peuvent être représentés par des forçages climatiques extrêmes ou des extrêmes environnementaux présents dans l'océan. Une cascade de conséquences dramatiques sera engendrée par la vulnérabilité des sociétés humaines et des écosystèmes face aux EE.

La compréhension de la manifestation, des conséquences et de l'évolution des évènements extrêmes est donc importante dans le cadre de la prise de décision en matière de gestion et d'élaboration des politiques publiques, particulièrement en zone côtière. Les études des évènements extrêmes (EE) restent cependant encore rares dans l'océan côtier en comparaison de l'océan global pourtant ils sont de plus en plus nombreux (Figure 1-1). L'analyse des extrêmes y est nécessaire pour mettre en place des indicateurs prédictifs (Machado et al., 2023) et pour améliorer la gestion de ces bandes côtières vulnérables en régulant les tendances et en explorant les disparités géographiques (Breitburg et al., 2018).

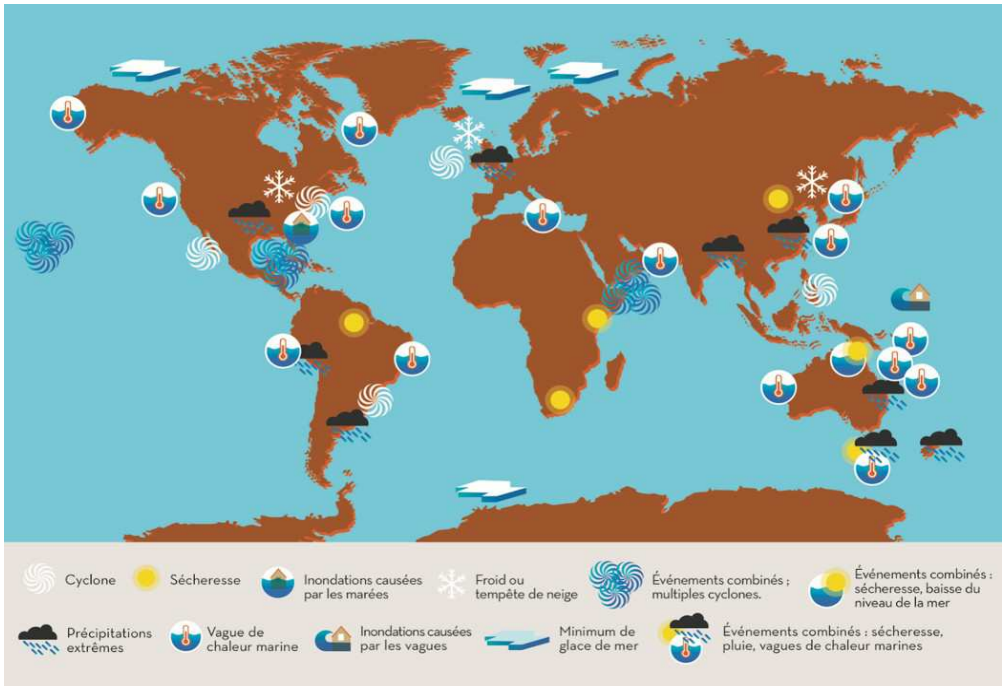

Figure 1-1 Localisation des EE les plus importants de 1998 à 2017 (IPCC, SROCC, 2019)

1.1.2 Les évènements extrêmes - définition

Les évènements extrêmes (EE) se manifestent de plus en plus fréquemment et les comprendre est devenu une nécessité (Trenberth et al., 2015). Le terme EE est utilisé pour définir différents processus et sa définition n'est pas unique (Stephenson, 2008) en fonction des disciplines scientifiques. Ainsi, l'EE se confond avec la "catastrophe" en science sociale, le "risque" en science naturelle, la "perturbation" en écologie, la "période de retour" en ingénierie. Mais, d'après une revue de littérature récente (McPhillips et al., 2018), le terme "événement extrême" est plus utilisé lorsque des extrêmes liés au climat sont abordés. Si le mot "extrême" signifie en latin *le plus fort*, la définition suivante du terme "extrême" est donnée par Coles (2001):

un extrême est une valeur anormalement différente par rapport à une dynamique moyenne de référence sur une courte période

Dans le rapport de l'IPCC (2023), l'extrême représente avant tout un événement rare à un endroit et à un moment donné. Les extrêmes peuvent être classés en termes d'intensité : on parle de "surprises" quand ils sont sans précédent d'intensité et/ou de durée, "d'extrême" quand les évènements sont rares et "d'extrême modéré" s'ils sont observés plusieurs fois dans l'année (IPCC - SREX, 2023; rapport spécial de l'IPCC sur les extrêmes). L'extrême se détermine également via l'intensité de son impact sur l'environnement (IPCC, 2023) ou de l'étendue de sa zone d'impact (évènements extrêmes régionaux, Ren et al., 2018). Enfin, l'extrême n'est pas forcément un évènement isolé mais peut être un ensemble d'évènements de natures différentes dont la succession est rapprochée dans le temps que l'on retrouve dans la littérature sous le terme d' « évènement extrême composé » (Broska et al., 2020).

Dans ce contexte, deux approches distinctes permettent d'analyser l'impact des EE (**Figure 1-2**):

- **1. Extrême d'une variable océanique dans l'écosystème côtier (extrême environnemental) :** consiste à repérer les extrêmes des valeurs du paramètre environnemental d'intérêt dans l'océan côtier et de remonter jusqu'à son origine et d'en comprendre les processus qui le contrôlent. C'est le cas des vagues marines de chaleur (Hobday et al., 2016; Oliver et al., 2019).

- **2. Extrême d'un forçage hydrométéorologique (forçage extrême) :** fonctionne à l'inverse du précédent, c'est-à-dire à partir d'un évènement météorologique climatique extrême (McPhillips et al., 2018), on étudie ses conséquences sur l'environnement marin côtier. L'étude d'EE par forçage extrême est notamment utilisée pour regarder l'impact des tempêtes sur les matières en suspension dans l'environnement côtier (Fettweis et al., 2010; Tavora et al., 2023).

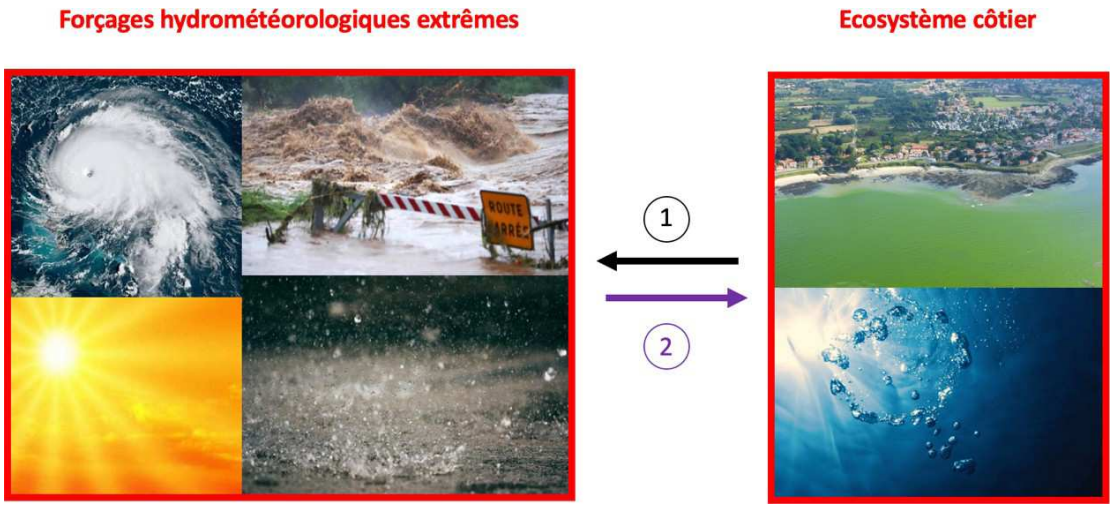

Figure 1-2 Schéma présentant les deux façons d'étudier un évènement extrême 1) à partir de la réponse aux extrêmes dans l'environnement côtier vers les forçages extrêmes et 2) à partir des forçages extrêmes vers la réponse aux extrêmes dans l'environnement côtier

A travers mon travail de thèse, les deux approches ont été explorées : les vagues marines de chaleur et de froid et les dessalures extrêmes sont étudiées sous forme d'extrêmes environnementaux à partir respectivement du signal de température de surface de la mer (SST) et de salinité. En revanche, les anomalies de turbidité en zones côtières et l'initiation de la période

productive du phytoplancton (IPGP) sont observées via les forçages extrêmes, tels que les tempêtes via l'impact du vent sur les vagues, des précipitations sur les crues.

La plupart des extrêmes suivent une évolution vers l'augmentation du fait d'un changement de la moyenne, de la variance ou de la forme de la distribution de probabilité, ou bien l'ensemble de ces trois paramètres (**Figure 1-3**; SREX, IPCC, 2023). Ces changements de distribution induisent des EE qui sont, soit plus intenses, soit plus longs, soit plus fréquents, soit qui impactent une zone plus grande ou bien qui réunissent l'ensemble de ces changements, comme c'est le cas pour la vague marine de chaleur (MHW) de 2023 en Irlande (McCarthy et al., en préparation).

Les évènements extrêmes ont ainsi gagné en intensité et en fréquence ce dernier siècle (Van Aalst, 2006). L'incertitude sur la caractérisation de ces EE limite leur possible prédiction et les possibilités de développement de mesures d'atténuation voire d'adaptation ce qui constitue un réel défi à relever pour les scientifiques qui est développé au sein de cette thèse. Certains de ces changements s'étendent sur des décennies à des siècles et sont irréversibles à l'échelle de l'Homme (IPCC, 2021). L'évolution des évènements extrêmes peut être aujourd'hui analysée grâce aux observations de l'océan menées depuis 1950 (SREX, IPCC, 2023; McPhillips et al., 2018). Ces phénomènes extrêmes sont complexes à étudier du fait de leurs grandes diversités en termes de typologie d'évènements (MHW, désoxygénation,,...). Ces évènements extrêmes sont par ailleurs difficiles à étudier en pratique. Du fait de l'imprévisibilité de leur occurrence, des instruments doivent être déployés en continu pour mesurer les extrêmes. De plus, les intensités extrêmes des évènements obligent les instruments à être robustes pour résister aux forçages extrêmes et à étendre leurs champs habituels de gamme de mesure. Comme les EE extrêmes sont rares par définition, leurs observations sont limitées. L'évolution des EE diffère aussi en fonction de l'échelle spatiale (global versus local). Ce petit nombre d'évènements et leurs échelles spatio-temporelles rend donc difficile l'étude de leur tendance à long terme.

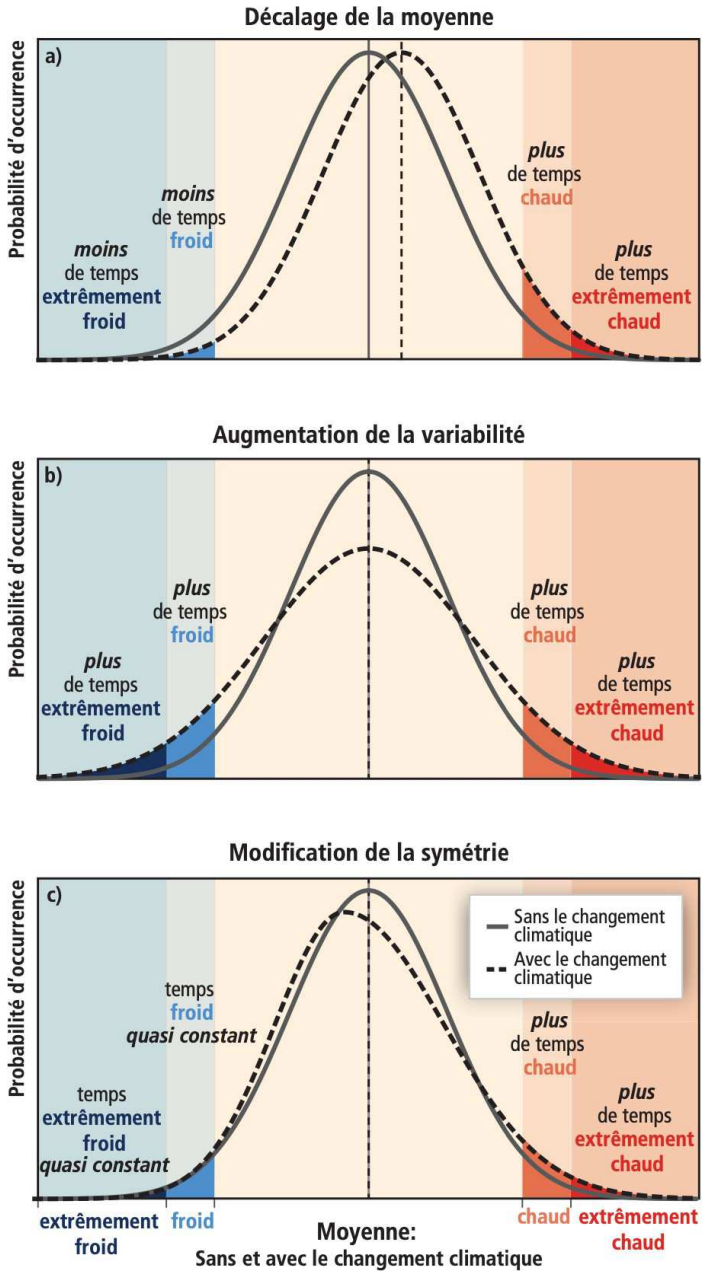

Figure 1-3 Évolution des phénomènes extrêmes selon la distribution d'un paramètre ici la température comme exemple. (a) Décalage de la distribution (b) Augmentation de la variabilité (c) Modification de la forme de la distribution (SREX, IPCC, 2023)

1.1.3 Manifestations et impacts des évènements extrêmes

Le panel intergouvernemental qui s'occupe du changement climatique (IPCC, 2023) informe que les prédictions futures tendent vers une augmentation des EE notamment pour les températures extrêmes (Domeisen et al., 2023 ; **Figure 1-4a**) avec une augmentation du nombre de jours où la température est supérieure à 35° dans le monde. Les précipitations extrêmes tendent vers une augmentation même si des disparités géographiques existent (Lehmann et al., 2015 ; **Figure 1-4b**). Ces EE liés au changement climatique pourraient ou ont déjà pour certains des conséquences écologiques, économiques et sociologiques majeures (Harris et al., 2018).

Ces évènements extrêmes menacent directement des vies humaines (Bell et al., 2018), par le recul du trait de côte sur les côtes atlantiques françaises (Castelle et al., 2018), par l'apport de virus comme lors de la contamination de l'eau potable lors de crues extrêmes en Afrique (Zou et al., 2023), par les étiages extrêmes engendrant des déficits en eau douce par salinisation des nappes phréatiques comme dans l'estuaire de la Loire (Paskoff, 2004). Les répercussions des EE sur l'environnement sont grandes (Thibault et Brown, 2008; Smale et Wernberg, 2013; Wernberg et al., 2013; Seuront et al., 2019 – **Figure 1-5**), en apportant des espèces invasives (Ummenhofer et Meehl, 2017) ou par exemple en induisant une extinction de biodiversité marine à l'échelle mondiale (Hodapp et al., 2023).

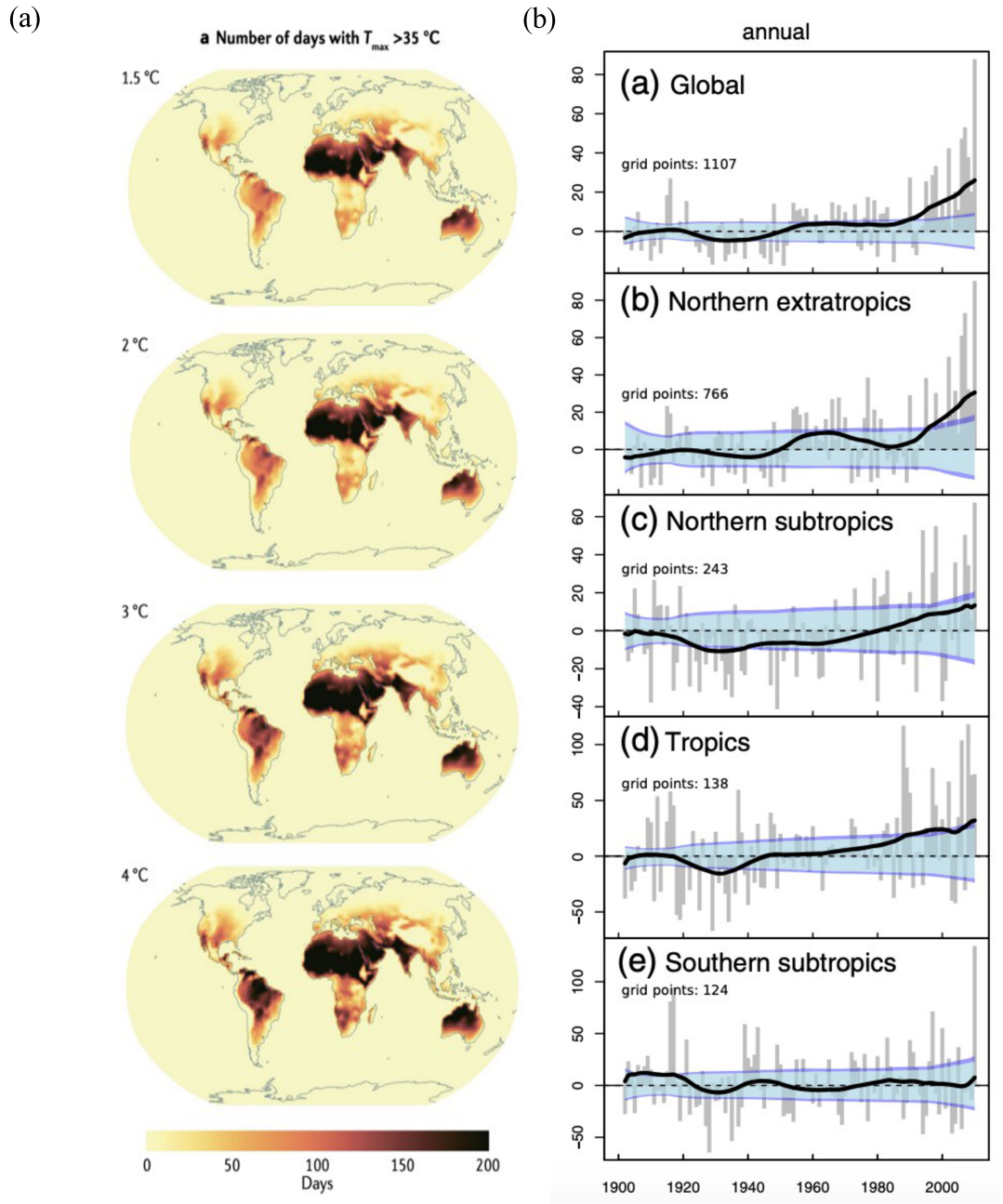

Figure 1-4 (a) Augmentation des jours chauds dans l'atmosphère selon plusieurs scénarios de l'IPCC au niveau mondial (Domeisen et al., 2023) (b) Augmentation du record des précipitations annuelles au niveau mondial (Lehmann et al., 2015)

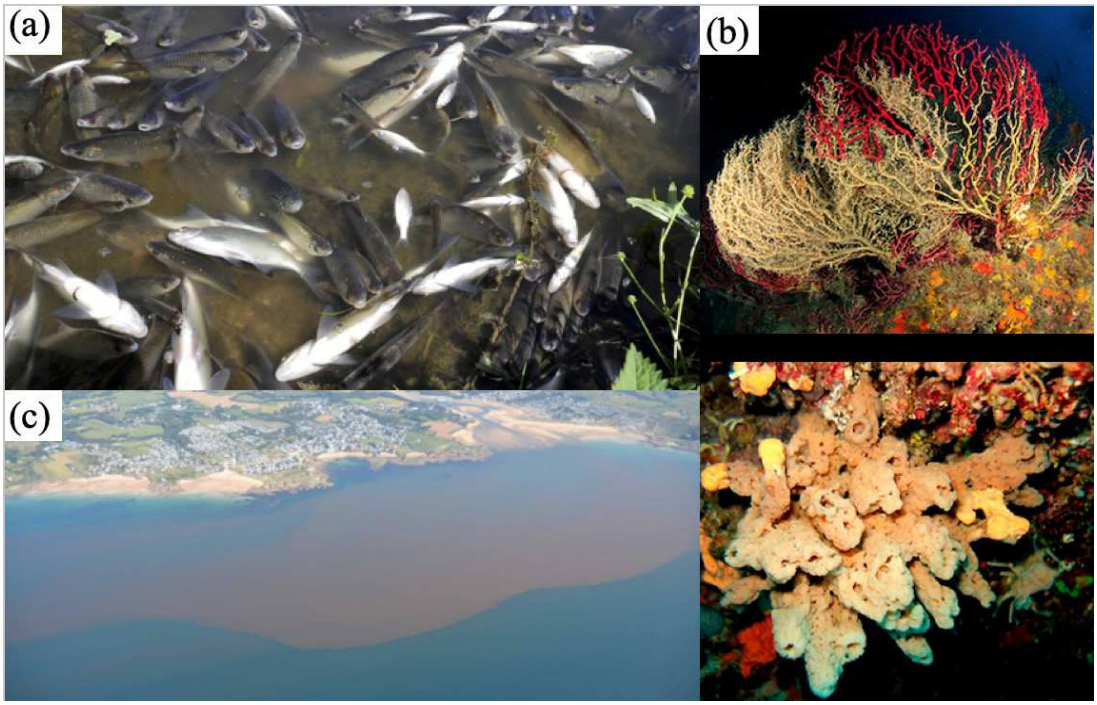

Figure 1-5 Photos de conséquences sur l'environnement côtier français face aux EE. (a) Mortalité de masse de poissons suite à un phénomène d'anoxie en baie de Vilaine (Chapelle et al., 1994) (b) Mortalité de masse de coraux dans la mer Méditerranée par la présence de MHW (Garrabou et al., 2022) (c) Efflorescence algale de Lingulodinium polyedra - algue toxique en baie de Vilaine liée à un phénomène d'hypoxie (Mertens et al., 2023)

L'impact des événements extrêmes sur le milieu côtier dépend principalement de l'exposition et de la vulnérabilité des écosystèmes. Une crue extrême a des conséquences très différentes selon la préparation des habitants à faire face aux inondations comme c'est le cas désormais en Indonésie (Muh Aris et al., 2007). Les impacts des EE peuvent être conséquents s'ils se cumulent, ces EE sont ainsi appelés évènements extrêmes cumulés (EEC). Les EEC sont également de plus en plus fréquents et de nouvelles relations en cascade se présentent : entre MHW et dessalure (Liu et al., 2023) ou encore entre MHW et faibles concentrations en chlorophylle après El Nino dans l'océan Pacifique (Le Grix et al., 2021).

Les évolutions des EE ne sont pas certaines mais la probabilité (degré de confiance élevé établi par l'IPCC) vers l'augmentation des vagues marines de chaleurs (Marine HeatWaves - MHW) apparaît clairement (Yao et al., 2022). D'autres se distinguent de la tendance du système océan-atmosphère global comme les précipitations extrêmes qui tendent à augmenter lorsque les précipitations moyennes tendent à diminuer (IPCC, 2023). Enfin, certaines évolutions restent difficiles à caractériser comme c'est le cas pour les tempêtes.

Afin d'évaluer ces impacts, plusieurs EE impactant l'environnement côtier peuvent être considérés. Dans un premier temps, les extrêmes environnementaux tels que les MHW et MCS ainsi que les dessalures extrêmes peuvent être analysés individuellement (Chapitre 3 & Chapitre 4). Ensuite, l'effet des forçages extrêmes de crues et de fortes vagues s'observe de façon séparée et cumulée sur la réponse des concentrations en SPM (Chapitre 5). Puis, tous ces EE peuvent être investigués en tant que forçages extrêmes sur la biomasse phytoplanctonique, compartiment biogéochimique de l'écosystème côtier (Chapitre 6).

1.1.3.1 Vagues marines de chaleur et de froid

Une MHW (vague marine de chaleur) ou une MCS – (vague marine de froid) est une anomalie de température observée au minimum sur 5 jours consécutifs et calculée à partir d'une climatologie d'au minimum 30 ans de données (Hobday et al., 2016). Une augmentation des MHW (Oliver et al., 2019; Plecha et al., 2021; Izquierdo et al., 2022) et une diminution des MCS (Schlegel et al., 2021; Simon et al., 2022) sont observées dans l'océan global et dans l'océan côtier. Cette tendance s'accentue avec des zones d'occurrence au niveau global plus importantes observées entre 1982 et 2020 (Yao et al., 2022) avec une étendue spatiale des MHW qui aurait triplé entre aujourd'hui et la période préindustrielle (Frölicher et al., 2018). Les MHW sont plus fréquentes (augmentation de 34% au cours du dernier siècle et doublement du nombre de jours entre 1982 et 2016, Frölicher et al., 2018) et plus longues de 17% (Oliver et al., 2018). Les MHW sont aussi plus intenses avec une intensité moyenne annuelle de +0.8°C par rapport à l'ère préindustrielle (Frölicher et al., 2018) ce qui dénote une activité des MHW au total plus importante (Simon et al., 2022). Les projections climatiques annoncent que l'augmentation des MHW en intensité, durée et nombre de jours à la fin du 21ème siècle induira un statut semi permanent de ces EE (Oliver et al., 2019; Plecha et Soares, 2020; Yao et al., 2022). Un premier processus responsable de cette tendance à l'augmentation des MHW (Frölicher et al., 2018) et à la diminution des MCS (Schlegel et al., 2021; Wang et al., 2022, Simon et al., 2023) est le réchauffement des eaux océaniques. Cependant, ces EE sont complexes et doivent prendre en compte des processus atmosphériques à grandes échelles comme des régimes de temps préférentiels (Folland et al., 2009; Izquiero et al., 2022; Simon et al., 2023) ou l'advection des courants océaniques (Deser et al., 2010). Certains processus locaux peuvent aussi jouer un rôle comme les anomalies de vent qui entraînent la modification des flux de température à l'interface air-mer (Crisp, 1964; Schlegel et al., 2021). Des liens entre la marée, le rayonnement solaire, la couverture nuageuse et l'intensité du vent ont aussi été observés au large de la France durant la MHW de 2022 (Guinaldo et al., 2023).

Les impacts les plus importants des MHW concernent le blanchissement des coraux (Hughes et al., 2017), la décroissance des herbiers (Izquierdo et al., 2022), la tropicalisation des communautés de poissons (Wernberg et al., 2016), la restructuration entière d'écosystèmes et la perturbation des biens et services issues de l'environnement (Smale et al., 2019). Des liens ont été montrés entre les MHW et le phytoplancton (Gomez et Souissi, 2008) ainsi qu'entre MHW et activité microbienne (Joint et Smale, 2017) en Manche. On retrouve des impacts liés aux MHW sur la production de macroalgues sur la côte Ibérique également (Izquierdo et al., 2022). Certains EE très intenses sont largement décrits dans la littérature comme c'est le cas pour la MHW de 2018 dans la Manche qui a entraîné des mortalités de masses de moules (Seuront et al., 2019), des changements de communauté - fucoïdes (Mieszkowska et al., 2020) et des efflorescences algales toxiques (Brown et al., 2022).

Les conséquences des MCS restent peu analysées par rapport à celles des MHW. La diminution globale des MCS change les températures de l'océan et entraîne de fortes modifications des écosystèmes au niveau de leurs structures et de leurs fonctions (Schlegel et

al., 2021). Les impacts liés aux MCS révèlent des mortalités de masses comme celles des coquilles Saint-Jacques (Crisp, 1964) et des huîtres ou encore la migration d'espèces telle que la limande (Sims et al., 2004) sur les côtes anglaises. Les MCS peuvent aussi, comme sur les côtes australiennes, être responsables d'une diminution de la production primaire (Feng et al., 2021).

L'étude des MHW et MCS est en plein essor du fait de l'augmentation de la fréquence de ces EE. La majorité des études actuelles sur les MHW sont concentrées sur des zones de forts impacts mais les MHW, comme les MCS, ne sont uniformes ni spatialement ni temporellement et leurs dynamiques restent incomprises, ou même non étudiées, dans certains écosystèmes côtiers. Au niveau européen, la Méditerranée est une zone d'étude privilégiée à cause des impacts importants liés à ces EE (Darmaraki et al., 2019 ; Juza et al., 2022 Simon et al., 2022) en comparaison de l'océan Atlantique où la dynamique des MHW et MCS reste méconnue. Ces EE doivent désormais être analysés en combinant des jeux de données divers comme les images satellites, les modèles numériques et les données *in situ* côtières pour caractériser au mieux ces EE. Pour que les modèles puissent devenir prédictifs des EE, ils devront apprendre à assimiler des données satellites multi paramètres telles que la SST mais aussi le vent. D'autres données devront être ajoutées à l'analyse comme par exemple, la bathymétrie, les courants et la marée.

1.1.3.2 Dessalures extrêmes

Les tempêtes impactent près de 55% des côtes mondiales (Mentaschi et al., 2017; Marcos et al., 2019). Les ondes de tempêtes sont responsables de vents extrêmes et de précipitations extrêmes (Leckebusch et al., 2006; Coumou et Rahmstorf, 2012) qui induisent des crues et des vagues importantes (Thompson et al., 2017). Les précipitations et les forçages atmosphériques ont une forte corrélation en Atlantique Nord (Msadek et Frankignoul, 2009). Les masses d'air au-dessus de l'Atlantique Nord à l'origine des précipitations ont des conséquences directes sur les changements de salinité au niveau de la côte. Les forçages hydro-climatiques à grande échelle ont un impact sur l'écosystème régional océanique (Goberville et al., 2014). Les processus tels que les crues induisent aussi des changements de salinité impactant la circulation des masses d'eaux côtières (Tréguer et al., 2014; Ceccaldi et al., 2020). Ces EE de dessalures tendent à s'intensifier en lien avec des précipitations extrêmes plus importantes (IPCC, 2023), des études complémentaires sur le sujet restent cependant nécessaires afin de déterminer les réponses des bassins versants et des régions marines côtières à ces évolutions.

En effet, les dessalures extrêmes sont des EE qui sont peu étudiés du fait notamment que ces EE concernent uniquement les zones impactées par les fleuves dans l'océan côtier. Pourtant, ces EE côtiers ont de nombreuses conséquences sur l'écosystème. Les fortes dessalures jouent un rôle sur la dynamique de la colonne d'eau et peuvent être reliées à des changements de concentrations en nutriments, en chlorophylle-*a*, en oxygène dissous et en matières particulaires en Manche et dans l'océan Atlantique (Goberville et al., 2010). Dans d'autres régions, telles que le golfe Persique, les dessalures sont associées à un doublement de

la distribution de chlorophylle après des précipitations extrêmes (Alosairi et al., 2019). La flore et la faune marine sont également impactées par les fortes dessalures, comme par exemple la croissance des herbiers de Zostera Marina en rade de Brest (Boyé et al., 2022), la survie du bivalve *Sinonovacula constricta* en Chine (Yang et al., 2022) et les mortalités d'huîtres en baie de Vilaine (La Peyre et al., 2013). Enfin, les précipitations extrêmes peuvent modifier l'infiltration des eaux souterraines en milieu côtier (Diego-Feliu et al., 2022).

1.1.3.3 Impacts des tempêtes via l'action des vagues et des crues sur les anomalies de turbidité

Un panache sédimentaire est caractérisé par une dispersion d'eau de mer contenant des particules sédimentaires minérales et organiques de diamètre supérieur à 0.45 µm en suspension dans la colonne d'eau (MES - Matières En Suspension). Les tempêtes et les crues contrôlent en partie la dynamique sédimentaire dans les baies côtières (Fettweis et al., 2010). Les concentrations en MES fluctuent sous l'effet du débit des rivières, des marées, des vagues et de l'intensité et la direction du vent (Fettweis et al., 2020; Paladini de Mendoza et al., 2018). Les crues jouent un rôle direct sur la stratification qui permet aux panaches sédimentaires de se développer en sortie d'estuaires avec le déplacement du bouchon vaseux regroupant de fortes concentrations de MES (Deloffre et al., 2005; Dufois et al., 2014). Ainsi, le bouchon vaseux (zone de concentration maximale de MES) situé en estuaire peut se retrouver à l'embouchure lors de crues (Burchard et al., 2018; Grasso et al., 2018). Les concentrations en MES présentent une grande variabilité saisonnière (Abarnou et al., 1987; Gohin et al., 2005; Mear et al., 2018) avec de fortes concentrations en hiver quand les vagues sont puissantes (Andersen et Pejrup, 2001) et que le débit des rivières est intense (Deloffre et al., 2005). Les fortes concentrations en MES jouent un rôle sur la pénétration de la lumière dans la colonne d'eau, comme observé par exemple en mer du Nord depuis les années 1900 en réponse à une activité des vagues plus intense en lien avec l'évolution du climat (Wilson et Heath, 2019).

Ces EE sont examinés à travers de forts niveaux de turbidité créés par des crues extrêmes (Imran et Syvitski, 2000). Le vent et les crues extrême dans l'estuaire de l'Escaut aux Pays-Bas augmentent la concentration en MES (Tavora et al., 2023). Souvent les EE sont étudiés à l'échelle d'un évènement particulier telle qu'une tempête qui n'est pas forcément une tempête extrême. Ainsi, la tempête Britta de 2006 en mer du Nord est reliée à une modification de la dynamique sédimentaire (Lettmann et al., 2009) par la présence d'importantes vagues. Sur les côtes belges, les 3 tempêtes de 2005 à 2007 (Fettweis et al., 2010) ont aussi induit de très fortes concentrations en MES.

Les fortes concentrations en MES et les panaches turbides jouent un rôle crucial dans l'environnement côtier en régulant les apports à la mer de matière organique et inorganique et de contaminants. Les crues sont ainsi responsables de l'augmentation de la concentration en polluants dans le fleuve du Rhin et ses alentours (Wölz et al., 2010) qui engendre des répercussions importantes sur le réseau trophique (Cailleaud et al., 2007). Les fortes vagues et les crues entraînent des concentrations élevées de MES qui, en limitant la pénétration de la lumière dans la colonne d'eau, entraînent la réduction des habitats photiques disponibles et la

visibilité des prédateurs (Dupont et Aksnes, 2013) ou encore des changements de la phénologie du phytoplancton (Opdal et al., 2019).

Les fortes concentrations en MES et les panaches turbides sont principalement étudiés en hiver alors que les EE de turbidité peuvent être détectés et analysés pour toutes les saisons. De plus, les études se concentrent souvent sur une tempête isolée et très peu d'études s'étendent sur le long terme (plusieurs années). Les incertitudes liées aux modèles prédictifs de ces EE restent à définir et nécessitent une assimilation de plus de données. La distribution dans la colonne d'eau de ces EE reste peu étudiée. Un autre aspect de ces EE qui reste peu exploré est la succession des tempêtes et leurs effets cumulatifs sur les concentrations en MES, les données étant éparses et succinctes, ce travail est difficile à réaliser. Enfin sur les côtes françaises, l'ensemble des études sur les concentrations en MES est généralement effectué dans les estuaires (Le Hir et al., 2011; Deloffre et al., 2005; Grasso et al., 2018) et non dans les baies côtières.

1.1.3.4 Impacts des vagues marines de froid et des tempêtes sur l'initiation de la période productive du phytoplancton

Le phytoplancton est à la base du réseau trophique dans l'océan. Le phytoplancton est soumis à de multiples influences environnementales telles que la température (Trombetta et al., 2019), l'ensoleillement (Glé et al., 2007), la turbidité (Iriarte et Purdie, 2004), le vent (Tian et al., 2011), la marée (Ragueneau et al., 1996), les concentrations en nutriments (Cloern, 1996) et les crues (Peierls et al., 2012). Ces paramètres agissent sur la production phytoplanctonique de façon plus ou moins importante selon les années. La difficulté dans l'étude de l'influence des EE sur le phytoplancton résulte dans les nombreux paramètres qui interagissent ensemble et qui doivent être mesurés conjointement. L'étude de l'initiation de la période productive du phytoplancton en fin d'hiver permet de s'affranchir des processus biogéochimiques car c'est une période pendant laquelle les concentrations de nutriments ne sont pas limitantes et l'activité du zooplancton est encore faible.

Les études sur le phytoplancton en zone côtière sont généralement effectuées lors de courtes périodes (quelques semaines) pour étudier un processus particulier sur un site donné (Labry et al., 2001) ou bien par le biais de réseaux d'observation à basse fréquence (Del Amo et al. 1997; Gailhard et al., 2002; Iriarte et Purdie, 2004; Tian et al., 2011). Comme l'étude des EE implique des données acquises à haute fréquence sur le long terme, le paramètre choisi pour cette étude est la fluorescence chlorophyllienne mesurée par des capteurs *in situ*. La fluorescence chlorophyllienne est considérée comme un proxy de la concentration en chlorophylle-a, paramètre de référence pour étudier la biomasse phytoplanctonique.

1.2 Objectifs de la thèse

Dans ce contexte, mon travail de thèse vise à comprendre les EE dans l'océan côtier et la délimitation des processus locaux face aux processus globaux. La réponse de différents compartiments (physiques et biologiques) de l'écosystème côtier aux EE est étudiée sous forme d'une cascade de processus s'articulant autour des différents compartiments de l'environnement marin côtier (**Figure 1-6**).

Le choix des EE étudiés provient des deux faits majeurs du changement climatique en lien avec les EE que sont le réchauffement des eaux océaniques (Su et al., 2023) et l'augmentation des tempêtes (Kim et al., 2023) comme vu précédemment. Donc dans un premier temps, les MHW et MCS sont étudiées en lien avec le réchauffement océanique. Puis les dessalures extrêmes sont analysées en lien avec l'augmentation des fortes précipitations liées aux tempêtes. Enfin, les tempêtes qui jouent un rôle via les forçages extrêmes de crues et de vagues sur la remise en suspension des particules et les panaches sédimentaires en milieu côtier sont analysées. Et pour finir, l'impact des extrêmes tels que les MCS, les rafales de vent et les crues est regardé sur l'initiation de la période productive du phytoplancton (IPGP).

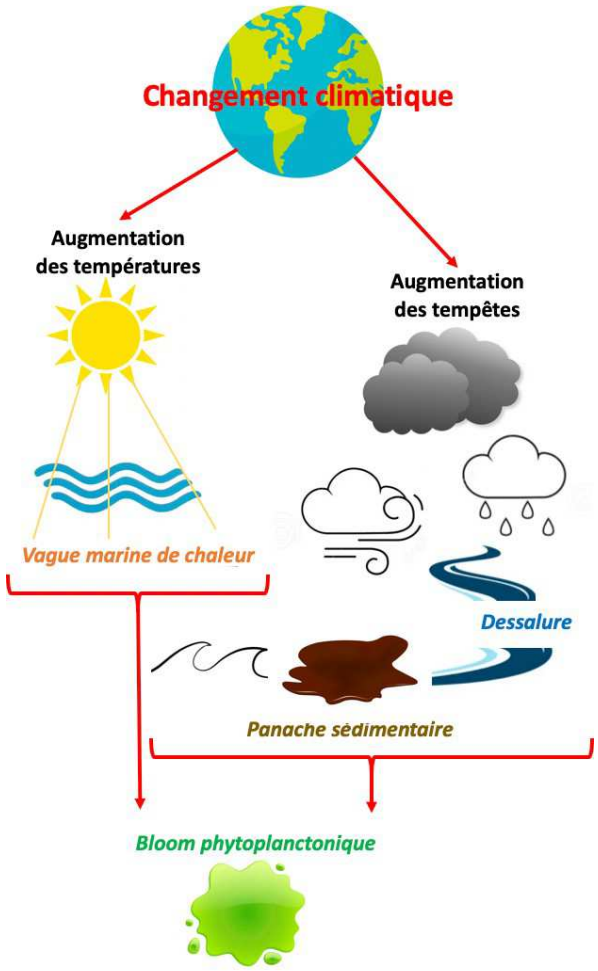

Figure 1-6 Schéma conceptuel reliant les évènements extrêmes dans le milieu côtier

Les principaux objectifs de cette thèse sont par conséquent de :

- Identifier les évènements extrêmes dans le milieu côtier à partir de plusieurs jeux de données.

- Décrire les évènements extrêmes dans l'océan côtier à partir de leurs caractéristiques telles que leurs durées, leurs intensités et leurs variabilités temporelles.

- Comprendre les processus en lien avec les évènements extrêmes dans le milieu côtier du forçage atmosphérique jusqu'à l'impact sur la biologie.

Ce travail a été réalisé sur les côtes françaises. La disponibilité de données haute fréquence sur plusieurs années récentes consécutives et inexploitées jusqu'à présent a été prise en considération dans le choix des sites d'études. Enfin, de ces travaux de thèse, émergent de nouveaux questionnements scientifiques liés aux EE.

1.3 Plan de thèse

La thèse est organisée comme suit :

- *Chapitre 1* : Le contexte, la définition d'extrême, les différents types d'extrêmes, les objectifs et le plan de la thèse sont introduits.

- *Chapitre 2* : Dans une première partie, les différents jeux de données multi-sources sont définis. Puis, la méthode de détection et les caractéristiques d'un évènement extrême sont détaillées. Enfin, les sites d'études sont présentés.

- *Chapitre 3* : L'évolution des vagues marines côtières de chaleur et de froid en Atlantique Nord-Est est observée. Ces phénomènes extrêmes sont analysés pour la première fois dans cette région via des mesures satellites et de bouées *in situ*.

- *Chapitre 4* : Les dessalures extrêmes hivernales dans la rade de Brest sont mises en avant à travers des données d'une bouée *in situ* et de simulations numériques. Les forçages tels que les précipitations, les crues, les régimes de temps et les tempêtes sont explorés.

- *Chapitre 5* : L'effet des tempêtes sur la réponse des matières en suspension en baie de Seine est investigué. Les forçages extrêmes jouant sur la dynamique sédimentaire que sont les crues et les vagues sont regardés avec des mesures d'une bouée *in situ* et des images satellites.

- *Chapitre 6* : L'impact des vagues marines de froid, des crues extrêmes et des fortes rafales de vent sur l'initiation de la période productive du phytoplancton est étudiée dans deux baies côtières de la façade Atlantique aux dynamiques contrastées. Un modèle simplifié est utilisé pour comprendre les processus associés ainsi que les données de bouées *in situ* haute et basse fréquence.

- *Chapitre 7* : Les conclusions principales sont énoncées ainsi que les perspectives mises en avant par cette thèse.

- *Chapitre 8* : Les perspectives mises en avant par cette thèse sont présentées.

Chapitre 2 Matériels et méthodes

2.1 Matériel

L'observation des évènements extrêmes (EE) constitue de réels défis vis-à-vis de leurs inhabituelles et soudaines périodes d'occurrences, de leurs intensités très élevées ou encore de leurs nouvelles étendues spatiales. Pour pouvoir identifier et analyser leurs fréquences et leurs intensités, il faut se baser sur des jeux de données cohérents et adaptés aux enjeux liés à ces processus de fortes intensités sur des périodes de temps limitées. Cette thèse est basée sur l'analyse de plusieurs types de données complémentaires : les données issues d'observations *in situ* à haute et basse fréquences, les données issues de différents satellites d'observation des océans et les données issues de simulations numériques. Les données *in situ* à haute fréquence (≤ 1h) présentent des signaux incomplets (données manquantes) et des incertitudes liées, par exemple, à la dérive des capteurs sous l'effet du biofouling. Les données *in situ* basse fréquence (> jour) sont généralement mesurées avec les techniques de référence de laboratoire ayant une limite de quantification et une précision meilleure que les capteurs déployés *in situ*. Par contre, les suivis basse fréquence ne permettent pas de détecter l'ensemble des EE, sauf dans le cas d'évènements en lien avec des dynamiques assez longues comme les crues. Les données satellitaires permettent d'analyser l'étendue spatiale des EE mais l'erreur sur la donnée à la côte peut être importante. De plus, la présence des nuages rend le signal souvent incomplet de façon saisonnièrement dissymétrique avec moins de données exploitables en hiver. Les EE ayant une dynamique très rapide (< 1 jour) ne peuvent être détectés à partir de ces données de télédétection. Par ailleurs, les modèles numériques génèrent des séries de données continues et régulières mais les variations des EE ne sont pas toujours bien représentées (en lien avec les processus sur lesquels sont calibrés les modèles, les équations résolues et les hypothèses retenues) ce qui se traduit par une incertitude importante sur les résultats simulés.

2.1.1 Données environnementales *in situ*

2.1.1.1 Paramètres physico-biogéochimiques in situ

Mesures haute fréquence

Les données issues de plusieurs réseaux d'observation à haute fréquence en mer côtière ont été utilisées dans le cadre de cette thèse (**Figure 2-1**).

Le Service National d'Observation COAST-HF[1] (Coastal OceAn observing SysTem High Frequency - www.coast-hf.fr; Cocquempot et al., 2019; Farcy et al., 2019; Répécaud et al., 2019) comprend 14 bouées placées le long des trois façades maritimes métropolitaines françaises faisant partie de l'infrastructure de recherche nationale ILICO (https://www.ir-ilico.fr). Les objectifs principaux de ce réseau sont de comprendre l'impact du changement climatique sur les zones côtières et les évènements extrêmes ainsi que de s'intéresser à la santé

des écosystèmes (Farcy et al., 2019). Ces bouées sont déployées tout au long de l'année[1] sauf en cas de maintenance. Les capteurs effectuent des mesures à haute fréquence (entre 10 min et 1 heure) de différents paramètres physiques et biogéochimiques en surface et, selon les sites, au fond. Les paramètres mesurés sur chaque station en surface (1 à 3 m de profondeur) sont la température, la salinité, la turbidité et la fluorescence. D'autres paramètres peuvent être mesurés sur certaines stations comme la concentration en oxygène dissous, le pCO_2, la production primaire, la diversité phytoplanctonique par cytométrie en flux ou encore la concentration en nitrates. La bouée pionnière du réseau COAST-HF est en place depuis 2000 en rade de Brest. Dans cette thèse, les données de huit bouées de mesures ont été utilisées (toutes dans le Chapitre 3): CARNOT (Halawi Ghosn et al., 2023) en Manche Est, SCENES (Chapitre 5), SMILE (Claquin et al., 2018) en Baie de Seine, ASTAN dans la Manche, MAREL-IROISE (Rimmelin-Maury et al., 2023; Chapitre 4 & Chapitre 6), SMART (Petton et al., 2021; Chapitre 4) en rade de Brest , MOLIT (Retho et al., 2022; Chapitre 6) en baie de Vilaine et ARCACHON à la sortie du bassin d'Arcachon.

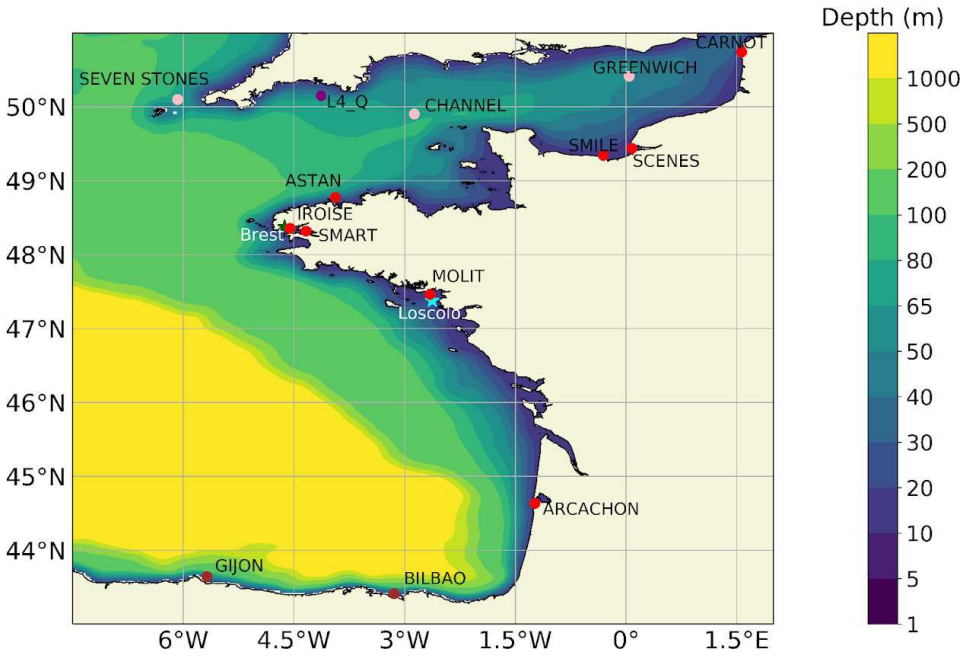

Figure 2-1 Localisation des stations de mesures utilisées dans cette thèse à haute fréquence du réseau COAST-HF (ronds rouges), du Met Office (ronds roses), du Western Channel Observatory (rond violet), de Puertos del Estado (ronds marrons) et à basse fréquence du réseau SOMLIT (étoile verte) et du réseau REPHY (étoile bleue)

Les données des bouées SEVEN STONES, CHANNEL et GREENWICH, gérées par le Met Office (www.metoffice.gov.uk) ont permis d'obtenir des données de température de surface de la mer en Manche le long des côtes anglaises. Le Met office gère ce réseau de mesure et les prévisions pour le Maritime & Coastguard Agency - MCA qui est responsable de fournir l'information maritime pour les bateaux en Angleterre. Une autre partie de l'observation en

[1] A l'exception de la bouée MOLIT en Baie de Vilaine qui n'était pas déployée sur la période hivernale avant 2018.

Manche est réalisée via le Western Channel Observatory (www.westernchannelobservatory.org.uk) qui gère la bouée haute fréquence L4_Q mise en place depuis l'année 2007. Cet observatoire est piloté par le Plymouth Marine Laboratory et la Marine Biological Association en Angleterre. Les mesures sont horaires et les paramètres clés sont la pénétration de la lumière dans la colonne d'eau, la température, la salinité et les concentrations en nutriments.

Les données de température de surface de la mer mesurées au nord de la côte ibérique sont issues du réseau d'observation de Puertos del Estado (www.puerto.es) qui opère les bouées BILBAO depuis 1990 et GIJON depuis 2001 (Chapitre 3) dans le cadre du volet *in situ* du Copernicus Marine Environment Monitoring Service européen. Plus largement, ce système opéré par les ports espagnols permet de récolter des données océano-météorologiques. Ce réseau de mesures et de prévisions de l'environnement marin est composé de plusieurs plateformes dont des bouées qui mesurent la SST.

Mesures basse fréquence

Les données de réseaux d'observation à long terme et à basse fréquence utilisées dans cette thèse sont :

- Le réseau REPHY - Réseau d'observation et de surveillance du phytoplancton et des phycotoxines (https://littoral.ifremer.fr/Reseaux-de-surveillance/Environnement/REPHY-la-surveillance-du-phytoplancton-et-des-phycotoxines) a été créé en 1984 et comporte des stations de mesure sur les trois façades maritimes de la France métropolitaine ainsi que dans les départements et régions d'outre-mer. L'objectif de ce réseau est d'assurer le suivi de la dynamique des populations phytoplanctoniques et des conditions hydrologiques afférentes pour contribuer à une meilleure connaissance du milieu marin côtier au travers de l'étude des réponses des communautés phytoplanctoniques aux changements environnementaux, de l'évaluation de la qualité du milieu littoral et de l'impact des espèces productrices de toxines. Les paramètres mesurés toutes les 2 semaines sur la station Ouest Loscolo (en Baie de Vilaine) sont la température, la salinité, la turbidité, la concentration en oxygène dissous, la concentration en chlorophylle-a, les concentrations en nutriments et la flore phytoplanctonique.

- Le réseau SOMLIT, Service d'Observation en Milieu LITtoral (https://www.somlit.fr/), s'intéresse aux échelles locales et régionales pour décrire les eaux de surface françaises au niveau de l'hydrologie, la biogéochimie et l'écologie à travers des mesures de 16 paramètres dont la température, la salinité, la turbidité, la concentration en oxygène dissous et la concentration en chlorophylle. SOMLIT est en place depuis 1996 afin d'observer 11 écosystèmes sur 19 points d'échantillonnage bi-mensuels à travers des protocoles et des contrôles qualités standardisés. Les mesures sont effectuées à pleine mer. Les données de la station Brest sont utilisées dans cette thèse (Chapitre 4 & Chapitre 6).

2.1.1.2 Débits des rivières

Les données journalières du débit des rivières sont enregistrées par les Agences de l'Eau du territoire français (www.hydro.eaufrance.fr). Les rivières considérées pour cette étude sont en partant du nord vers le sud : la Seine (Chapitre 5), l'Elorn, la Mignonne et l'Aulne qui se déversent en rade de Brest (Chapitre 4) et puis la Vilaine et la Loire qui influencent la baie de Vilaine (Chapitre 6). Les stations les plus proches des zones d'études sont utilisées et pour la Vilaine, l'influence du barrage d'Arzal est pris en compte dans le débit analysé.

2.1.1.3 Niveaux d'eau

La marée est un processus clé de l'environnement côtier. La hauteur d'eau est mesurée toutes les minutes depuis plusieurs décennies à l'aide de marégraphes du réseau SONEL (Système d'Observation du Niveau des Eaux Littorales, https://www.sonel.org). Dans cette étude plusieurs marégraphes sont utilisés tous opérés par le Shom (www.data.shom.fr) qui sont : Le Havre en baie de Seine (Chapitre 5), Brest en rade de Brest (Chapitre 4) et Le Crouesty en baie de Vilaine (Chapitre 6).

2.1.1.4 Paramètres météorologiques

Les mesures atmosphériques, libres d'accès (Météo-France) sont disponibles à haute fréquence avec une fréquence comprise entre 6 minutes et 1 heure (https://donneespubliques.meteofrance.fr) en fonction des stations. Plusieurs paramètres sont utilisés pour prendre en compte les processus jouant sur les événements extrêmes: les précipitations, le flux solaire, la température de l'air et le vent (direction et intensité). Les données de trois stations sont mobilisées pour cette étude: Guipavas et Vannes-Séné (Chapitre 4 & Chapitre 6); Cap de la Hève (Chapitre 5).

2.1.2 Données environnementales satellitaires

Le satellite AQUA lancé par la NASA en 2002 a pour mission d'étudier le cycle de l'eau et reste opérationnel encore en 2023. AQUA embarque le radiomètre MODIS (Gohin et al., 2019; Chapitre 5) mesurant les propriétés optiques physiques de la couleur de l'eau avec plusieurs résolutions dont celle à 1 km utilisée ici. Les données de réflectance collectées sont des proxys de la concentration en matières en suspension. Elles sont converties en concentration MES via l'algorithme OC5 (Gohin, 2011). Les produits satellites ont plusieurs niveaux de traitement allant de la donnée brute (niveau 0) à des produits sur lesquels un traitement avancé est appliqué (niveau 4) définis par la NASA en 1986. Le niveau 3 (L3) est constitué de données projetées sur une grille mais non interpolées (présence de nuages). Les données MODIS à 1km ont été utilisées avec ce niveau de traitement L3. Le niveau 4 (L4) permet d'avoir un produit multi-capteurs interpolé sans données manquantes du paramètre étudié malgré la présence de nuages par exemple. Le produit L4 utilisé dans cette thèse (Chapitre 5) combine trois capteurs de couleurs de l'eau : MERIS, MODIS/Aqua et SeaWiFS (Saulquin et al., 2011). Les données sont accessibles via le portail Européen CMEMS (Copernicus Marine Environment Monitoring Service - https://marine.copernicus.eu).

Le produit OISST - Interpolation optimale de SST (Chapitre 3) procure une carte complète de SST à l'échelle du globe. OISST (Reynolds et al., 2007; Huang et al., 2021; **Figure 2-2**) combine différents jeux de données tels que des données issues de satellites, de navires, de bouées et de flotteurs Argo. L'ensemble des données de SST collectées est interpolé sur une grille régulière globale au quart de degré. Les données sont disponibles depuis 1981 sous forme de produits journaliers, hebdomadaires et mensuels qui sont libres d'accès via le portail de la NOAA (National Oceanic and Atmospheric Administration - https://www.noaa.gov).

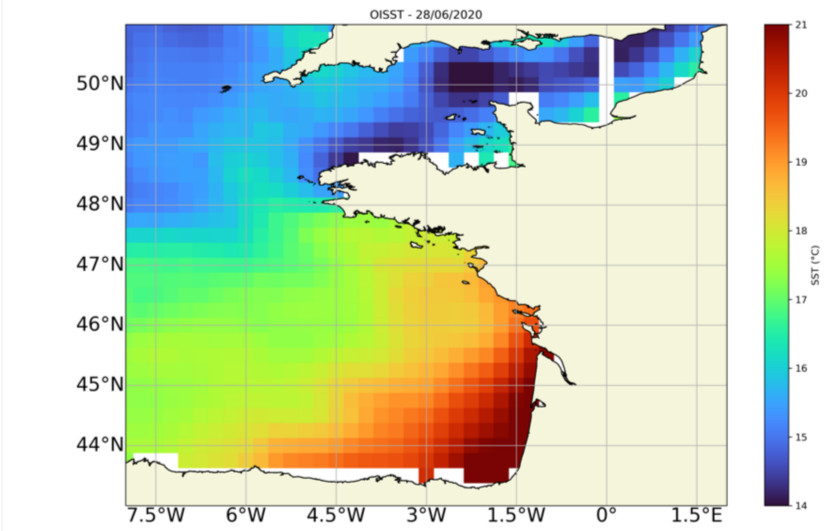

Figure 2-2 Illustration du produit OISST dans l'Atlantique Nord-Est avec une carte de SST pour le 28 juin 2020

2.1.3. Régimes de temps

A plus grande échelle, des régimes de temps peuvent être identifiés représentant une variabilité caractéristique des pressions atmosphériques. En Atlantique Nord, quatre régimes de temps sont principalement présents (Cassou et al., 2011 – **Figure 2-3**). Dans le cadre de la thèse (Chapitre 4), ces quatre cartes d'anomalies de pression atmosphérique au niveau de la mer sont représentées à partir des données de la réanalyse ERA5 du Centre Européen pour les Prévisions Météorologiques à Moyen Terme (CEPMMT, Hersbach et al., 2019).

- L'Oscillation Nord-Atlantique (NAO) décrit le gradient des pressions atmosphériques à l'échelle du bassin de Atlantique Nord, entre les hautes pressions centrées sur l'Atlantique subtropical et les basses pressions sur l'Islande (Hurrell et al., 2003). La phase positive (NAOp) induit des hivers chauds et pluvieux en Europe occidentale et est associée à des tempêtes météorologiques extrêmes. La phase négative (NAOn) induit des hivers froids et secs en Europe occidentale (Barrier et al., 2014).

- La dorsale atlantique (AR) représente un régime météorologique de blocage avec des anomalies de pression négatives autour de 60°N-20°E, et positives autour de 50°N-

25°W. L'AR apporte des anomalies de températures froides sur l'Europe occidentale et des précipitations pendant l'hiver.

- Le régime de blocage scandinave (BLK) montre une région d'anomalies de pression au niveau de la mer négatives (positives) sur le sud du Groenland (Europe du Nord). Ces anomalies de pression sont associées à un déplacement vers le nord des vents à 20°W et à des conditions de temps sec (faibles précipitations) dans le nord de l'Europe.

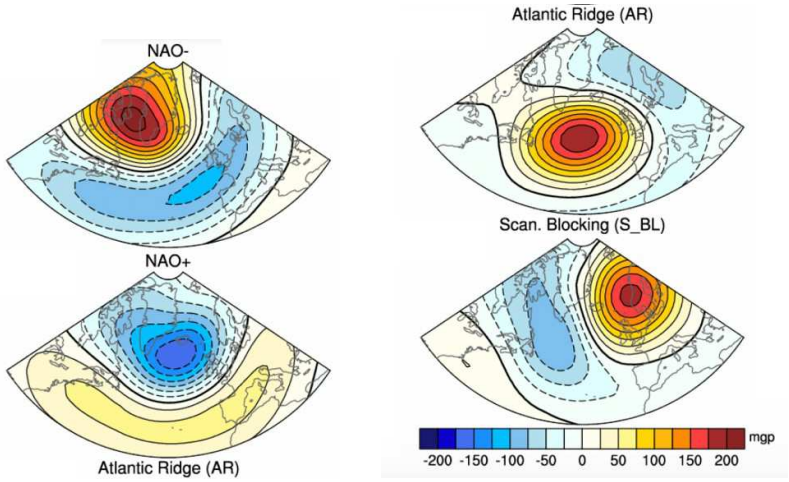

Figure 2-3 Illustration des régimes de temps dominant la variabilité de la pression atmosphérique en Atlantique Nord exprimés en mètres géopotentiels (mgp; Cassou et al., 2011)

D'autre part, les hauteurs géopotentielles de 500 hPa ont aussi été utilisées (Chapitre 3) comme références des conditions de forçages atmosphériques. Les données mensuelles comprenant les flux de rayonnement et de chaleur proviennent de la réanalyse ERA5 du CEPMMT avec une résolution spatiale de 0.25°× 0.25° (Hersbach et al., 2019).

2.1.4 Données environnementales simulées

Les modèles numériques sont des aides précieuses pour comprendre les processus et pour avoir une idée de la variabilité d'un signal complet. Les simulations numériques sont basées sur des hypothèses et certaines entrées et sorties de modèles peuvent rester peu réalistes avec une résolution spatiale à l'échelle côtière qui reste à améliorer.

2.1.4.1 MARS3D

Le modèle MARS3D est un modèle hydrodynamique 3D créé pour des applications régionales à côtières (Lazure et Dumas, 2008; Petton et al., 2023) développé par l'Institut Français pour la recherche et l'exploitation de la mer – l'Ifremer. MARS3D est un modèle numérique semi-implicite à surface libre. L'intégration des modes barotrope et baroclines est réalisée sur le même pas de temps. Les équations primitives sont résolues en prenant en compte les hypothèses de Boussinesq et les hypothèses hydrostatiques. La conservation de masse, du moment et des traceurs (salinité et température) est aussi prise en compte. La grille du modèle est constituée d'éléments finis (grille Arakawa C décalée) avec des niveaux sigmas sur la

verticale. Le modèle est décrit et validé dans plusieurs études (Lazure et al., 2009; Charria et al., 2017; Petton et al., 2020; Petton et al., 2023). Les simulations utilisées pendant la thèse - BACH et MARC (Chapitre 4), CURVISEINE3D (Chapitre 5) et MANGA ainsi que le développement du modèle MARS sous forme 1DV (Chapitre 6) – sont décrites ci-dessous.

- La simulation MARS3D-BACH (BiscAy CHannel) existe de 2001 à 2012 avec des sorties moyennes journalières. Les résolutions horizontale et verticale étaient respectivement de 1 km et de 100 niveaux sigma verticaux. Les forçages atmosphériques sont fournis par la simulation ERA-Interim (réanalyse produite par le Centre européen pour les prévisions météorologiques à moyen terme - CEPMMT; Berrisford et al., 2011) et les conditions initiales proviennent de la configuration globale DRAKKAR ORCA12_L46-MJM88 (Molines et al., 2014).

- La simulation MARS3D-MARC (Modelling and Analysis for Coastal Research) existe de 2010 à 2018 avec des sorties toutes les 5 min. Les résolutions horizontale et verticale étaient respectivement de 50 m et 20 niveaux sigma verticaux. Les forçages atmosphériques ont été extraits d'une analyse du modèle AROME (Applications de la Recherche à la Méso-échelle Opérationnelle, résolution 1.3 km ; Ducrocq et al., 2005) fournie par Météo-France. Les conditions initiales de salinité proviennent d'une autre simulation utilisant le modèle MARS3D (Caillaud et al., 2016).

- La simulation CURVISEINE3D existe de 2006 à 2019 avec des sorties horaires (ARES project, Grasso *et al*., 2021). La résolution verticale est de 10 niveaux sigma et la résolution horizontale fluctue de 2 à 4 km au large jusqu'à 100 m dans l'estuaire de la Seine sur la base d'une grille curvilinéaire. Cette simulation MARS3D (hydrodynamique) est couplée au modèle spectral de vague WaveWatch3 (WW3) et au modèle de dynamique sédimentaire MUSTANG (Le Hir et al., 2011 ; Grasso et al. 2015 ; Mengual et al., 2017). Les conditions aux frontières proviennent de WW3 à 10 km de résolution pour les vagues et de MARS3D à 2.5 km de résolution pour la température, la salinité et la marée. Les forçages atmosphériques viennent d'AROME à 1.3 km de résolution.

Un modèle 1DV (unidimensionnel vertical) a aussi été mis en œuvre pour tester dans le détail les impacts des évènements extrêmes sur l'initiation de la période productive du phytoplancton (IPGP) à partir du modèle MARS3D (Poppeschi et al., 2022). Ce modèle utilise 10 niveaux sigma pour 15 m de fond avec un temps d'intervalle de 30 s. Ce modèle 1DV couple les trois modèles décrits ci-après qui sont pour l'hydrodynamique - MARS3D, pour la dynamique sédimentaire - MUSTANG et pour la biogéochimie - BLOOM. Le modèle MARS3D-1DV permet de simuler la dynamique des nutriments et du phytoplancton. Les conditions initiales sont basées sur une simulation couplée réaliste 3D de 2015 (Plus et al., 2021).

2.1.4.2 Wave Watch 3

Le modèle physique spectral de vague Wave Watch 3 (WW3, Rolland et Ardhuin, 2014) a été exploité. Ce modèle aux conditions aux frontières ouvertes et à la grille non structurée a été développé pour mieux s'adapter à la géographie régionale. WW3, dans la configuration utilisée, a une résolution temporelle horaire et une résolution spatiale allant jusqu'à 100 m à la côte. L'avantage de ce modèle réside dans la prise en compte des courants, de la réflexion côtière et du type de substrat sédimentaire. Son utilisation en libre accès est disponible couplé à MARS3D à 2,5 km de résolution sous https://marc.ifremer.fr/ pour la baie de Seine (ARES report - Grasso et al., 2020). Les données issues du modèle sont notamment la hauteur significative (Hs), la période, la direction et la vitesse orbitale des vagues (Chapitre 5).

2.1.4.3 MUSTANG

MUSTANG est un modèle qui simule les processus hydrosédimentaires dans la colonne d'eau et dans le compartiment sédiment (Chapitre 6). Ce modèle est multiclasse avec des sédiments de type vase, sable ou gravier. La résolution verticale du modèle est adaptative dans le sédiment en fonction des processus pris en compte que sont l'advection, l'érosion, la chute et le dépôt et la consolidation (Grasso et al., 2018). Le modèle MUSTANG sert notamment à déterminer les concentrations en MES dans la colonne d'eau (Chapitre 5).

2.1.4.4 BLOOM

BLOOM (BiogeochemicaL cOastal Ocean Model) est un modèle conçu pour reproduire la dynamique des efflorescences algales à l'échelle côtière (Chapitre 6). Ces modèles biogéochimiques couplés à MARS3D permettent de simuler les processus biogéochimiques au travers de 3 cycles : azote, phosphore et silicium dans la colonne d'eau. Le phytoplancton est représenté par les diatomées, les dinoflagellés et les nanoflagellés. Le zooplancton se décompose en micro et en mésoplancton (Plus et al., 2021). Le modèle est utilisé dans la configuration 1DV et est initialisé avec une simulation ECO-MARS3D avec une résolution spatiale de 4 x 4 km et 30 niveaux sigmas (Ménesguen et al., 2019).

2.1.4.5 AROME

Le modèle atmosphérique AROME a été conçu pour améliorer les prévisions à court terme des EE de type canicule ou orage par exemple. Le modèle est développé par Météo France (https://donneespubliques.meteofrance.fr). Les simulations issues de ce modèle à 1.3 km de résolution sont disponibles depuis 2008. Les principales données accessibles sont les précipitations, la température, la vitesse du vent, l'ensoleillement et la nébulosité.

2.2 Méthodes de détection des évènements extrêmes

2.2.1 Détection des extrêmes

Deux grandes méthodes statistiques exposées par Coles (2001) permettent de détecter les extrêmes:

- la méthode des maximas par bloc (Block Maxima)
- la méthode de seuil (Peak Over Threshold – POT)

La méthode des maximas par bloc consiste à découper le signal en blocs temporels constants et à en extraire le maximum dans chacun de ces blocs. Ces valeurs sont alors considérées comme extrêmes.

La méthode de seuil consiste à choisir un seuil haut (ou bas) selon une loi statistique basée sur un percentile de la série temporelle et les valeurs au-dessus (ou en dessous) du seuil sont alors qualifiées extrêmes (**Figure 2-4**). Plusieurs variantes de la méthode de seuil existent telle que la méthode multivariée de percentiles qui permet une approche spatio-temporelle des extrêmes avec la prise en compte de la profondeur notamment (Hallin et al., 2010). Les évènements composés peuvent également être pris en compte par cette méthode, chaque paramètre est indépendamment analysé puis le cumul est reconnu extrême (Seneviratne et al., 2021).

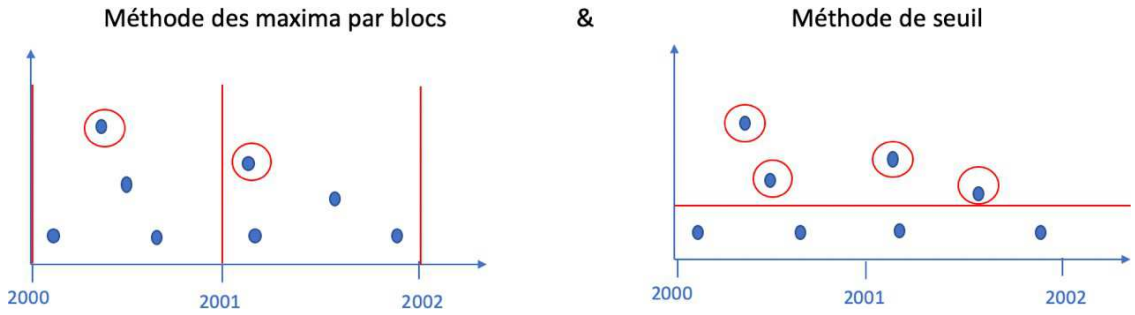

Figure 2-4 Présentation des deux principales méthodes statistiques de détection d'extrêmes avec les seuils (lignes rouge) et les évènements extrêmes (cercles rouges)

D'autres méthodes statistiques moins répandues existent. Sura (2011) explique que les extrêmes sont les valeurs qui ne font pas partie de la distribution gaussienne du paramètre étudié. Enfin, les périodes de retour sont souvent utilisées pour définir les EE météo-océaniques (Arena et al., 2015) reliés à l'ingénierie côtière (par exemple dans le cadre des énergies marines renouvelables) et à la protection du littoral. Ces périodes de retour consistent à déterminer statistiquement la durée moyenne temporelle au cours de laquelle un EE d'une même intensité va se reproduire. L'utilisation de cette méthode est pertinente mais nécessite de longues séries de mesures. Elle est utilisée pour définir l'évènement le plus intense des extrêmes, par exemple la période de retour de la tempête du 10 mars 2008 en Atlantique et en Manche sur les vents et les vagues a été évaluée à 2 ans (Cariolet, 2010). Ces méthodes statistiques sont souvent utilisées sur des données de modèle car les données manquantes dans les séries temporelles ou les interpolations conduisent à d'importants biais.

Les méthodes récentes sont basées sur l'Intelligence Artificielle (IA) et le Machine Learning. Le « multilevel spectral clustering » par exemple consiste à classer les données selon leur degré de ressemblance, les données ne rentrant pas dans une classe étant désignées comme extrêmes (Grassi et al., 2019). L'avantage de ces méthodes réside dans le non jugement de l'opérateur au regard des séries temporelles sur d'éventuelles points ou tendances peu logiques. Mais c'est aussi leur désavantage, car tout travail confié à une machine nécessite un avis d'expert avant validation. Enfin, d'autres méthodes utilisent les réseaux sociaux pour évaluer les EE passés (par exemple les tremblements de terre) via les posts en ligne de la population (Poblete et al., 2018).

Le changement climatique bouleverse les méthodes de détection existantes et certains scientifiques (Anderson et Kostinski, 2011; Rahmstorf et Coumou, 2011) prônent les méthodes dites de « record breaking » pour y palier. Les évènements records sont identifiés par rapport à la tendance moyenne du paramètre et des ratios de records faibles sur records forts sont calculés (Anderson et Kostinski, 2011). Les évènements records peuvent être détectés tout simplement via une nouvelle valeur jamais rencontrée précédemment dans le signal (Rahmstorf et Coumou, 2011). Ces méthodes sont intéressantes pour distinguer les extrêmes de la tendance du signal mais elles sont très dépendantes du site d'étude et ne permettent pas forcément d'aborder la question de la variabilité interannuelle.

La seule méthode qui convienne aux données issues de systèmes d'observations ayant un échantillonnage temporel irrégulier est la méthode de seuil. La méthode de seuil permet de détecter plusieurs extrêmes pour une même période de temps, comme illustré par Schmidt et Stadtmüller (2006). D'après une récente revue de littérature (McPhillips et al., 2018), c'est la méthode la plus utilisée dans la littérature, notamment par l'IPCC (Ren et al., 2018). Contrairement à la méthode des maximas par bloc, la méthode de seuil ne conditionne pas le nombre d'évènements extrêmes détectés ce qui permet l'étude de variations temporelles. Elle permet également d'étudier les extrêmes sous forme d'anomalies du signal. C'est une méthode efficace en termes de temps et de coût de calcul. Comme elle n'utilise pas de machine learning ou d'intelligence artificielle, elle est facile d'utilisation. Sa reproductibilité par le plus grand nombre de personnes du fait d'une paramétrisation simple et la possibilité d'analyser la sensibilité des résultats sont un point fort également. En revanche, le point faible de la méthode de seuil peut être la difficulté à justifier la valeur choisie comme seuil.

2.2.2 Le choix du seuil

Les seuils

D'après Stephenson (2008), quatre types de seuils peuvent être utilisés:

(1) le seuil constant issu du dire d'expert – par exemple, 3 mg L^{-1} d'oxygène dissous est le seuil généralement utilisé pour caractériser une hypoxie en raison des effets néfastes observés sur la faune et la flore en deçà de cette concentration (Howell et Simpson, 1994)

(2) le seuil constant issu de la loi de distribution - par exemple le percentile 90 utilisé pour définir les vagues marines de chaleur (Hobday et al., 2016)

(3) le seuil variable dans le temps issu d'une valeur record – seuil basé sur une rupture établie lors d'un record jamais atteint auparavant (Rahmstorf et Coumou, 2011)

(4) le seuil variable dans le temps issu du changement global – seuil rattaché à l'évolution de la tendance globale (Walsh et al., 2020)

Dans mon étude, le type de seuil doit être adapté au paramètre analysé et être applicable sur l'ensemble des côtes françaises.

Le seuil concernant les dessalures extrêmes a été choisi comme un seuil constant fixe basé sur le percentile P85 (Poppeschi et al., 2021). Il est appliqué uniquement aux données enregistrées à marée basse (à +/- 20 min du pic de marée), période propice à l'observation des desssalures les plus extrêmes. Pour éviter plusieurs détections d'une même dessalure, une dessalure extrême doit durer au moins un cycle de marée complet (soit 12 heures). Le choix d'une valeur seuil statistique basée sur percentile plutôt que d'une valeur seuil issue d'un dire d'expert permet d'appliquer la même méthode dans des zones géographiques ayant des caractéristiques très différentes (ex : Méditerranée ou Manche).

Le seuil concernant les vagues marines de chaleur et de froid est issu d'un consensus scientifique (Hobday et al., 2016 ; Simon et al., 2023). Ce seuil est un seuil statistique comme celui utilisé pour la détection des dessalures extrêmes sauf qu'il est variable car calculé à partir d'une climatologie journalière sur au moins 30 ans de données (Oliver et al., 2018). Le percentile utilisé pour les vagues marines de chaleur est le P90 et pour les vagues marines de froid le P10. Ces seuils doivent être dépassés pendant une durée minimale de 5 jours pour détecter un EE. Les EE de vagues de chaleur seront détectés uniquement en été et les EE de vagues marines de froid en hiver.

Le seuil choisi pour définir les EE de turbidité est basé sur les forçages extrêmes de vagues et de crues (Poppeschi et al., soumis, 2023). Ce seuil est basé sur le percentile P90, des vagues et des crues, lissé sur un mois. Ce seuil varie donc au cours de l'année pour prendre en compte les variations propres au signal. Il est transposable sur plusieurs sites.

La justification du seuil

Afin de développer des méthodes optimales de détection des EE, certains tests sur les seuils employés sont réalisés. Le premier point consiste à déterminer quel est percentile de distribution prendre pour détecter des extrêmes. Statistiquement, le Mean Residual Life Plot permet de différencier une série temporelle d'une autre série temporelle présentant une distribution normale parfaite (Coles, 2001). Ainsi selon la forme de la courbe on peut identifier la longueur de la queue de distribution (courte ou longue) ou bien encore en apprendre sur la distribution du paramètre par rapport à sa variance par exemple. Cependant, ce calcul est généralement

utilisé avec des modèles de prédictions et n'est pas adapté aux données *in situ* qui sont souvent discontinues, bruitées et dont la distribution ne suit pas toujours la loi normale. Le percentile pour les valeurs fortes extrêmes le plus couramment utilisé est le percentile 90 et le percentile 10 pour les valeurs faibles extrêmes (Hobday et al., 2016 ; McPhillips et al., 2018). Ce choix provient généralement d'un bon compromis vis-à-vis de la longueur de la série utilisée car à partir de seuils plus élevés les statistiques sont calculés sur très peu de points pas forcément représentatifs d'un évènement dans sa globalité (Oliver et al., 2021). Dans la littérature d'autres seuils sont utilisés pour parler d'extrêmes, le percentile 95 (Tavora et al., 2023) voir même le percentile 99 (Anagnostopoulou et Tolika, 2012). Une première étape consiste à comparer différents percentiles entre eux et à analyser le nombre d'évènements extrêmes détectés. Ces études comparatives de seuil se retrouvent dans la littérature comme c'est le cas entre les percentiles 1, 5 et 10 sur des données d'observation par satellite pour les extrêmes climatiques à partir de la fraction du rayonnement photosynthétiquement actif absorbé (Zscheischler et al., 2013) ou encore entre les percentiles 80, 85 et 90 sur des données de bouées *in situ* pour les dessalures extrêmes (Poppeschi et al., 2021).

Ensuite, on s'intéresse à la période sur laquelle le seuil peut être calculé. Les climatologues ont tendance à préconiser la période de temps la plus longue possible, de minimum 30 ans (Schlegel et Smit, 2016). Cependant, récemment le calcul de seuil sur 10 ans de données a été montré comme suffisant pour détecter des EE (Schlegel et al., 2019). Les océanographes n'ont pas forcément des données d'observations sur des périodes aussi longues du fait de la difficulté de mesure et de l'avènement récent des systèmes d'observation océaniques. De plus, du fait du changement climatique la période de référence pour le calcul du seuil est remise en question car les évolutions rapides du signal sont très différentes parfois entre les décennies.

Enfin, la variabilité du seuil est un paramètre important à prendre en compte si l'on s'intéresse à la variabilité interannuelle ou saisonnière. Les seuils sont fixés dans la littérature quand on fait référence à un état écologique, par exemple l'abondance et la diversité de poissons est plus forte si l'oxygène dissous excède 3 mg L^{-1} que lorsqu'il est en dessous de 2 mg L^{-1} (Howell et Simpson, 1994). La plupart du temps les seuils sont saisonniers comme par exemple les vagues de chaleur qui sont étudiées selon une climatologie établie en été et les vagues marines de froid sont étudiées selon une climatologie calculée sur l'hiver (Hobday et al., 2016). Seulement, avec le changement climatique certains extrêmes sont détectés en bordure de ces saisons. Ou même, certains extrêmes sont détectés en dehors des saisons attendues et c'est d'ailleurs des évènements qui engendrent bien souvent des dégâts importants en favorisant le développement de bactéries si les crues extrêmes se produisent en même temps qu'une température de l'eau élevée par exemple (Esteves et al., 2015).

Analyses sur le choix du seuil

Les paramètres extrêmes ou les forçages extrêmes peuvent être classés selon leurs distributions statistiques. Les distributions sont tracées pour le débit, la température, la salinité, la turbidité, la fluorescence et l'oxygène dissous (**Figure 2-5**). Le débit et la turbidité (**Figure 2-5ab**) présentent des distributions avec des variances importantes (GROUPE A), la

température, la salinité, la fluorescence et l'oxygène (GROUPE B) ont des variances beaucoup plus faibles (**Figure 2-5cdef**). Ces représentations statistiques de chaque paramètre extrême peuvent être un outil dans la méthode de détection des EE pour déterminer le choix du seuil à prendre en compte comme expliqué ci-dessous.

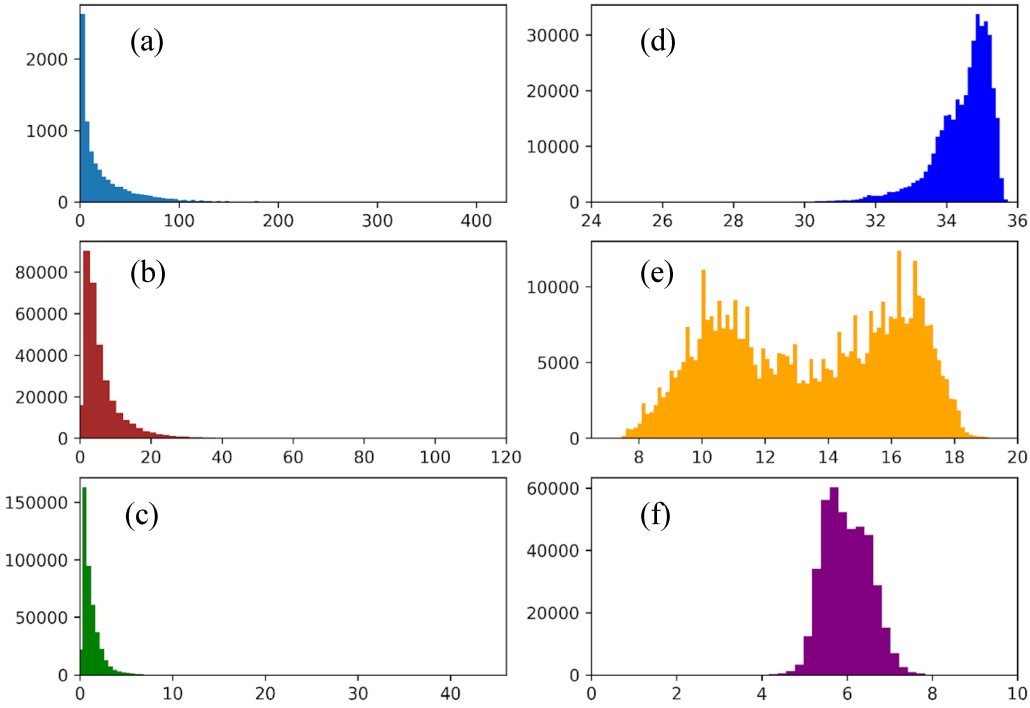

Figure 2-5 Distribution statistique des paramètres environnementaux issus de COAST-HF tels que (a) le débit (m^3 s^{-1}), (b) la turbidité (NTU), (c) la fluorescence (FFU), (d) la salinité, (e) la température (°C) et (f) l'oxygène dissous (mg L^{-1})

Le choix du percentile pour la détection des extrêmes est important à considérer. De 2000 à 2022 en rade de Brest, les percentiles 80, 85, 90, 95 et 99 sont calculés pour le débit, la température, la turbidité et la fluorescence. On s'intéresse aux MHW, pics de turbidité pendant les tempêtes et pics de biomasse phytoplanctonique. Les percentiles 1, 5, 10, 15, 20 sont calculés pour la température, la salinité et l'oxygène dissous afin de regarder les MCS, les dessalures extrêmes et les phénomènes d'hypoxie/anoxie détectés (**Figure 2-6**).

Pour l'ensemble des paramètres, les percentiles les plus extrêmes que sont 99 et 1 se distinguent fortement des autres seuils testés et permettent d'avoir des évènements extrêmes qui ne sont pas détectés tous les ans. Ensuite, les paramètres se classent en deux catégories avec d'un côté le débit, la turbidité et aussi la salinité mais de façon moins marquée (**Figure 2-6a**) qui présentent des seuils qui se distinguent aisément et donc où le choix du percentile a beaucoup d'impact sur la détection des EE. Et d'un autre côté, ceux où les seuils sont très rapprochés comme pour la température, la fluorescence et l'oxygène dissous et donc des

paramètres pour lesquels le choix du percentile aura peu d'influence sur la détection des EE en terme de nombres notamment (**Figure 2-6b**). Ces deux catégories d'EE se distinguent alors par leurs distributions et la variabilité de leurs signaux.

(a)

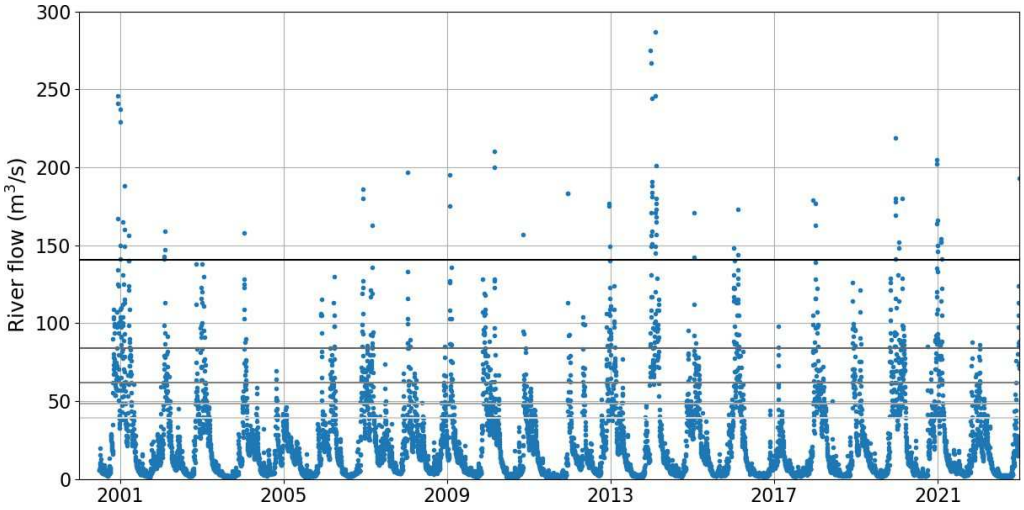

(b)

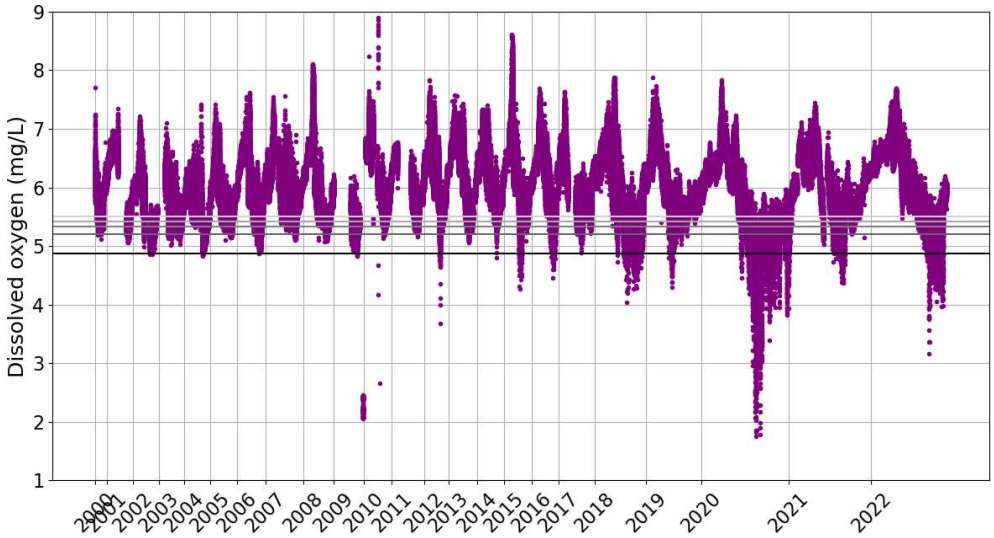

Figure 2-6 Séries temporelles enregistrées à la bouée Marel-Iroise en rade de Brest et pour la rivière Aulne de 2000 à 2022. (a) Les percentiles 80, 85, 90, 95 et 99 fixes sont testés sur le débit représentant le groupe A et (b) Les percentiles 1, 5, 10, 15 et 20 fixes sont testé sur la concentration en oxygène dissous représentant le groupe B. **Les percentiles sont représentés par un dégradé de gris avec le noir représentant les valeurs les plus extrêmes comme le percentile 1 et 99 et le blanc représentant les valeurs les moins extrêmes telles que le percentile 20 et 80.**

Des analyses sont aussi effectuées pour comparer les extrêmes détectés selon les durées sur lesquelles le seuil est calculé (**Tableau 2-1**). Le percentile 90 des séries de débit, température, salinité, turbidité, fluorescence et oxygène dissous est appliqué sur une période de 10 ans à partir de maintenant, puis de 15, 20, 30, 40 et 50 ans quand les données existent. Le percentile calculé sur 10 ans est pris comme référence.

Les paramètres peuvent être classés en deux groupes avec des seuils qui varient énormément selon la période de calcul du seuil comme c'est le cas pour la turbidité et le débit (GROUPE A) avec une diminution de 42% de la valeur du seuil entre l'application du percentile 90 sur 10 ans en comparaison avec son application sur 20 ans - pour la turbidité ou de 15% sur 50 ans - pour le débit (en grisé – **Tableau 2-1**). La température, la salinité, la fluorescence et l'oxygène (GROUPE B) semblent avoir peu de variations selon la durée retenue pour le calcul du seuil, qu'elle soit égale à 10 ans ou 20 ans avec une légère diminution de 2% pour la température. La salinité, l'oxygène dissous et la fluorescence présentent même un seuil identique pour une durée de 10 comme de 20 ans (en gras – **Tableau 2-1**). Les diminutions de seuil impliquent des seuils de détection plus bas pour ceux calculés sur de plus longues années. Cela a pour conséquence un plus grand nombre d'EE détectés en comparaison des détections sur la base d'un seuil calculé uniquement sur la dernière décennie.

Percentile 90	Débit	Turbidité	Température	Salinité	Oxygène	Fluorescence
10 ans	67.01	25.10	17.34	**35.16**	**6.69**	**2.26**
15 ans	61.72	17.11	17.14	**35.31**	**6.77**	**2.20**
20 ans	59.80	14.69	17.03	**35.29**	**6.72**	**2.26**
30 ans	61.60					
40 ans	59.40					
50 ans	57.30					

Tableau 2-1 **Valeurs de seuil déterminées par le percentile 90 fixe calculé sur des périodes de 10, 15, 20, 30, 40 et 50 ans de données consécutives pour la turbidité (NTU), le débit (m^3 s^{-1}), la température (°C), la salinité (PSU), l'oxygène dissous (mg L^{-1}) et la fluorescence (FFU)**

Enfin, la variabilité du seuil est testée à travers des seuils fixés par bloc temporel ou encore des seuils variables temporellement selon une climatologie choisie. Les paramètres testés sont la température, la salinité, la turbidité, la fluorescence et l'oxygène dissous. Tous les seuils sont calculés à partir du percentile 90 sur les données existantes entre 2000 et 2022. Les seuils testés sont les suivants: fixé par saison, fixé par mois, variable par saison et variable par mois. Les seuils fixés correspondent à la valeur du percentile 90 calculé sur chacune des 4 saisons de l'année et sur chacun des 12 mois de l'année de façon individuelle. Les seuils variables correspondent à des moyennes glissantes journalières du percentile 90 calculées sur +/- 1.5 mois pour les saisons et sur +/- 15 jours pour les mois.

Pour tous les paramètres, les deux seuils fixes (par mois ou par saison) se retrouvent proches l'un de l'autre et la situation est identique pour les seuils variables. Les seuils fixés ont des valeurs très basses (ou très élevées) à certains moments de l'année et vont détecter plus d'évènements que les seuils variables qui restent à des valeurs de détection plus constantes et assez élevées (ou assez basses) tout au long de l'année (**Figure 2-7**).

(a)

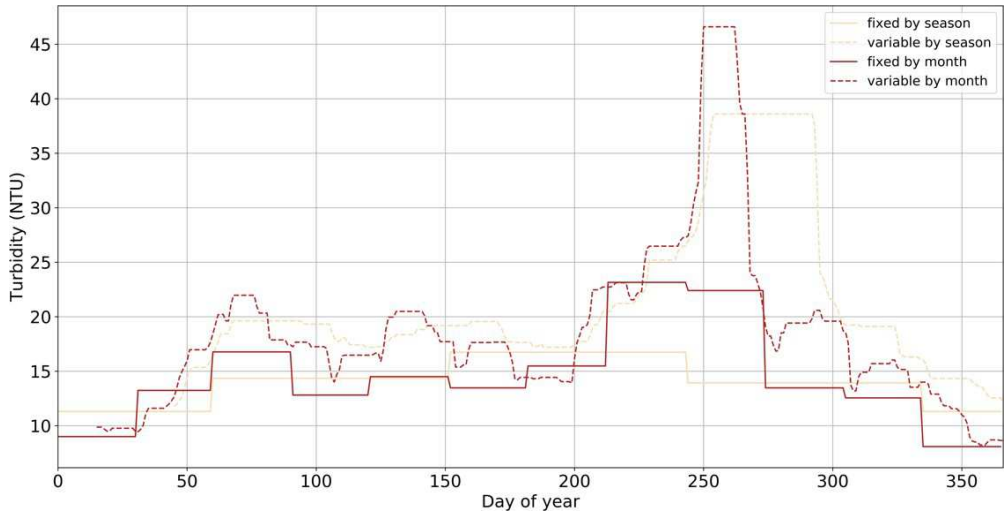

(b)

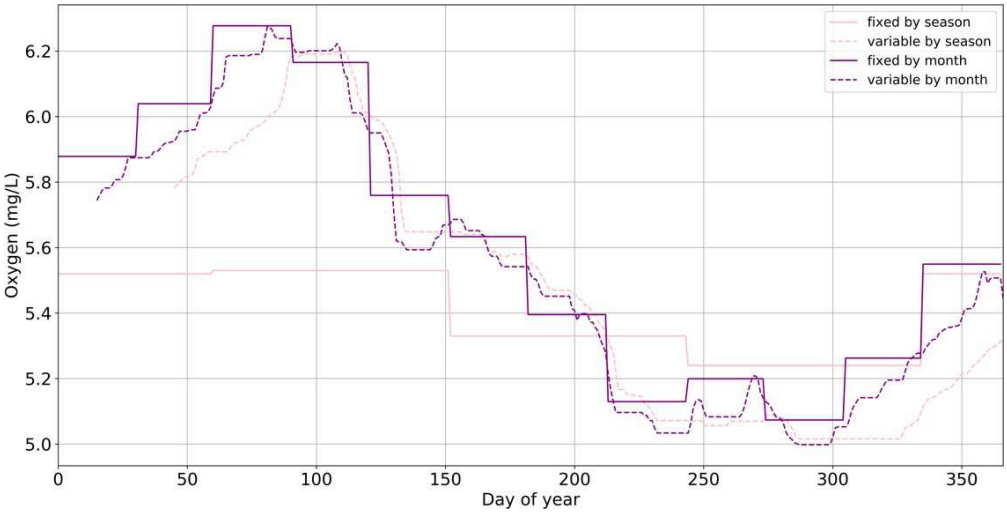

Figure 2-7 Percentile 90 fixé ou variable par saison ou par mois calculé pour (a) la turbidité et (b) l'oxygène dissous en rade de Brest de 2000 à 2022

2.2.3 Les filtres à appliquer pour la détection d'extrêmes

Pré-traitement des données

Pour toute étude scientifique, le prétraitement des données est primordial (Zscheischler et al., 2013). Les extrêmes sont souvent des points éloignés et isolés de la moyenne qu'il ne faut pas confondre avec des points aberrants. Toutes les données doivent faire l'objet, si possible d'un contrôle qualité par un expert et doivent être qualifiées en conséquence. Pour éviter les biais, il est nécessaire de quantifier le nombre de données manquantes. Par exemple, l'étude de certaines années sera abandonnée si le nombre de données disponibles est trop restreint. Si le

nombre de données manquantes n'est pas trop important, on peut avoir recours à l'interpolation si les analyses le nécessitent.

Certaines données nécessitent un filtrage pour éliminer des interférences de mesures. C'est le cas pour les données de fluorescence chlorophyllienne qui sont soumises à l'effet Quenching, c'est à dire à la diminution de la fluorescence en présence de lumière (**Figure 2-8**, Lehmuskero et al., 2018). Les données de fluorescence sont alors sélectionnées pour ne garder que celles de la nuit. Un autre filtre couramment utilisé est celui de la marée (**Figure 2-9**). La marée, par son amplitude intratidale durant le flot/jusant et de pleine mer/basse mer, influence des paramètres tels que la salinité (Poppeschi et al., 2021) ou la turbidité (Poppeschi et al., à soumettre, 2023).

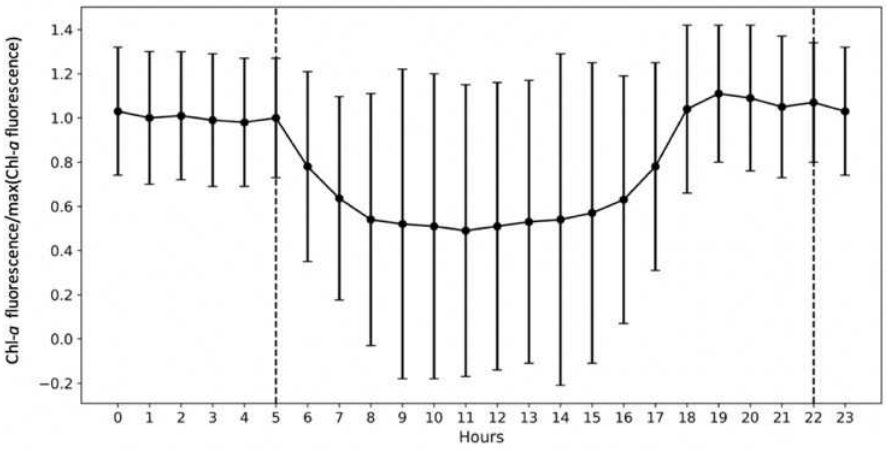

Figure 2-8 Influence de la lumière sur la variation du signal de fluorescence chlorophylienne selon les heures de la journée (Poppeschi et al., 2021)

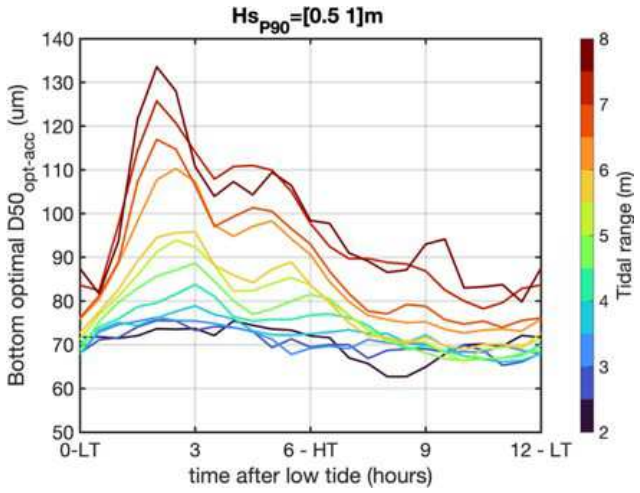

Figure 2-9 Influence de la marée sur la taille des matières en suspension - Climatologie intratidale de D50$_{opt-acc}$ (diamètre médian des matières en suspension) calculée sur la période 2015-2022 par rapport à l'amplitude de marée dans des conditions de faibles vagues (Hs$_{P90}$=[0.5-1]m) (Verney et al., à soumettre, 2023)

Validation et données in situ

Les données *in situ* sont considérées comme des données vraies mais elles n'ont pas forcément une résolution temporelle et spatiale suffisante. Les données issues de modèles et d'images satellites sont alors utilisées et dépendent d'algorithmes complexes liés à notre connaissance du milieu. Par conséquence, ces données issues de modèles et d'images satellites ont besoin d'être validées avec les données *in situ* (**Figure 2-10**). Il est important de comparer les jeux de données entre eux et voir s'ils observent une variabilité du signal identique et si celle-ci diffère de savoir comment et pourquoi. Une première étape de validation consiste à superposer les jeux de données entre eux comme c'est le cas pour les SPM en baie de Seine entre les données modèles et les données de la bouée (**Figure 2-10**). Ensuite, un coefficient de corrélation peut aussi être calculé entre les jeux de données.

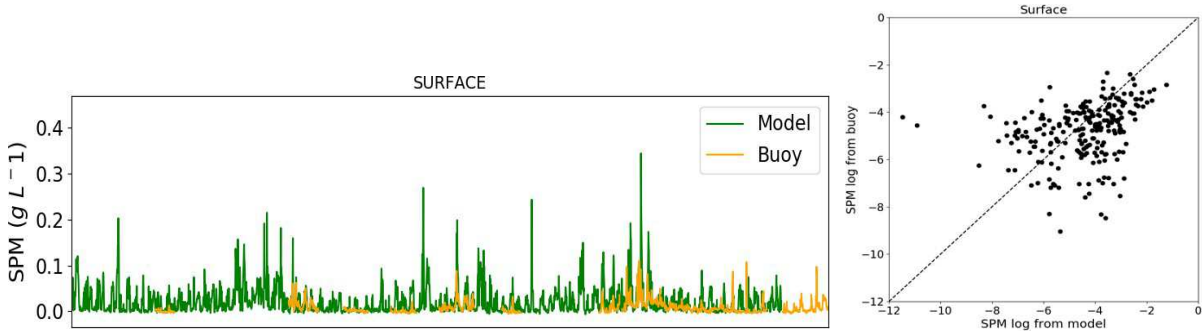

Figure 2-10 Exemple de la validation de données de concentration de matières en suspension issues de simulations numériques et comparées à des données *in situ* (Poppeschi et al., 2023)

Filtres sur la durée des évènements extrêmes

L'évènement extrême se doit d'être borné pour être qualifié d'évènement. On considère qu'il ne doit pas être trop long pour ne pas englober plusieurs petits EE qui seraient représentatifs d'un seul EE unique au final. Il ne doit pas être trop court non plus pour constituer un évènement et ne pas englober uniquement un point de mesure par exemple ou encore de prendre en compte un cycle de marée entier si non filtré au préalable.

Evolutions et référence temporelle

On peut envisager de traiter les données en amont de la détection des extrêmes en retirant la tendance linéaire ou non linéaire du paramètre choisi. Plusieurs calculs de tendances classiques existent du type Mann Kendall mais de nombreuses nouvelles méthodes apparaissent. Amaya et al. (2023) proposent de retirer la tendance linéaire pour la prise en compte des évènements extrêmes. Rahmstorf et Coumou (2011) rappellent que la tendance entre extrême et moyenne climatique n'est pas vraiment linéaire. La tendance sera d'autant plus visible et présente dans les données si celles-ci sont à basse fréquence plutôt qu'à haute fréquence comme l'indiquent Anderson et Kostinski (2011) en comparant des données mensuelles et journalières. Des tests peuvent là aussi être réalisés comme fait par Zscheischler

et al. (2013) en retirant la tendance, en retirant le cycle saisonnier puis les deux et enfin en retirant la déviation standard de chaque donnée. Izquierdo et al. (2022) expliquent que la tendance est dynamique plutôt que statique et que c'est celle-ci qu'il faut prendre en compte. Ce qui vient à introduire les points de ruptures, de bascules et de changements très importants à prendre en compte dans les tendances. Le point de rupture est associé à un changement de tendance abrupte et irréversible (Milkoreit et al., 2018). Le point de bascule ou d'inflexion représente un changement dans la continuité de la tendance lié au changement climatique (Werners et al., 2015). Le point de changement ou juste aussi appelé le seuil est le moment où un seuil de préoccupation est susceptible d'être dépassé et remarquable dans la tendance globale (Werners et al., 2013). Ces points de changements peuvent être remarqués via l'étude des trajectoires d'écosystèmes par analyse en composante principale par exemple (Lheureux et al., 2021).

Le changement climatique est en constante évolution et cette évolution est d'autant plus rapide ces dernières décennies. Ces différents points dans les tendances sont d'intérêt majeur pour adapter la détection des extrêmes dans le temps et garder une définition commune. Ils doivent être pris en compte lors de l'analyse des évolutions dans la dynamique des EE.

2.2.4 Les caractéristiques d'un événement extrême

L'évènement extrême présente des caractéristiques propres (**Figure 2-11**). Après avoir réalisé un état de l'art sur les caractéristiques des extrêmes, cinq grandes catégories ressortent.

Le **nombre ou le taux d'occurrence** ou encore la fréquence des évènements extrêmes (McPhillips et al., 2018). C'est un des premiers paramètres lié aux extrêmes qui est mis en avant notamment pour parler de tendances.

L'**intensité** définit un extrême par sa très forte ou très faible valeur. Dans cette catégorie plusieurs paramètres existent :

- l'intensité cumulée qui est la somme de l'intensité pendant sa durée.
- l'intensité moyenne ou sévérité (Stephenson et al., 2008) qui est la moyenne de l'intensité au-dessus du seuil de détection.
- l'intensité par rapport au seuil qui est la valeur maximale de l'évènement retiré au seuil de détection.
- l'intensité maximale ou dite valeur de pic (Biondi et al., 2008) qui est la valeur maximale de l'évènement.

La **durée** de l'évènement extrême est le temps écoulé entre le début et la fin de l'évènement. La durée se retrouve sous le terme de rapidité (Stephenson et al., 2008) et peut être cumulée (McPhillips et al., 2018).

L'**étendue spatiale** de l'évènement extrême est souvent regardée vis-à-vis de son impact sur l'environnement. Le terme de zone d'impact ou distribution spatiale est employé.

L'évènement extrême peut être rangé de façon régionale (Ren et al., 2018) et plus globalement dans une classe géographique du type hauturier, côtier, national ou local (Ren et al., 2018).

La **période temporelle** de l'évènement est décisive en termes d'impact également. Certains extrêmes sont étudiés à l'échelle d'une saison quand d'autres sont étudiés toute l'année. La rareté temporelle de l'occurrence de l'évènement est un facteur de dégâts potentiels important.

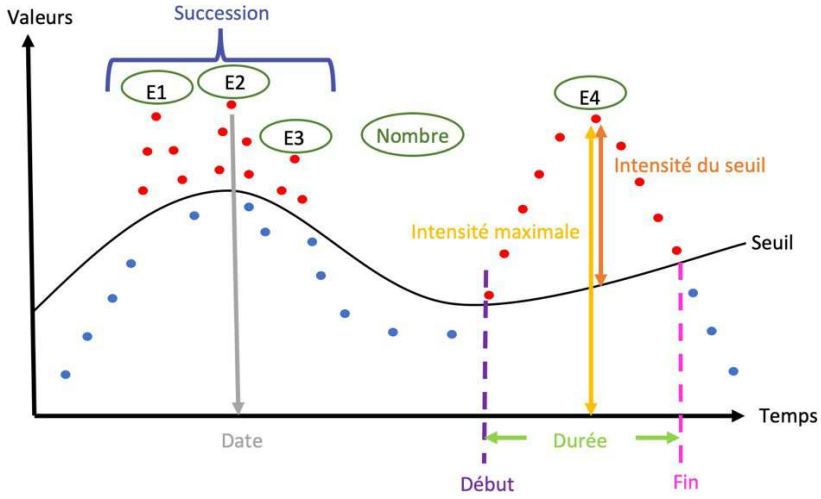

Figure 2-11 Caractéristiques majeures d'un évènement extrême

D'autres paramètres sont intéressants à mentionner. Parmi eux, la période de retour des évènements extrêmes est une caractéristique propre aux EE (Coles, 2001; McPhillipps et al., 2018; IPCC, 2023). La période de retour d'un évènement est la durée pour laquelle statistiquement un évènement extrême d'une même intensité se reproduit (Olsen et al., 2006). Les dépendances d'un évènement extrême à diverses variables de l'environnement sont à prendre en compte pour mieux les caractériser et comprendre les processus qui les contrôlent dans l'objectif de mieux les prédire aussi par la suite (Stephenson, 2018). Enfin le cumul des évènements extrêmes ou autrement dit leurs successions rapprochées est un paramètre supplémentaire à identifier. Un évènement extrême seul peut avoir peu d'impact mais plusieurs évènements rapprochés sur une courte période de temps peuvent avoir un impact important.

Enfin, des paramètres intégrateurs regroupent les caractéristiques générales des extrêmes. Nous pouvons, par exemple, mentionner l'activité (Simon et al., 2022; Simon et al., 2023). L'activité combine l'intensité moyenne, la durée et l'étendue spatiale de l'évènement extrême. Les paramètres intégrateurs ou indices permettent de classer les extrêmes selon leurs caractéristiques.

Au cours de la thèse une classification liée aux cinq caractéristiques principales a été mise en place. Les 10% des EE détectés sont ainsi classés en ordre croissant selon leur nombre, leur intensité, leur durée, leur étendue spatiale et leur période temporelle d'occurrence. Toutefois cette classification n'est pas exhaustive et un poids différent à chaque caractéristique pourrait être attribué en lien avec l'impact des EE dans le futur.

2.3 Régions étudiées

La méthodologie ainsi mise en place est appliquée sur les sites d'études suivants. Pour chaque paramètre étudié, un environnement donné est pris en exemple afin de mieux comprendre les processus qui le régulent et d'adapter notre méthode de détection des extrêmes. Ces environnements côtiers (**Figure 2-12**) sont sélectionnés pour plusieurs raisons scientifiques mais également du fait qu'ils présentent des séries de mesures à hautes fréquences sur plusieurs années consécutives.

Les dessalures sont étudiées en rade de Brest, baie semi-fermée à régime macrotidal, où les sols des bassins versants sont imperméables et saturés en eau directement reliés à l'influence des rivières (Tréguer et al., 2014). Ce qui permet une réponse directe de l'écosystème aux forçages que sont les tempêtes pluvieuses gouvernées par les régimes de temps dans l'Atlantique Nord (Cassou et al., 2011). La rade de Brest est un site majeur de pêche qui pourrait être perturbé par ces extrêmes dans le futur.

Les vagues marines de chaleur et de froid sont désormais des phénomènes extrêmes étudiés à l'échelle mondiale (Oliver et al., 2021). Leur étude est ici étendue et détaillée dans l'Atlantique Nord-Est pour la première fois afin d'y étudier leurs évolutions ces dernières décennies et d'y comprendre les processus qui les dirigent.

Les plus grands panaches turbides sont principalement liés aux crues des rivières. L'étude est basée en baie de Seine qui est reliée à l'estuaire de la Seine, l'un des trois plus grands estuaires français (Etcheber et al., 2007). Les estuaires et les mers adjacentes sont des environnements soumis à des forçages majeurs comme le débit, la marée et les vagues. Les estuaires sont des zones d'intérêt au niveau écologique, économique et sociétal. L'estuaire de la Seine possède un bouchon vaseux qui est intéressant à prendre en compte quand on s'intéresse à la dynamique sédimentaire, il est aussi connu pour transporter d'importantes concentrations en contaminants.

Les sites de la rade de Brest et de la baie de Vilaine ont été choisis pour l'étude de l'initiation de la période productive du phytoplancton (IPGP) car, s'ils sont proches géographiquement et considérés tous les deux comme eutrophes, ils sont différents en termes d'hydrodynamique : une baie semi fermée à régime macrotidal en rade de Brest comparée à une baie semi-ouverte à régime mésotidal en baie de Vilaine.

Ainsi pour chaque site d'étude et chaque paramètre associé, une analyse scientifique commune des extrêmes est mise en place à travers trois étapes majeures : Détecter, caractériser et comprendre les processus associés aux évènements extrêmes.

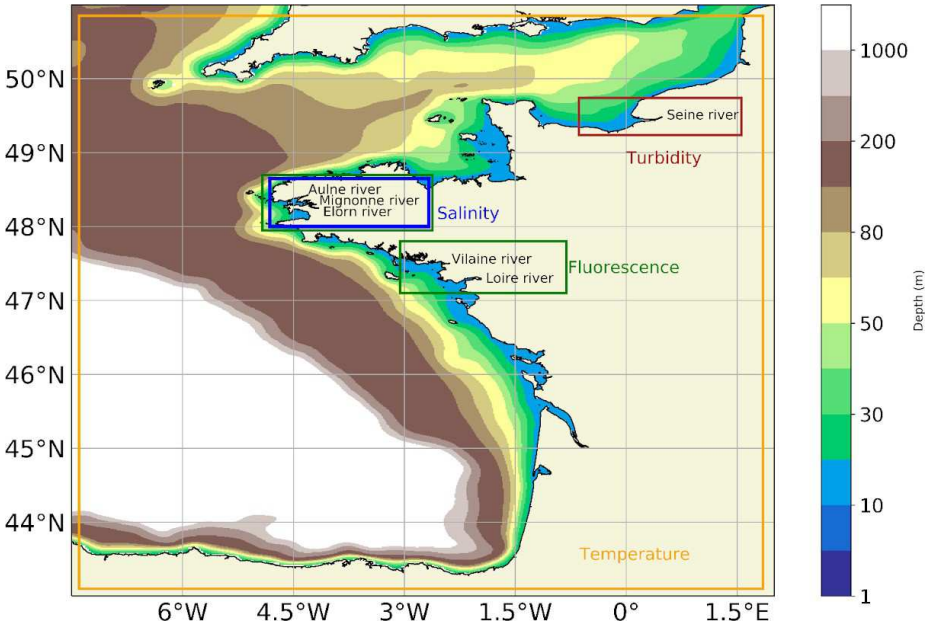

Figure 2-12 Carte avec les sites d'études de la thèse pour les cinq paramètres clés de l'environnement côtier reliés aux extrêmes

Chapitre 3 Les vagues marines de chaleur et de froid en Atlantique Nord-Est

Dans ce chapitre, le premier compartiment de l'écosystème, soit la physique, est analysé à partir du signal de température. La dynamique des MHW et MCS est étudiée dans l'Atlantique Nord-Est.

3.1 Résumé

Le changement climatique entraîne l'augmentation des MHW et la diminution des MCS (Oliver et al., 2019). Les MHW et MCS se caractérisent par une anomalie de température de surface de la mer pendant plusieurs jours par rapport à une référence saisonnière. Les MHW et MCS dans l'océan sont directement reliées aux vagues atmosphériques de chaleur et de froid à l'échelle globale. En Méditerranée, ces phénomènes sont très étudiés (Darmaraki et al., 2019 ; Simon et al., 2021) comme dans l'océan global, car les impacts sur la biologie sont nombreux (Smith et al., 2023). Ces évènements extrêmes peuvent induire la destruction d'habitats à la base de l'écosystème comme les herbiers et les coraux par exemple (Fordyce et al., 2019 ; Stipcich et al., 2022). Dans notre étude, ces phénomènes extrêmes sont caractérisés, pour la première fois à cette échelle, dans l'océan Atlantique Nord-Est. Pour cela, nous avons analysé les données issues du produit OISST qui regroupe des données de satellite et d'autres types de mesure en mer et qui permet de connaître l'étendue spatiale de ces phénomènes extrêmes. Des données de 13 bouées *in situ* issues de plusieurs réseaux européens, anglais, français et espagnol, ont aussi été analysées. L'étude se concentre sur 3 régions qui sont la Manche, la rade de Brest et le Golfe de Gascogne de 1982 à 2022. Une fois détectées, les MHW et MCS sont caractérisées selon plusieurs paramètres : le nombre d'événements, l'intensité, la durée et l'étendue spatiale. Un paramètre intégrateur appelé « activité » exprimé en °C.jour.km^2 permet d'évaluer l'importance de ces événements extrêmes en combinant les paramètres énoncés ci-dessus (Simon et al., 2022).

Les résultats de l'ensemble des bouées et des images satellites pour chacune des régions étudiées sont en accord, ce qui confirme l'applicabilité de la méthode. La variabilité interannuelle pour chaque zone s'accorde autant pour les MHW que pour les MCS. La quasi-disparition des MCS après 2000 est mise en évidence. Cette étude montre par ailleurs une augmentation de l'activité des MHW depuis le début des années 2000 et plus prononcée depuis les années 2010. Deux années se distinguent en termes de forte activité des MHW qui sont 2018

et 2022. Cette étude plus spécifique de l'océan côtier montre une même évolution par rapport à l'océan ouvert avec une augmentation des MHW en été et une diminution des MCS en hiver, et cela, au cours des quatre dernières décennies. Une importante variabilité régionale est remarquée. Ces changements sont rapides pour les 3 régions, la Manche présente les plus importantes évolutions. Les forçages atmosphériques globaux contrôlent la dynamique de ces MHW et MCS même à l'échelle côtière. Pendant les MHW, on retrouve un anticyclone au-dessus de Europe du Nord et une dépression à l'ouest de la péninsule ibérique au niveau atmosphérique et l'inverse pour les MCS.

Ce travail, en collaboration avec l'institut Dom Luiz au Portugal, est publié dans Ocean Sciences (Simon et al., 2023).

3.2 Article : Coastal and regional marine heatwaves and cold-spells in the Northeast Atlantic

Ocean Sci., 19, 1339–1355, 2023
https://doi.org/10.5194/os-19-1339-2023

Ocean Science Open Access EGU

Coastal and regional marine heatwaves and cold spells in the northeastern Atlantic

Amélie Simon[1], Coline Poppeschi[2], Sandra Plecha[1], Guillaume Charria[2], and Ana Russo[1]

[1]Instituto Dom Luiz (IDL), Faculdade de Ciências, Universidade de Lisboa, 1749-016, Lisbon, Portugal
[2]Univ. Brest, CNRS, Ifremer, IRD, Laboratory for Ocean Physics and Satellite remote sensing (LOPS), IUEM, 29280 Plouzané, France

Correspondence: Amélie Simon (ajsimon@fc.ul.pt)

Received: 8 March 2023 – Discussion started: 28 March 2023
Revised: 13 July 2023 – Accepted: 17 July 2023 – Published: 6 September 2023

Abstract. The latest Intergovernmental Panel on Climate Change (IPCC) report describes an increase in the number and intensity of marine heatwaves (MHWs) and a decrease in marine cold spells (MCSs) in the global ocean. However, these reported changes are not uniform on a regional to local basis, and it remains unknown if coastal areas follow the open-ocean trends. Surface ocean temperature measurements collected by satellites (from 1982–2022) and 13 coastal buoys (from 1990–2022) are analyzed in the northeastern Atlantic and three subregions: the English Channel, Bay of Brest and Bay of Biscay. The activity metric, combining the number of events, intensity, duration and spatial extent, is used to evaluate the magnitude of these extreme events. The results from in situ and satellite datasets for each of the studied regions are quite in agreement, although the satellite dataset underestimates the amplitude of activity for both MHWs and MCSs. This supports the applicability of the method to both in situ and satellite data, albeit with caution on the amplitude of these events. Also, this localized study in European coastal northeastern Atlantic water highlights that similar changes are being seen in coastal and open oceans regarding extreme events of temperature, with MHWs being more frequent and longer and extending over larger areas, while the opposite is seen for MCSs. These trends can be explained by changes in both the mean of and variance in sea-surface temperature. In addition, the pace of evolution and dynamics of marine extreme events differ among the subregions. Among the three studied subregions, the English Channel is the region experiencing the strongest increase in summer MHW activity over the last 4 decades. Summer MHWs were very active in the English Channel in 2022 due to long events, in the Bay of Biscay in 2018 due to intense events and in the Bay of Brest in 2017 due to a high occurrence of events. Winter MCSs were the largest in 1987 and 1986 due to long and intense events in the English Channel. Finally, our findings suggest that at an interannual timescale, the positive North Atlantic Oscillation favors the generation of strong summer MHWs in the northeastern Atlantic, while low-pressure conditions over northern Europe and a high off the Iberian Peninsula in winter dominate for MCSs. A preliminary analysis of air–sea heat fluxes suggests that, in this region, reduced cloud coverage is a key parameter for the generation of summer MHWs, while strong winds and increased cloud coverage are important for the generation of winter MCSs.

1 Introduction

Heatwaves and cold spells are extreme events in which there is a strong anomaly in temperature for a certain period which can occur at a regional spatial scale. This type of phenomenon can occur both in the atmosphere and in the ocean, with remarkable consequences for both terrestrial and marine ecosystems (Ruthrof et al., 2018). In the case of marine events (hereafter referred to as marine heatwaves, MHWs, or marine cold spells, MCSs), severe large-scale biodiversity losses may occur such as species extinction, habitat destruction, and abrupt changes in the geographical distribution and structure of communities as well as the nutrient cycle (Frölicher and Laufkötter, 2018; Ruthrof et al., 2018; Smale et al., 2019). Additionally, a decrease in the density of ma-

Published by Copernicus Publications on behalf of the European Geosciences Union.

rine algae forests and coral bleaching (Wernberg et al., 2016; Smale et al., 2019) have also been reported.

The frequency, duration and intensity of these extreme phenomena affecting ocean systems have been increasing in recent decades (among others, Lima and Wethey, 2012; Oliver et al., 2018; Frölicher et al., 2018; Plecha and Soares, 2020; Simon et al., 2022). As a result of global and regional warming heavily influenced by anthropogenic factors, the intensity and annual number of MHWs will continue to accelerate globally (Oliver et al., 2019; Plecha et al., 2021). Conversely, as oceans warm, MCSs are diminishing (Schlegel et al., 2021; Simon et al., 2022) and are expected to continue to decline in the future (Yao et al., 2022). However, these changes are not uniform regionally, and it remains unknown if coastal areas follow the open-ocean trends.

This paper focuses on the coastal and regional northeastern Atlantic and three subregions (English Channel, Bay of Brest and Bay of Biscay) as these zones are important for socio-economic activities (e.g., fishery; Guo et al., 2022) and have contrasting dynamical environments. Plecha et al. (2021) studied MHW annual features in the whole northern Atlantic using low-resolution satellite data at $1° \times 1°$ over the period 1971–2000. They show that in the Bay of Biscay, the mean frequency is about 12 events per year and is characterized by ~ 12 d of mean duration and 0.4 °C of mean intensity. Marin et al. (2021) did a global analysis of MHWs in coastal areas over the period 1992–2016 based on a multi-satellite product at a resolution from $0.25° \times 0.25°$ to $0.05° \times 0.05°$. They found that, in the Bay of Biscay and English Channel from 1992–2016, MHWs occurred on average three times per year, lasting about 20 d with a mean intensity of 1.5 °C. Here we focus on these regions at the seasonal timescale, such as summer MHWs and winter MCSs, using a satellite product at $0.25° \times 0.25°$.

Long-term ocean warming is an important driver of the increase in MHWs (Frölicher et al., 2018) and the diminishing of MCSs (Schlegel et al., 2021; Wang et al., 2022) but does not explain shorter variabilities in these events or their interannual variability. These marine extreme events are also driven by other local and remote processes acting across a large range of spatial and temporal scales (Holbrook et al., 2019; Schlegel et al., 2021). Modes of atmospheric circulation variability can induce anomalous sea-surface temperature (SST) through modification of air–sea heat fluxes and/or displacement due to ocean current advection (Deser et al., 2010), which, for extreme cases, can lead to MHWs or MCSs.

Interannual summer atmospheric variability in the northern Atlantic–European sector has been shown to be predominantly led by the Summer North Atlantic Oscillation (SNAO) pattern. The SNAO is identified as strong high-pressure anomalies dominating northern Europe and weaker low pressure over Greenland and the Iberian Peninsula, which explains about 20 % of the variance using sea-level pressure (Hurrell et al., 2003). The SNAO is recognized as at a more northerly location and smaller spatial scale than the winter NAO pattern. During the positive phase of the SNAO, northern Europe experiences drier, warmer and reduced-cloudiness conditions, and the Bay of Biscay, the English Channel, and the North and Baltic seas undergo warmer SST (Folland et al., 2009). The East Atlantic (EA) pattern is also identified as a dominant mode of northern Atlantic atmospheric variability (Barnston and Livezey, 1987), which is particularly important for the northwestern Iberian Peninsula climate in all seasons (Lorenzo et al., 2008). It is a north–south dipole that spans the entire northern Atlantic Ocean, with centers southeastward of the NAO pattern (winter and summer).

Although there is strong evidence of the influence of large-scale features, no consensus exists on atmospheric patterns associated with summer MHWs in the Bay of Biscay and the English Channel. On the one hand, Holbrook et al. (2019) identify the Bay of Biscay as a region for which there is a significant increase in annual MHW days during a positive phase of the NAO, based on a linearly detrended SST with satellite data and the NAO index. On the other hand, Izquierdo et al. (2022a) suggest, based on the analysis of two in situ buoys in the coastal south of the Bay of Biscay, that the incidence, duration and intensity of spring–summer MHWs are higher during the positive phase of the EA. However, for each of these two studies, only one climate index out of the numerous modes of summer atmospheric variability in the northern Atlantic–European sector was considered.

MCSs have also been reported to occur as a response to atmospheric forcing through anomalous winds and air–sea heat fluxes, especially in coastal regions where cold-air outbreaks over shallow water can cause rapid chilling of water (Crisp, 1964; Schlegel et al., 2021). But to the best of our knowledge, no study has been published focusing on the connection between MCSs and atmospheric circulation in the Bay of Biscay and the English Channel.

At a more regional scale, Guinaldo et al. (2023) linked the 2022 MHW off France to anomalies of above-average solar radiation, below-average cloud coverage and negative wind speed, also showing the importance of hydrodynamic conditions such as the tide that allow for turbulent vertical mixing. This explains why the Mediterranean Sea with weak tidal ranges presents a more pronounced response to MHWs (Darmaraki et al., 2019; Simon et al., 2022). Other studies have been carried out in terms of the processes and detection of MHWs in the Bay of Biscay but only along the Spanish Cantabrian coast. Namely, Izquierdo et al. (2022b) found a steady increase in SST from 1998 to 2019, which was reflected in MHW occurrence and a consequent matchup to report population shifts in coastal macroalgae. In a second study, Izquierdo et al. (2022a) compared MHWs with satellite data and found a 6-fold increase in their incidences in the last 4 decades, with half of this increase related to climate change.

Several studies focus on the impact of MHWs or MCSs on biological systems, covering the areas of the Bay of Biscay, the English Channel or the Spanish Cantabrian coast, reaching as far back as the 1960s. These studies analyzed the atmospheric cold spells of winter 1962–1963 on the English coast and the impact on marine animal mortality such as that of *Pecten maximus* (Crisp, 1964) or migration of species such as flounder (Sims et al., 2004). In the English Channel, Gómez and Souissi (2008) made the link between the MCS of 2005 and the absence of the spring bloom of *Phaeocystis*. A delay in the initiation of the phytoplankton bloom caused by the presence of MCSs at the end of winter in the Bay of Brest and in the Bay of Vilaine (in the northern part of the Bay of Biscay) is observed by Poppeschi et al. (2022). The impact of MHWs on biology is even more studied than the cold counterpart. Gómez and Souissi (2008) show the link between the heatwave of 2003 in the English Channel and the abundance of dinoflagellates. Joint and Smale (2017) demonstrate a link between MHWs and microbial activity assemblage in the English Channel which controls biogeochemical cycles in the ocean. The MHW of 2018 in the English Channel is present in the literature for its mortality mass impact on mussels (Seuront et al., 2019), link to fucoids (Mieszkowska et al., 2020) or harmful phytoplankton blooms (Brown et al., 2022). Predictions at the atmospheric scale point to an increase in the future of heatwaves in the Bay of Biscay (Chust et al., 2011) and a decrease in marine fauna (Wethey and Woodin, 2022).

In this context, we aim to describe and explain the evolutions of the MHWs over summer and MCSs over winter activity in the northeastern Atlantic and to investigate the regional variability in three subregions: the English Channel, the Bay of Brest and the Bay of Biscay. The analysis will rely on both in situ and satellite data to address MHW and MCS activity, aiming to evaluate the impact of such events in coastal regions and in the open ocean. This approach will allow us to evaluate the potential use of in situ measurements to detect, characterize and understand such extreme events. In the last section of this paper, we focus on the influence of the interannual atmospheric mode of variability involved in the occurrence of MHWs and MCSs in the northeastern Atlantic by finding the atmospheric circulation occurring in phase with most of the strongest events.

2 Material and methods

2.1 Satellite and reanalysis data

The global SST data used in this study result from a combination of different observational platforms, including satellites, ships, buoys and Argo floats, provided by the National Oceanic and Atmospheric Administration (hereafter OISST, optimum interpolation sea-surface temperature; Reynolds et al., 2007; Huang et al., 2020). The satellite products have a daily temporal coverage for the 1982–2022 period and are interpolated to a regular global grid of 0.25° spatial resolution. Monthly geopotential height at 500 hPa (z500), surface net shortwave radiation flux, surface net longwave radiation flux, surface sensible heat flux and latent radiation heat flux data were obtained from the European Center for Medium-Range Weather Forecasts (ECMWF) reanalysis data (ERA5) at a spatial resolution of 0.25° × 0.25° (Hersbach et al., 2020).

2.2 Buoy data

The in situ SST data are from autonomous coastal buoys that take continuous high-frequency measurements from 10 min to 1 h (Fig. 1a). These buoys are from different European organizations, detailed below and in Table S1 in the Supplement, covering the coastal areas of the English Channel, the Bay of Brest and the Bay of Biscay.

The national observation infrastructure network (Coastal OceAn observing SysTem – High Frequency, COAST-HF; http://www.coast-hf.fr, last access: 2 January 2023) operates 14 buoys taking measurements of several physical and biogeochemical parameters all around French coasts, among which, 7 buoys are used here and are located in the English Channel (Carnot, CARN, https://doi.org/10.17882/39754; Smile, SMIL, https://doi.org/10.17882/53689; Astan, ASTA), in the Bay of Brest (Iroise, IROI, https://doi.org/10.17882/74004; Smart, SMAR, https://doi.org/10.17882/86020) and in the Bay of Biscay (Molit, MOLI, https://doi.org/10.17882/46529; Arcachon, ARCA). The Met Office (https://www.metoffice.gov.uk, last access: 2 January 2023) manages several buoys and also offshore sites. The buoys used here are located in the English Channel, on the southern coast of England, at Seven Stones (SEVE), Channel (CHAN) and Greenwich (GREEN). The Western Channel Observatory (WCO; https://www.westernchannelobservatory.org.uk, last access: 4 April 2023), situated within the western English Channel, operates two oceanographic moorings. The station L4_Q located near the city of Plymouth, approximately 7 km offshore, is used here. Puertos del Estado (http://www.puertos.es, last access: 2 January 2023) operated two buoys along the Spanish coast: Bilbao (BILB) and Gijón (GIJO), located in the Cantabrian Sea; both of them are used here.

2.3 Detection of MHWs and MCSs

To detect marine temperature extreme anomalies, we use the definition of Hobday et al. (2016). First, a climatology over 40 years, from 1982 to 2022, is calculated from the satellite product. Then, we apply the 90th percentile to summers (JJAS, June–July–August–September) for MHW and the 10th to winters (DJFM, December–January–February–March) for MCS. Finally, an MHW (MCS) is detected if values are above (below) the threshold for at least 5 d. For in situ

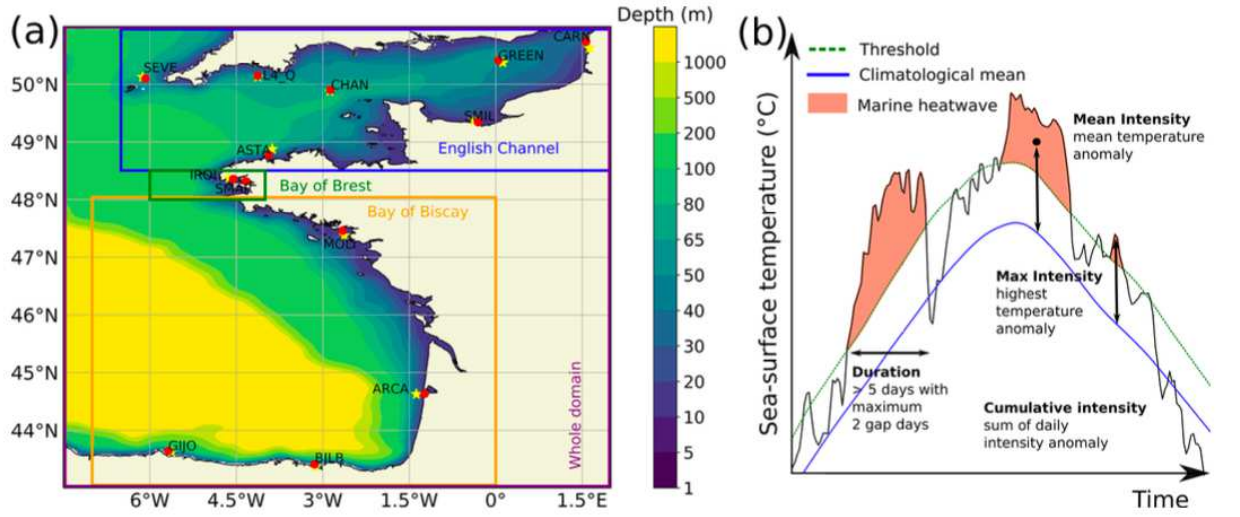

Figure 1. **(a)** Map of the study area including the whole domain (northeastern Atlantic) (purple box) as well as the three subregions which are the English Channel (blue box), the Bay of Brest (green box) and the Bay of Biscay (orange box). The buoys are represented by red dots, and the closest satellite points are represented by yellow stars. **(b)** Schematic of MHW detection and properties as defined by Hobday et al. (2016).

data, the same detection method is applied considering the climatology calculated from the satellite product. Only seasons (summer or winter) with more than 80 % of available data are analyzed.

To characterize MHWs and MCSs, we analyze parameters such as the number of events, the duration, the spatial extent and the cumulative intensity, defined as in Hobday et al. (2016) (Fig. 1b). We also explore an integrated indicator of these different parameters characterizing the marine temperature extreme events (MHWs and MCSs), called activity and defined by Simon et al. (2022). This indicator estimates for each grid point the cumulative combination of the mean intensity, the duration and the affected area of each extreme event within a selective time range (for example JJAS). This activity index accounts explicitly for the area, as in most SST products a grid cell area differs from one latitude to another and marine thermal events can expand over large areas. The activity is calculated for each grid point. It sums the product of the mean intensity, duration within the selected time range and area of each detected event occurring within the selected time range. The activity is written as follows:

$$\text{activity} = \sum_{\text{EE} \in \text{TimeRange}} \text{meanintensity}_{\text{EE}} \times \text{duration}_{\text{EE} \cap \text{TimeRange}} \times \text{area}_{\text{EE}},$$

where EE $\in$ TimeRange denotes the extreme event (EE) that occurs within the selected time range, the mean intensity of EE (in °C) is the mean temperature anomaly with respect to the climatology of the event, duration EE $\cap$ TimeRange (in days) is the duration of the event that remains within the considered time range and area_{EE} (in km^2) is the area affected by the discrete event within a predefined domain. Time series involving the activity metric for a domain are calculated as the mean of every grid cell considered. The activity for each station is computed in °C d without considering the area influenced by the events, as it can not be estimated from single localized stations.

This method of detection and characterization of marine thermal extreme events is performed over the whole domain of this study, referred to as the northeastern Atlantic (43–51° N, 8° W–2° E), and at each station where in situ observations are available. As illustrated in Fig. 1, three different subregions will be analyzed in detail, namely (i) the English Channel (48.5–51° N, 6.5° W–2° E), (ii) the Bay of Brest (48–48.5° N, 6–4° W) and (iii) the Bay of Biscay (43–48° N, 7–0° W). This will allow us to explore these regions separately and highlight regional patterns. Those three subregions can be associated with three contrasting hydrodynamical regimes: macrotidal (English Channel), semi-enclosed bay (Bay of Brest) and mesotidal (Bay of Biscay; Charria et al., 2013).

3 Results

3.1 Evolution of marine heatwave activity

3.1.1 An integrated regional view

MHWs were detected over the northeastern Atlantic. The activity index (Fig. 2a) highlights two main periods in the MHW dynamics. Before 2003, MHW activity remained moderate to weak with activity generally lower than 5 °C d 10^3 km^2 corresponding to 1.2 mean occurrences per

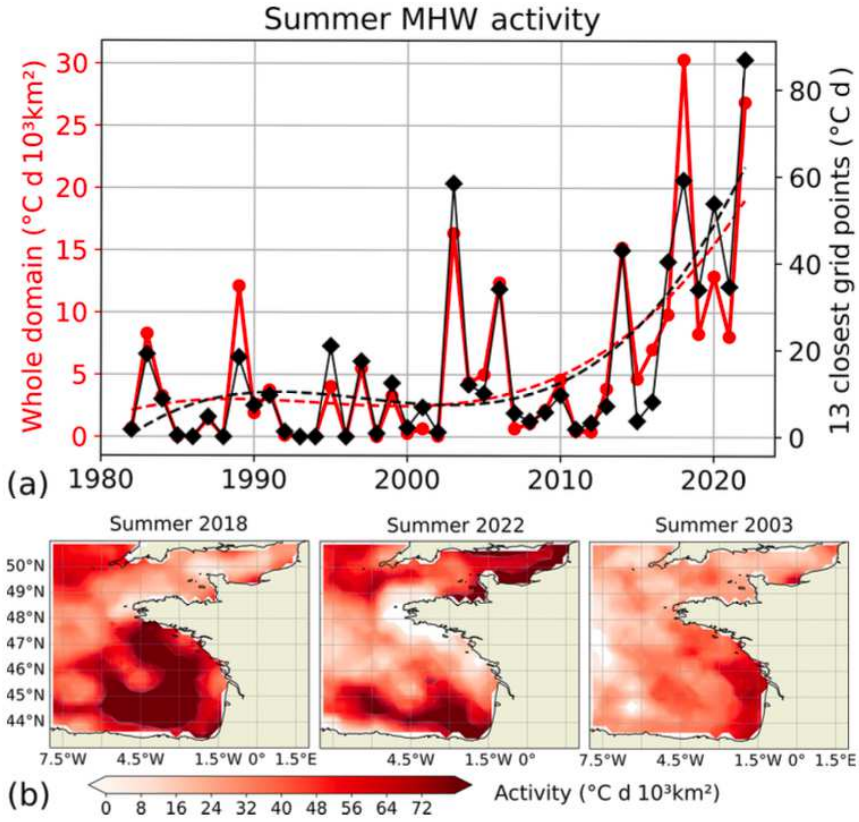

Figure 2. **(a)** Times series of summer (JJAS) MHW mean activity in the northeastern Atlantic from the satellite product (red curves with circle marks) and for the average of the 13 grid cells closest to the buoys from the satellite product (black curves with diamond marks). Dashed lines represent the regression of a third-order polynomial of the solid line with the same color. **(b)** Summer (JJAS) activity (first row; in °C d 10^3 km^2) for the top three summers in terms of activity in the northeastern Atlantic (from left to right).

summer with a mean duration limited to 8 d (Fig. 3). Only summer 1989 displayed strong MHW activity (exceeding 10 °C d 10^3 km^2) before 2000. From 2003 onward, the activity increased to over 30 °C d 10^3 km^2 for summers 2018 and 2022 associated with more than 2.5 mean occurrences lasting around 20 d. The mean intensity remains quasi-steady during the whole period. The interannual variability and trend of the summer MHW activity for the whole domain is similar to the ones obtained for the average activity of the 13 grid cells closest to the buoy locations (black lines of Fig. 2), suggesting that, at 1 order of magnitude, coastal and open-ocean regions follow the same evolution.

The three most active summers are 2018, 2022 and 2003 (Fig. 2a). During 2018 (Fig. 2b), the maximum activity is located in the Bay of Biscay over the outer continental shelf and the continental slope from the southern part of the bay. These events also extend to the north to southern Brittany and are limited by the Ushant tidal front (Le Boyer et al., 2009; Müller et al., 2010). Regions of minimum activity during 2018 are west of French Brittany in the Ushant front region, where tides are efficiently mixing the water column. Similarly, the activity remains weak in the English Channel, as it is a macrotidal region. In terms of duration, longer events are observed in the southern part of the Bay of Biscay, exceeding 30 d (Fig. S1 in the Supplement). The 2022 summer is the second most active year for the whole domain, with over 25 °C d 10^3 km^2, and also the strongest in terms of marine activity over coastal regions as shown by the maximum value of the average activity near the 13 buoys considered (Fig. 2a). Spatially, the English Channel and the north of Spain record the strongest MHW activity, while the French Brittany coast has no occurrence over this year (Fig. 2b). In the English Channel, the mean duration of the summer 2022 events was around 35 d (Fig. S2 in the Supplement), with localized events lasting more than 50 d (Fig. S1). In northern Spain, the duration of the events was around 20 d; however, they occurred very frequently over the summer with strong mean MHW intensities of around 2 °C (Fig. S1). In 2003 (Fig. 2c), the MHW activity spatial distribution was different than in 2018 and 2022. The activity is larger over the inner continental shelf along western French coasts in the Bay of Biscay. This region is under the influence of significant river

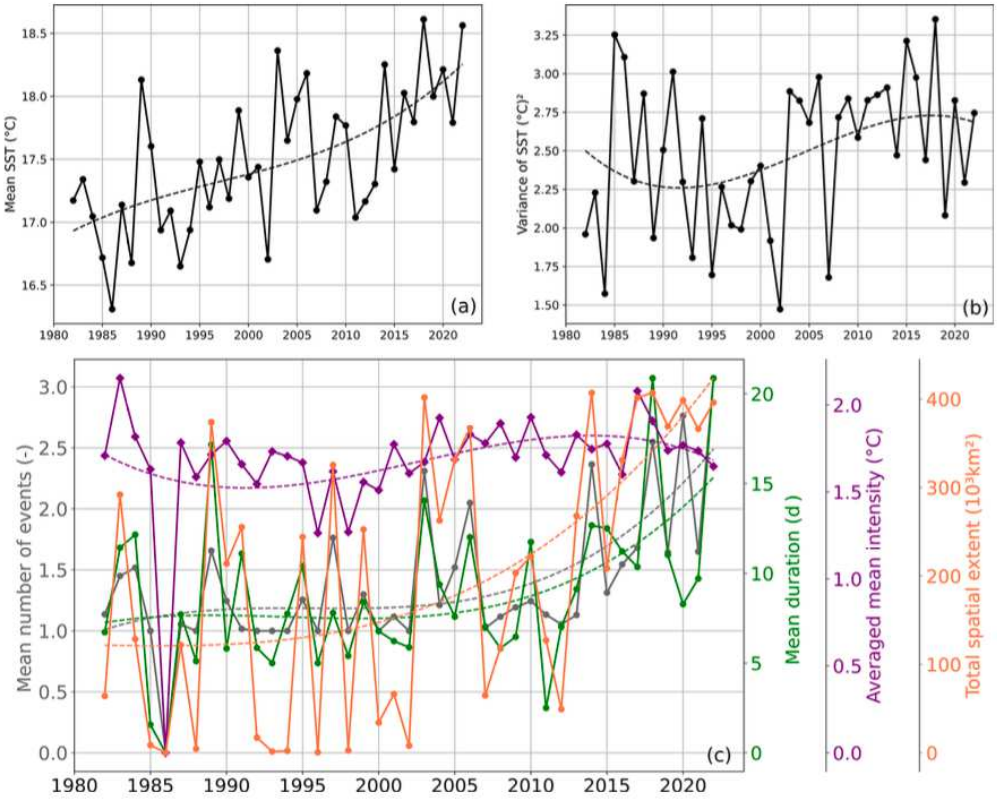

Figure 3. Time series of the **(a)** mean and **(b)** variance of SST (black curve) of summers (JJAS) over the northeastern Atlantic for the period 1982–2022. The SST variance is calculated for each year over the respective domain and measures the spread of the spatial distribution. **(c)** Mean properties of summer (JJAS) MHWs in the northeastern Atlantic. The mean number of events (grey curve with circle marks) is the number of events within the summer averaged over the domain (without considering cells with no event). The mean duration (green curve with circle marks) is the average duration of every event within the summer and domain. The averaged mean intensity (purple curve with diamond marks) is the average of the mean intensity of every event within the period and domain. The total spatial extent (orange curve with circle marks) is the sum of each grid cell area where one or more events occur. If more than one MHW occurs in the same cell, only one grid cell area is taken into account. Dashed lines represent the regression of a third-order polynomial of the solid line with the same color.

plumes along this coast (Adour, Gironde and Loire rivers). During this year, river discharge could have induced stratification (inducing faster warming of the surface mixed layer in regions of freshwater influence; Oh et al., 2023), and warmer waters from rivers suggest that observed MHWs were sustained by an atmospheric event more centered over lands. During this summer, the number of events is larger in the western English Channel, but the events are shorter and less intense than in the Bay of Biscay. These top three active summers highlight the interannual spatial variability in MHW activity. The detailed mean features (number of events, duration and mean intensity) of summer MHWs over the period 1982–2022 in the northeastern Atlantic, English Channel, Bay of Brest and Bay of Biscay are documented in Table S2 in the Supplement.

The mean SST has been increasing over the 40 years with an approximately linear trend, showing a mean warming of nearly 1.5 °C for the whole domain since 1982 (Fig. 3). Regionally, it is observed that the increase in the mean SST is almost yearly constant for the Bay of Biscay region and quadratic for the English Channel and Bay of Brest, where a plateau is observed around 1995–2010 (Fig. S2).

The SST variance is calculated for each year over the respective domain and measures the spread of the spatial distribution. Over the northeastern Atlantic, 1985–2002 and the 5 most recent years are characterized by a decline in the SST variance, while around 1992–2017 an increase in the SST variance is observed. This interannual trend is similar to the ones observed for the events' intensity, with the exception of the English Channel showing a direct relationship between the SST variance and the mean intensity of the MHW events. In the English Channel, Bay of Brest and Bay of Biscay, the mean SST is warming and the variance is increasing. This estimation suggests that they both contribute to the changes in the respective MHW activity (Fig. S2).

The English Channel and the Bay of Biscay in situ stations highlight the year 2022 as the most active year exceeding 140 °C d. In the Bay of Brest, the impact of the 2022 MHWs is less pronounced, in agreement with satellite observation (Fig. 2b), due to tidally driven vertical mixing.

When we compare MHW activity estimated from in situ stations and satellite products, values are generally larger from in situ stations. Those differences are explained by the underestimation of extreme temperatures in coastal regions in remotely sensed products.

3.2 Evolution of marine-cold-spell activity

3.2.1 An integrated regional view

Figure 5 depicts winter MCS evolution for the whole domain over the last 4 decades (1982–2022). MCS activities decrease linearly during the first half of the period, showing almost no occurrence after 2000 with the exception of 2006 and 2009 to 2011. A similar evolution is seen by considering the average of the 13 grid points closest to each in situ station.

The three most active MCSs occur in winter 1987 ($-24\,°C\,d\,10^3\,km^2$), 1986 ($-18\,°C\,d\,10^3\,km^2$) and 1994 ($-13\,°C\,d\,10^3\,km^2$). In the two coldest winters, MCSs were dominant in the English Channel, especially off the northern French coast in winter 1987. These two winters are characterized by a few (~ 1 event; Fig. S4 in the Supplement) long (~ 50 d) and intense (~ -2.5 °C anomalous SST) events. This region is subject to high turbulent mixing generated by the tidal current, which could favor cold conditions. By contrast to these two winters (1987 and 1986), winter 1994 featured strong MCS activity in the center of the Bay of Biscay, due to numerous (~ 5 events) but moderately intense (~ -1.3 °C) and relatively short (20 d) events. The three winters of 2009–2011 present very localized extremely cold conditions along the coastal Armorican shelf and additionally in the English Channel for 2011 (not shown). The detailed mean features (number of events, duration and mean intensity) of winter MCSs over the period 1982–2022 in the northeastern Atlantic, English Channel, Bay of Brest and Bay of Biscay are documented in Table S3 in the Supplement.

The mean and variance evolution of SST, as well as the mean evolution of MCS properties (occurrence, duration, mean intensity and spatial extent), is presented over the whole domain (Fig. 6) and separately for the English Channel, the Bay of Brest and the Bay of Biscay (Fig. S5 in the Supplement). Over the whole northeastern Atlantic domain, the SST mean increases and spatial dispersion (variance) decreases, with both showing a plateau around 1995–2010, following the English Channel and the Bay of Biscay evolution. On the contrary, a steady increase in the mean SST and a nearly constant variance of SST are seen in the Bay of Brest.

The warmer winter seen over the whole domain and for the three subregions is consistent with the decrease in the extremely cold conditions, depicted by the mean MCS activity. The decrease in the mean MCS activity is controlled by the strong decrease in spatial extent (350×10^3 to $50 \times 10^3\,km^2$), the moderate decrease in the number of events (2 to 1.2 events) and the small decrease in duration (13 to 9 d). The mean intensity does not show any trend (~ -1.5 °C).

The decrease in spatial dispersion (variance) of SST over the whole domain indicates a more uniform evolution which is explained by a dominant warming trend that is stronger for colder areas. Indeed, the relatively cold English Channel's temperature increased by 1.5 °C (from 9 to 10.5 °C), and the relatively warmer Bay of Biscay increased by 0.8 °C (from 11.8 to 12.6 °C) over the 1982–2022 period. When considering the three subregions individually, localized enough to be under a similar trend, the variance also decreases (Fig. S5). The decrease in variance is more pronounced for the English Channel than for the Bay of Brest and Bay of Biscay. Therefore, a first estimate shows that the mean SST warming and the variance changes both contribute to the changes in MCS activity in the English Channel, Bay of Brest and Bay of Biscay.

MCS activity generally follows the SST evolution, albeit with small differences. Indeed, winter 1991 and 1994 have a similar mean SST (10.8 °C), but the MCS activity is 3 times higher in 1994 than in 1991, driven by a higher number of events (three instead of two events with similar duration, mean intensity and spatial extent).

Even if changes in winter occur in the Bay of Brest and Bay of Biscay, more drastic changes are seen in the English Channel over the period 1982–2022 (see trend in Fig. S6 in the Supplement). In the English Channel, the trend of MCSs shows, at the beginning of the period, a mean occurrence of two events per winter, lasting 15 d with a mean intensity of -1.5 °C over an area of $100 \times 10^3\,km^2$, followed by a sharp decline ending with no detected MCSs in the last 4 years (2019–2022). In the Bay of Brest over the same period, MCS properties decrease from 1.5 events during 15 d at a mean intensity of -1.4 °C over $11 \times 10^3\,km^2$ to 0.5 events during 8 d at a mean intensity of -0.8 °C over $0.5 \times 10^3\,km^2$. Exceptional long events occurred in winter 1987 with a mean duration of 55 d. In the Bay of Biscay, the MCSs decline in occurrence (from two to one event), duration (from 11 to 9 d) and spatial extent (170×10^3 to $40 \times 10^3\,km^2$), while the mean intensity rises from -1.3 to -1.5 °C. The increase is explained by winter 2021; without these events, the mean intensity would have been nearly constant around -1.3 °C. Indeed, winter 2021 shows little activity but the highest mean intensity (-3 °C over the whole domain), which is explained by a localized event in the coastal area off southwestern France with a maximum intensity of -5.6 °C. Apart from a very intense and localized event in the coastal area off southwestern France in winter 2021 and a very long event in the Bay of Brest in winter 1987, severe MCSs occurred predominantly in the English Channel (winter 1987 and 1986).

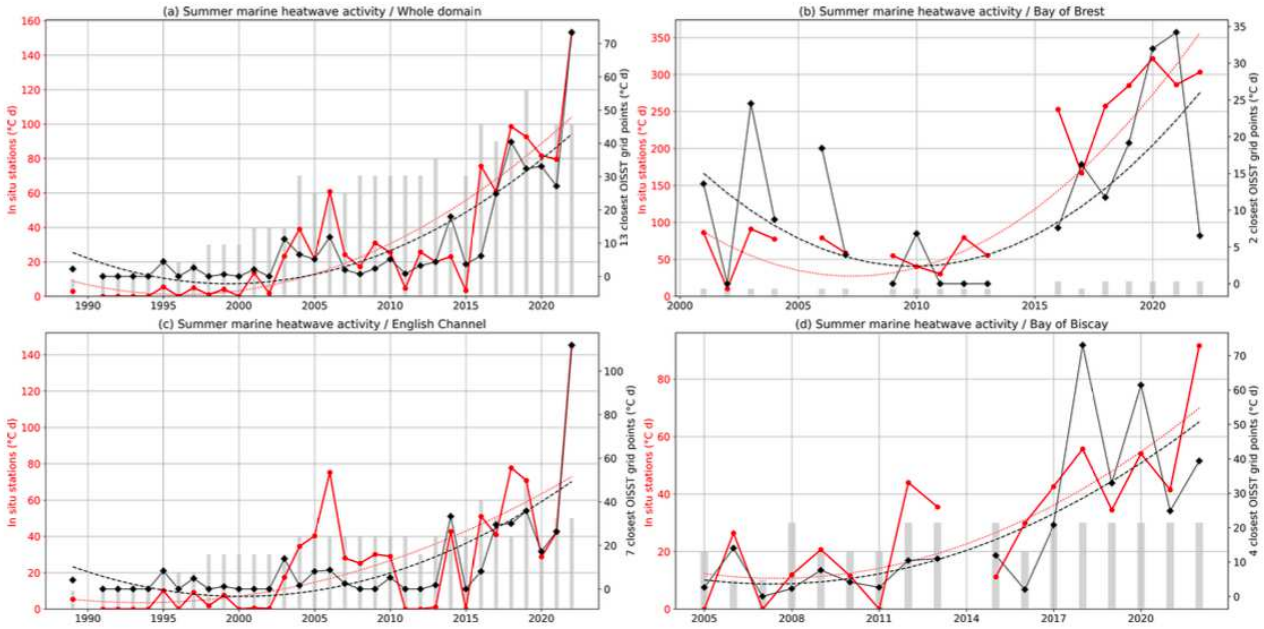

Figure 4. Time series of summer (JJAS) MHW mean activity **(a)** in the whole domain (northeastern Atlantic) and **(b–d)** in three subregions: **(b)** the Bay of Brest, **(c)** the English Channel and **(d)** the Bay of Biscay. The red curve with circle marks represents the activity based on in situ observations. The black curve with diamond marks represents the activity based on satellite dataset for the closest non-masked points with in situ stations when in situ data exist. Dashed lines represent the regression of a third-order polynomial of the solid line with the same color. Grey bars are proportional to the number of considered in situ time series. MHW activity from in situ time series with less than 80 % of observation during the analyzed season is not computed.

Contributing to this recent increase in the northeastern Atlantic is primarily the sharp trend of the events' spatial extent ($\sim$ 180 to 400 °C d 10^3 km^2), followed by the rise in the number of events (1.2 to 2.5) and also their duration (7 to 15 d; Fig. 3). One should note that, for the same number of events, the events' spatial extent can differ depending on their spatial repartition, as in the events' spatial extent only one grid cell area is taken into account when more than one event occurs on the same grid. Furthermore, over the most recent years the mean number of events, their mean duration and the total spatial extent reached the maximum recorded values. Since 2017, the total spatial extent over the northeastern Atlantic has recorded consecutive high values, exceeding 360×10^3 km^2. The summers of 2018, 2020 and 2022 recorded on average more than 2.5 events for almost all subregions, with events lasting on average more than 20 d in 2018 (Bay of Biscay) and 2022 (English Channel; Fig. S2). Among the three studied subregions, the English Channel is the region experiencing the strongest increase in summer MHW activity over the last 4 decades (see trend in Fig. S3). The longest mean duration is seen in the English Channel (35 d in summer 2022), the highest mean number of events occurred in the Bay of Brest (2.7 in summer 2020) and the highest mean intensity is present in the Bay of Biscay (2.2 °C in 2017; Fig. S2).

3.1.2 Coastal MHW activity

The spatial heterogeneity of the MHW occurrence and activity can influence the impact of MHWs along the coastline. We now explore MHW activity detected along the coast from in situ observations compared with remotely sensed observations. Figure 4 shows the activity detected for the whole northeastern Atlantic domain and in the three subregions where long-term in situ observations exist. To compare in situ and satellite data, for each station, time series based on satellite data consider only years where in situ data exist (see Table S1 for the starting date) and exceed 80 % of available data for the considered season. Linked with the whole domain activity (Fig. 4a), we observe an increase in the MHW activity in the three subregions (Fig. 4b–d). Similar evolutions are observed when the satellite product or coastal buoys are considered. In the Bay of Brest, we also observe a similar increase but with larger activity in in situ observation as the intensity of extreme events is underestimated by the satellite in this semi-enclosed bay. The use of in situ observation limits the length of the analyzed time series. However, we can observe larger activity in recent years from both datasets. For most cases, the most active years are detected with in situ observations and satellite data.

Considering coastal stations over the observed periods, we see a more pronounced increase in MHW activity from 2010.

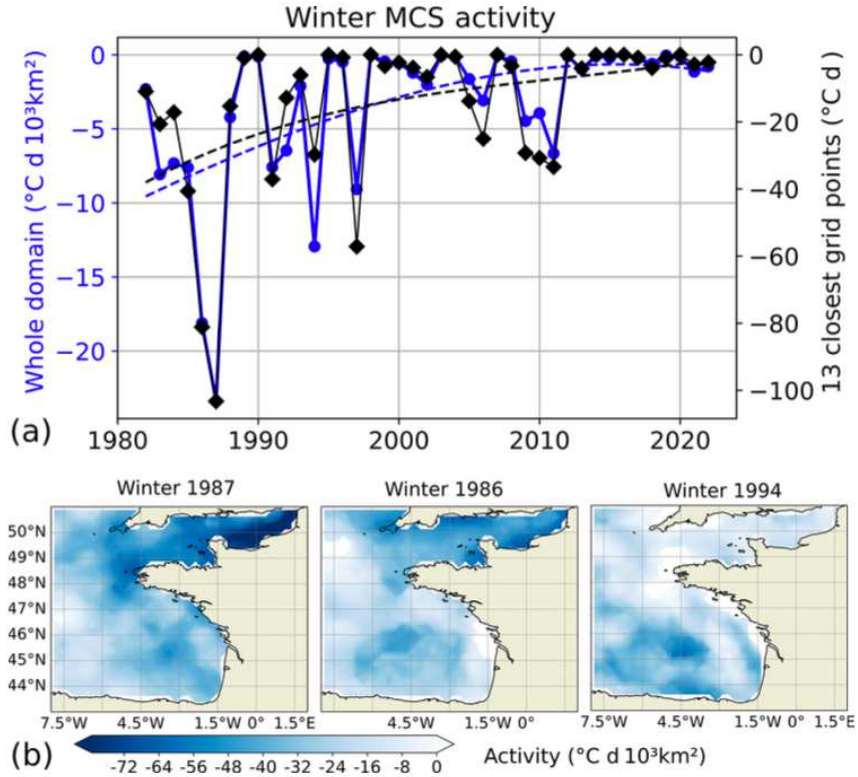

Figure 5. Same as Fig. 2 but for MCSs in winter (DJFM).

3.2.2 Coastal MCS activity

Figure 7 shows the time series of MCS activity for in situ data and satellite data considering the same missing data as each in situ station data point. Along the coasts, MCS activity as determined by local buoys remains weaker than MHW activity as defined using satellite data. As for the MHWs, MCS intensity is underestimated in satellite observations, but evolutions are similar. From in situ observations from coastal stations, 2 years can be highlighted due to their intense MCSs: 2006 and 2010 (Fig. 7). The year 2010 is the most intense, in terms of MCSs. The mean activity reaches $-100\,^{\circ}\mathrm{C\,d}$ in the Bay of Brest and around $-60\,^{\circ}\mathrm{C\,d}$ in the Bay of Biscay and the English Channel. In 2006, the activity was also important compared with other years: around $-80\,^{\circ}\mathrm{C\,d}$ in the Bay of Brest and around $-50\,^{\circ}\mathrm{C\,d}$ in the English Channel. This extreme year 2006 was also unique with a peak in MHW activity during the summer (Fig. 4). Before the year 2000, 2 other years reveal intense MCS activity in the coastal English Channel: 1997 and 1991 (from the most intense to the less active winter).

We do not detect a significant trend in the interannual evolution of MCS activity along the coasts. For the Bay of Biscay and the Bay of Brest, it can be directly connected to the lack of observation before 2000 when the largest MCS occurs. In the English Channel, the lack of observation also explains the lack of a clear trend. Indeed, only one time series was available before 1995, and this station (Greenwich, GREEN) does not detect important MCS activity before 2000.

3.3 Associated atmospheric patterns

Apart from the long-term trend of increasing SST, we also see high interannual variability, which is potentially connected with atmospheric forcing modes (Holbrook et al., 2019; Izquierdo et al., 2022a). Figure 8 presents the atmospheric circulation in the northern Atlantic associated with strong interannual MHWs in the Bay of Biscay and the English Channel. For each summer of the 1982–2022 period, the MHW total activity anomaly in the studied area box (northeastern Atlantic) with respect to the third-order long-term trend (dashed red curve in Fig. 2a) was computed. This anomaly represents the detrended or interannual MHW activity. Eight summers were identified as having high interannual activities (anomalous total activity exceeding a threshold of $4\,^{\circ}\mathrm{C\,d\,10^6\,km^{-2}}$, colored marker in Fig. 8a). The years 2018 ($23\,^{\circ}\mathrm{C\,d\,10^6\,km^{-2}}$), 2003 ($17\,^{\circ}\mathrm{C\,d\,10^6\,km^{-2}}$) and 2006 ($12\,^{\circ}\mathrm{C\,d\,10^6\,km^{-2}}$) are the three strongest summers. Six out of these eight summers (all except 2018 and 2022) have an

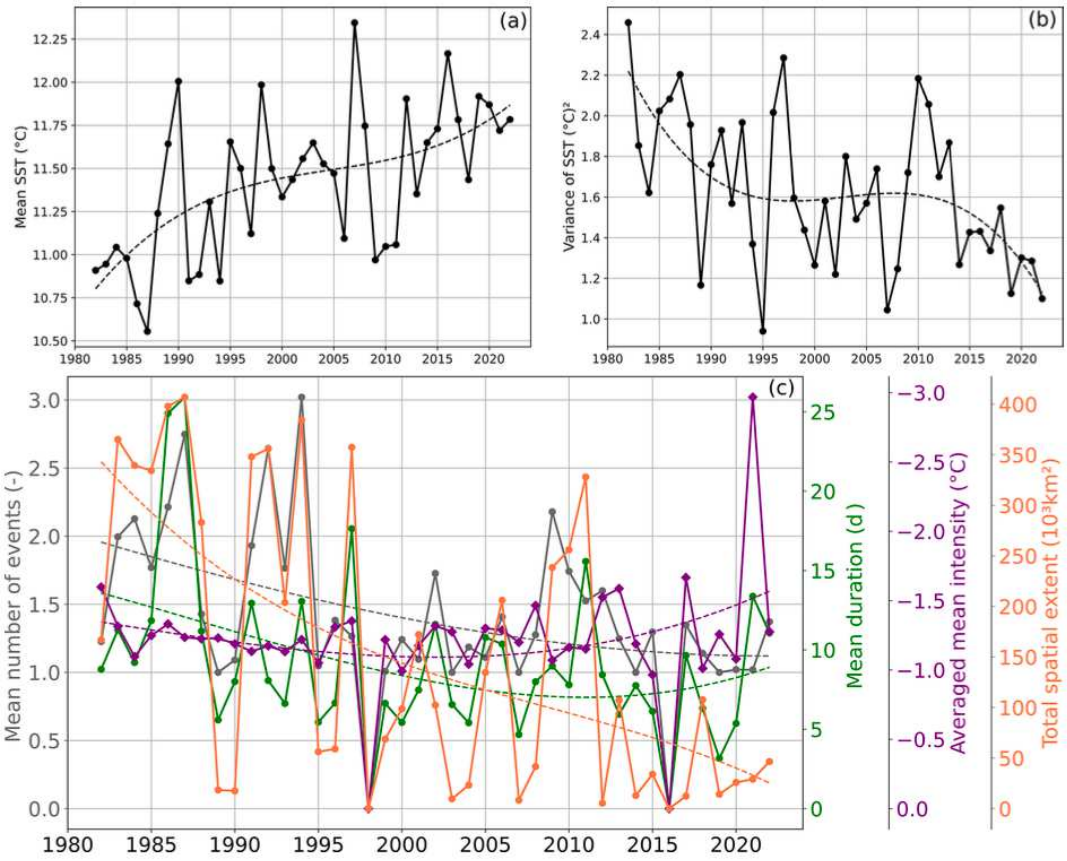

Figure 6. Same as Fig. 3 but for MCSs in winter (DJFM).

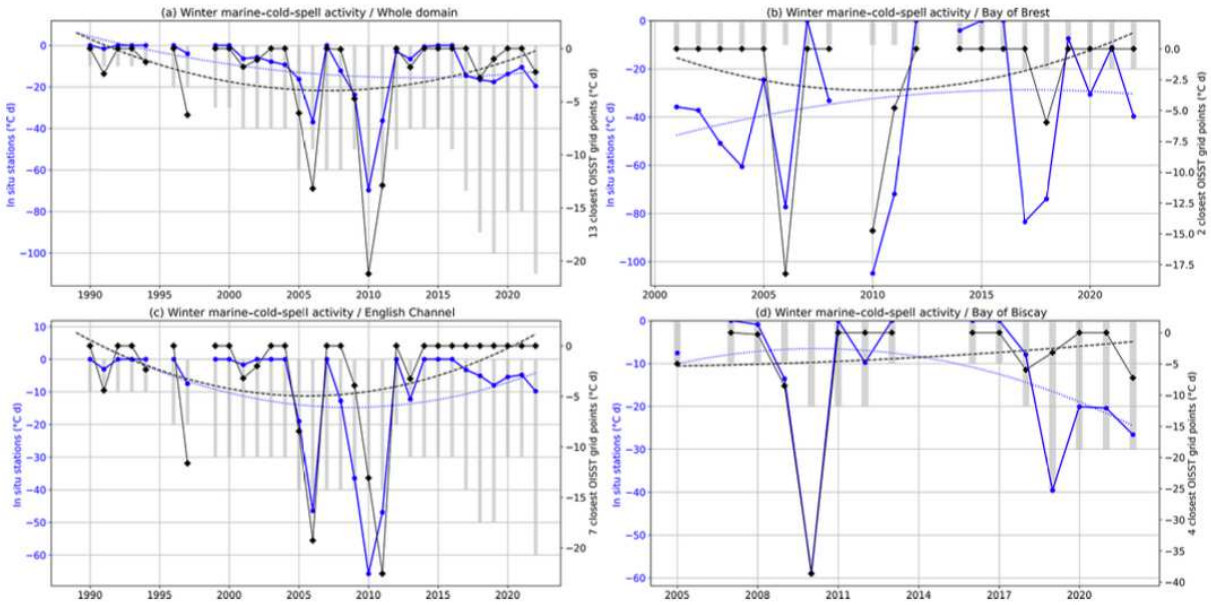

Figure 7. Same as Fig. 4 but for MCSs in winter (DJFM).

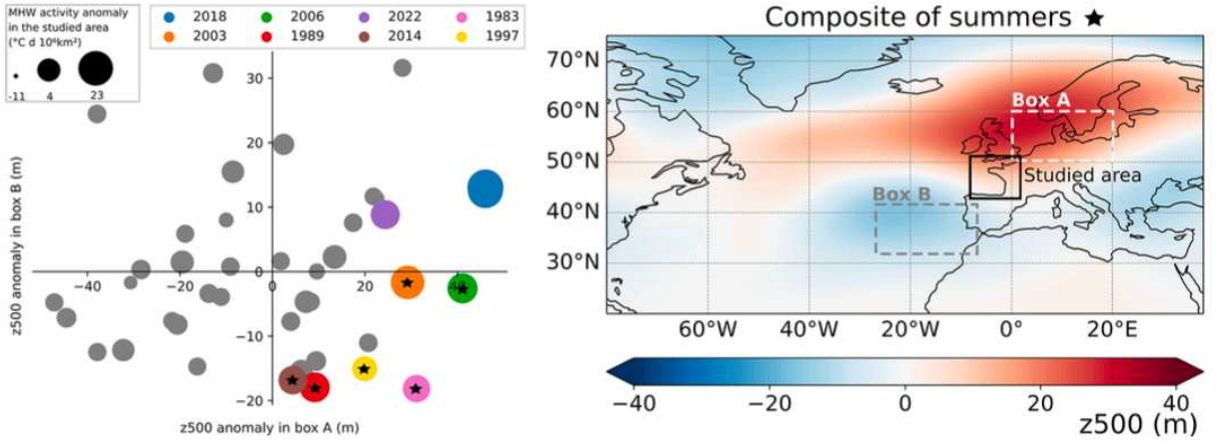

Figure 8. **(a)** Scatterplot of anomalous summer (JJAS) geopotential height at 500 hPa (z500; in m) in box *A* versus the anomalous geopotential height at 500 hPa in box *B* with respect to the summer period 1982–2022. The size of the marker is proportional to the anomalous summer (JJAS) MHW total activity, calculated as the sum of all grid point activity in the studied area (in $°C\,d\,10^6\,km^2$) with respect to the trend (dashed red curve in Fig. 2a). Markers are in color when this value exceeds $4\,°C\,d\,10^6\,km^{-2}$, and the stars are indicated when markers in color are in the lower-right "cluster" of the graph. **(b)** Composite of summers (JJAS) marked with stars in the left panel of the anomalous geopotential height at 500 hPa (m) with respect to the summer period 1982–2022. Box *A* is the domain 50–60° N, 0–20° E, and box *B* is the domain 31–41° N, 33–13° W.

anomalous geopotential height at 500 hPa, which is positive over northern Europe (box A in Fig. 8) and negative west of the Iberian Peninsula (box B in Fig. 8). The composite of the anomalous geopotential height at 500 hPa for these six summers shows a positive summer NAO-like pattern in the northern Atlantic–European sector, with a high over the Nordic seas and two lows over the Iberian Peninsula and Greenland. This overall result is not sensitive to small displacements of boxes (a few degrees of latitude and longitude; not shown).

Summer (JJAS) 2018 has the strongest anomalous MHW activity in the northeastern Atlantic but, differently from the next six summers in the ranking of detrended MHW activity, does not present a decrease in the geopotential height at 500 hPa west of the Iberian Peninsula (box B). A broad high-pressure system in the northern Atlantic–European sector is seen (including box A), except in the eastern Mediterranean and to 60° N, where a low occurs (Fig. S7 in the Supplement). This response in box B for summer 2018 is primarily due to late-summer (August and September) atmospheric circulation (Fig. S7). These months make a minor contribution to MHW total activity for the whole summer (JJAS; Fig. S8 in the Supplement). When considering the month of June, with 2018 MHW peaks (Fig. S8), the northern Atlantic shows a positive summer NAO regime, similar to the next six summers' highest MHW activity. This analysis demonstrates that MHWs in the northeastern Atlantic are closely associated with a high-pressure system over northern Europe, as well as a low off the Iberian Peninsula, resembling the positive phase of the summer NAO. By performing this analysis with SST instead of MHW activity, we obtain similar results, albeit with a less extended high over northern Europe (Fig. S9 in the Supplement).

Regarding MCSs, the three highest detrended MCS activities are winter 1987 ($-20\,°C\,d\,10^6\,km^{-2}$), 1986 ($-13\,°C\,d\,10^6\,km^{-2}$) and 1994 ($-10\,°C\,d\,10^6\,km^{-2}$; Fig. 9). These three most active winters are in the same "cluster", with anomalous 500 hPa geopotential height negative over northern Europe and positive west of the Iberian Peninsula. A composite of the anomalous geopotential height at 500 hPa for these three winters shows in the northern Atlantic–European sector a broad and strong low in northern Europe, a weaker low-pressure system sitting in the northwestern Atlantic, and two highs off the Iberian Peninsula and over the Hudson Bay. This analysis suggests that extreme MCSs in the northeastern Atlantic might be closely associated with a low over northern Europe and a high off the Iberian Peninsula. By performing this analysis with SST instead of the MCS activity (Fig. S10 in the Supplement), the results are sparse, showing only winter 1986 as having a strong anomalous cold SST linked to an anomalous geopotential height at 500 hPa over northern Europe and positive west of the Iberian Peninsula.

When comparing the anomalous geopotential height conditions for the most intense summer MHWs and winter MCSs, we see that the geopotential height conditions are opposite, although the amplitude is stronger for winter, consistent with stronger climatology (Folland et al., 2009). However, while summer MHWs are associated with a positive summer NAO, winter MCSs are not associated with a negative winter NAO pattern.

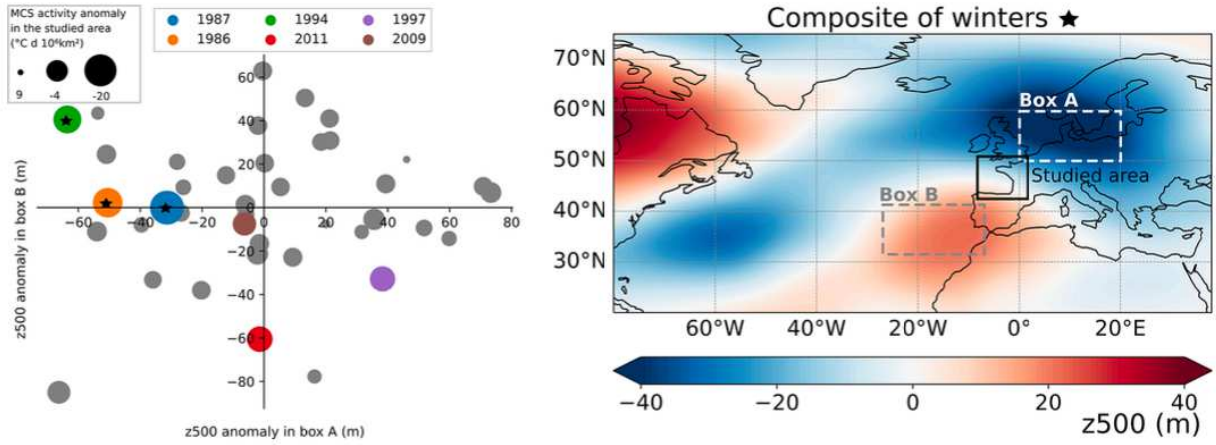

Figure 9. Same as Fig. 8 but for MCSs in winter (DJFM). MCS anomalies are calculated with respect to the third-order trend (dashed blue curve in Fig. 5a). Markers are in color when this value is below $-4\,°C\,d\,10^6\,km^{-2}$, and stars are indicated when markers in color are in the upper-left section of the graph.

To investigate potential drivers of these events, we have considered the different components of air–sea heat flux anomalies concomitant with MHWs and MCSs. For the eight most severe interannual summer MHWs (see marker in color Fig. 8) and the six most severe interannual winter MCSs (see marker in color Fig. 9), the anomalous (i) shortwave radiation flux, (ii) surface net longwave radiation flux, (iii) surface sensible heat flux and (iv) latent heat flux are depicted, respectively, in Figs. S11 and S12 in the Supplement. The interannual (or detrended) summer MHWs are predominantly driven by high shortwave radiation flux, except for years 1983 and 1997, which only show an important positive downward latent heat flux. The other air–sea fluxes make a smaller contribution. The interannual winter MCSs seem to be mostly driven by high sensible heat flux and low shortwave radiation flux. This suggests that, in this region, a decrease in cloud cover is a key parameter for the generation of summer MHWs, while strong winds and an increase in cloud cover are important for the apparition of winter MCSs. Further analysis needs to be done to quantitatively attribute the contribution of each air–sea heat flux component.

4 Discussion

In the northeastern Atlantic, an increase in the MHW activity and a decrease in MCS activity were observed. Interannual changes confirm that general large-scale trends (Oliver et al., 2018; Schlegel et al., 2021) are also observed in regions where the coastal hydrodynamics could limit the impact due to active vertical mixing processes (e.g., barotropic and internal tides, wind-driven mixing in shallow waters).

The most active summer MHWs analyzed over the northeastern Atlantic and in the period 1982–2022 occurred in the Bay of Biscay (2018), and the most active winter MCSs occurred in the English Channel (1987). This is consistent with Schlegel et al. (2021), who found that the maximum intensity of MHWs dominates MCSs in the Bay of Biscay and vice versa in the English Channel. Along the coasts, the maximum of MHW activity is detected in 2022 in the English Channel, which might be related to the summer European heatwaves recorded (ECMWF, 2022; Savu, 2022; Guinaldo et al., 2023).

In the Bay of Biscay, we see a linear warming rate in summer since the beginning of the studied period. This is in accordance with DeCastro et al. (2009), who show a steady linear warming rate since the 1970s, based on data from 1854–2006. Mean SST together with the SST variance increase may explain the increase in MHWs. This increase in MHWs is consistent with Izquierdo et al. (2022a), who determined more precisely an equal contribution of each of these two factors for the southern coast of the Bay of Biscay. This is specific to this region (as well as for the Bay of Brest and the English Channel), as for most of the other regions of the world, the mean warming and not the SST variability changes contributes to the increase in MHW features (Alexander et al., 2018; Oliver et al., 2021). In addition, we found a positive trend for the MHW activity parameter using both satellite data and the four buoys in the Bay of Biscay and for the duration and occurrence using satellite data. The trends are quasi-similar considering only the two buoys on the southern coast of the Bay of Biscay (GIJO and BILB) and the two on the western coast of the Bay of Biscay (ARCA and MOLI; not shown) and are marked by the high activity present in the more recent summers. This evolution in the occurrence and duration of MHWs was not seen in Izquierdo et al. (2022b) using two buoys in the southern coastal Bay of Biscay over the period 1998–2018, which could be explained by local processes or the studied season (March to August).

The results from in situ and satellite datasets for each of the studied regions are quite in agreement, although the satellite underestimates the amplitude of activity for both MHWs and MCSs. Conversely, Izquierdo et al. (2022a) found an overestimation of the MHWs using satellites compared to in situ data in the coastal upwelling region south of the Bay of Biscay, which might be related to local processes. The satellite's coarse resolution mostly (i) smoothes small-scale and short events and (ii) interpolates with offshore regions, having greater thermal inertia (Marin et al., 2021), which can lead to the overestimation of the duration of events and the underestimation of the intensity. However, we show that coastal in situ stations distributed along the northeastern Atlantic coasts allow for the detection of large-scale evolutions of MHW and MCS activity. Analyzed locally, they can also inform about evolutions related to local hydrodynamics.

Internal variability in winter MCSs is related to low pressure over northern Europe and high pressure west of the Iberian Peninsula for three (1987, 1986 and 1994) out of the six most intense events. Among other strong interannual MCSs, winter 2011 does not present this pattern but could have been generated by a cold-air outbreak brought by a ridge over Greenland (Norris et al., 2013). A relation at an interannual timescale could exist between MCSs (Fig. 7, top right) and extreme low-salinity events (Poppeschi et al., 2021) in winter in the Bay of Brest, as, using the same in situ buoys (COAST-HF Iroise from 2000–2018), two out of the four most severe low-salinity events are concomitant with MCSs (winter 2001 and 2007). These extreme events could be both influenced by intense mid-latitude depressions, but river discharges are also an important driver in this region. Unlike MHWs (Fig. 2), extremely cold conditions occurred several winters in a row: three in 2009–2011 and two in 1986–1987. This might be explained by the re-emergence of cold water originating from the previous winter, as for the 2013–2016 northern Atlantic cold blob (Duchez et al., 2016a; Josey et al., 2018; Schlegel et al., 2021).

Summer 2018 presents the most active MHWs in the northeastern Atlantic for the period 1982–2022, consistent with the reported warmer SST the same summer (+1 to +3 °C above the long-term climatology) in the proximity of the United Kingdom (McCarthy et al., 2019). Over land, this summer was also recorded as the hottest in the United Kingdom since 1884 (McCarthy et al., 2019) and one of the hottest over northwestern Europe (Met Office, 2018; Météo-France, 2018). On top of the underlying warming climate forcing (Vogel et al., 2019; Yiou et al., 2020), these extreme continental warm conditions in 2018 have been previously reported as a consequence of the positive summer NAO anomalies combined with elevated SST (McCarthy et al., 2019) or combined with stationary Rossby waves in synoptic anomalies (Drouard et al., 2019; Kornhuber et al., 2019). More generally, the positive phase of the summer NAO is associated with warm anomalies from the west of the United Kingdom to the Baltic (Folland et al., 2009). Our findings for MHWs corroborate the continental counterpart as extremely warm conditions in the Bay of Biscay and the English Channel are likely associated with positive summer NAO, consistent with the result of Holbrook et al. (2019).

Depending on the region and the event, MHWs can be associated with anomalous air–sea heat fluxes which can include high shortwave fluxes, due to less cloud cover and greater insolation, high sensible heat fluxes when the surface air is warm, and/or low latent heat loss from the ocean due to weak winds (Oliver et al., 2021). In the English Channel and the Bay of Biscay, Guinaldo et al. (2023) linked summer 2022 sea-surface temperature to abnormally high shortwave radiation in the Bay of Biscay and English Channel. In this study, a similar conclusion is found by considering the eight most severe interannual MHWs in the northeastern Atlantic (which includes the English Channel and the Bay of Biscay and summer 2022). Abnormally high shortwave radiation is likely associated with reduced cloudiness, and Folland et al. (2009) have found that during the positive index phase of the summer NAO, northwestern Europe experiences significantly reduced cloudiness. This is consistent with our suggestion that the positive phase of the summer NAO favors the generation of summer MHWs in the northeastern Atlantic through reduced cloudiness. MCSs in the English Channel are associated with high sensible heat fluxes, consistent with reported MCSs often driven by strong winds in shallow waters, enabling a rapid cooling of the surface water (Crisp, 1964; Schlegel et al., 2021). We also found a possible role of weaker shortwave radiation, which might be related to increased cloud coverage.

In the future and under increasing greenhouse gas concentrations, climate models predict a continued warming of the ocean surface in the Bay of Biscay and the English Channel (Fox-Kemper et al., 2021) and a trend toward a positive summer NAO pattern (Faranda et al., 2019). Both of these effects imply the long-term likelihood of increased MHWs in the northeastern Atlantic, but the extent of the long-term and the interannual variability in the contributions remains to be shown. Also, the role of large-scale ocean circulation features, such as the shelf edge current (Alheit et al., 2019) or Iberian Poleward Current (Charria et al., 2013) and upper-ocean preconditioning (Josey et al., 2018), and the importance of remote large-scale climate modes of variability, such as the Indian Ocean Dipole (Holbrook et al., 2019), in amplifying or suppressing MHW occurrences in the Bay of Biscay and English Channel would need specific investigation. Along the coasts, the role of main river inflow at the land–sea continuum can also lead to specific answers on the coastal ocean to future climate evolutions.

5 Conclusions

The activity index, a combination of the properties of marine extreme events, shows a positive trend for summer MHWs in

the northeastern Atlantic (since 2000 and more pronounced since 2010) and in the three subregions, the English Channel, the Bay of Brest and the Bay of Biscay, for both in situ and satellite data. This is explained by an increase in both the mean and variance of SST. Conversely, a decrease in MCS activity was detected, with almost no events after 2000, more clearly shown with the satellite data due to the longer time series (40 years) compared with the in situ data (20 to 30 years). These changes are fast for the three subregions, with the English Channel being the subregion with the most drastic growth.

In the northeastern Atlantic, MHWs are more frequent and longer and extend over larger areas, while the opposite is seen for MCSs. For both MHWs and MCSs, the mean intensity shows only weak changes over the last 4 decades.

Moreover, we found that the satellite dataset used is in good accordance with in situ data in the northeastern Atlantic, except for the fact that satellites underestimate the amplitude of both hot summer and cold winter marine extreme events in the coastal areas. The implemented in situ stations appear to be a well-designed observing system to detect the long-term evolution of MHW and MCS activity and to document local features related to coastal hydrodynamics.

MHW activity is particularly high in 2018 and 2022 through two different situations. The year 2018 is characterized by a large extent of MHWs in the Bay of Biscay with long events in the south of the bay and intense events over the Armorican shelf. Summer 2022 features long MHWs mainly in the English Channel. MCS activity is the highest in 1986 and 1987 due to long and intense events in the English Channel.

Our findings show that summers with strong MHW activity due to internal variability (after removing the trend) in the northeastern Atlantic have often been associated with a ridge over the North Sea and a trough west of the Iberian Peninsula; the opposite situation is seen for MCSs. In the case of MHWs, the wide atmospheric pattern resembles the positive phase of the summer NAO. This preliminary analysis of air–sea heat fluxes suggests that in the northeastern Atlantic interannual (or detrended) summer MHWs are predominantly driven by high shortwave radiation flux and interannual winter MCSs are driven by high sensible heat flux and low shortwave radiation. This suggests that, in this region, decreased cloud cover is a key parameter for the generation of summer MHWs, while strong winds and increased cloud cover are important for the apparition of winter MCSs. We caution the reader that the proposed connection does not necessarily indicate causal links but that these relations can provide indications of drivers.

Despite contrasting hydrodynamical regimes (mesotidal and macrotidal) and circulation (shallow water under freshwater influence, shelf circulation, active submesoscale), the northeastern Atlantic region displays similar changes in MHW and MCS activity between coastal and open-ocean regions. Those changes need to be anticipated to mitigate the impacts on coastal ecosystems.

Data availability. All datasets included in the present study are accessible from the following publicly available repositories. Satellite dataset OISST is available on ftp://ftp2.psl.noaa.gov/Datasets/noaa.oisst.v2.highres/, last access: 24 January 2023 and ERA5 reanalyses on https://www.ecmwf.int/en/forecasts/dataset/ecmwf-reanalysis-v5, last access: 25 August 2023. Buoy in situ datasets are available on http://data.coriolis-cotier.org, last access: 2 January 2023 for COAST-HF data, https://www.westernchannelobservatory.org.uk, last access: 4 April 2023 for the Western Channel Observatory, and https://emodnet.ec.europa.eu, last access: 2 January 2023 for other datasets.

Supplement. The supplement related to this article is available online at: https://doi.org/10.5194/os-19-1339-2023-supplement.

Author contributions. All authors contributed to the conception and design of the study. AS performed the calculations and designed the figures involving the satellite dataset, and GC and CP did so for the in situ dataset. All authors contributed to the discussion, writing and review of the manuscript.

Competing interests. The contact author has declared that none of the authors has any competing interests.

Disclaimer. Publisher's note: Copernicus Publications remains neutral with regard to jurisdictional claims in published maps and institutional affiliations.

Acknowledgements. We thank Oregan Segalen for fruitful discussions. We thank Tim Smyth for providing data from the Western Channel Observatory. We acknowledge the COAST-HF (http://www.coast-hf.fr, last access: 2 January 2023) national observing network component of the ILICO national research infrastructure. Additionally, we express our gratitude to the two reviewers and editor for their valuable feedback, which has greatly contributed to improving the quality of our work. Coline Poppeschi and Guillaume Charria acknowledge the support of the regional project (Contrat de Plan État-Région) ObsOcean/ROEC-ILICO and the regional COXTCLIM project funded by the Loire-Brittany Water Agency, the region of Brittany and Ifremer.

Financial support. This research has been supported by the Fundação para a Ciência e a Tecnologia, I.P./MCTES, through national funds (PIDDAC; grant no. UIDB/50019/2020) to Instituto Dom Luiz and through project ROADMAP (grant no. JPIOCEANS/0001/2019).

Review statement. This paper was edited by Bernadette Sloyan and reviewed by two anonymous referees.

References

Alexander, M. A., Scott, J. D., Friedland, K. D., Mills, K. E., Nye, J. A., Pershing, A. J., and Thomas, A. C.: Projected sea surface temperatures over the 21st century: Changes in the mean, variability and extremes for large marine ecosystem regions of Northern Oceans, Elementa: Science of the Anthropocene, 6, https://doi.org/10.1525/elementa.191, 2018.

Alheit, J., Gröger, J., Licandro, P., McQuinn, I. H., Pohlmann, T., and Tsikliras, A. C.: What happened in the mid-1990s? The coupled ocean-atmosphere processes behind climate-induced ecosystem changes in the Northeast Atlantic and the Mediterranean, Deep-Sea Res. Pt. II, 159, 130–142, https://doi.org/10.1016/j.dsr2.2018.11.011, 2019.

Barnston, A. G. and Livezey, R. E.: Classification, seasonality and persistence of low-frequency atmospheric circulation patterns, Mon. Weather Rev., 115, 1083–1126, https://doi.org/10.1175/1520-0493(1987)115<1083:CSAPOL>2.0.CO;2, 1987.

Brown Ross, A., Lilley, M. K. S., Shutler, J., Widdicombe, C., Rooks, P., McEvoy, A., Torres, R., Artioli, Y., Rawle, G., Homyard, J., Tyler, C. R., and Lowe, C.: Harmful Algal Blooms and their impacts on shellfish mariculture follow regionally distinct patterns of water circulation in the western English Channel during the 2018 heatwave, Harmful Algae, 111, 102166, https://doi.org/10.1016/j.hal.2021.102166, 2022.

Charria, G., Lazure, P., Le Cann, B., Serpette, A., Reverdin, G., Louazel, S., Batifoulier, F., Dumas, F., Pichon, A., and Morel, Y.: Surface layer circulation derived from Lagrangian drifters in the Bay of Biscay, J. Marine Syst., 109, 60–76, https://doi.org/10.1016/j.jmarsys.2011.09.015, 2013.

Chust, G., Borja, Á., Caballero, A., Irigoien, X., Sáenz, J., Moncho, R., Marcos, M., Liria, P., Hidalgo, J., Valle, M., and Valencia, V.: Climate change impacts on coastal and pelagic environments in the southeastern Bay of Biscay, Clim. Res., 48, 307–332, https://doi.org/10.3354/cr00914, 2011.

Crisp, D. J.: The Effects of the Severe Winter of 1962–63 on Marine Life in Britain, J. Anim. Ecol., 33, 165–210, https://www.jstor.org/stable/2355 (last access: 20 January 2022), 1964.

Darmaraki, S., Somot, S., Sevault, F., and Nabat, P.: Past Variability of Mediterranean Sea Marine Heatwaves, Geophys. Res. Lett., 46, 9813–9823, https://doi.org/10.1029/2019GL082933, 2019.

DeCastro, M., Gómez-Gesteira, M., Alvarez, I., and Gesteira, J. L. G.: Present warming within the context of cooling–warming cycles observed since 1854 in the Bay of Biscay, Cont. Shelf Res., 29, 1053–1059, https://doi.org/10.1016/j.csr.2008.11.016, 2009.

Deser, C., Alexander, M. A., Xie, S. P., and Phillips, A. S.: Sea surface temperature variability: Patterns and mechanisms, Annu. Rev. Mar. Sci., 2, 115–143, 2010.

Drouard, M., Kornhuber, K., and Woollings, T.: Disentangling dynamic contributions to summer 2018 anomalous weather over Europe, Geophys. Res. Lett., 46, 12537–12546, https://doi.org/10.1029/2019GL084601, 2019.

Duchez, A., Frajka-Williams, E., Josey, S. A., Evans, D. G., Grist, J. P., Marsh, R., McCarthy, G. D., Sinha, B., Inglis Berry, D., and Hirschi, J. J.: Drivers of exceptionally cold North Atlantic Ocean temperatures and their link to the 2015 European heat wave, Environ. Res. Lett., 11, 074004, https://doi.org/10.1088/1748-9326/11/7/074004, 2016.

ECMWF: Update on European heatwave of July 2022, ecmwf, https://www.ecmwf.int/en/about/media-centre/focus/2022/update-european-heatwave-july-2022 (last access: 25 August 2023), 2022.

Faranda, D., Alvarez-Castro, M. C., Messori, G., Rodrigues, D., and Yiou, P.: The hammam effect or how a warm ocean enhances large scale atmospheric predictability, Nat. Commun., 10, 1–7, https://doi.org/10.1038/s41467-019-09305-8, 2019.

Folland, C. K., Knight, J., Linderholm, H. W., Fereday, D., Ineson, S., and Hurrell, J. W.: The summer North Atlantic Oscillation: past, present, and future, J. Climate, 22, 1082–1103, 2009.

Fox-Kemper, B., Hewitt, H. T., Xiao, C. , Aðalgeirsdóttir, G., Drijfhout, S. S., Edwards, T. L., Golledge, N. R., Hemer, M., Kopp, R. E., Krinner, G., Mix, A., Notz, D., Nowicki, S., Nurhati, I. S., Ruiz, L., Sallée, J.-B., Slangen, A. B. A., and Yu, Y.: Ocean, Cryosphere and Sea Level Change, in: Climate Change 2021: The Physical Science Basis. Contribution of Working Group I to the Sixth Assessment Report of the Intergovernmental Panel on Climate Change, edited by: Masson-Delmotte, V., Zhai, P., Pirani, A., Connors, S. L., Péan, C., Berger, S., Caud, N., Chen, Y., Goldfarb, L., Gomis, M. I., Huang, M., Leitzell, K., Lonnoy, E., Matthews, J. B. R. , Maycock, T. K., Waterfield, T., Yelekçi, O., Yu, R., and Zhou, B., Cambridge University Press, Cambridge, United Kingdom and New York, NY, USA, 1211–1362, https://doi.org/10.1017/9781009157896.011, 2021.

Frölicher, T. and Laufkötter, C.: Emerging risks from marine heat waves, Nat. Commun., 9, 2015–2018, https://doi.org/10.1038/s41467-018-03163-6 , 2018.

Frölicher, T. L., Fischer, E. M., and Gruber, N.: Marine heatwaves under global warming, Nature, 560, 360–364, https://doi.org/10.1038/s41586-018-0383-9, 2018.

Gómez, F. and Souissi, S.: The impact of the 2003 summer heat wave and the 2005 late cold wave on the phytoplankton in the north-eastern English Channel, C. R. Biol., 331, 678–685, https://doi.org/10.1016/j.crvi.2008.06.005, 2008.

Guinaldo, T., Saux Picart, S., and Roquet, H.: Response of the sea surface temperature to heatwaves during the France 2022 meteorological summer, EGUsphere [preprint], https://doi.org/10.5194/egusphere-2022-1119, 2022.

Guo, X., Gao, Y., Zhang, S., Wu, L., Chang, P., Cai, W., Zscheischler, J., Ruby Leung, L., Small, J., Danabasoglu, G., Thompson, L., and Gao, H.: Threat by marine heatwaves to adaptive large marine ecosystems in an eddy-resolving model, Nat. Clim. Change, 12, 179–186, 2022.

Hersbach, H., Bell, B., Berrisford, P., Hirahara, S., Horányi, A., Muñoz-Sabater, J., Nicolas, J., Peubey, C., Radu, R., Schepers, D., Simmons, A., Soci, C., Abdalla, S., Abellan, X., Balsamo, G., Bechtold, P., Biavati, G., Bidlot, J., Bonavita, M., De Chiara, G., Dahlgren, P., Dee, D., Diamantakis, M., Dragani, R., Flemming, J., Forbes, R., Fuentes, M., Geer, A., Haimberger, L., Healy, S., Hogan, R. J., Hólm, E., Janisková, M., Keeley, S., Laloyaux, P., Lopez, P., Lupu, C., Radnoti, G., de Rosnay, P., Rozum, I., Vamborg, F., Villaume, S., and Thépaut, J. N.: The ERA5 global reanalysis, Q. J. Roy. Meteor. Soc., 146, https://doi.org/10.1002/qj.3803, 1999–2049, 2020.

Hobday, A. J., Alexander, L. V., Perkins, S. E., Smale, D. A., Straub, S. C., Oliver, E. C. J., Benthuysen, J. A., Burrows, M. T., Donat, M. G., Feng, M., Holbrook, N. J., Moore, P. J., Scannell, H. A., Sen Gupta, A., and Wernberg, T.:. A hierarchical approach to defining marine heatwaves, Prog. Oceanogr., 141, 227–238, https://doi.org/10.1016/j.pocean.2015.12.014, 2016.

Holbrook, N. J., Scannell, H. A., Sen Gupta, A., Benthuysen, J. A., Feng, M., Oliver, E. C., Alexander, L., Burrows, M., Donat, M., Hobday, A., Moore, P., Perkins-Kirkpatrick, S., Smale, D., Straub, S., and Wernberg, T.: A global assessment of marine heatwaves and their drivers, Nat. Commun., 10, 1–13, https://doi.org/10.1038/s41467-019-10206-z, 2019.

Huang, B., Liu, C., Banzon, V., Freeman, E., Graham, G., Hankins, B., Smith, T., and Zhang, H.-M.: Improvements of the Daily Optimum Interpolation Sea Surface Temperature (DOISST) Version 2.1, J. Climate, 34, 2923–2939, https://doi.org/10.1175/JCLI-D-20-0166.1, 2020.

Hurrell, J. W., Kushnir, Y., Ottersen, G., and Visbeck, M.: An overview of the North Atlantic oscillation, in: Geophysical Monograph Series, edited by: Geophysical Monograph Series, American Geophysical Union, 134, 1–36, https://doi.org/10.1029/134GM01, 2003.

Izquierdo, P., Rico, J. M., Taboada, F. G., González-Gil, R., and Arrontes, J.: Characterization of marine heatwaves in the Cantabrian Sea, SW Bay of Biscay, Estuar. Coast. Shelf S., 274, https://doi.org/10.1016/j.ecss.2022.107923, 2022a.

Izquierdo, P., Taboada, F. G., González-Gil, R., Arrontes, J., and Rico, J. M.: Alongshore upwelling modulates the intensity of marine heatwaves in a temperate coastal sea, Sci. Total Environ., 835, 155478, https://doi.org/10.1016/j.scitotenv.2022.155478, 2022b.

Joint, I. and Smale, D. A.: Marine heatwaves and optimal temperatures for microbial assemblage activity, FEMS Microbiol. Ecol., 93, 1–9, https://doi.org/10.1093/femsec/fiw243, 2017.

Josey, S. A., Hirschi, J.-M., Sinha, B., Duchez, A., Grist, J. P., Marsh, R.: The recent Atlantic cold anomaly: Causes, consequences, and related phenomena, Annu. Rev. Mar. Sci., 10 , 475–501, 2018.

Kornhuber, K., Osprey, S., Coumou, D., Petri, S., Petoukhov, V., Rahmstorf, S., and Gray, L.: Extreme weather events in early summer 2018 connected by a recurrent hemispheric wave-7 pattern, Environ. Res. Lett., 14, 054002, https://doi.org/10.1088/1748-9326/ab13bf, 2019.

Le Boyer, A., Cambon, G., Daniault, N., Herbette, S., Le Cann, B., Marie, L., and Morin, P.: Observations of the Ushant tidal front in September 2007, Cont. Shelf Res., 29, 1026–1037, 2009.

Lima, F. P. and Wethey, D. S.: Three decades of high-resolution coastal sea surface temperatures reveal more than warming, Nat. Commun., 3, 704, 2012.

Lorenzo, M. N., Taboada, J. J., and Gimeno, L.: Links between circulation weather types and teleconnection patterns and their influence on precipitation patterns in Galicia (NW Spain), Int. J. Climatol., 28, 1493–1505, https://doi.org/10.1002/joc.1646, 2008.

Marin, M., Feng, M., Phillips, H. E., and Bindoff, N. L.: A global, multiproduct analysis of coastal marine heatwaves: Distribution, characteristics, and long-term trends, J. Geophys. Res.-Oceans, 126, e2020JC016708, https://doi.org/10.1029/2020JC016708, 2021.

McCarthy, M., Christidis, N., Dunstone, N., Fereday, D., Kay, G., Klein-Tank, A., Lowe, J., Petch, J., Scaife, A., and Stott, P.: Drivers of the UK summer heatwave of 2018, Weather, 74, 390–396, https://doi.org/10.1002/wea.3628, 2019.

Met Office: Summer 2018, Met Office, https://www.metoffice.gov.uk/binaries/content/assets/metofficegovuk/pdf/weather/learn-about/uk-past-events/interesting/2018/summer-2018---met-office.pdf (last access: 7 July 2023), 2018.

Météo-France: Bilan climatique de l'été 2018, Météo-France, https://meteofrance.fr/sites/meteofrance.fr/files/files/editorial/Bilan-climatique-annee2018.pdf (last access: 7 July 2023), 2018.

Mieszkowska, N., Burrows, M., and Sugden, H.: Impacts of climate change on intertidal habitats, relevant to the coastal and marine environment around the UK, MCCIP Science Review, 2020, 256–271, https://doi.org/10.14465/2020.arc12.ith, 2020.

Müller, H., Blanke, B., Dumas, F., and Mariette, V.: Identification of typical scenarios for the surface Lagrangian residual circulation in the Iroise Sea. J. Geophys. Res.-Oceans, 115, C7, https://doi.org/10.1029/2009JC005834, 2010.

Norris, J., Vaughan, G., and Schultz, D. M.: Snowbands over the English Channel and Irish Sea during cold-air outbreaks, Q. J. Roy. Meteor. Soc., 139, 1747–1761, https://doi.org/10.1002/qj.2079, 2013.

Oh, H., Kim, G. U., Chu, J. E., Lee, K., and Jeong, J. Y.: The record-breaking 2022 long-lasting marine heatwaves in the East China Sea, Environ. Res. Lett., 18, 064015, https://doi.org/10.1088/1748-9326/acd267, 2023.

Oliver, E. C., Donat, M. G., Burrows, M. T., Moore, P. J., Smale, D. A., Alexander, L. V., Benthuysen, J. A., Feng, M., Sen Gupta, A., Hobday, A. J., Holbrook, N. J., Perkins-Kirkpatrick, S. E., Scannell, H. A., Strauband, S. C., and Wernberg, T.: Longer and more frequent marine heatwaves over the past century, Nat. Commun., 9, 1–12, https://doi.org/10.1038/s41467-018-03732-9, 2018.

Oliver, E. C. J., Burrows, M. T., Donat, M. G., Sen Gupta, A., Alexander, L. V., Perkins-Kirkpatrick, S. E., Benthuysen, J. A., Hobday, A. J., Holbrook, N. J., Moore, P. J., Thomsen, M. S., Wernberg, T., and Smale, D. A.: Projected Marine Heatwaves in the 21st Century and the Potential for Ecological Impact, Frontiers in Marine Science, 6, 1–12, https://doi.org/10.3389/fmars.2019.00734, 2019.

Oliver, E. C., Benthuysen, J. A., Darmaraki, S., Donat, M. G., Hobday, A. J., Holbrook, N. J., Schlegel, R. W., and Sen Gupta, A.: Marine heatwaves, Ann. Rev. Mar. Sci., 13, 313–342, 2021.

Plecha, S. and Soares, P. M. M.: Global marine heatwave events using the new CMIP6 multi-model ensemble: from shortcomings in present climate to future projections, Environ. Res. Lett., 15, 124058, https://doi.org/10.1088/1748-9326/abc847, 2020.

Plecha, S. M., Soares, P. M. M., Silva-Fernandes, S. M., and Cabos, W.: On the uncertainty of future projections of Marine Heatwave events in the North Atlantic Ocean, Clim. Dynam., 56, 2027–2056, https://doi.org/10.1007/s00382-020-05529-3, 2021.

Poppeschi, C., Charria, G., Goberville, E., Rimmelin-Maury, P., Barrier, N., Petton, S., Unterberger, M., Grossteffan, E., Repecaud, M., Quemener, L., Theetten, S., Le Roux, J.-F., and Tréguer, P.: Unraveling salinity extreme events in coastal environments: A winter focus on the bay of brest, Frontiers in Marine Science, 8, 705403, https://doi.org/10.3389/fmars.2021.705403, 2021.

Poppeschi, C., Charria, G., Daniel, A., Verney, R., Rimmelin-Maury, P., Retho, M., Goberville, E., Grossteffan, E., and Plus, M.: Interannual variability of the initiation of the phytoplankton growing period in two French coastal ecosystems, Biogeosciences, 19, 5667–5687, https://doi.org/10.5194/bg-19-5667-2022, 2022.

Reynolds, R. W., Smith, T. M., Liu, C., Chelton, D. B., Casey, K. S., and Schlax, M. G.: Daily high-resolution-blended analyses for sea surface temperature, J. Climate, 20, 5473–5496, 2007.

Ruthrof, K. X., Breshears, D. D., Fontaine, J. B., Froend, R. H., Matusick, G., Kala, J., Miller, B. P., Mitchell, P. J., Wilson, S. K., van Keulen, M., Enright, N. J., Law, D. J., Wernberg, T., and Hardy, G. E. S. J.: Subcontinental heat wave triggers terrestrial and marine, multi-taxa responses, Sci. Rep.-UK, 8, 1–9, https://doi.org/10.1038/s41598-018-31236-5, 2018.

Savu, A.: Temperature Highs, Climate Change Salience, and Eco-Anxiety: Early Evidence from the 2022 United Kingdom Heatwave, SSRN, https://doi.org/10.2139/ssrn.4294843, 2022.

Seuront, L., Nicastro, K. R., Zardi, G. I., and Goberville, E.: Decreased thermal tolerance under recurrent heat stress conditions explains summer mass mortality of the blue mussel *Mytilus edulis*, Sci. Rep.-UK, 9, 1–14, https://doi.org/10.1038/s41598-019-53580-w, 2019.

Schlegel, R. W., Darmaraki, S., Benthuysen, J. A., Filbee-Dexter, K., and Oliver, E. C. J.: Marine cold-spells, Prog. Oceanogr., 198, 102684, https://doi.org/10.1016/j.pocean.2021.102684, 2021.

Simon, A., Plecha, S. M., Russo, A., Teles-Machado, A., Donat, M. G., Auger, P. A., and Trigo, R. M.: Hot and cold marine extreme events in the Mediterranean over the period 1982–2021, Frontiers in Marine Science, 9, 1–12, https://doi.org/10.3389/fmars.2022.892201, 2022.

Sims, D. W., Wearmouth, V. J., Genner, M. J., Southward, A. J., and Hawkins, S. J.: Low-temperature-driven early spawning migration of a temperate marine fish, J. Anim. Ecol., 73, 333–341, 2004.

Smale, D. A., Wernberg, T., Oliver, E. C. J., Thomsen, M., Harvey, B. P., Straub, S. C., Burrows, M. T., Alexander, L. V., Benthuysen, J. A., Donat, M. G., Feng, M., Hobday, A. J., Holbrook, N. J., Perkins-Kirkpatrick, S. E., Scannell, H. A., Sen Gupta, A., Payne, B. L., and Moore, P. J.: Marine heatwaves threaten global biodiversity and the provision of ecosystem services, Nat. Clim. Change, 9, 306–312, https://doi.org/10.1038/s41558-019-0412-1, 2019.

Wang, Y., Kajtar, J. B., Alexander, L. V., Pilo, G. S., and Holbrook, N. J.: Understanding the changing nature of marine cold-spells, Geophys. Res. Lett., 49, e2021GL097002, https://doi.org/10.1029/2021GL097002, 2022.

Wethey, D. S. and Woodin, S. A.: Climate change and Arenicola marina: Heat waves and the southern limit of an ecosystem engineer, Estuar. Coast. Shelf S., 276, 108015, https://doi.org/10.1016/j.ecss.2022.108015, 2022.

Wernberg, T., Bennett, S., Babcock, R. C., De Bettignies, T., Cure, K., Depczynski, M., Dufois, F., Fromont, J., Fulton, C. J., Hovey, R. K., Harvey, E. S., Holmes, T. H., Kendrick, G. A., Radford, B., Santana-Garcon, J., Saunders, B. J., Smale, D. A., Thomsen, M. S., Tuckett, C. A., Tuya, F., Vanderklift, M. A., and Wilson, S.: Climate-driven regime shift of a temperate marine ecosystem, Science, 353, 169–172, https://doi.org/10.1126/science.aad8745, 2016.

Vogel, M. M., Zscheischler, J., Wartenburger, R., Dee, D., and Seneviratne, S. I.: Concurrent 2018 hot extremes across Northern Hemisphere due to human-induced climate change, Earths Future, 7, 692–703, https://doi.org/10.1029/2019EF001189, 2019.

Yao, Y., Wang, C., and Fu, Y.: Global Marine Heatwaves and Cold-Spells in Present Climate to Future Projections, Earths Future, 10, e2022EF002787, https://doi.org/10.1029/2022EF002787, 2022.

Yiou, P., Cattiaux, J., Faranda, D., Kadygrov, N., Jézéquel, A., Naveau, P., Ribes, A., Robin, Y., Thao, S., Oldenborgh, G. J., and Vrac, M.: Analyses of the Northern European summer heatwave of 2018, B. Am. Meteorol. Soc., 101, S35-S40, https://doi.org/10.1175/BAMS-D-19-0170.1, 2020.

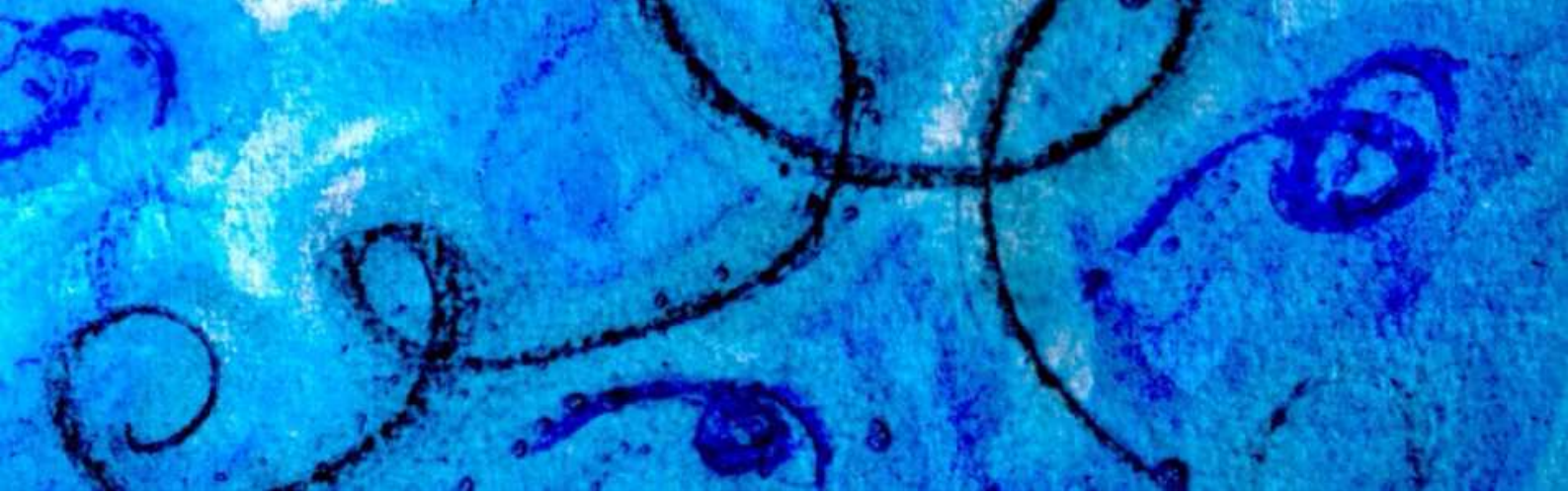

Chapitre 4 Dessalures extrêmes hivernales en rade de Brest

Après avoir détaillé l'évolution des extrêmes de température de surface de l'océan et tout en restant dans la composante physique de l'écosystème, une analyse des évènements extrêmes sur la salinité a été menée afin de déterminer comment ce second paramètre clé de la densité océanique est impacté par cette dynamique évènementielle. Dans ce chapitre, l'évolution des dessalures extrêmes en rade de Brest est étudiée.

4.1 Résumé

Les tempêtes hivernales peuvent apporter de fortes précipitations et celles-ci engendrent des crues qui se déversent alors dans l'océan. Ces forts apports en eau douce créent des dessalures dans l'environnement marin côtier. Ces dessalures souvent intenses et soudaines (plusieurs psu en seulement quelques heures) peuvent avoir un impact sur l'écosystème en jouant notamment sur la stratification des eaux dans la bande côtière. Les dessalures hivernales les plus extrêmes (décembre à mars) sur plusieurs décennies (2000 à 2018) sont analysées à partir de mesures *in situ* hautes fréquences nécessaires à la détection des extrêmes et de simulations numériques à haute résolution. Les bassins versants autour de la rade de Brest (côte Atlantique française) possèdent des sols imperméables du fait de la composition géologique. La rade de Brest a donc une réponse rapide à ces précipitations à l'origine des dessalures extrêmes observées dans la rade (baie semi-fermée). Les dessalures restent peu étudiées car leurs impacts sur la biologie marine n'ont pas encore été clairement mis en évidence malgré quelques études (Osborn et al., 2019). Cependant, le changement global pourrait renforcer le nombre de tempêtes et/ou leurs intensités et ainsi favoriser les dessalures, entraînant des modifications de l'hydrologie et l'hydrodynamique côtière.

Les dessalures extrêmes détectées sont caractérisées par leurs intensités, leurs durées et leurs dates d'occurrence. En examinant la variabilité interannuelle des événements extrêmes de faible salinité, l'influence des conditions météorologiques locales et régionales sur les précipitations et le débit des rivières est montrée. Les événements extrêmes de dessalure en rade de Brest sont contrôlés par des forçages à grande échelle. Pendant la phase positive de l'Oscillation Nord-Atlantique (NAO) et les périodes de faibles occurrences du régime météorologique de la dorsale médio-Atlantique (AR), les dessalures sont plus importantes. Cette relation entre épisodes hydrométéorologiques extrêmes et dessalures extrêmes pourrait aboutir à la mise en place d'un indicateur de densité de l'océan en surface. Enfin, l'augmentation des tempêtes pluvieuses

observées dans l'ouest de la France depuis 2010 a conduit à un doublement de l'occurrence et de la durée des événements extrêmes de dessalure en rade de Brest.

Cette étude a été publiée en 2021 dans le journal Frontiers of Marine Science (https://doi.org/10.3389/fmars.2021.705403) et les résultats sont détaillés dans ce chapitre.

4.2 Article : Unraveling Salinity Extreme Events in Coastal Environments: A Winter Focus on the Bay of Brest

frontiers in Marine Science

ORIGINAL RESEARCH
published: 21 July 2021
doi: 10.3389/fmars.2021.705403

Unraveling Salinity Extreme Events in Coastal Environments: A Winter Focus on the Bay of Brest

Coline Poppeschi[1], Guillaume Charria[1], Eric Goberville[2], Peggy Rimmelin-Maury[3], Nicolas Barrier[4], Sébastien Petton[5], Maximilian Unterberger[1], Emilie Grossteffan[3], Michel Repecaud[6], Loïc Quéméner[6], Sébastien Theetten[1], Jean-François Le Roux[1] and Paul Tréguer[7]*

[1] Laboratoire d'Océanographie Physique et Spatiale (LOPS), IUEM, CNRS, IRD, Ifremer, Université de Brest, Brest, France, [2] Unité Biologie des Organismes et Ecosystèmes Aquatiques (BOREA), Muséum National d'Histoire Naturelle, CNRS, IRD, Sorbonne Université, Université de Caen Normandie, Université des Antilles, Paris, France, [3] UMS 3113, OSU-Institut Universitaire Européen de la Mer (IUEM), Plouzané, France, [4] CNRS, Ifremer, IRD, MARBEC, University of Montpellier, Sète, France, [5] CNRS, IRD, LEMAR, Ifremer, Université de Brest, Argenton, France, [6] REM/RDT/DCM, Ifremer, Centre de Brest, Plouzané, France, [7] CNRS, IRD, Ifremer, Institut Universitaire Européen de la Mer, LEMAR, Université de Brest, Plouzané, France

OPEN ACCESS

Edited by:
Geórgenes Hilário Cavalcante, Federal University of Alagoas, Brazil

Reviewed by:
Zhaoqing Yang, Pacific Northwest National Laboratory (DOE), United States
Eduardo Siegle, University of São Paulo, Brazil

***Correspondence:**
Coline Poppeschi
coline.poppeschi@ifremer.fr

Specialty section:
This article was submitted to Coastal Ocean Processes, a section of the journal Frontiers in Marine Science

Received: *05 May 2021*
Accepted: *28 June 2021*
Published: *21 July 2021*

Citation:
Poppeschi C, Charria G, Goberville E, Rimmelin-Maury P, Barrier N, Petton S, Unterberger M, Grossteffan E, Repecaud M, Quéméner L, Theetten S, Le Roux J-F and Tréguer P (2021) Unraveling Salinity Extreme Events in Coastal Environments: A Winter Focus on the Bay of Brest. Front. Mar. Sci. 8:705403. doi: 10.3389/fmars.2021.705403

Extreme weather events affect coastal marine ecosystems. The increase in intensity and occurrence of such events drive modifications in coastal hydrology and hydrodynamics. Here, focusing on the winter period (from December to March), we investigated multi-decade (2000–2018) changes in the hydrological properties of the Bay of Brest (French Atlantic coast) as an example of the response of a semi-enclosed bay to extreme weather episodes and large-scale atmospheric circulation patterns. The relationships between extreme weather events and severe low salinity conditions (as a proxy for changes in water density) were investigated using high-frequency *in situ* observations and high-resolution numerical simulations. The identification of intense episodes was based on the timing, duration, and annual occurrence of extreme events. By examining the interannual variability of extreme low salinity events, we detect a patent influence of local and regional weather conditions on atmospheric and oceanic circulation patterns, precipitation, and river runoff. We revealed that low salinity events in Brittany were controlled by large-scale forcings: they prevailed during the positive phase of the North Atlantic Oscillation and periods of low occurrences of the Atlantic Ridge weather regime. The increase in severe storms observed in western France since 2010 has led to a doubling of the occurrence and duration of extreme low salinity events in Brittany.

Keywords: Bay of Brest, salinity, river plume, atmospheric weather regimes, extreme events

INTRODUCTION

Although coastal zones–including continental shelves–cover only a small fraction of the global ocean (about 8%; Yool and Fasham, 2001), they are key economical (e.g., 90% of the fish catch) and ecological (e.g., 30% of the global primary productivity; Wollast, 1998) regions. Coastal ecosystems occur in a transition zone, between land and open ocean, under environmental and anthropogenic pressures. How coastal ecosystems are influenced by climate at local, regional and global scales

is therefore a crucial question to assess in order to predict their possible response to changing environmental conditions, and to determine the impact of human expansion (Cloern et al., 2016).

Strong and significant relationships between atmospheric circulation and precipitation patterns have already been detected over the North Atlantic Ocean. Changes in large-scale atmospheric variability over the North Atlantic modulate precipitation patterns and hydrological processes in western Europe (Bojarriu and Reverdin, 2002; Msadek and Frankignoul, 2009), which in turn can modify both the properties and dynamics of the water column in coastal ecosystems (Goberville et al., 2010). Previous studies have demonstrated that air masses, that circulate over the North Atlantic Ocean, significantly influence the exchanges between the ocean and the atmosphere, with putative consequences on long-term trends in sea surface waters (such as alternating between warming and cooling episodes) and changes in salinity in coastal and estuarine ecosystems (Chaalali et al., 2013). Investigating the relationships between changes in the regional physico-chemical environment and large-scale hydro-climatic forcing, Goberville et al. (2014) highlighted the influence of the Atlantic Multidecadal Oscillation and the East Atlantic Pattern (EAP) on long-term (1958–2007) changes in the North-East Atlantic and the North Sea ecosystems. In western Europe, Tréguer et al. (2014) and Charria et al. (2020) demonstrated the connection between changes in coastal waters of western Europe in winter and large-scale hydro-climate processes, as well as the influence of local factors, such as river discharge, during the 1998–2013 period.

Although the influence of climate variability on long-term trends and abrupt state transitions in coastal ecosystems is now well documented, changes in large-scale atmospheric and oceanic circulation patterns can also trigger "hazards" or extreme events (Mann et al., 2017; Shi et al., 2017; Trouet et al., 2018) with direct consequences for species and communities (Thibault and Brown, 2008; Van de Pol et al., 2010; Smale and Wernberg, 2013; Wernberg et al., 2013; Seuront et al., 2019), and for socio-economic, human health and lifestyle status (Bell et al., 2018). Since the second half of the 20th century, an increase in the frequency and the magnitude of heat waves, droughts, storms, or floods has been observed (Jentsch and Beierkuhnlein, 2008; Smith, 2011; Coumou and Rahmstorf, 2012; IPCC et al., 2012, 2019). Over the last decade, heat waves have increased in duration (Seuront et al., 2019) and frequency (a doubling in recent years, Christidis et al., 2015). Storm surges have already impacted 55% of the world coastlines and with increasing frequency (Mentaschi et al., 2017; Marcos et al., 2019). Extreme precipitation episodes since the early 2000s have been related to the human influence on climate (Coumou and Rahmstorf, 2012), inducing unprecedented extreme river flooding and wave conditions such as were encountered during the winter 2013–2014 (Matthews et al., 2014; Schaller et al., 2016; Thompson et al., 2017).

Winter is a conducive season to the quantify the links between physical ocean processes and climate variability in coastal ecosystems of western Europe (Tréguer et al., 2014; Charria et al., 2020). Winter is often referred as the "dormant season," in contrast to the productive spring bloom period (Zingone et al., 2010), assuming that biological activity–especially that involving marine phytoplankton–is reduced. Nutrient levels are therefore maximum during this period (Del Amo et al., 1997). Continental and marine hydrodynamics are energetically at their maximum during winter (Margalef, 1978), with high wind speeds, large precipitation rate and important freshwater inputs from land to coastal areas. In western Europe, winter storms are one of the most typical meteorological-hydrological extreme events, leading to extreme precipitation, intense winds and wave heights (Leckebusch et al., 2006).

Open or semi-enclosed bays of western Europe can react in different ways to extreme weather events. By investigating recent changes in the physical characteristics of the Bay of Brest (a semi-enclosed bay located around 48.3°N, western France), we aimed to identify, document and understand the impacts of winter extreme weather events on the properties of coastal waters from 2000 to 2018. We used long-term *in situ* observations and numerical simulations, with a special emphasis on salinity as a key indicator of water density in coastal regions under river plume influence. Considering river runoffs, precipitation, currents, and wind patterns, we characterised the signature of extreme weather events on ocean salinity in the Bay of Brest. We then explored the interannual variability in extreme low salinity events, in relationship to large-scale hydro-climate processes.

MATERIALS AND METHODS

Study Area

The Bay of Brest, in western Europe, is a shallow macro-tidal ecosystem: more than 50% of the bay is shallower than 5 m depth, with a maximum depth around 50 m (Auffret, 1983). The Bay of Brest is influenced by freshwater inflows from three rivers: the Aulne, Elorn, and Mignonne rivers with an average winter flow of 54, 10, and 3 $m^3\ s^{-1}$, respectively. With a watershed of 1,842 km^2 and providing more than 63% of the freshwater supply, the Aulne River is the dominant source of the freshwater inflows to the Bay of Brest (Auffret, 1983; Frère et al., 2017). The Elorn and Mignonne rivers account for less than 15% of the inflows. The watersheds of western Brittany consist mainly of impermeable rocks and soils (i.e., layers through which water cannot pass) and winter precipitation directly influences river discharges (Tréguer et al., 2014).

Environmental *in situ* Observation Data

Environmental data were collected from long-term *in situ* monitoring stations (see **Figure 1** for the location of sampling sites and **Table 1** for their characteristics).

COAST-HF-Iroise (Rimmelin-Maury et al., 2020) and COAST-HF-Smart (Petton et al., 2020a) are automated moored buoys that measure a wide range of environmental parameters (temperature, salinity, turbidity, dissolved oxygen concentration, fluorescence, and pCO_2/pH). Salinity is derived from a conductivity sensor (accuracy ± 0.03 psu). Measurements are taken at 2 m depth for the COAST-HF-Iroise buoy and at 50 cm over the bottom sediment for the COAST-HF-Smart buoy. The COAST-HF-Iroise buoy is located at the interface between the Bay of Brest and the Atlantic Ocean (Iroise Sea) where fresh and

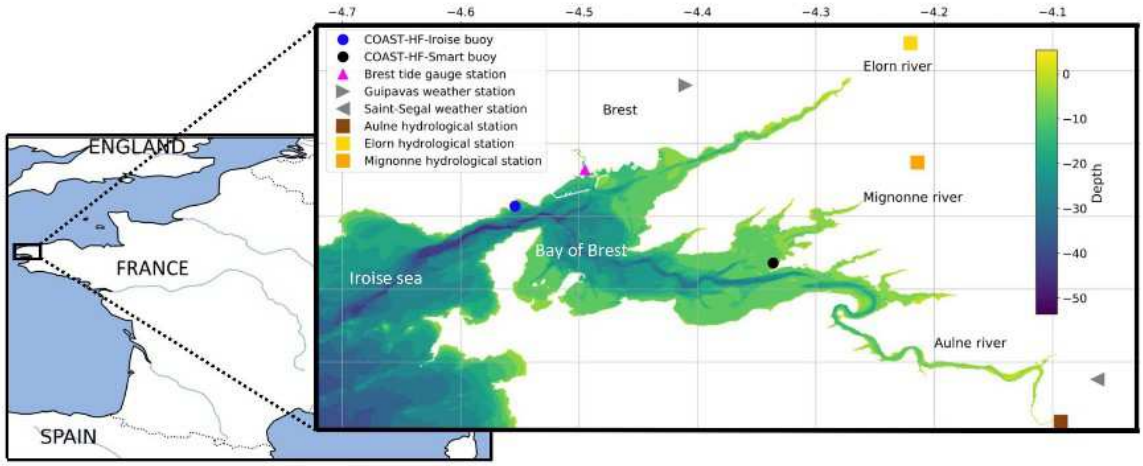

FIGURE 1 | The study area (black square) is located in the western part of France. The COAST-HF-Iroise buoy (blue circle) is at the interface between the Iroise Sea (Atlantic) and the Bay of Brest. The COAST-HF-Smart (black circle) is more inland, in the eastern part of the Bay of Brest. The Brest tide gauge station (pink triangle), and weather (grey triangles) and hydrological (coloured squares) stations are indicated.

marine waters mix. The depth of the mooring site ranges from 5 to 12 m, depending on the tide (Blain et al., 2004). The COAST-HF-Smart buoy is located in the eastern part of the Bay of Brest to monitor the land-sea continuum. The mooring site is located in a shallow embayment with a maximum depth of 8 m and receives the freshwater inputs from the Mignonne River (Petton et al., 2020a). December to March data were analysed from 2000 to 2018. All data are available on https://doi.org/10.17882/74004 (Rimmelin-Maury et al., 2020) or www.coriolis-cotier.org/ and the two high-frequency[1] monitoring buoys are part of the French COAST-HF national observation network[2] (Cocquempot et al., 2019; Farcy et al., 2019; Répécaud et al., 2019).

To assess the impact of freshwater inputs on salinity changes, we used daily flows of the three main rivers, measured daily by the regional water authority Agence de l'eau Loire-Bretagne[3]. Because the sampling stations are not located at the outlet, daily flows were normalised by the total area of the watersheds to be representative (**Figure 1**).

Precipitation data were retrieved from two weather stations from the Météo-France observation network: Saint-Ségal and Guipavas[4] (**Figure 1**). No differences were observed between the two weather stations (less than 0.01 mm, with no temporal lag), supporting that precipitation patterns were consistent over the region during the 2000–2018 period. Therefore, we only considered the Guipavas station in our study.

[1]In the French coastal observing systems, high-frequency autonomous observing systems, and low-frequency sampled sites (weekly or biweekly manual water sampling campaigns) are distinguished based on sampling frequency.
[2]www.coast-hf.fr

TABLE 1 | Locations and characteristics of the *in situ* sampling sites.

Sampling sites	Longitude	Latitude	Time period	Sampling frequency
COAST-HF-Iroise buoy	4.582°W	48.357°N	2000–2021	20 min
COAST-HF-Smart buoy	4.331°W	48.317°N	2008–2021	15 min
Brest tide gauge station	4.495°W	48.382°N	1846–2021	1 min
Saint-Segal weather station	4.062°W	48.238°N	1900–2021	6 min
Guipavas weather station	4.410°W	48.440°N	1929–2021	6 min
Aulne hydrological station	4.093°W	48.205°N	1993–2021	1 day
Elorn hydrological station	4.220°W	48.469°N	1984–2021	1 day
Mignonne hydrological station	4.214°W	48.387°N	1971–2021	1 day

Numerical Model Simulation Data

Numerical simulations can help to better understand the processes involved and to evaluate the ocean hydrodynamics when *in situ* observations are lacking. To cover the 2000–2018 period, two numerical simulations were used: the MARS3D–BACH *(BiscAy Channel;* modelled fields available from 2001 to 2012) and the MARS3D–MARC (*Modelling and Analysis for Coastal Research*; modelled fields available from 2010 to 2018) simulations. These realistic simulations are based on the primitive equation MARS3D model (3D hydrodynamical Model for Application at Regional Scale; Lazure and Dumas, 2008), developed by French Institute for Research and Exploitation of the Sea (IFREMER). The MARS3D–BACH and MARS3D–MARC simulations are thoroughly described in Theetten et al. (2017); Charria et al. (2017), and Petton et al. (2020b) and were validated by Charria et al. (2017) and Petton et al. (2020b).

Briefly, they differ mainly in their spatial resolution and how they were forced by atmospheric forcings. The horizontal and vertical resolutions of the MARS3D–BACH simulation were 1 km and 100 vertical sigma levels, respectively. The MARS3D–BACH simulation was carried out for the 2001–2012 period

[3]www.hydro.eaufrance.fr/
[4]https://donneespubliques.meteofrance.fr/

(i.e., 11 years) with daily average outputs, using the ERA-Interim simulation [reanalysis produced by the European Centre for Medium-Range Weather Forecasts (ECMWF); Berrisford et al., 2011] for atmospheric forcings. The DRAKKAR global configuration ORCA12_L46-MJM88 was used for the open boundary and initial conditions (Molines et al., 2014).

For the MARS3D–MARC simulation, the horizontal and vertical resolutions were 50 m and 20 vertical sigma levels, respectively. The simulation was carried out from January 2010 to July 2018 (i.e., 8 years) and produced instantaneous fields every 5 min. Atmospheric forcings were extracted from an analysis of the Applications from Research to Operational Mesoscale (AROME, 1 km resolution; Ducrocq et al., 2005) model provided by Météo-France. Initial salinity conditions originated from another simulation using the MARS3D model (Caillaud et al., 2016).

Here, we compared these simulations with *in situ* observations by extracting a model grid point as close as possible to the COAST-HF-Iroise measurement site: at 4.551°W, 48.357°N for MARS3D–BACH and at 4.546°W, 48.354°N for MARS3D–MARC.

Large-Scale Atmospheric Weather Regime Data

To evaluate the link between Bay of Brest hydrodynamics (including extreme low salinity events) and atmospheric circulation, we investigated four weather regimes associated with surface pressure, wind, air-temperature and precipitation anomalies (Barrier, 2013) and which represent the main large-scale atmospheric forcings that act in western Europe (Cassou et al., 2011; Barrier et al., 2014; Tréguer et al., 2014).

The North Atlantic Oscillation (NAO) describes the basin-scale gradient of atmospheric pressures over the North Atlantic between the high pressures centred on the subtropical Atlantic and the low pressures over Iceland (Hurrell et al., 2001). The positive phase (NAOp) induces warm and rainy winters in western Europe and is associated with extreme meteorological storm events. The negative phase (NAOn) induces cold and dry winters in western Europe (Barrier et al., 2014). Using the weather regimes to describe the NAO emphasises the asymmetry between the two phases, because they cannot be superimposed.

The Atlantic Ridge (AR) is directly related to the negative phase of the EAP and represents a blocking weather regime (high-pressure wind in Europe) with negative pressure anomalies around 60°N–20°E, and positive ones around 50°N–25°W. The AR brings cold temperature anomalies over western Europe and precipitation during the winter.

The Scandinavian Blocking (BLK) regime shows a region of negative (positive) sea-level pressure anomalies over southern Greenland (northern Europe), which are associated with a northward displacement of winds at 20°W dry weather (low precipitation) conditions in northern Europe.

Data Analysis

To identify low salinity extreme events that occurred in the Bay of Brest, we focused on the winter period (December to March) from 2000 to 2018. We developed a data processing chain that first identifies and filters tides. We then detected extreme low salinity events and analysed the relationship with precipitation, river runoffs and atmospheric weather regimes.

The Bay of Brest is governed by a strong tidal regime with a tidal range of about 6 m. During the ebb tide, freshwater accumulates in the bay from river water flowing to the open ocean; seawater inflow from the Iroise Sea is observed during the flood tide. To detect a freshwater signature at the COAST-HF-Iroise buoy, several tidal cycles are necessary. The lag between river discharge and its detection at the sampling station is mainly modulated by the tidal amplitude and phase (Frère et al., 2017). Water masses at the COAST-HF-Iroise buoy mainly represent oceanic water during high tides and inland water at low tides. To characterise the extreme low salinity events in the Bay of Brest, we therefore considered low tide periods. Due to the 20-min measurement period of the COAST-HF-Iroise buoy and the water mass inertia, salinity time series were constructed by computing, for each selected observation, the values recorded 20 min before and 40 min after each low tide cycle.

An extreme event can refer to a value that exceeds a threshold determined numerically, experimentally, graphically or arbitrarily (e.g., expert judgement). Here, we used the percentile method to identify extreme episodes: an extreme event was defined when exceeding the percentile threshold. For example, Wan Zin et al. (2010) used the 95th percentile to detect extreme daily precipitation events, but a 10th–90th percentile interval was used by Barnett et al. (2006) to investigate changes in atmospheric CO_2. Here, we tested three threshold values (10th, 15th, and 20th percentiles) and determined the 15th percentile as the best compromise between sensitivity and precision to detect extreme low salinity events (**Table 2**). Finally, we considered a minimum duration of a full M2 lunar semi-diurnal tidal cycle (i.e., 12 h 25 min 12 s) for an extreme event, to avoid double detection of a single episode.

The relationship between low salinity events, precipitation and rivers flows was assessed by estimating the time scales of the processes that took place in the Bay of Brest. During the winter period, a peak in river discharge systematically appeared around 24 h after a peak in precipitation. Direct evaporation and

TABLE 2 | Percentage of detection of extreme low salinity events (identified from *in situ* observations) in model simulations as a function of a percentile threshold.

Percentile	% of extreme low salinity events captured by the numerical models	
	MARS3D–BACH (%)	**MARS3D–MARC (%)**
10th	32	47
15th	**46**	**63**
20th	39	64

Note that these percentages are higher when a 5-days lag was considered: based on the 15th percentile, 63 and 74% of extreme observed low salinity events were detected for MARS3D–BACH and –MARC simulations, respectively. Bold values highlight the 15th percentile.

evapotranspiration are negligible processes in winter compared with the influence of precipitation (Tréguer et al., 2014). Following previous numerical simulations (Petton et al., 2020b), we used the Constituent-oriented Age and Residence time Theory (CART[5]) to estimate the influence of precipitation on water masses of the Bay of Brest: the effect of flooding on low salinity extreme events is visible about 12 days after a storm event (Frère et al., 2017; Petton et al., 2020b). Based on the most intense precipitation period of 2000–2018, i.e., the winter 2013–2014 (Petton et al., 2020b), we found that water residence times in the Bay of Brest ranges from 7 to 25 days (not shown). This study showed that when peaks of flow occur (>200 m^3 s^{-1}), the water age is always less than 14 days. We therefore used a maximum time lag of 14 days to determine whether precipitation had an effect on low salinity extreme events.

To explore the link with changes in large-scale atmospheric circulation, we used daily atmospheric Sea Level Pressure Anomalies (SLPA) from the ERA-5 reanalysis (Copernicus Climate Change Service, 2017) to calculate the daily occurrences of the four weather regimes. For each extreme event, the Euclidian distance between the ERA-5 SLPA and the centroids of the four winter weather regimes (i.e., mean SLPA associated with each weather regime) was computed and the regime that minimised the distance was assigned. To highlight the relationship between daily SLPA and the four weather regimes, daily spatial correlations were then computed and represented using the Kernel Density Estimation (KDE) method (Turlach, 1993; Yang et al., 2018), a non-parametric approach to estimate the probability density functions of SLPA correlations. A Gaussian kernel function was used to smooth the probability density function and to obtain the distribution of correlations for (1) the winter period and for (2) pre-extreme event periods (i.e., 14 days). Finally, Pearson correlation coefficients between winter precipitation and the occurrence of winter weather regimes were computed.

RESULTS

Detection and Characterisation of Extreme Low Salinity Events

The observed *in situ* salinity, which ranged from 21 to 35.8 at COAST-HF-Iroise and from 5 to 35.1 at COAST-HF-Smart, exhibited a seasonal cycle with higher values in summer than in winter due to low river runoffs. In winter, salinity decreased, with peaks of low salinity for short durations (26 at COAST-HF-Iroise and 15 at COAST-HF-Smart; **Figure 2**). These peaks, defined as extreme low salinity events, were threshold dependent. Using the 15th percentile, the thresholds of salinity were 32.59 for *in situ* observations at COAST-HF-Iroise, 33.3 and 33.9 for the BACH and MARC simulations at the same point. Numerical simulations allowed us to identify 46% (MARS3D–BACH) and 63% (MARS3D–MARC) of the *in situ* observed extreme events. Note that the 15th percentile showed the best detection rate (**Table 2**). At the COAST-HF-Smart buoy, the threshold was lower (equal to 23.73) due to its location close to the Aulne river estuary.

When analysing *in situ* measurements (**Figure 2**), we detected 46 (COAST-HF-Iroise) and 52 (COAST-HF-Smart) extreme low salinity events over the common sampling period (2008–2018). From 2000 to 2018, 72 events were reported at COAST-HF-Iroise, i.e., an average occurrence of four events per winter. For both *in situ* datasets, we found a mean duration of the extreme low salinity events of about 2–3 days (**Table 3**), the maximum duration of an event being 27 days. The same number of events is not exactly similar due to differences in: amplitude, duration and lack of *in situ* data. Then, in some cases, observed *in situ* events are not detected in modelled time series due to modelled less intense events. Modelled events can also be too short in the simulation to be identified as events. Missing observations can explain modelled detected events not observed.

To explore the dynamics during periods with missing observations, model simulations are essential. We therefore compared *in situ* dataset between the COAST-HF-Iroise buoy and the MARS3D–BACH and MARS3D–MARC simulations. We reproduced the seasonal cycle well with the MARS3D–BACH simulation, with both and increase in salinity from March to September and a decrease during autumn and winter (**Figure 2A**); we also obtained similar intensity signals. The MARS3D–MARC simulation also reproduced the salinity seasonal cycle well, but salinity was overestimated in summer (**Figure 2A**), most likely because of the use of different forcing parameters in both simulations. Winter salinity was not affected, however. During extreme low salinity events, and for both simulations, modelled minimum values were higher than minimum *in situ* values (29.7 and 25.5 versus 23.5 at COAST-HF-Iroise; **Table 3**). The MARS3D–BACH simulation reproduced 78% (32 of 41) of the observed events over the 2001–2012 period. While 35 extreme salinity events were observed from 2010 to 2018, we modelled 46 events from the MARS3D–MARC simulation. This supports the use of the two numerical simulations, in combination, as an alternative to complete *in situ* observations and to better characterise extreme events.

By applying this analysis, 72 extreme low salinity events were detected at the COAST-HF-Iroise buoy with an average duration of 2 days and a drop in salinity of up to 6.5. Such a large variability in salinity may influence the functioning of the Bay of Brest. To assess possible consequences, the processes behind the emergence of extreme low salinity events need to be evaluated.

Dynamics of Low Salinity Events and Underlying Processes

Precipitation and Low Salinity Events

To better understand and illustrate the origin of extreme low salinity events, we explored the possible link with precipitation patterns (**Figure 3**). By focusing our interpretation on two periods during the year 2007, we detected that a peak in precipitation was always observed before an extreme low salinity event: (1) From 6 to 15 February 2007, precipitation reached

[5]www.climate.be/cart

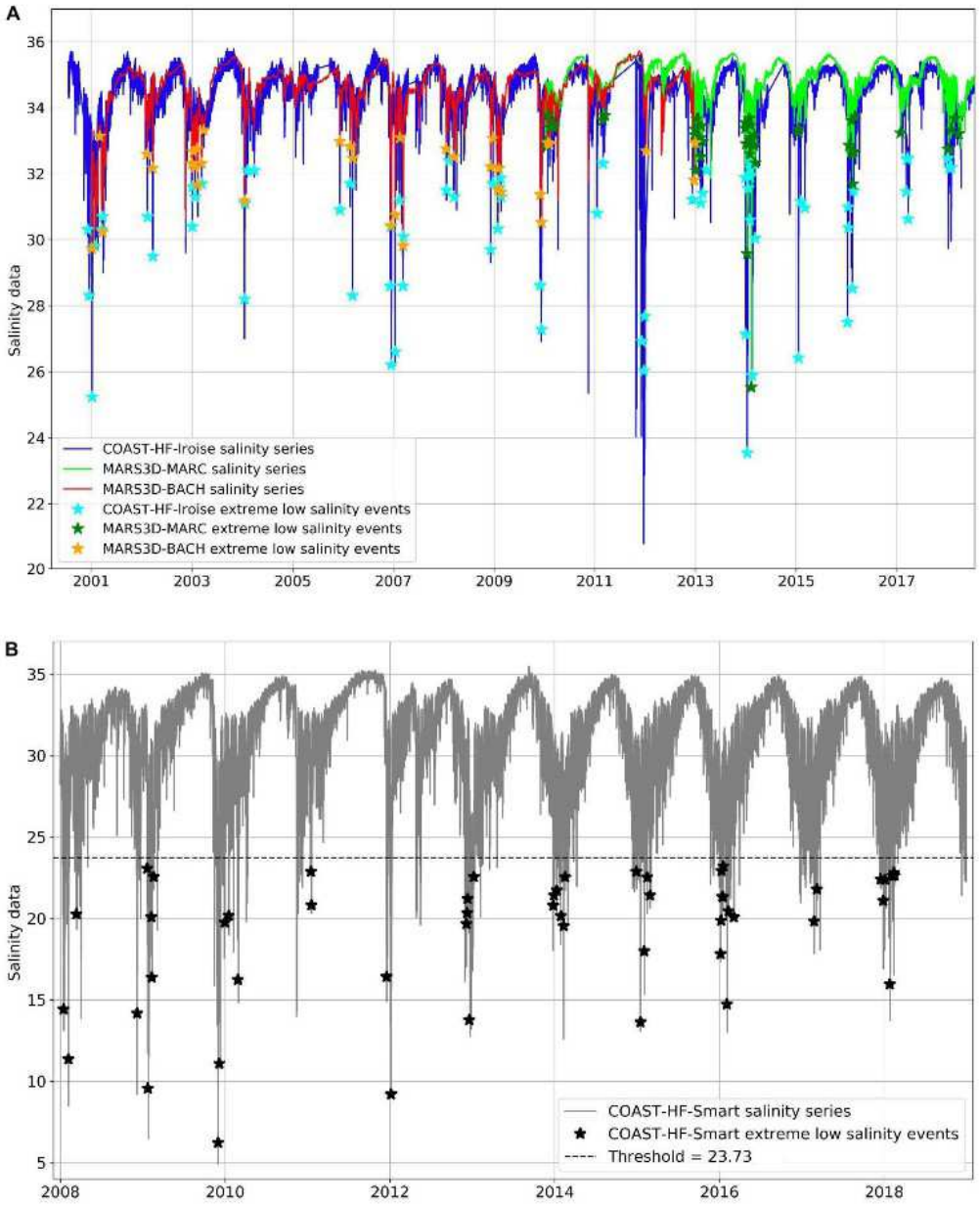

FIGURE 2 | Time series of salinity and detected extreme low salinity events indicated with stars for **(A)** the observed data at COAST-HF-Iroise buoy (in blue) and the modelled data of the MARS3D–BACH (2001–2013, in red) and the MARS3D–MARC (2010-mid-2018, in green) simulations and **(B)** the observed data at the COAST-HF-Smart buoy (in grey). The dashed line represents the threshold salinity value of 23.73 determined from the percentile method.

32 mm and a strong decrease in salinity (31.2) was observed 2–3 days later; (2) From 28 February to 3 March 2007, precipitation reached 29 mm and a marked decrease in salinity (28.5) was detected approximately 5 days later. Two low salinity extreme events were observed.

Considering the 14-day period before an extreme event, the average precipitation was 103 mm (not shown). The precipitation before extreme events was about twice (42% larger) as much as the average winter precipitation during the 2000–2018 period.

Underlying Processes of Low Salinity Events

Several ocean processes can explain the observation of low salinity events at the entrance of the Bay of Brest (around COAST-HF-Iroise buoy). Both model simulations allow reproducing the surface salinity dynamics with a bias of 0.23 (comparison between MARS3D–MARC and observations) and 0.17 (comparison between MARS3D–BACH and observations). The Root Mean Square Error reaches 0.87 (comparison with MARS3D–MARC) and 0.92 (comparison with MARS3D–BACH). In the water column, the stratification is also reproduced

TABLE 3 | Key characteristics of the observed and simulated events.

		Mean	Minimum	Maximum
Duration (days)	COAST-HF-Iroise	3	0.5	27
	COAST-HF-Smart	2	0.5	20
	MARS3D–BACH	5	1	17
	MARS3D–MARC	2.6	0.5	20
Salinity intensity	COAST-HF-Iroise	30	23.5	32.5
	COAST-HF-Smart	19	6.2	23
	MARS3D–BACH	32	29.7	33.2
	MARS3D–MARC	32.8	25.5	33.8

during the low salinity events in both simulations (not shown). For example, considering the difference between bottom and surface salinities (two-layer model), both simulations, during the common time period (2010–2012), are correlated at 0.59 with a Root Mean Square Error of 0.32 between MARS3D–BACH and MARS3D–MARC bottom/surface difference. Major peaks in the time series are then reproduced in both simulations. Based on the MARS3D–MARC model (with a finer spatial resolution) to investigate the processes behind extreme events, we observed a plume–mainly fed by freshwaters from the Aulne River (**Figure 4B**)–that was associated with increased westward and north-westward residual currents that reached 0.6 m s^{-1} (**Figures 4A–C**). The Aulne river flow increased during the event in parallel to changes in wind circulation: westerly/south-westerly winds decreased or veered to easterly winds (**Figure 4B**). During the event, at the end of December 2013, surface circulation induced by easterly winds (lower than 5 m s^{-1}) has a limited impact on the river plume extent and the total surface circulation. We estimate that the wind forcings action will induce a surface circulation, which is not exceeding 0.15 m s^{-1} (considering that the surface current intensity corresponds to 3% of the wind intensity). The vertical extent of the river plume remained restricted (around 7 m) and flowed along the northern coast of the entrance of the Bay of Brest due to the Coriolis effect.

The analysis of all winter events confirmed that advection processes in the Bay of Brest explained the extent of the river plume and that the intensity of the events (combination of the influence of precipitation pattern and wind circulation) modulated the intensity and duration of the low salinity events: they can either be strong as during the winter 2013–2014, or weak as observed in the winter 2017–2018.

Variability of Low Salinity Events

A strong interannual variability in the number of extreme low salinity events was observed at the COAST-HF-Iroise buoy (**Figure 5**): 10 events were detected during the winter 2013–2014, but less than five events during the previous 4 years. The four most active winters were 2000–2001, 2006–2007, 2008–2009, and 2013–2014. Since 2010, at least three events per winter were detected, whereas only 1 or 2 events were detected before (**Figure 5A**). A clear variability in the duration of extreme low salinity events was also visible (**Figure 5B**). The winters 2000–2001 and 2013–2014, characterised by the strongest precipitation and winds, showed low salinity events that lasted more than 50 days, they rarely exceed 15 days during other winters. The mean duration of extreme low salinity has nearly doubled when comparing the periods 2000–2009 and 2010–2018 (10 versus 18 days).

By comparing observed and modelled data, no event was detected in 2004–2005, but more than 10 events were observed in 2013–2014 (**Figure 5A**). Simulations reproduced the number of observed extreme events such as in 2002–2003, 2005–2006, 2009–2010, and 2017–2018. When investigating the duration of events, we found that MARS3D–BACH overpredicted the

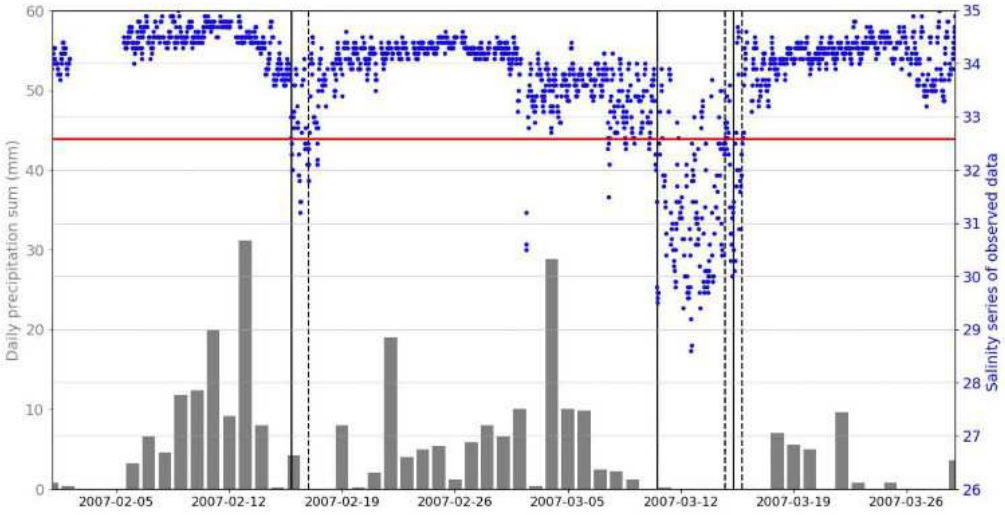

FIGURE 3 | Average daily precipitation (in mm, histograms in grey) and salinity at high and low tides (blue dots) for the period from 1st February 2007 to 29th March 2007. The red line indicates the 32.59 salinity threshold. The continuous and dashed black vertical lines show the beginning and the end of an extreme event, respectively.

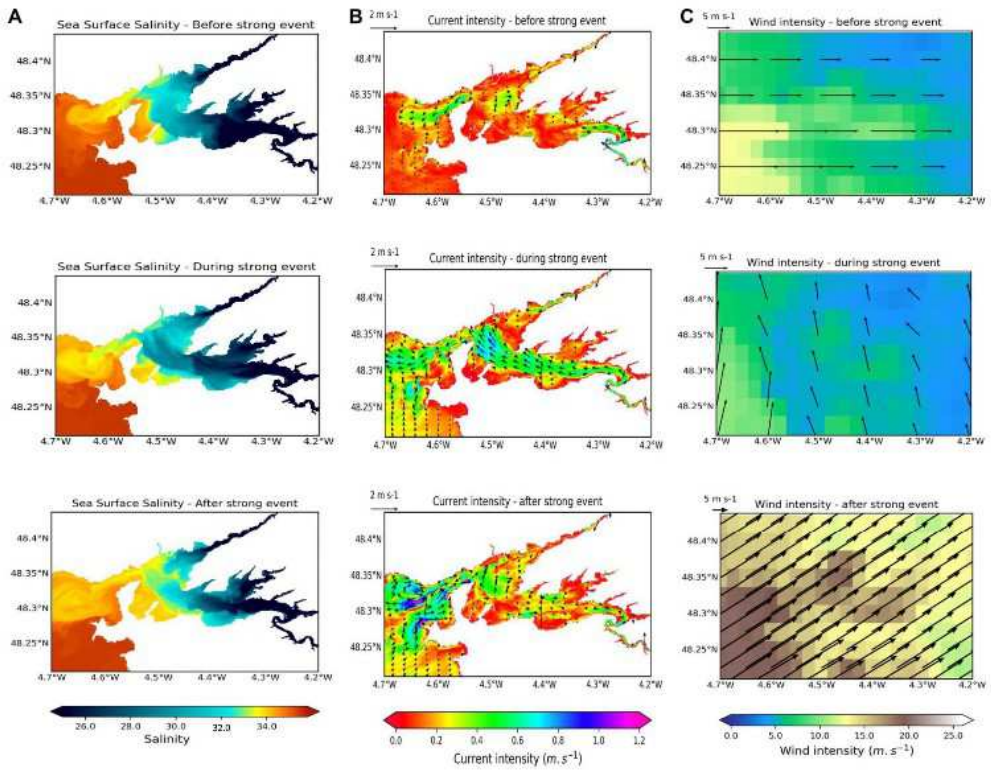

FIGURE 4 | Maps of **(A)** sea surface salinity at 2 m depth, **(B)** surface current intensity (in m s^{-1}) and its associated vectors, **(C)** surface wind intensity (in m s^{-1}) and its associated vectors: before (28/12/2013; upper panels), during (30/12/2013; middle panels), and after (03/01/2014; lower panels) a low salinity event during the winter 2013–2014.

number of extreme low salinity events duration (on median average, 7.5 days for MARS3D–BACH and 3.7 days for the observations) and that MARS3D–MARC underpredicted those durations with 2.4 days on average compared with 9.2 days observed (**Figure 5B**). However, the MARS3D–BACH and MARS3D–MARC simulation show strong correlations with the *in situ* data, 0.94 and 0.98, respectively. The two most intense winters (2000–2001 and 2013–2014) stood out in the duration of extreme events.

Dynamics of Low Salinity Events at Global Scale

The correlations between atmospheric sea level pressure and the four weather regimes (NAOp, NAOn, AR, and BLK) were calculated for winter *in situ* observations using the KDE method for the 14 days before extreme events (**Figure 6**). Similar features were observed when the method was applied on results from numerical simulations. For the entire winter period (blue line; **Figure 6**), the KDE was centred around 0, suggesting no significant influence of large-scale processes. By examining density distributions of correlations when considering a 14-day period before extreme low salinity events (orange line; **Figure 6**), we detected a possible influence of the AR (correlations between −0.5 and −0.25) and the NAOp (correlations between 0.2 and 0.6) on the occurrence of extreme low salinity events. This relationship was related to the interconnection between winter precipitation and the AR and NAOp winter regimes in the north-eastern Atlantic (Pearson correlation coefficients of −0.29 and 0.26 for AR and NAOp, respectively).

DISCUSSION

Extreme events influence coastal ecosystems worldwide: in the Tagus estuary (Costa et al., 2007), in the south-eastern Bay of Biscay (Ferrer et al., 2009), in the Central Oregon coast (Mazzini et al., 2015), in the Bay of San Pablo (Poulton et al., 2004), in California estuaries (Maynard et al., 2018), or in the north-western Arabian Gulf (Alosairi et al., 2019). Despite the profound consequences for ecosystem functioning (Bell et al., 2018; Seuront et al., 2019), the root causes underlying extreme episodes remain only rudimentarily documented. We lack understanding of how extreme events begin, and whether they propagate and induce alterations at the ecosystem scale. To bridge this gap, it is essential to better appreciate the interannual variability of extreme events to detect their occurrence and changes in intensity.

Impacts of Extreme Weather Events and Changes in Salinity in the Bay of Brest

Temporal changes in the physical characteristics of coastal waters of western Europe during winter revealed the clear occurrence

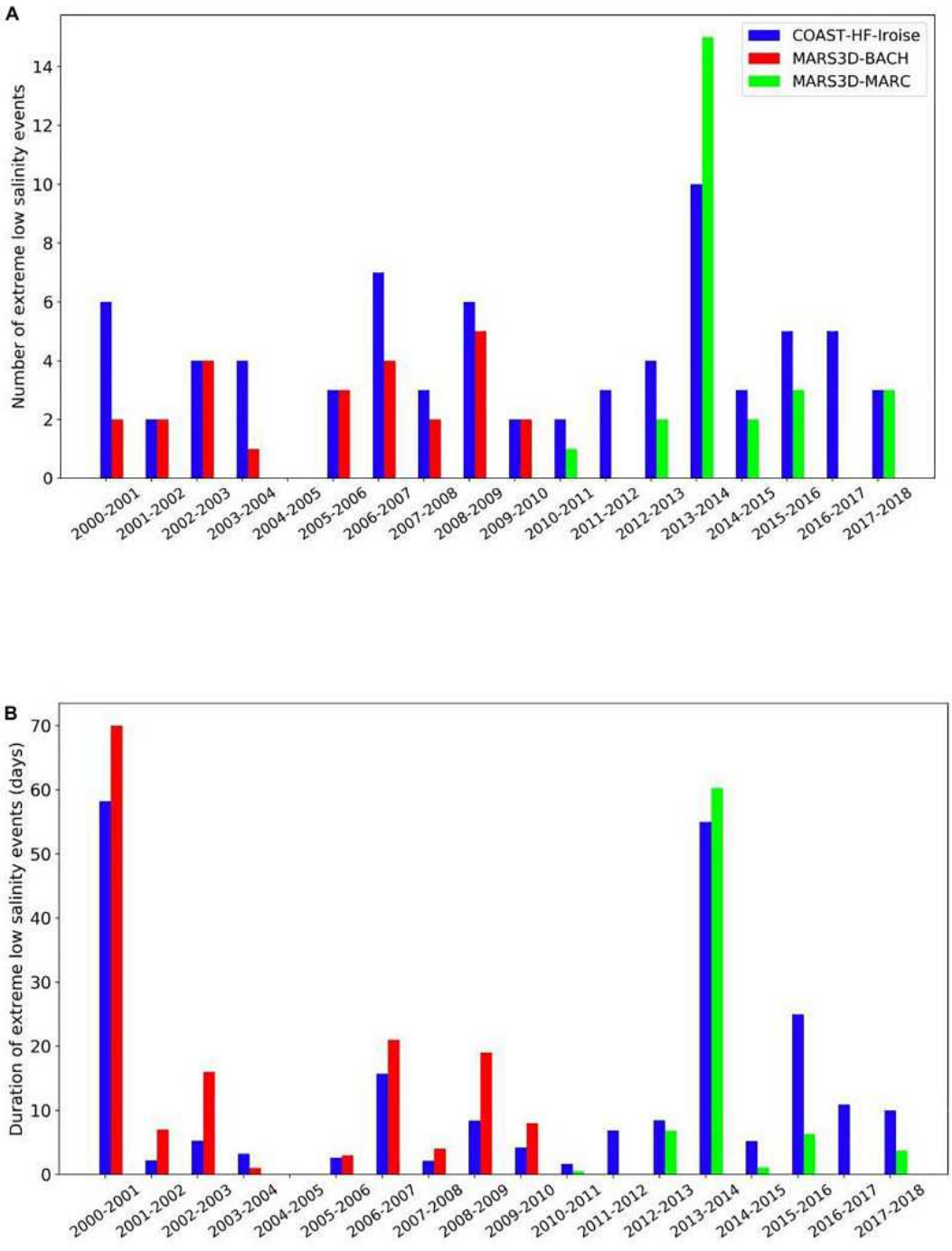

FIGURE 5 | Histograms of **(A)** the number and **(B)** duration (in days) of extreme low salinity events concomitant in time with observed (COAST-HF-Iroise buoy, in blue) and simulated (MARS3D–BACH model and MARS3D–MARC, in red and green, respectively) data during the 2000–2018 period.

of extreme low salinity events in the Bay of Brest since the early 2000s. Such "hazards" are relevant indicators of the response of semi-enclosed bay ecosystems to increasingly intense weather episodes, such as extreme storm surges, and floods (Jentsch and Beierkuhnlein, 2008; Smith, 2011; Coumou and Rahmstorf, 2012; IPCC et al., 2012, 2019). It is therefore essential to identify the contribution of the main drivers that influence the dynamic balance of freshwaters and marine waters.

Freshwater inputs in the Bay of Brest come predominantly from (i) river discharges (i.e., the Aulne, Elorn, and Mignonne rivers; Ménesguen and Piriou, 1995; Merot and Buffin, 1996; Guillaud and Bouriel, 2007), (ii) local precipitation, and (iii)

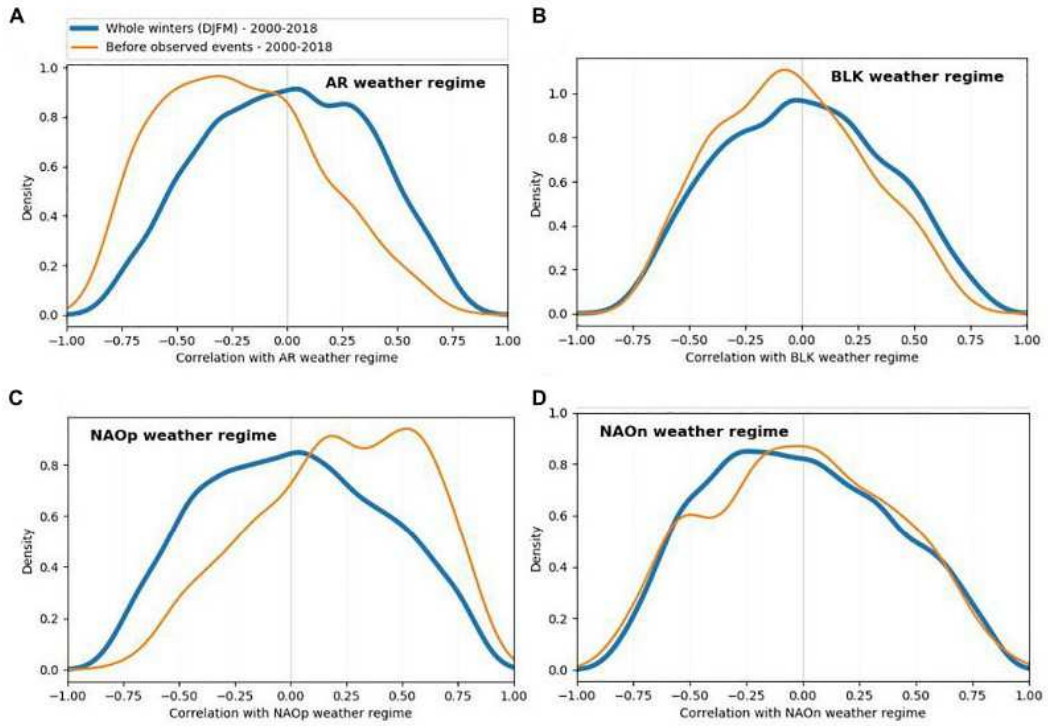

FIGURE 6 | Kernel density based on the correlation values calculated between the atmospheric sea level pressure and **(A)** the Atlantic Ridge (AR), **(B)** the Scandinavian Blocking regime (BLK), **(C)** the positive (NAOp) and **(D)** negative (NAOn) phases of the NAO for the winter months of the period 2000–2018. Kernel density curves were calculated by considering either all winter months from 2000 to 2018 (blue curve) or only the 14-day periods before extreme low salinity events using *in situ* observations (orange curve).

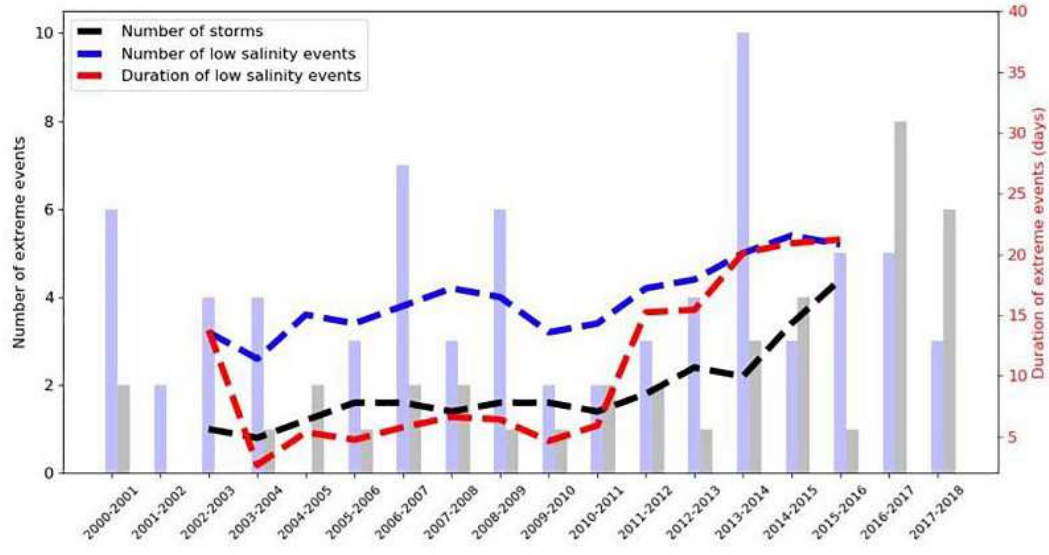

FIGURE 7 | Interannual changes (after application of a 5-years running mean) in the number of extreme weather episodes (in black) with its raw data (in grey), *in situ* extreme low salinity events (in blue) with its raw data (in light blue) and their duration (in days, in red) at the COAST-HF-Iroise buoy.

ocean water mass exchanges between the bay and the Iroise Sea. During the winter period, precipitation has a cardinal influence on river flow (McCabe and Ayers, 1989). Therefore, precipitation over the watersheds and associated river runoffs can explain low salinity events (Cayan and Peterson, 1993; Poulton et al., 2004). Due to the nature and properties of the Aulne river basin (dominated by granite and schist; Acolas et al., 2006; Moskalski et al., 2018), floods directly mirror precipitation.

This phenomenon is amplified during winter when soils are water-saturated. Here, we clearly demonstrated that an excess in precipitation induces–most of the time–to the occurrence of a low salinity event with a maximum time lag of 14 days.

To thoroughly analyse the interannual variability of extreme events, we demonstrated that numerical modelling provides essential information, when *in situ* observations are too scarce, to reproduce the freshwater pathway in the Bay of Brest and to help in better defining the relationship between river runoffs and low salinity events. These simulations can be refined, however, by improving the spatial resolution and/or the parametrisation of diffusion processes (Petton et al., 2020b). These improvements can help mitigate the underestimated values we simulated.

Extreme Low Salinity Events: A Specific Answer of the Bay of Brest to Intense Precipitation

The relationship between river runoff and extreme low salinity events was highlighted by our simulations which included only river runoff as external freshwater input (precipitation was not considered). The macro-tidal regime of the Bay of Brest, which contributed to both the advection and the diffusion of the river plumes (Ayouche et al., 2020; Petton et al., 2020b), explains the lag between precipitation and low salinity events.

To characterise changes in the amplitude of low salinity episodes, the duration of each event was compared with *in situ* minimum salinity, providing support that the intensity of each event and its duration were linked. Duration was not only related to precipitation, however, but also to the dynamics of the Bay of Brest. By investigating the contribution of external forcing during two contrasting events (winter 2013–2014 vs. winter 2017–2018), we showed that the surface circulation in the Bay of Brest played an important role in the advection of the Aulne River freshwater plume as a source of the low salinity events in the entrance of the bay. River flows, driven by the high precipitation rate, feed the Bay of Brest with freshwater, which in turn affects the properties of the water column. The tidal regime does not affect the amplitude of observed and modelled events during both neap and spring tides. But the stratification can be highly affected by the neap-spring tidal cycle under different environmental conditions (e.g., different stratification, open bay; Chegini et al., 2020 in the German Bight). The amplitude of modelled and observed events is also influenced by wind directions, speeds, and frequencies, as a driver of the river plume spreading (Kourafalou et al., 1996; Liu et al., 2008; Kastner et al., 2018). Changes in wind directions, as well as decrease in intensity, contribute to the extent of the river plume and influence the modelled surface currents. By considering the different forcings during the winter period (in 2013–2014 and 2017–2018), we showed that the seasonal circulation of surface layers was affected by an increase in river flow and by winds. And a strong high-frequency variability of the surface circulation in the Bay was also revealed. The occurrence of low salinity events at the entrance of the Bay of Brest resulted from a combination of high river discharge and north-westward downwelling-favourable winds (or at least with a weaker wind intensity). The key role of these downwelling-favourable winds on the river plume spreading was also further South in the Bay of Brest, in the Loire and Gironde estuaries (Lazure and Jegou, 1998). The sequence of events in the winter 2013–2014 induced longer and more frequent events.

Interannual Changes in Extreme Low Salinity Events

Since the early 2000s, the occurrence of observed and modelled winter extreme low salinity events has varied between 0 and 10 in the Bay of Brest, and pronounced interannual variability was characterised. Winters associated with intense mid-latitude depressions, such as in 2000–2001, 2006–2007, 2008–2009, and 2013–2014, showed a high number of events, but the winter 2004–2005 was a calm period. By investigating changes in hydro-climatological processes, we demonstrated a clear influence of extreme salinity with 2004–2005 and 2013–2014 being the most extreme winters. The winter 2004–2005 was particularly cold and dry (Somavilla et al., 2009, 2011, 2016; Charria et al., 2017) and only one storm, centred in the north of France, was observed. During the 2013–2014 period, intense winter storms were observed in western Europe (12 storms, including the two longest, 26 and 13.75 days, over the past 18 years, i.e., before 2013; Blaise et al., 2015; Castelle et al., 2015; Davies, 2015; Gohin et al., 2015; Masselink et al., 2016), explaining why we detected 10 extreme low salinity events.

By investigating interannual changes in both the occurrence and duration of extreme low salinity events in relationship to storm episodes (as identified by Météo-France; **Figure 7**), we detected a constant increase (in occurrence and duration of events) over the last two decades. This suggests that an intensification in the number of storms may have paralleled an increase in both the occurrence and magnitude of extreme events.

Impacts of Large-Scale Hydro-Climate Processes on Extreme Events

Investigating interannual changes in the physical and chemical characteristics of coastal waters, Tréguer et al. (2014) highlighted the connection between the Bay of Brest and the North Atlantic atmospheric circulation. Here, we confirmed the impact of large-scale North Atlantic atmospheric processes on the coastal waters in the Bay of Brest. Extreme events are triggered by large-scale processes, with a dominance of low salinity events (1) during the NAOp and (2) when SLPA correspond to the reversed AR regime. Extreme precipitation and the winter NAO are strongly interrelated, underlining that the NAOp, by favouring storms, is the dominant regime in winter (Donat et al., 2010; Cassou et al., 2011; Gomara et al., 2014; Tabari and Willems, 2018).

CONCLUSION

Here, by combining two decades of *in situ* observations and numerical simulations, our study quantified–for the first time in the Bay of Brest–the occurrence of extreme low salinity events and their links with large-scale atmospheric circulation. We demonstrated that the signature of extreme weather events on trends in salinity was only visible when *in situ* high-frequency measurements and high-resolution numerical modelling were combined. In the Bay of Brest, the intensity of winter

extreme episodes was mainly related to changes in precipitation patterns, with consequences on both the Aulne and Elorn river watersheds. A detailed analysis of underlying processes showed that extreme low salinity events occurred not only after a peak in river discharge, but also under favourable atmospheric (wind) conditions that contribute to the advection of the river plume within the Bay of Brest. By investigating interannual changes in the occurrence of extreme events, we revealed that two contrasted winter periods have taken place since the early 2000s, with a clear increase in both the number and duration of extreme low salinity events as a response to an intensification of winter storms. Large-scale hydro-climatic processes (i.e., the NAOp and the AR) significantly modulate precipitation and flooding events and triggered extreme low salinity episodes.

DATA AVAILABILITY STATEMENT

The original contributions presented in the study are included in the article, further inquiries can be directed to the corresponding author.

AUTHOR CONTRIBUTIONS

CP and GC designed the study and wrote the first draft of the manuscript. PR-M, MR, LQ, EGr, NB, SP, ST, and J-FR provided and pre-processed datasets. CP, GC, and MU performed most of the *in situ* and numerical analyses. NB provided expertise on weather regimes. J-FR contributed to **Figure 1**. MU contributed to **Figure 3**. GC computed **Figure 6**. EGo, PR-M, PT, and SP made substantial contributions in the successive versions of the manuscript. All authors contributed to manuscript revision, read and approved the submitted version.

ACKNOWLEDGMENTS

This study is part of the *Contrat Plan Etat-Région* ROEC partly supported by European Regional Development Funds. *In situ* observations were provided by the COAST-HF (http://www.coast-hf.fr) and the SOMLIT (http://somlit.epoc.u-bordeaux1.fr) national observation network from the ILICO research infrastructure. Modelling experiments (BACH configuration) were performed with GENCI (French Big National Equipment Intensive Computing) computational resources administered at CINES (National Computing Center for Higher Education). Data processing and figures were partly carried out using the open-source Python library VACUMM (http://www.ifremer.fr/vacumm/) and the Geographical Information System (QGIS–http://www.qgis.org). Tide gauges data were provided by the French Naval and Hydrographic Service (Shom). We also thank Michel Aïdonidis for insightful discussions. We thank Armel Bonnat for processing Météo-France *in situ* observations.

REFERENCES

Acolas, M. L., Véron, V., Jourdan, H., Bégout, M. L., Sabatié, M. R., and Baglinière, J. L. (2006). Upstream migration and reproductive patterns of a population of allis shad in a small river (L'Aulne, Brittany, France). *J. Mar. Sci.* 6, 476–484. doi: 10.1016/j.icesjms.2005.05.022

Alosairi, Y., Alsulaiman, N., Petrov, P., and Karam, Q. (2019). Responses of salinity and chlorophyll-a to extreme rainfall events in the northwest Arabian Gulf: emphasis on Shatt Al-Arab. *Mar. Pollut. Bull.* 149:110564. doi: 10.1016/j.marpolbul.2019.110564

Auffret, G. (1983). *Dynamique sédimentaire de la Marge Continentale Celtique-Evolution Cénozoïque- Spécificité du Pléistocène Supérieur et de l'Holocène.* Ph.D. thesis. Talence: Université de Bordeaux I, 355.

Ayouche, A., Carton, X., Charria, G., Theetten, S., and Ayoub, N. (2020). Instabilities and vertical mixing in river plumes: application to the Bay of Biscay. *Geophys. Astrophys. Fluid Dyn.* 114, 650–689. doi: 10.1080/03091929.2020.1814275

Barnett, D. N., Brown, S. J., Murphy, J. M., Sexton, D. M., and Webb, M. J. (2006). Quantifying uncertainty in changes in extreme event frequency in response to doubled CO2 using a large ensemble of GCM simulations. *Clim. Dyn.* 26, 489–511. doi: 10.1007/s00382-005-0097-1

Barrier, N. (2013). *Variability of the Ocean Circulation in the North-Atlantic in Response to Atmospheric Weather Regimes. Earth Science,* Ph. D. thesis. Brest: Université de Bretagne occidentale, 180.

Barrier, N., Cassou, C., Deshayes, J., and Treguier, A.-M. (2014). Response of north atlantic ocean circulation to atmospheric Weather Regimes. *J. Phys. Oceanogrogr.* 44, 179–201. doi: 10.1175/jpo-d-12-0217.1

Bell, J., Brown, C., Conlon, K., Herring, S., Kunkel, K. E., Laurimore, J., et al. (2018). Changes in extreme events and the potential impacts on human health. *J. Air Waste Manag. Assoc.* 68, 265–287. doi: 10.1007/3-540-28862-7_26

Berrisford, P., Kâlberg, P., Kobayashi, S., Dee, D., Uppala, S., Simmons, A. J., et al. (2011). Atmospheric conservation properties in ERA-Interim. *Q. J. R. Meteorol. Soc.* 137, 1381–1399. doi: 10.1002/qj.864

Blain, S., Guillou, J., Tréguer, P., Woerther, P., Delauney, L., Follenfant, E., et al. (2004). High frequency monitoring of the coastal marine environment using the MAREL buoy. *J. Environ. Monit.* 6, 569–575. doi: 10.1039/b314073c

Blaise, E., Suanez, S., Stéphan, P., Fichaut, B., David, L., Cucq, V., et al. (2015). Review of winter storms 2013-2014 on shoreline retreat dynamic on Brittany coast. *Géomorphol. Relief Processus Environ.* 21, 267–292.

Bojarriu, R., and Reverdin, G. (2002). Large-scale variability modes of freshwaterflux and precipitation over the Atlantic. *Clim. Dyn.* 18, 369–381. doi: 10.1007/s003820100182

Caillaud, M., Petton, S., and Dumas, F. (2016). *Hydrodynamic Hindcast at 500m Resolution with MARS3D-AGRIF Model - Channel-Biscay Zone.* Brest: IFREMER.

Cassou, C., Minvielle, M., Terray, L., and Périgaud, C. (2011). A statistical dynamical scheme for reconstructing ocean forcing in the Atlantic. Part I : weather regimes as predictors for ocean surface variables. *Clim. Dyn.* 36, 19–39. doi: 10.1007/s00382-010-0781-7

Castelle, B., Marieu, V., Bujan, S., Splinter, K., Robinet, A., Sénéchal, N., et al. (2015). Impact of the winter 2013-2014 series of severe Western Europe storms on a double-barred sandy coast: Beach and dune erosion and megacusp embayments. *Geomorphology* 238, 135–148. doi: 10.1016/j.geomorph.2015.03.006

Cayan, D. R., and Peterson, D. H. (1993). Spring climate and salinity in the San Francisco Bay Estuary. *Water Resour. Res.* 29, 293–303. doi: 10.1029/92wr02152

Chaalali, A., Beaugrand, G., Raybaud, V., Goberville, E., David, V., Boët, P., et al. (2013). Climatic facilitation of the colonization of an estuary by Acartia tonsa. *PLoS One* 8:e74531. doi: 10.1371/journal.pone.0074531

Charria, G., Rimmelin-Maury, P., Goberville, E., L'Helguen, S., Barrier, N., David-Beausire, C., et al. (2020). "Temperature and salinity changes in coastal waters of western europe: variability, trends and extreme events," in *Evolution of Marine Coastal Ecosystems under the Pressure of Global Changes,* eds H. J. Ceccaldi, Y. Hénocque, T. Komatsu, P. Prouzet, B. Sautour, and J. Yoshida (Cham: Springer), 207–226. doi: 10.1007/978-3-030-43484-7_15

Charria, G., Theetten, S., Vandermeirsch, F., Yelekçi, O., and Audiffren, N. (2017). Interannual evolution of (sub)mesoscale dynamics in the Bay of Biscay. *Ocean Sci.* 13, 777–797. doi: 10.5194/os-13-777-2017

Chegini, F., Holtermann, P., Kerimoglu, O., Becker, M., Kreus, M., Klingbeil, K., et al. (2020). Processes of stratification and destratification during an extreme river discharge event in the German Bright ROFI. *J. Geophys. Res. Oceans* 125:e2019JC015987.

Christidis, N., Jones, G., and Stott, P. (2015). Dramatically increasing chance of extremely hot summers since the 2003 European heatwave. *Nat. Clim. Change* 5, 46–50. doi: 10.1038/nclimate2468

Cloern, J. E., Abreu, P. C., Carstensen, J., Chauvaud, L., Elmgren, R., Grall, J., et al. (2016). Human activities and climate variability drive fast-paced change across the world's estuarine-coastal ecosystems. *Glob. Change Biol.* 22, 513–529. doi: 10.1111/gcb.13059

Cocquempot, L., Delacourt, C., Paillet, J., Riou, P., Aucan, J., Castelle, B., et al. (2019). Coastal ocean and nearshore observation: a french case study. *Front. Mar. Sci.* 6:324. doi: 10.3389/fmars.2019.00324

Copernicus Climate Change Service (2017). *ERA5: Fifth Generation of ECMWF Atmospheric Reanalyses of the Global Climate*. Reading: Copernicus Climate Change Service Climate Data Store (CDS).

Costa, M. J., Vasconcelos, R., Costa, J. L., and Cabral, H. N. (2007). River flow influence on the fish community of the Tagus estuary (Portugal). *Hydrobiologia* 587, 113–123. doi: 10.1007/s10750-007-0690-x

Coumou, D., and Rahmstorf, S. (2012). A decade of weather extremes. *Nat. Clim. Change* 2, 491–496. doi: 10.1038/nclimate1452

Davies, H. (2015). Weather chains during the 2013/2014 winter and their significance for seasonal prediction. *Nat. Geosci.* 8, 833–837. doi: 10.1038/ngeo2561

Del Amo, Y., Le Pape, O., Treguer, P., Queguiner, B., Menesguen, A., and Aminot, A. (1997). Impacts of high-nitrate freshwater inputs on macrotidal ecosystems. I. Seasonal evolution of nutrient limitation for the diatom-dominated phytoplankton of the Bay of Brest (France). *Mar. Ecol. Prog. Ser.* 161, 213–224. doi: 10.3354/meps161213

Donat, M., Leckebusch, G., Pinto, J., and Ulbrich, U. (2010). Examination of wind storms over Central Europe with respect to circulation weather types and NAO phases. *Int. J. Climatol.* 30, 1289–1300.

Ducrocq, V., Bouttier, F., Melardel, S., Montmerle, T., and Seity, Y. (2005). Le projet Arome, crues méditerranéennes : les réponses scientifiques et techniques de l'Etat. *La Houille Blanche* 2, 39–44.

Farcy, P., Durand, D., Charria, G., Painting, S. J., Tamminem, T., Collingridge, K., et al. (2019). Toward a European coastal observing network to provide better answers to science and to societal challenges; the JERICO research infrastructure. *Front. Mar. Sci.* 6:529. doi: 10.3389/fmars.2019.00529

Ferrer, L., Fontán, A., Mader, J., Chust, G., González, M., Valencia, V., et al. (2009). Low-salinity plumes in the oceanic region of the Basque Country. *Cont. Shelf Res.* 29, 970–984. doi: 10.1016/j.csr.2008.12.014

Frère, L., Paul-Pont, I., Rinnert, E., Petton, S., Jaffré, J., Bihannic, I., et al. (2017). Influence of environmental and anthropogenic factors on the composition, concentration and spatial distribution of microplastics : a case study of the Bay of Brest (Brittany, France). *Environ. Pollut.* 225, 211–222. doi: 10.1016/j.envpol.2017.03.023

Goberville, E., Beaugrand, G., and Edwards, M. (2014). Synchronous response of marine plankton ecosystems to climate in the Northeast Atlantic and the North Sea. *J. Mar. Syst.* 129, 189–202. doi: 10.1016/j.jmarsys.2013.05.008

Goberville, E., Beaugrand, G., Sautour, B., Tréguer, P., and Somlit Team. (2010). Climate-driven changes in coastal marine systems of Western Europe. *Mar. Ecol. Prog. Ser.* 408, 129–147. doi: 10.3354/meps08564

Gohin, F., Bryère, P., and Griffiths, J. (2015). The exceptional surface turbidity of the North-West European shelf seas during the stormy 2013-2014 winter : consequences for the initiation of the phytoplankton blooms. *J. Mar. Syst.* 148, 70–85. doi: 10.1016/j.jmarsys.2015.02.001

Gomara, I., Rodriguez-Fonseca, B., Zurita-Gotor, P., and Pinto, J. G. (2014). A statistical-dynamical scheme for reconstructing ocean forcing in the Atlantic. Part I : weather regimes as predictors for ocean surface variables. *Geophys. Res. Lett.* 41, 2182–2190.

Guillaud, J.-F., and Bouriel, L. (2007). Relationships between nitrate concentration and river flow, and temporal trends of nitrate in 25 rivers of Brittany (France). *J. Water Sci.* 20, 213–226.

Hurrell, J. W., Kushnir, Y., and Visbeck, M. (2001). The north Atlantic oscillation. *Science* 291, 603–605. doi: 10.1126/science.1058761

IPCC, Field, C. B., Barros, V., Stocker, T. F., Qin, D., Dokken, D. J., Ebi, K. L., et al. (2012). Cambridge: Cambridge University Press, 582.

IPCC, Pörtner, H.-O., Roberts, D. C., Masson-Delmotte, V., Zhai, P., Tignor, M., Poloczanska, E., et al. (2019). *IPCC Special Report on the Ocean and Cryosphere in a Changing Climate*. Geneva.

Jentsch, A., and Beierkuhnlein, C. (2008). Research frontiers in climate change: Effects of extreme meteorological events on ecosystems. *C. R. Geosci.* 340, 621–628. doi: 10.1016/j.crte.2008.07.002

Kastner, S., Horner-Devine, E., and Thomson, A. (2018). The influence of wind and waves on spreading and mixing in the Fraser River plume. *J. Geophys. Res. Oceans* 123:6840.

Kourafalou, V., Lee, T., Oey, L., and Wang, J. (1996). The fate of river discharge on the continental shelf. *J. Geophys. Res.* 101, 3435–3455.

Lazure, P., and Dumas, F. (2008). An external–internal mode coupling for a 3D hydrodynamical model for applications at regional scale (MARS). *Adv. Water Resour.* 31, 233–250. doi: 10.1016/j.advwatres.2007.06.010

Lazure, P., and Jegou, A. M. (1998). 3D modelling of seasonal evolution of Loire and Gironde plumes on Biscay Bay continental shelf. *Oceanol. Acta* 21, 165–177. doi: 10.1016/s0399-1784(98)80006-6

Leckebusch, G. C., Koffi, B., Ulbrich, U., Pinto, J. G., Spangehl, T., and Zacharias, S. (2006). Analysis of frequency and intensity of European winter storm events from a multi-model perspective, at synoptic and regional scales. *Clim. Res.* 31, 59–74. doi: 10.3354/cr031059

Liu, W., Chen, W., Cheng, R., and Hsu, M. (2008). Modelling the impact of wind stress and river discharge. *Appl. Math. Model.* 32, 1255–1280. doi: 10.1016/j.apm.2007.03.009

Mann, M., Rahmstorf, S., Kornhuber, K., Steinman, B. A., Miller, S. K., and Coumou, D. (2017). Influence of anthropogenic climate change on planetary wave resonance and extreme weather events. *Sci. Rep.* 7:45242.

Marcos, M., Rohmer, J., Vousdoukas, M. I., Mentaschi, L., Le Cozannet, G., and Amores, A. (2019). Increased extreme coastal water levels due to the combined action of storm surges and wind waves. *Geophys. Res. Lett.* 46, 4356–4364. doi: 10.1029/2019gl082599

Margalef, R. (1978). Life-forms of phytoplankton as survival alternatives in an unstable environment. *Oceanol. Acta* 1, 493–509.

Masselink, G., Castelle, B., Scott, T., Dodet, G., Suanez, S., Jackson, D., et al. (2016). Extreme wave activity during 2013/2014 winter and morphological impacts along the Atlantic coast of Europe. *Coast Eur.* 43, 2135–2143. doi: 10.1002/2015gl067492

Matthews, T., Murphy, C., Wilby, R. L., and Harrigan, S. (2014). Stormiest winter on record for Ireland and UK.Nat. *Clim. Change* 4, 738–740. doi: 10.1038/nclimate2336

Maynard, A., Bible, J. M., Pespeni, M. H., Sanford, E., and Evans, T. G. (2018). Transcriptomic responses to extreme low salinity among locally adapted populations of Olympia oyster (*Ostrea lurida*). *Mol. Ecol.* 27, 4225–4240. doi: 10.1111/mec.14863

Mazzini, P., Risien, C., Barth, J., Pierce, S. D., Erofeev, A., Dever, E. P., et al. (2015). Anomalous near-surface low-salinity pulses off the central oregon coast. *Sci. Rep.* 5:17145.

McCabe, G. J., and Ayers, M. A. (1989). Hydrologic effects of climate change in the Delaware River Basin. *Water Resour. Bull.* 25, 1231–1242. doi: 10.1111/j.1752-1688.1989.tb01335.x

Ménesguen, A., and Piriou, J.-Y. (1995). Nitrogen loadings and macroalgal (*Ulva* sp.) mass accumulation in Brittany (France). *J. Ophelia* 42, 227–237. doi: 10.1080/00785326.1995.10431506

Mentaschi, L., Vousdoukas, M. I., Voukouvalas, E., Dosio, A., and Feyen, L. (2017). Global changes of extreme coastal wave energy fluxes triggered by intensified teleconnection patterns. *Geophys. Res. Lett.* 44, 2416–2426. doi: 10.1002/2016gl072488

Merot, P., and Buffin, D. (1996). Essai de caractérisation de la variabilité hydrologique en Bretagne. *Les Colloq.* 79, 127–134.

Molines, J., Barnier, B., Penduff, T., Tréguier, A.-M., and Le Sommer, J. (2014). *ORCA12.L46 Climatological and Interannual Simulations Forced With DFS4.4: GJM02 and MJM88. Drakkar Group Experiment Report GDRI-DRAKKAR-2014- 03-19*. Available online at: https://www.drakkar-ocean.eu/publications/reports/orca12_reference_experiments_2014

Moskalski, S., Floc'h, F., Verney, R., Fromant, G., Le Dantec, N., and Deschamps, A. (2018). Sedimentary dynamics and decadal-scale changes in the macrotidal Aulne River Estuary, Brittany, France. *J. Coast. Res.* 34, 1398–1417. doi: 10.2112/jcoastres-d-17-00126.1

Msadek, R., and Frankignoul, C. (2009). Atlantic multidecadal variability and its influence on the atmosphere in a climate model. *Clim. Dyn.* 33, 45–62. doi: 10.1007/s00382-008-0452-0

Petton, S., Le Roy, V., Bellec, G., Queau, I., Le Souchu, P., and Pouvreau, S. (2020a). *Marine Environmental Station Database of Daoulas bay*. SEANOE. doi: 10.17882/42493

Petton, S., Pouvreau, S., and Dumas, F. (2020b). Intensive use of Lagrangian trajectories to quantify coastal area dispersion. *Ocean Dyn.* 70, 541–559. doi: 10.1007/s10236-019-01343-6

Poulton, V. K., Lovvorn, J. R., and Takekawa, J. Y. (2004). Spatial and overwinter changes in clam populations of San Pablo Bay, a semiarid estuary with highly variable freshwater inflow. *Estuar. Coast. Shelf Sci.* 59, 459–473. doi: 10.1016/j.ecss.2003.10.005

Répécaud, M., Quemener, L., Charria, G., Pairaud, I., Rimmelin, P., Claquin, P., et al. (2019). "National observation infrastructure: an example of a fixed-platforms network along the French Coast: COAST HF," in *Proceedings of the OCEANS 2019*, (Marseille: IEEE), 1–6.

Rimmelin-Maury, P., Charria, G., Repecaud, M., Quemener, L., Beaumont, L., Guillot, A., et al. (2020). *Iroise Buoy s Data From Coriolis Data Center as Core Parameter Support for Brest Bay and Iroise Sea Studies*. Brest, France. SEANOE.

Schaller, N., Kay, A. L., Lamb, R., Massey, N. R., Van Oldenborgh, G. J., Otto, F. E. L., et al. (2016). Human influence on climate in the 2014 southern England winter floods and their impacts. *Nat. Clim. Change* 6, 627–634. doi: 10.1038/nclimate2927

Seuront, L., Nicastro, K. R., Zardi, G. I., and Goberville, E. (2019). Decreased thermal tolerance under recurrent heat stress conditions explains summer mass mortality of the blue mussel *Mytilus edulis*. *Sci. Rep.* 9:17498.

Shi, J., Cui, L., Ma, Y., Du, M., and Wen, K. (2017). Trends in temperature extremes and their association with circulation patterns in China during 1961-2015. *Atmos. Res.* 212, 259–272. doi: 10.1016/j.atmosres.2018.05.024

Smale, D. A., and Wernberg, T. (2013). Extreme climatic event drives range contraction of a habitat-forming species. *Proc. R. Soc.* 280, 1–9.

Smith, M. (2011). The ecological role of climate extremes: current understanding and future prospects. *J. Ecol.* 99, 651–655. doi: 10.1111/j.1365-2745.2011.01833.x

Somavilla, R., González-Pola, C., Rodriguez, C., Josey, S. A., Sánchez, R. F., and Lavín, A. (2009). Large changes in the hydrographic structure of the Bay of Biscay after the extreme mixing of winter 2005. *J. Geophys. Res.* 114, 1–14.

Somavilla, R., González-Pola, C., Ruiz-Villarreal, M., and Montero, A. L. (2011). Mixed layer depth (MLD) variability in the southern Bay of Biscay. Deepening of winter MLDs concurrent with generalized upper water warming trends ? *Ocean Dyn.* 61, 1215–1235. doi: 10.1007/s10236-011-0407-6

Somavilla, R., González-Pola, C., Schauer, U., and Budéus, G. (2016). Mid-2000s North Atlantic shift: heat budget and circulation 35 changes. *Geophys. Res. Lett.* 43, 2059–2068. doi: 10.1002/2015gl067254

Tabari, H., and Willems, P. (2018). Lagged influence of Atlantic and Pacific climate patterns on European extreme precipitation. *Sci. Rep.* 8:5748.

Theetten, S., Vandermeirsch, F., and Charria, G. (2017). *BACH1000_100lev-51: a MARS3D model configuration for the Bay of Biscay*. SEANOE. doi: 10.17882/43017

Thibault, K. M., and Brown, J. H. (2008). Impact of an extreme climatic event on community assembly. *Proc. Natl. Acad. Sci. U.S.A.* 105, 3410–3415. doi: 10.1073/pnas.0712282105

Thompson, V., Dunstone, N. J., Scaife, A. A., Smith, D., Slingo, J. M., Brown, S., et al. (2017). High risk of unprecedented UK rainfall in the current climate. *Nat. Commun.* 8:107.

Tréguer, P., Goberville, E., Barrier, N., L'Helguen, S., Morin, P., Bozec, Y., et al. (2014). Large and local-scale influences on physical and chemical characteristics of coastal waters of Western Europe during winter. *J. Mar. Syst.* 139, 79–90. doi: 10.1016/j.jmarsys.2014.05.019

Trouet, V., Babst, F., and Meko, M. (2018). Recent enhanced high-summer North Atlantic jet variability emerges from three century context. *Nat. Commun.* 9:180.

Turlach, B. A. (1993). Bandwidth selection in kernel density estimation: a review. *Core Institut Statistique* 19, 1–33.

Van de Pol, M., Jenouvrier, S., Cornelissen, J. H. C., and Visser, M. E. (2010). Behavioural, ecological and evolutionary responses to extreme climatic events: challenges and directions. *Philos. Trans. R. Soc.* 372, 1–16. doi: 10.1016/j.ecocom.2013.12.001

Wan Zin, W. Z., Jamaludin, S., Mohd Deni, S., and Aziz Jemain, A. (2010). Recent changes in extreme rainfall events in Peninsular Malaysia: 1971-2005. *Theor. Appl. Climatol.* 99, 303–314. doi: 10.1007/s00704-009-0141-x

Wernberg, T., Smale, D. A., Tuya, F., Thomsen, M. S., Langlois, T. J., Bettignies, T., et al. (2013). An extreme climatic event alters marine ecosystem structure in a global biodiversity hotspot. *Nat. Clim. Change* 3, 78–82. doi: 10.1038/nclimate1627

Wollast, R. (1998). "Evaluation and comparison of the global carbon cycle in the coastal zone and in the open ocean," in *The Sea—Vol 10: The global Coastal Ocean: Processes and Methods*, eds K. H. Brink and A. R. Robinson (Chichester: J Wiley & Sons), 213–252.

Yang, X., Ma, X., Kang, N., and Maihemuti, M. (2018). Probability interval prediction of wind power based on KDE method with rough sets and weighted markov chain. *IEEE Access* 6, 51556–51565. doi: 10.1109/access.2018.2870430

Yool, A., and Fasham, M. (2001). An examination of the "continental shelf pump" in an open ocean general circulation model. *Glob. Biogeochem. Cycles* 15, 831–844. doi: 10.1029/2000gb001359

Zingone, A., Dubroca, L., Ludicone, D., Margiotta, F., Corato, F., Ribera d'Alcala, M., et al. (2010). Coastal phytoplankton do not rest in winter. *Estuar. Coasts* 33, 342–361. doi: 10.1007/s12237-009-9157-9

Conflict of Interest: The authors declare that the research was conducted in the absence of any commercial or financial relationships that could be construed as a potential conflict of interest.

Chapitre 5 La réponse des matières en suspension aux forçages extrêmes

Dans ce chapitre, un deuxième compartiment de l'écosystème, la dynamique sédimentaire, est analysé à partir des forçages extrêmes que sont les vagues et les crues. La réponse des MES face à ces forçages extrêmes est explorée en baie de Seine.

5.1 Résumé

L'action des vagues et des crues est capable de remettre en suspension les sédiments dans la colonne d'eau de façon significative ou encore d'advecter le bouchon vaseux. L'impact de ces forçages extrêmes qui tendent à s'intensifier est analysé en baie de Seine de 2006 à 2019 via des données *in situ* à haute fréquence combinées à des images satellites et des données issues de simulations numériques. La dynamique des matières en suspension (MES) et leurs liens avec les forçages extrêmes est importante à déchiffrer vu leur rôle crucial sur l'écosystème côtier via le transport de contaminants, de matière organique, de nutriments, de sédiments et les évolutions morphologiques long terme. La baie de Seine située dans la Manche est une zone côtière sous régime macrotidal très turbide du fait de son rattachement avec l'estuaire de la Seine. De plus, une station d'observation à haute fréquence se trouve à l'embouchure de l'estuaire de la Seine ce qui en fait une zone d'étude privilégiée. L'effet de la marée étant filtré, les deux forçages principaux affectant les MES, débit et vagues, sont analysés. Les crues impactent la dynamique sédimentaire en modifiant le déplacement du maximum de turbidité estuarienne (ETM) dans l'estuaire de la Seine jusqu'à la baie. Les vagues extrêmes impactent la dynamique sédimentaire en érodant les sédiments de fond, avec un effet plus fort dans les zones à faible fond.

Une méthode de détection des forçages extrêmes originale est proposée et discutée. Les forçages extrêmes sont définis par le percentile 90 à partir d'une climatologie et analysés au travers de leurs intensité, durée, période d'occurrence et succession. Les forçages extrêmes se comportent de manière similaire aux forçages moyens liés aux vagues et aux crues de la Seine. Les deux forçages extrêmes (vagues et crues) présentent une forte saisonnalité, avec les évènements les plus extrêmes majoritairement en hiver, qui se retrouve dans la réponse de la dynamique sédimentaire en général. Une relation de proportionnalité est mise en évidence entre

l'intensité ainsi que la durée des vagues extrêmes et les concentrations en MES. Le rôle de la succession des crues extrêmes n'a que peu d'importance sur les concentrations en MES. La variabilité du signal en MES n'est pas entièrement expliquée par les extrêmes. Enfin, l'exploration de la variabilité des forçages extrêmes sur le long terme montrent une légère augmentation en lien avec leurs évolutions moyennes cette dernière décennie.

Ce travail explicité dans la partie suivante a été soumis dans le journal Marine Geology. L'article référencé comme Verney et al. (2023) est accessible dans l'annexe 1 du présent manuscrit de thèse.

5.2 Article : Suspended particulate matter response to extreme forcings in the Bay of Seine

Suspended particulate matter response to extreme forcings in the Bay of Seine

Coline Poppeschi[1], Romaric Verney[2], Guillaume Charria[1]

[1] Ifremer, Univ. Brest, CNRS, IRD, Laboratory for Ocean Physics and Satellite remote sensing (LOPS), IUEM, 29280 Brest, France.
[2] Ifremer, DYNECO, Hydrosedimentary Dynamics Laboratory (DHYSED), 29280 Brest, France.

Abstract

The latest Intergovernmental Panel on Climate Change report of 2023 alerts about an increase in the occurrence and intensity of extreme hydro-meteorological events such as storms and extreme river flows, i.e. drought and floods. Investigating the occurrence of these extreme events in the past 15 years and their impacts on sediment dynamics will provide crucial knowledge for anticipating future trajectories of coastal ecosystems. Time series from *in situ* observations are analyzed to identify extreme forcings of river flows and waves and examine their impact on Suspended Particulate Matter (SPM) dynamics in a highly turbid coastal area equipped with a high frequency *in situ* monitoring station at the interface between the Seine Estuary and the Bay of Seine (South of English Channel). Extreme events from two dominant forcings are investigated : extreme river flow forcing events that can transport the Estuarine Maximum Turbidity (ETM) along the Seine estuary and deliver high SPM to the bay; and extreme wave forcing events that can erode the bottom sediment inducing high SPM concentration in the bay. An original detection method is proposed, based on high frequency *in situ* observations combined with satellite and model data from 2006 to 2019. Extreme forcings are examined through their specific characteristics (high intensity, long duration, season of occurrence, succession of events), their impact on SPM in the coastal environment and the comparison to mean seasonal dynamics. Extremes are more frequent and intense in winter for both forcings. A proportional relationship exists between SPM and forcing intensity and duration. A weak effect of the succession of extreme events is highlighted, and the occurrence of an extreme wave event often but not automatically coincides with an extreme response in SPM concentration.

Keywords

Suspended particulate matter, Surface waves, River flows, Extreme events, Coastal ocean.

The Bay of Seine is located in a river/estuary/bay continuum, and more particularly at the interface between the estuary of the Seine river and the eastern part of the Bay of Seine connected to the English Channel (Figure 1). It is a shallow bay with a maximum depth of 30 m and has an area of about 4000 km^2 (Aminot *et al.*, 1997). The Bay of Seine is a semi-diurnal macrotidal environment (tidal range up to 7 m at Le Havre) with average tidal currents of 0.5 to 1 m s^{-1} (Salomon and Breton, 1991) during spring tides. The Bay of Seine is connected to the Seine estuary, one of the largest northwestern European estuaries, and driven by the Seine River with a flow rate between 100 and 2300 m^3 s^{-1} (Schulz *et al.*, 2018). Tides in the Bay of Seine play an important role in sediment distribution by depositing mud from the shallow subtidal zone to the open estuary and distributing sand, especially from the sandbanks at the mouth of the estuary (Lesourd *et al.*, 2003). The Seine estuary has an Estuarine Turbidity Maximum (ETM) located 10 km upstream the mouth around Fatouville (Figure 1). During periods of high flow this ETM is moved to the mouth of the estuary and during opposite conditions it can go up to the upstream freshwater limit (0.722°E, 49.524°N) (Grasso *et al.*, 2019). The average cumulative sediment supply from the Seine river is 725 10^3 tons per year (Grasso *et al.*, 2018; Schulz *et al.,* 2018) and mainly during high river flow (Landemaine, 2016). The prevailing winds come from the southwest with speeds that can exceed 8 m s^{-1}. Surface waves mainly enter the bay from the northwest (Schulz *et al.*, 2018) with a wave orbital speed that can exceed 0.7 m s^{-1}.

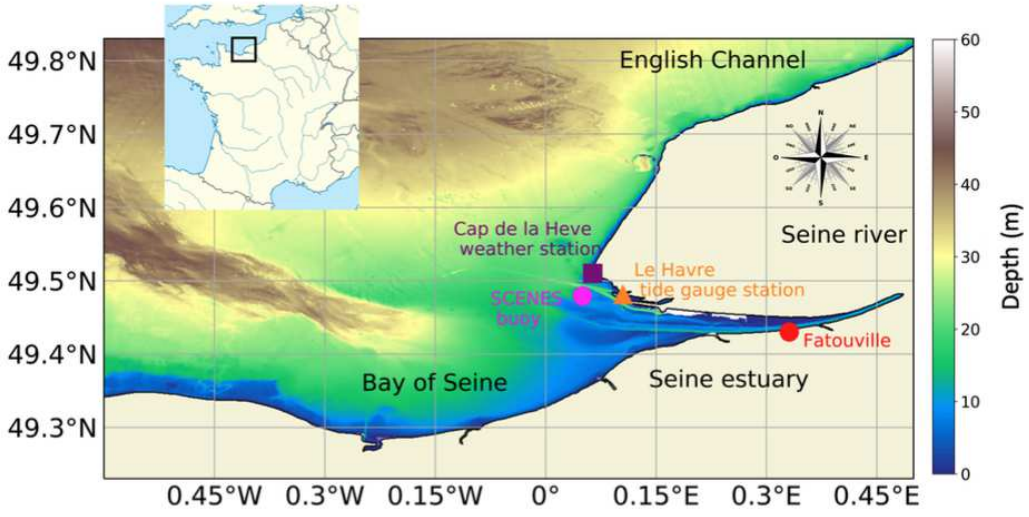

Figure 1: Bathymetry of the Bay of Seine. The pink circle indicates the COAST-HF Scenes buoy, the orange triangle "Le Havre" tide gauge station, the purple square the "Cap de la Hève" weather station and the red circle the ETM location at Fatouville.

2.2 Datasets

2.2.1 Forcings data

Daily river flows are measured at the Vernon gauging station located upstream the estuary tidal limit (1.477°E, 49.083°N - French hydrology database: www.hydro.eaufrance.fr). The gauging station is located 200 km upstream the mouth (Figure 1), and we consider that the propagation time of the river flow to the mouth is on average 5 days (Artelia, 2019). Over the

period considered, from 2006 to 2019, river flows vary from 40 to 2280 $m^3 s^{-1}$ with a maximum in late winter.

If significant wave height (Hs) is often used to represent wave forcing, we have chosen to consider the square of wave orbital velocity which is a better proxy for erosion processes (Soulsby *et al.*, 1993). Hourly wave orbital velocity data are available from WaveWatch3 model simulations (Rolland and Ardhuin, 2014) through the MARC web portal (marc.ifremer.fr) and extracted at the nearest grid point of the SCENES buoy.

Sea levels are provided at high and low tides by the Shom (http://data.shom.fr) at Le Havre tide gauge station (Figure 1).

Wind direction and intensity are retrieved every hour from the meteorological station *Cap de la Hève* (Figure 1) from Météo-France observation network (https://donneespubliques.meteofrance.fr).

2.2.2 *In situ* SPM data measured at the SCENES buoy

This study is based on high-frequency data measured by a moored coastal buoy called SCENES, part of the French national observation network COAST-HF (Répécaud *et al.*, 2019; Farcy *et al.*, 2019; Cocquempot *et al.*, 2019) from the French national Research Infrastructure ILICO (https://www.ir-ilico.fr/). SCENES has been deployed at the Seine estuary mouth since 2016 at 15m depth (Figure 1). The SCENES buoy monitors SPM every 15 min at the surface (-2 m below surface) and 30 min at the bottom (+0.5 m above bottom) using Wetlabs optical turbidimeters, whose measurements are converted to SPM (g L^{-1}) using *in situ* water samples according to Verney et al. (submitted, 2023). Before October 2017, SPM measurements were taken +1.5 m over the bottom. After this date, a Nortek AWAC Acoustic Doppler Current Profiler (ADCP) together with optical measurements are used to evaluate SPM at the bottom (Verney *et al.*, submitted, 2023). To analyze the influence of wave and flow forcings, and because the tide contributes significantly to the variability of the SPM concentration signal, SPM concentration anomalies are used. These anomalies correspond to the difference between the raw signal and the mean intratidal high frequency variability(Verney et al., submitted, 2023).

2.2.3 Results of the hydro-sedimentary hindcast model (ARES archive)

The 3D "CurviSeine" model provides hourly SPM in g L^{-1} in the Seine estuary and its bay (ARES project, Grasso *et al.*, 2021) from 2006 to 2019. The model has 10 sigma levels and a spatial resolution ranging from 4 km offshore to 100 m in the Seine estuary. This model configuration couples a curvilinear primitive equation hydrodynamic core model (MARS3D, Lazure and Dumas, 2008) and a hydro-sedimentary model that takes into account for advection, erosion, deposition and consolidation processes of different sand/mud sediment classes (MUSTANG, Le Hir *et al.*, 2011; Grasso *et al.,* 2015; Mengual et al., 2017). This model is forced by a spectral wave model (WW3, Rolland and Ardhuin, 2014).

Model open boundary forcings are hourly and derived for waves from a WW3 regional model at 10 km resolution, for temperature, salinity and tides from MARS3D at 2.5 km resolution (https://marc.ifremer.fr/, Grasso *et al.,* 2018) and for atmospheric forcings from the Meteo-France AROME atmospheric model at 1.3 km resolution (https://donneespubliques.meteofrance.fr). The temperature, salinity and SPM outputs from the model have been compared and validated with the PHRESQUES measurement network (Grasso *et al.,* 2020 - ARES report). Model data are considered for the second vertical level from the bottom (k=2). We use validated model data in addition to observation (Figure S1) to assess the overall behavior of the events for all years and seasons.

2.2.4 Satellite data

Images essentially from the MODIS instrument from the AQUA satellite are processed with the OC5 algorithm (Gohin, 2011) to explore the spatial extent of the sediment river in the Bay of Seine. Data are available since October 1st 2002 and projected onto a regular 1 km^2 grid. Validated satellite data are compared with *in situ* data (Figure S2) and used to observe the spatial extent of extreme river flow on SPM, even if SPM concentrations estimated from satellite observations are underestimated. Data is from Copernicus platform - Earth observation component of the European Union (https://www.copernicus.eu/fr/acces-aux-donnees-satellitaires-de-copernicus). In this study, L3 and L4 satellite products are used.

2.3 Data processing

2.3.1 Detection and characterization of extreme events

The Peak Over Threshold (POT) method (derived from Poppeschi *et al.,* 2021) is used to detect extreme wave and river flow events from 2006 to 2019 (Figure 2). Daily river flow data are interpolated at each high tide (semi-diurnal cycle, i.e. ~2 per day). The percentile 90 of hourly square wave orbital velocity is used to characterize wave conditions at each tidal cycle. These tidal percentiles 90 are aggregated by successive tides from January 1 to December 31 to create an annual climatology (Figure 2). This climatology computed at each tidal cycle is smoothed on a 30-day rolling average of the percentile 90 to obtain a dynamic threshold. Extreme wave events correspond to wave orbital velocities exceeding the tidal 90 percentile smoothed threshold.

The same method is applied to detect extreme river flow events, but in order to detect start and end dates of these events properly the smoothed percentile 50 is used. Thus, floods are fully detected and isolated peaks in river flows are discarded.

In this paper, SPM concentrations are represented by anomalies for observations and model results. SPM data from the model show a similar qualitative dynamic behavior as observations, while overestimated compared to the buoy data (Figure S1).

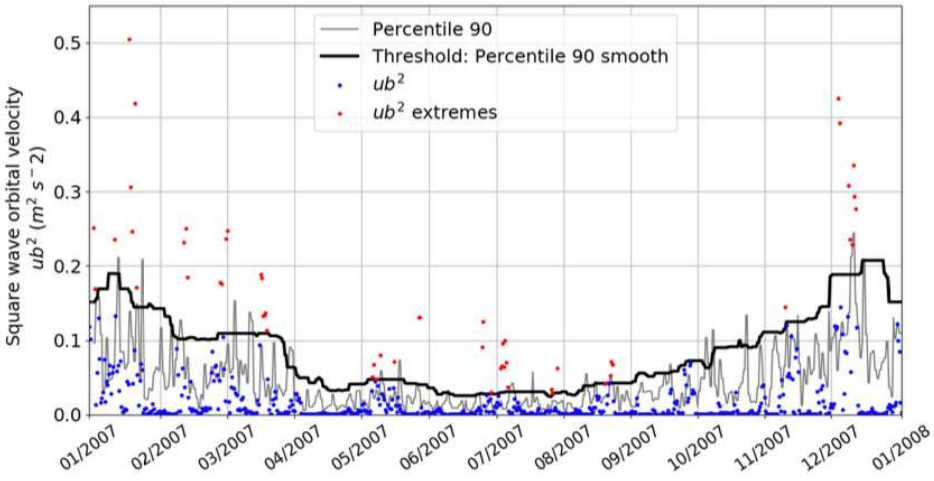

Figure 2: Scheme of the extreme detection method with the example of wave forcing for the year 2007. Square wave orbital velocity (ub^2) data sorted by tide are represented by blue dots

and extreme values by red dots. The annual climatology computed with the percentile 90 is shown by the grey line. The threshold (black line) corresponds to the smoothing over one month of the grey line by the percentile 90. Values above this threshold (black line) are therefore called extreme and are represented by red dots.

Five key parameters have been considered to characterize extreme events: intensity, intensity above threshold, duration, succession of events and seasonal rarity (Stephenson, 2008; Figure 3). A succession of events is detected when there are less than a week between two consecutive events. The seasonal rarity is the month of the year with the lowest number of events over the whole period 2006-2019. The concomitance of extreme river flow and wave forcings is studied to observe the response of SPM during cumulated forcings.

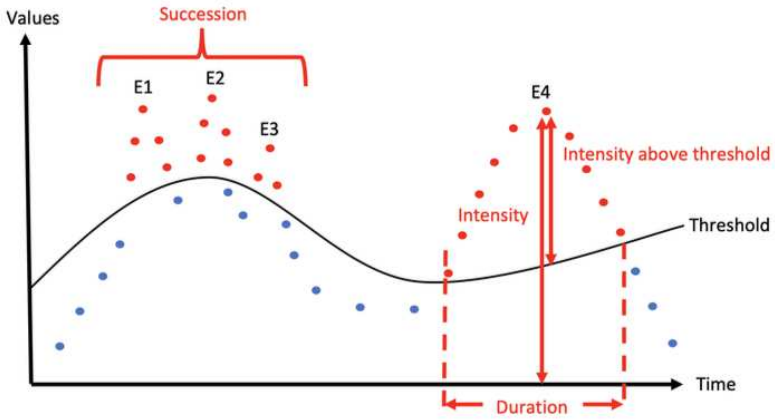

Figure 3: The succession of extreme events, their intensities, their intensities above the threshold and their durations are illustrated on this scheme : extreme events with extreme values in red points, non-extreme values in blue points and the threshold in black line. In this example there are 4 extreme events detected: E1, E2, E3 and E4.

2.3.2 Spatial extent of SPM events

A subset of MODIS satellite data is used at the estuary/bay interface (0.3°W;0.3°E and 49.3°N; 49.7°N, Figure S2) to study SPM spatial variability in the bay of Seine. Only data with at least 50% of valid pixels are analyzed. Following Gangloff et al. (2017), a characteristic SPM concentration threshold is used to delineate the surface turbid plume against the average background SPM concentration observed in the Eastern Bay of Seine. For our study area, a surface SPM threshold value of 5 mg L^{-1} was calculated from the mean SPM distribution from all available images during the study period (2006 - 2019).

3. Results

3.1 Extreme forcings

A significant interannual variability in the number of wave and river flow extreme events (Figure 4) is observed from 2006 to 2019. Every time a flood event is detected, at least one extreme wave event is detected. These concomitant events appear every year and during all seasons.

21 extreme river flow events are detected: from 0 to 4 events per year (average of 2 per year), none in 2009 and 2011 and 4 in 2013.

200 extreme wave events were detected during the same period: from 7 to 25 events per year (average of 14 per year), 7 in 2010 and 25 in 2007.

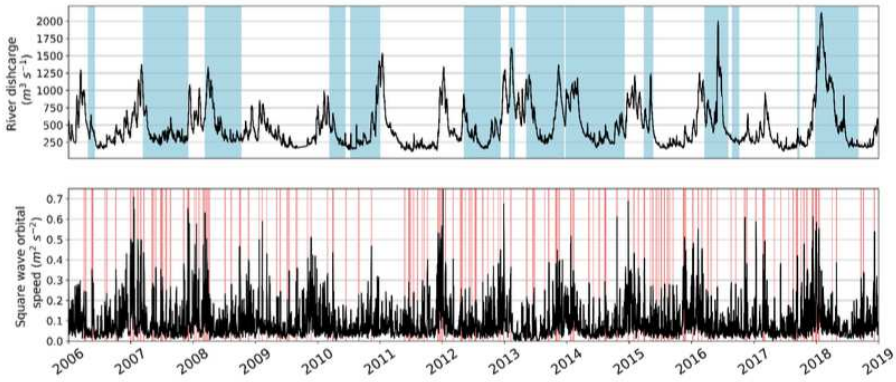

Figure 4: Extreme forcing events from river flow (blue period on top figure) and square wave orbital speed (red period on bottom figure).

Extreme river flow events show a marked seasonality with low intensity events in July and August (<500 $m^3 s^{-1}$) versus intense floods in winter reaching above 1250 $m^3 s^{-1}$ (Figure 5a). Most frequent extreme river flows occur in March, August and September with up to 7 events per month (not shown).

Extreme waves are few in October (11 events) and most frequent in January, May, November and December (20 events per month) (not shown). The seasonality stands out with very intense peaks of square wave orbital speed in winter (maximum >0.4 $m^2 s^{-2}$, average 0.25 $m^2 s^{-2}$) and weaker in summer (minimum <0.2 $m^2 s^{-2}$, average 0.05 $m^2 s^{-2}$; Figure 5b).

Extreme forcing is observed over a wide range of intensity and duration values, but in general, if the event is longer it is also more intense in both datasets (Figure 5).

The average duration for an extreme river flow event is 101 tides (M2 tide cycle) and the longest lasts more than 250 tides (i.e. approximately 4 months). Half of the extreme river flow events have an intensity between 300 and 700 $m^3 s^{-1}$ and the other half between 1000 and 1700 with a maximum of 2150 $m^3 s^{-1}$ (Figure 5a).

Most of the extreme wave forcings detected are short and last on average 2 tides per event, and the longest can reach 7 tides. The distribution of extreme wave event intensity is continuous with values ranging from 0.02 to 0.55 $m^2 s^{-2}$ compared to river events, where extreme events are either below 750 $m^3 s^{-1}$ or above 1000 $m^3 s^{-1}$ (Figure 5b).

(a)

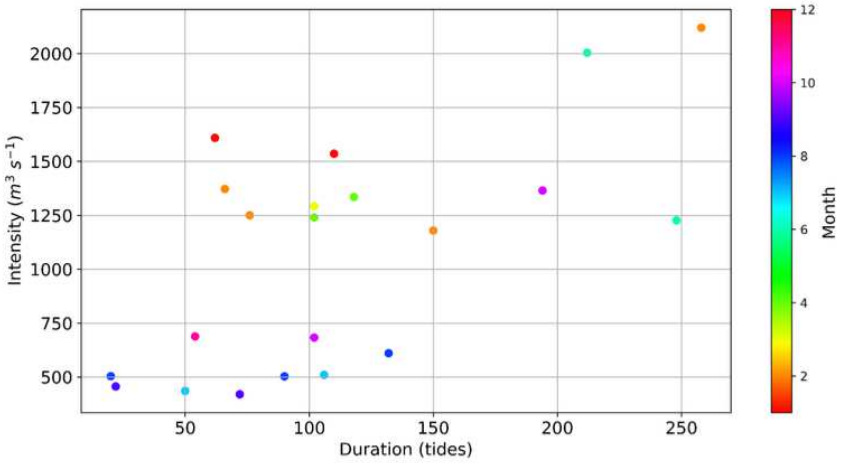

(b)

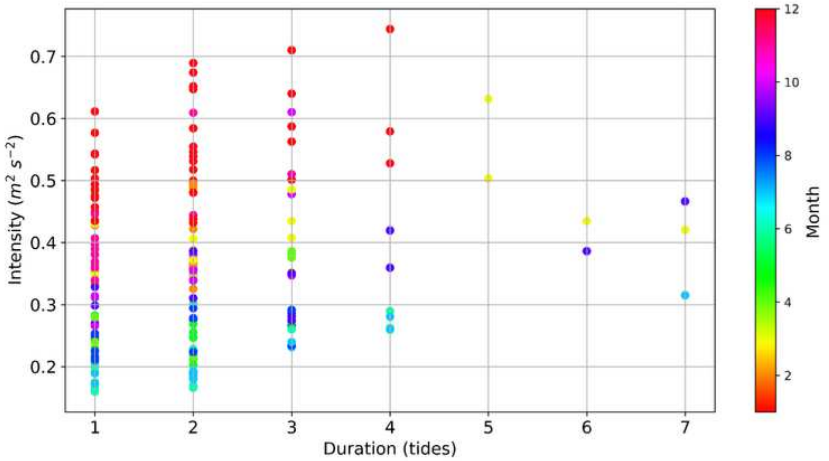

Figure 5: Characterization of extreme forcing events of (a) river flow and (b) square wave orbital speed through their duration, their intensity and the month of occurrence.

Several successions of events are observed over the study period characterized most of the time by only 2 events together (Figure 4).

Only one river flow succession is detected in December 2010 (2 events together). This succession is not related to high intensity or long duration of extreme river flow events.

Winter is the favorable season for succession of wave events to occur. 40 wave event successions are detected, the most important one is in 2006 (4 individual events). The second highest intensity event (0.71 m^2 s^{-2}) in January 2007 and the longest duration event (7 tides) in March 2019 occur both during a succession of two wave events.

3.2 Suspended Particulate Matter (SPM)

The response in SPM to extreme flow and wave forcings present a high interannual variability (Figure 6). SPM anomalies are observed at each extreme event. SPM anomalies are higher at the bottom (values between 0 and -10 g L^{-1}) than at the surface (values between -2 and -12 g L^{-1}). An extreme river flow or wave event is associated with a peak in SPM anomaly, but not necessarily to an extreme anomaly value. Hence, extreme forcings do not explain all the sediment variability observed in the mouth and in particular do not coincide with all the strong SPM anomalies. Finally, river flow-related events exhibit a weaker signature (Figure 7) in SPM (anomalies > 0.3 times the threshold) than the wave-related events (anomalies > 0.75 times the threshold).

(a)

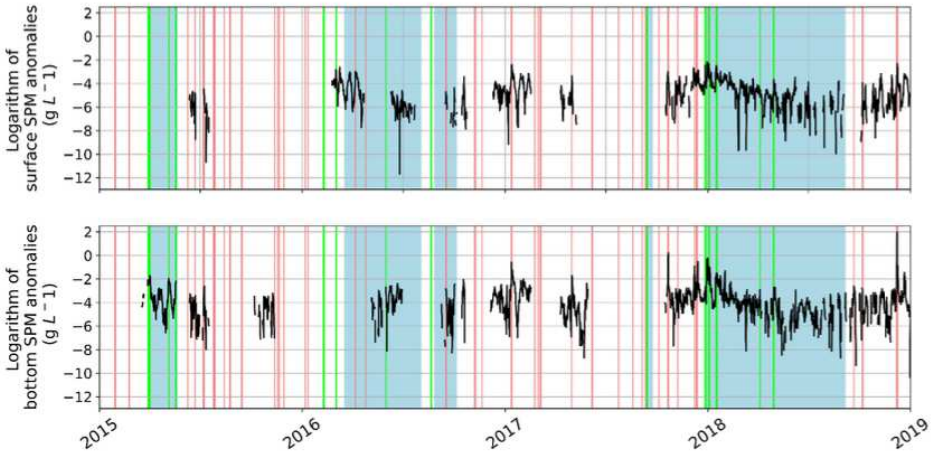

(b)

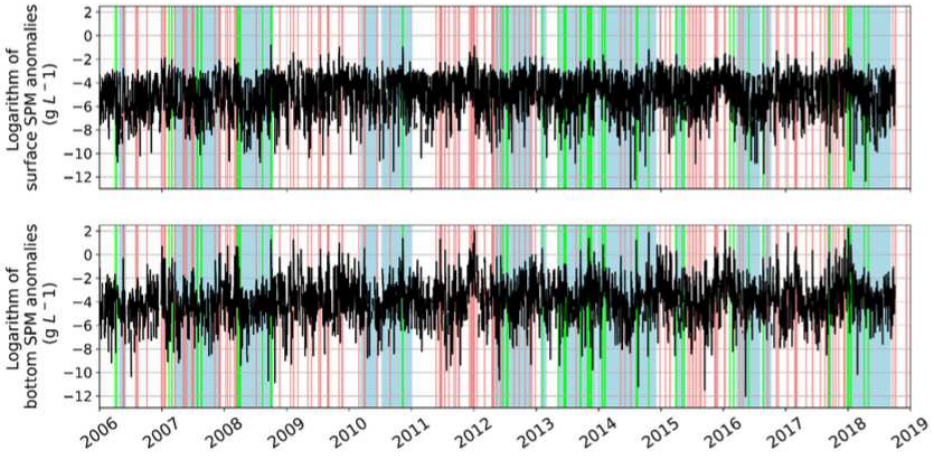

Figure 6: SPM anomalies observed with *in situ* data (a) and model data (b) during extreme river flow events (blue), extreme wave events (red) and concomitant events (green).

3.3 SPM response to extreme hydrodynamical forcings

The impact of river flow and wave forcings on SPM is investigated. First, we question whether one forcing has a greater effect than the other. Second, we explore if seasonality plays a role in extreme events in terms of SPM response. We also want to know if the accumulation of successive extreme events will have a greater impact on the sediment response. Finally, we explore the impact of the duration of the river forcing on the SPM response and its proportionality effect.

3.3.1 Relation between extreme forcings and SPM anomalies

SPM anomalies are extracted simultaneously to events, extreme forcings and datasets are compared. The observed dynamics are similar between the *in situ* and the model data, with stronger anomalies for wave events than for river flow events (Figure 7). SPM anomalies related to wave forcing can often exceed those related to floods; this effect is visible at the surface (with for the river, values less or around 0.02 g L^{-1} for *in situ* and model data versus 0.05 g L^{-1} for *in situ* data and 0.08 g L^{-1} for model data for the waves values) and less at the bottom. The model and the observations for mean SPM intensity present similar trends.

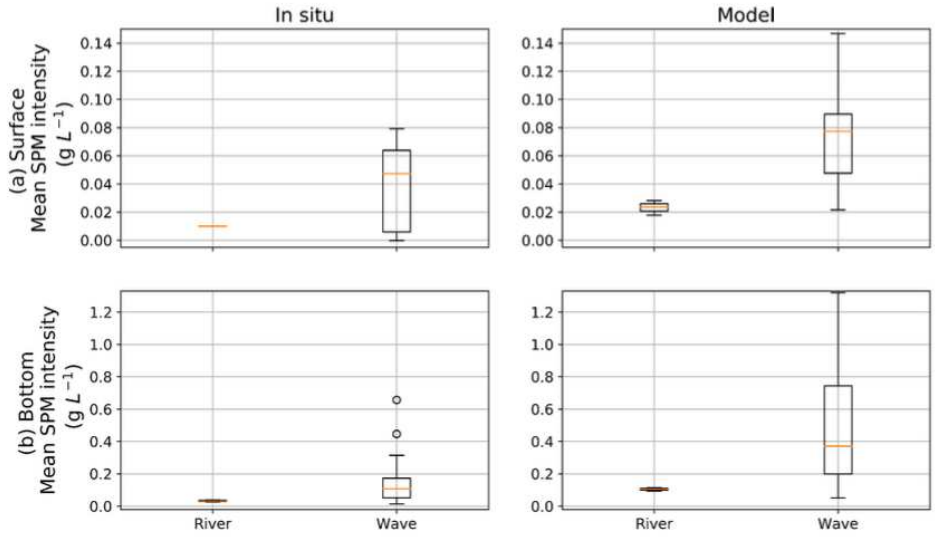

Figure 7: Distribution of mean SPM intensity during extreme forcings of river flow and square wave orbital speed between 2015 to 2019 at the surface (a) and at the bottom (b) for *in situ* (left) and model data (right).

3.3.2 Relation between SPM anomalies and extreme wave intensity

A proportional relationship is observed between wave forcing and SPM anomalies (Figure 8). The more intense the forcing is, the stronger the SPM response is (Figure 8): from 0 to 0.1 g L^{-1} at the surface and from 0 to 0.73 g L^{-1} at the bottom. Seasonality is observed with SPM anomaly values close to 0 in summer and highest SPM anomalies (>0.05 and 0.25 g L^{-1} for *in situ* data at the surface and the bottom respectively) in winter related to stronger forcings.

Sediment erosion fluxes are governed by an excess bed shear stress and an erosion rate. This excess bed shear stress is the difference between wave-current bed shear stress and the

critical erosion shear stress, a threshold that expresses the resistance of the bed to erosion. Hence, in general, the larger the orbital velocity, the bed shear stress and the eroded sediment flux are then higher the SPM anomaly is. In winter, a high wave energy season, extreme events detected are characterized by high wave orbital velocity values, and hence high excess shear stress and high SPM anomalies. In summer, wave extreme events are generally weaker, and then both the excess shear stress, the erosion flux and SPM anomalies are weaker.

Linear regression is calculated between extreme wave forcing and the response in SPM anomalies showing r correlation coefficient close to 0.9 for *in situ* data (0.89 at the surface and 0.97 at the bottom) and 0.3 for model data (0.34 at the surface and 0.29 at the bottom) with p values between 0.003 et 0.0002. Knowing that *in situ* data are evaluated over a shorter period than model data.

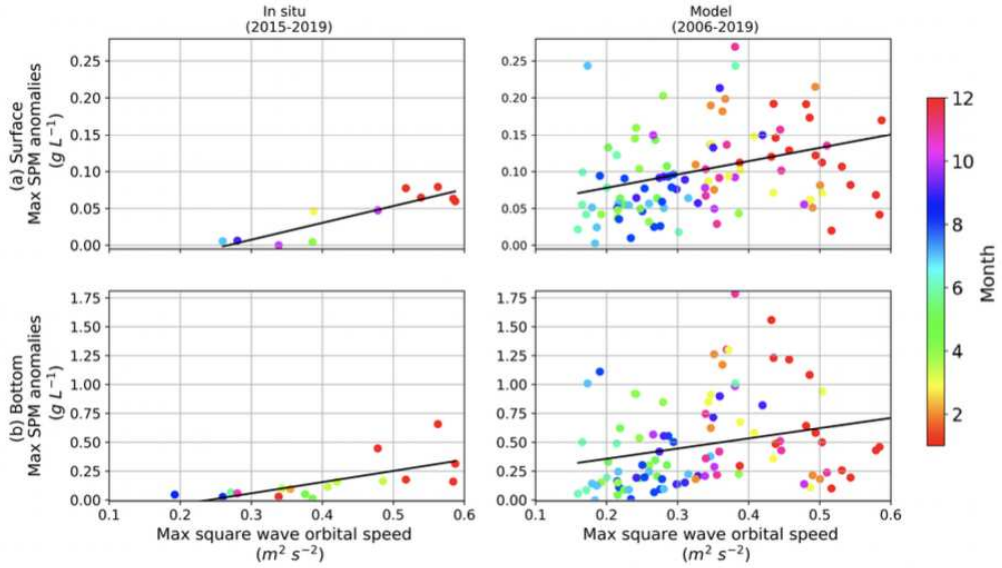

Figure 8: Relation between maximum square wave orbital speed and maximum SPM anomalies during extreme wave events. The colors represent the months of the year and the black line represents the linear regression. (a) Surface data and (b) bottom data. *In situ* data (2015-2019) are on the left and model data (2006-2019) are on the right.

3.3.3. Impact of river flow duration on SPM anomalies

To explore the relationship that may exist between the duration of extreme floods and the duration of extreme SPM events (Figure. 9), the same method is applied to detect extreme SPM events. Then, the duration of the 20 extreme flood events is examined through *in situ* and model data. If extreme SPM anomalies are detected during extreme flood events, their duration is cumulated over the time of the flood event. *In situ* and model data show that extreme SPM duration in surface and bottom are proportional to extreme river flow duration: longest river flow events (>150 tides, M2 tidal cycle) correspond to longest SPM extreme events (>5 tides in surface and >10 tides at the bottom). During short extreme river flow events (<150 tides) most of the SPM events are also short (< 7.5 tides at the surface and the bottom).

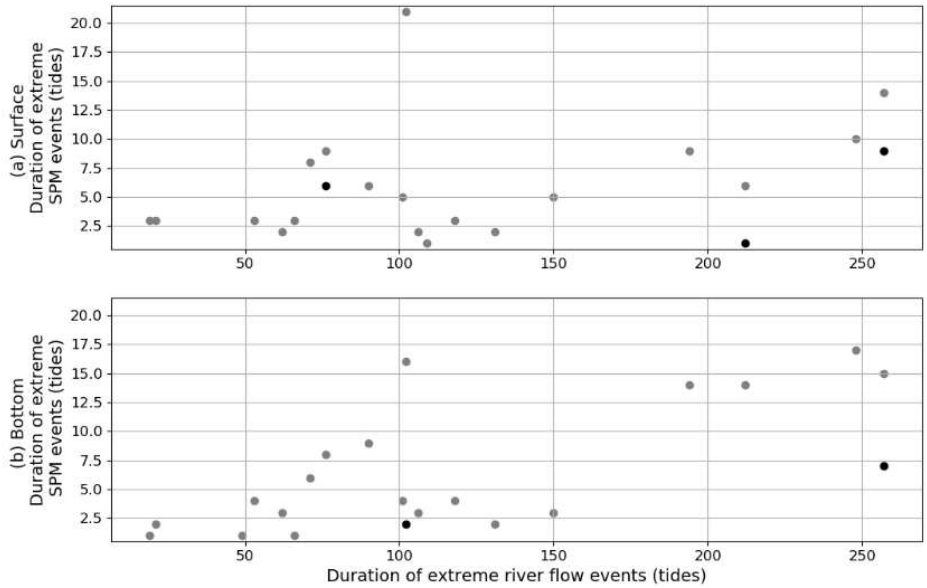

Figure 9: Relation between the duration of extreme river flow events and the duration of extreme events for *in situ* SPM (black dots) and model SPM (grey dots) expressed in number of tides at the surface (a) and at the bottom (b).

3.3.4. Impact of successive extreme events on the intensity of SPM anomalies

No clear trends on the consequence of successive events on peak anomaly intensities are detected: no significant increase in SPM anomalies, corresponding to an increasingly destabilized bed, or decrease in SPM, related to fine sediment being washed out from the bed by successive waves. The effect of succession of events is also examined by studying the time lag effect on sediments maintained in suspension after each event (Figure 10).

$$SPM_{diff} = \frac{([max(SPM)]_{event\ A} + [max(SPM)]_{event\ B}) / 2}{[min(SPM)]_{between\ A\ and\ B}} \quad (equation\ 1)$$

Equation 1 is used to define the normalized difference of SPM. If the normalized difference of SPM is large, the minimum between 2 consecutive events is low. Conversely, if the normalized difference is small, the minimum between 2 consecutive events is high. SPM anomalies are then not decreasing but stabilize and reach a plateau. *In situ* and model observations show the same dynamics, with normalized difference values higher than 0.7 after 2.5 days on average, time for suspended particles to settle and reach their concentration level outside events. When the successive extreme events are very close (<3 tides), the difference decreases, the two successive events are then considered as a merge event in terms of SPM because resuspended particles do not have time to settle.

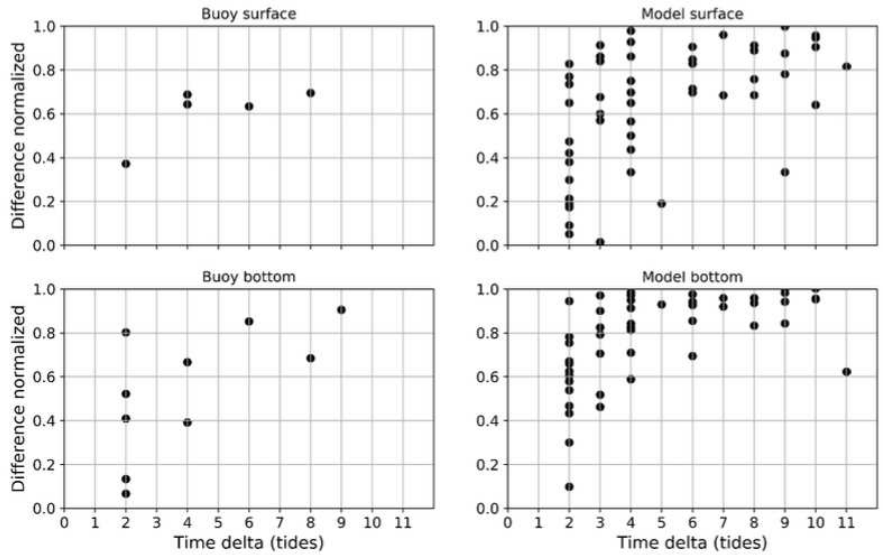

Figure 10: Relation between the time delta (tides) between 2 consecutive extreme wave events and the difference normalized of SPM. Surface data (a), bottom data (b) *in situ* data (left) and model data (right).

3.4 Spatial extent of SPM events

3.4.1 Understanding the distribution of satellite surface SPM concentrations in the environment

Satellite data are processed to examine how extreme events spatially impact the estuary-sea interface. The number of (valid, i.e. no clouds) pixels in the turbid surface area and the mean SPM concentration above 5 mg L^{-1}, the amplitude of the tide, the wind intensity, the season and the forcing (river flows or waves) are concurrently analyzed . The SPM spatial response to wave and river flow forcings is examined using the surface percentage of the target area above a threshold of 5 mg L^{-1} (Figure 11). The SPM concentrations are mainly driven by river discharge (enhanced advection, stratification and plume stability together with a shift of ETM toward the mouth) and wave-induced resuspension processes.

The relation between SPM concentrations and the wave intensity shows a linear correlation. Square wave orbital speeds are in majority (54%) below 0.1 $m^2 s^{-2}$ (20 % >0.2 $m^2 s^{-2}$ and 30% between 0.1 and 0.2 $m^2 s^{-2}$). The very few observed flood events do not allow to describe a pattern (not shown).

For both forcings, the surface of high SPM concentration (>5 mg L^{-1}) is not completely responding to forcings intensity, and is further investigated below. Outliers, distant from linear trend, are not due to the number of pixels available of the satellite image, because most images have at least 50% of valid pixels (Figure 11a). Tidal range was first investigated as its impact on mixing could either de-stratify surface plume or bring to surface wave-induced bottom sediment and could next decrease or increase surface SPM concentration respectively. For low-intensity wave events, the impact of tidal range can be observed, with larger plume area values during neap tides. For intense wave events, the impact of tidal range does not clearly elucidate data scattering (Figure 11b). We can observe that globally cumulating high river flow and intense wave events generate larger high surface SPM concentration areas than wave events

associated with low river flow (Figure 11c). However, still outliers persist, which were not explained by wind observation (Figure 11d). Possibly the temporal history of these events could explain this additional variability. This will be further explored in the next section. It is also observed that seasonality plays a role with higher SPM response in winter than in summer (Figure 11e), as observed and expected from *in situ* observation.

(a)

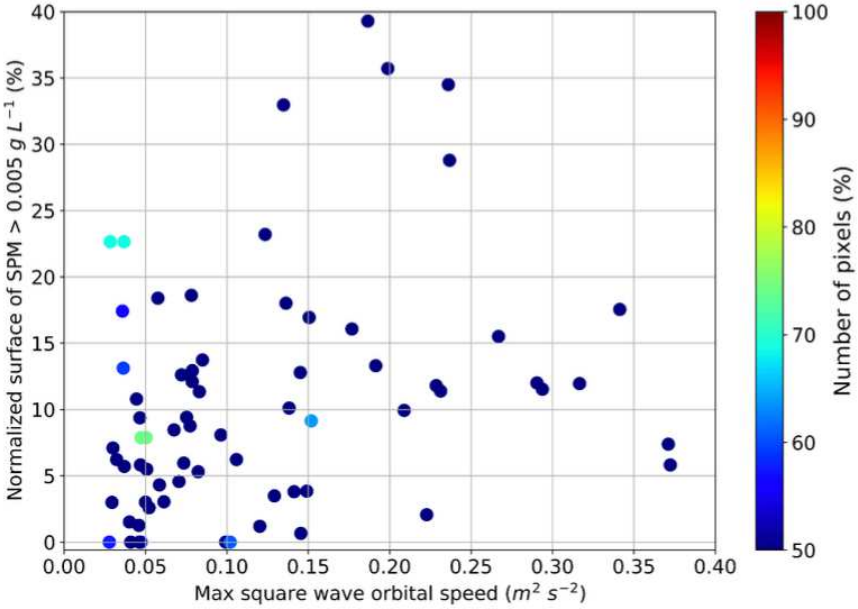

(b)

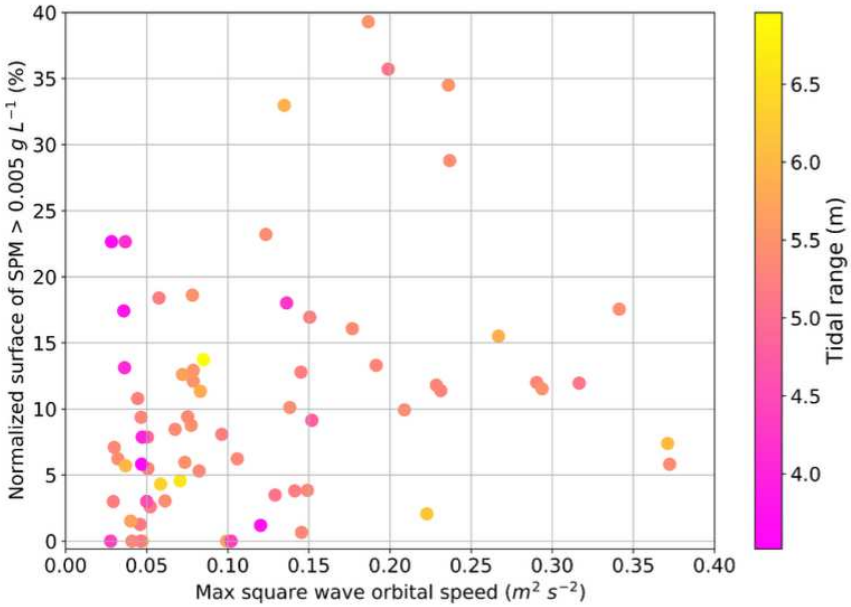
Normalized surface of SPM > 0.005 g L^{-1} (%)
Max square wave orbital speed (m^2 s^{-2})
Tidal range (m)
0
5
10
15
20
25
30
35
40
0.00
0.05
0.10
0.15
0.20
0.25
0.30
0.35
0.40
4.0
4.5
5.0
5.5
6.0
6.5

(c)

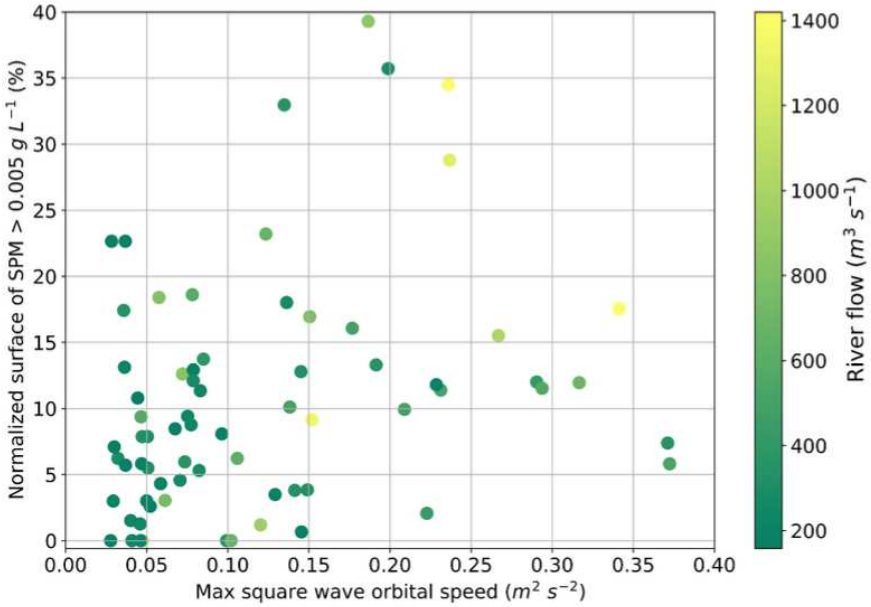
Normalized surface of SPM > 0.005 g L^{-1} (%)
Max square wave orbital speed (m^2 s^{-2})
River flow (m^3 s^{-1})
0
5
10
15
20
25
30
35
40
0.00
0.05
0.10
0.15
0.20
0.25
0.30
0.35
0.40
200
400
600
800
1000
1200
1400

(d)

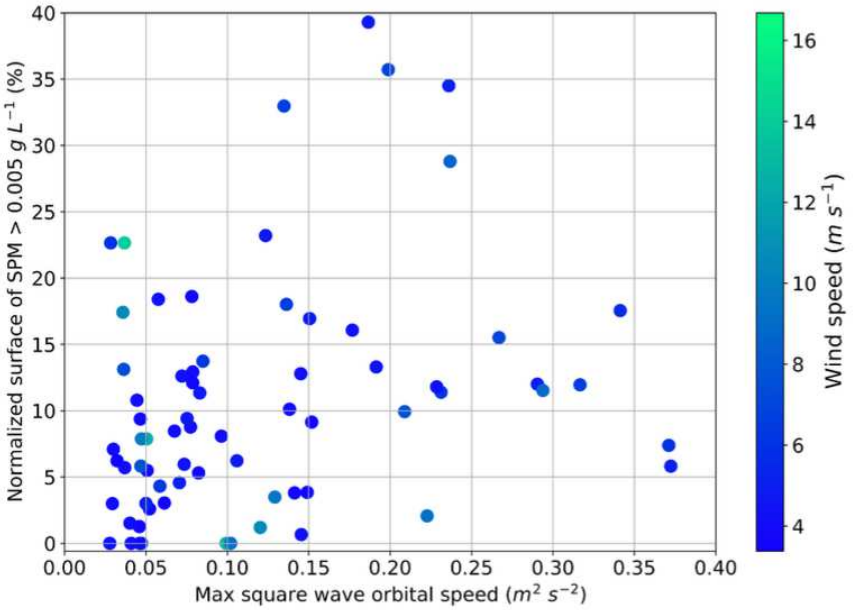

(e)

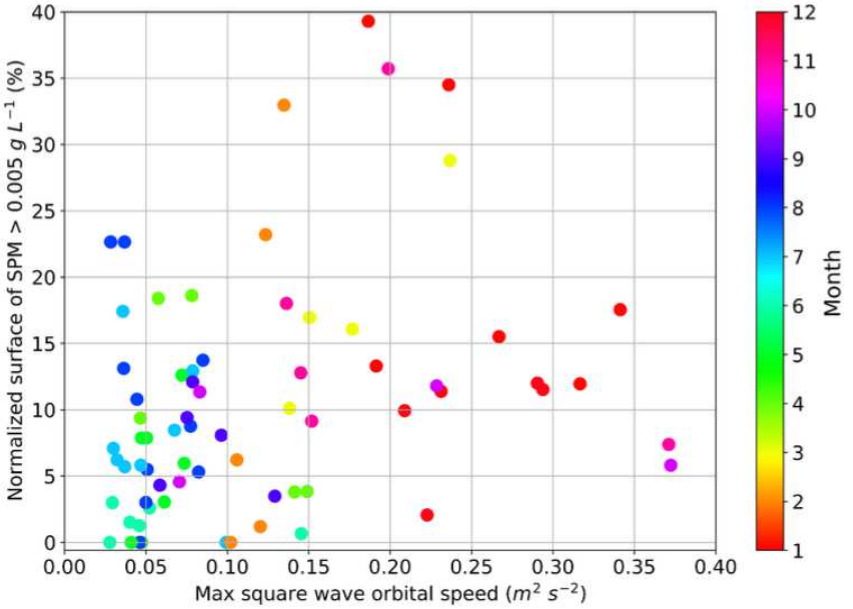

Figure 11: Normalized satellite surface SPM concentrations superior to 5 mg L^{-1} in relation to maximum of extreme wave forcing based on the (a) number of pixels, (b) tidal range, (c) complementary forcing, (d) wind speed and (e) season.

3.4.2 Characterization of satellite surface SPM plume spatial extent

The sediment river plumes are analyzed during each of the 20 extreme flood events (Figure 12). For each event, the date of the maximum river flow is identified and the satellite images that correspond to the week following this date are selected to plot the mean contour of SPM equal to 5 mg L^{-1}. The events are classified in 2 groups using a color gradient corresponding to the median extreme river flow: the strongest events in shades of red and the weakest events in shades of blue. When river flow is high, the sediment plume extends into the bay toward the North-West (and the South-East - depending wind dynamics) with contours beyond 0.15°W and above 49.6°N (Figure 12). The more intense flood (in dark red, Figure 12) leads to the largest sediment plume area. In contrast, low-intensity floods yield to a sediment plume that remains close to the river mouth and which does not exceed 0.10°W and 49.6°N (Figure 12). The less intense flood (in dark blue, Figure 12) forms only a tight bulge in front of the estuary.

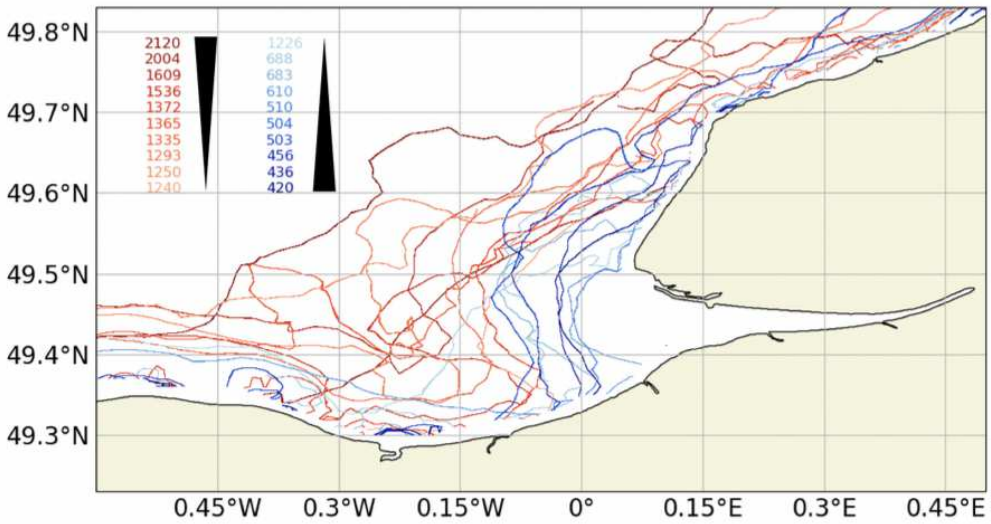

Figure 12: Sediment river plumes of the 20 extreme river flow events with the most intense events in red shades and the least intense events in blue shades and the palest colors being the closest to the median (1226 m^3 s^{-1}) of all events. Values represent the maximum river flow for each event expressed in m^3 s^{-1}.

3.4.3 Processes driving sedimentary plume extents: three case studies

When focusing on specific events representative of typical flood events, the plume dynamics is observed, averaging available images every 15 days from the beginning to the end of each event (Figure 13). Three specific examples are studied.

First, we consider the weakest and shortest extreme flood event (1.2 times the threshold) from mid-September to mid-October 2008 (Figure 13a). A rounded plume faces the Seine estuary close to the coast as it does not exceed 0.05°W. This extreme flow is weak with a maximum peak around 400 m^3 s^{-1} and without waves (average square wave orbital velocities below 0.2 m^2 s^{-2}). This situation explains the weak evolution of the sediment plume during the event.

Secondly, the opposite situation is studied with the longest and strongest flood event occurring from January to May 2018 (Figure 13b). The sediment plume is highly spread out in January with a plume that exceeds 0.3°W and 49.7°N during the first half of the event (brown

and yellow shades). Then the plume gradually moves closer to the estuary mouth with a boundary around 0.15°W (red shades) as the river discharge decreases. It can be seen that the evolution of the SPM contour is important between each 15 day period. This event, which is divided into two phases, presents first a very important flood peak higher than 2000 $m^3 s^{-1}$ but also important waves with square wave orbital velocity peaks higher than 0.5 $m^2 s^{-2}$ and then lower conditions of river flows with less than 1300 $m^3 s^{-1}$ and square wave orbital velocities below 0.2 $m^2 s^{-2}$.

Finally, the rarest event is examined (Figure 13c): it is the second most intense event which happens in summer 2016, a season in which such discharge is unexpected. Similarly to the strongest event, the sediment plume is present in the bay up to 0.15°W when the peak flood discharge is observed. The weak North wind favors an extension of the turbid plume towards the West, confined close to the coast. Then rapidly after 15 days, the plume extension becomes progressively reduced and centered close to the mouth, around 0.05 to 0.1°W, as expected during medium to low river flow conditions. This event presents a sudden and very intense peak of flood close to 2000 $m^3 s^{-1}$ and does not present any concurrent impact of waves, which are weak all the time during the event (square wave orbital velocities below 0.25 $m^2 s^{-2}$). The occurrence of such an event in a dry period leads to a rapid response of the system.

It can be concluded that the intensity and duration of the event are proportionally related to the extent of the plume. The evolution of the sediment plume is fast and important in winter while it is smaller and slower in summer. It can be remembered that the wave effect is not distinguishable from the river flow effect.

(a)

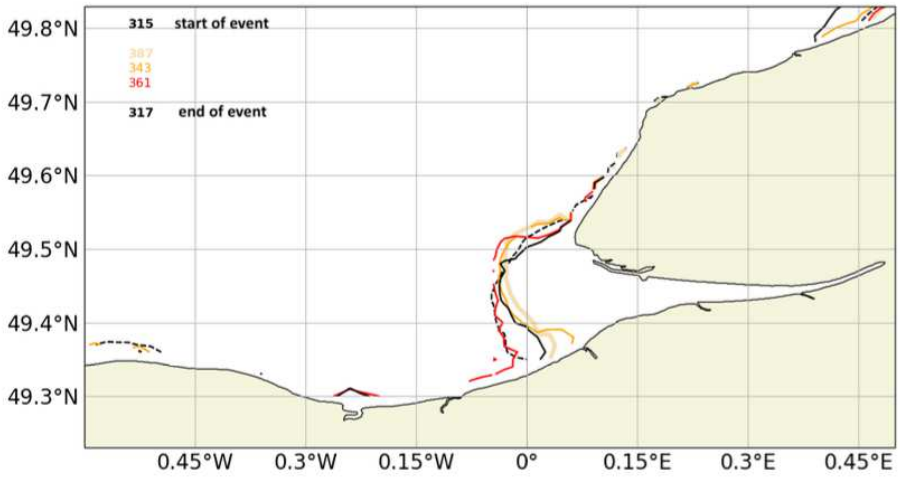

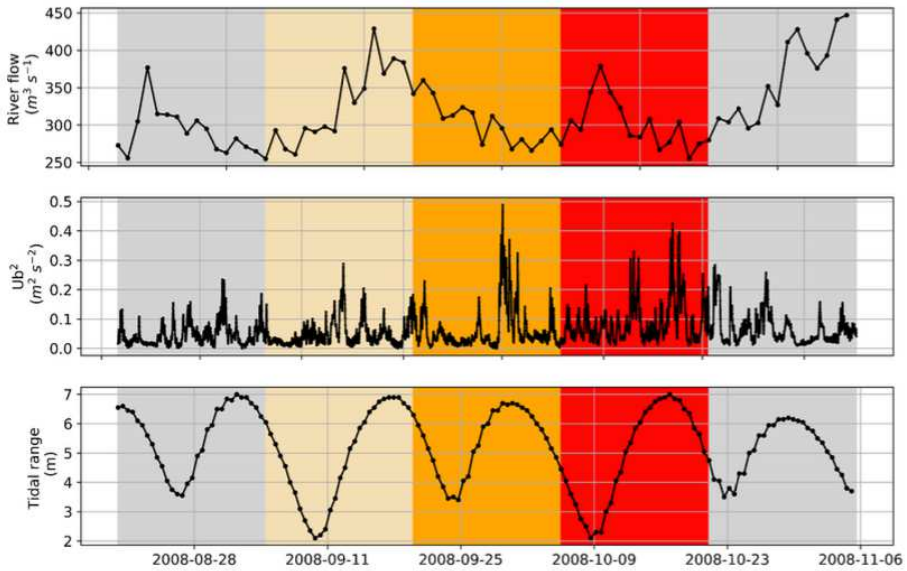
River flow
(m^3 s^{-1})
450
400
350
300
250
Ub²
(m^2 s^{-2})
0.5
0.4
0.3
0.2
0.1
0.0
Tidal range
(m)
7
6
5
4
3
2
2008-08-28
2008-09-11
2008-09-25
2008-10-09
2008-10-23
2008-11-06

547
548 (b)

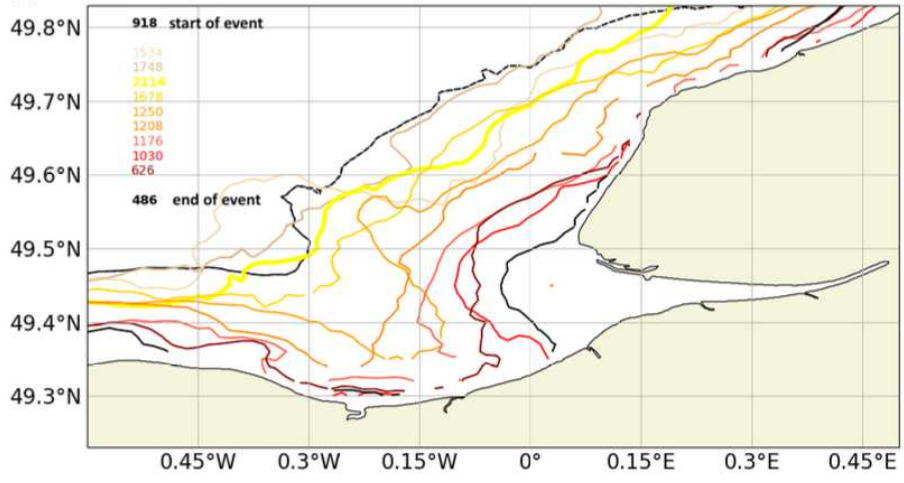
918 start of event
1534
1748
2114
1678
1250
1208
1176
1030
626
486 end of event
49.8°N
49.7°N
49.6°N
49.5°N
49.4°N
49.3°N
0.45°W
0.3°W
0.15°W
0°
0.15°E
0.3°E
0.45°E

549

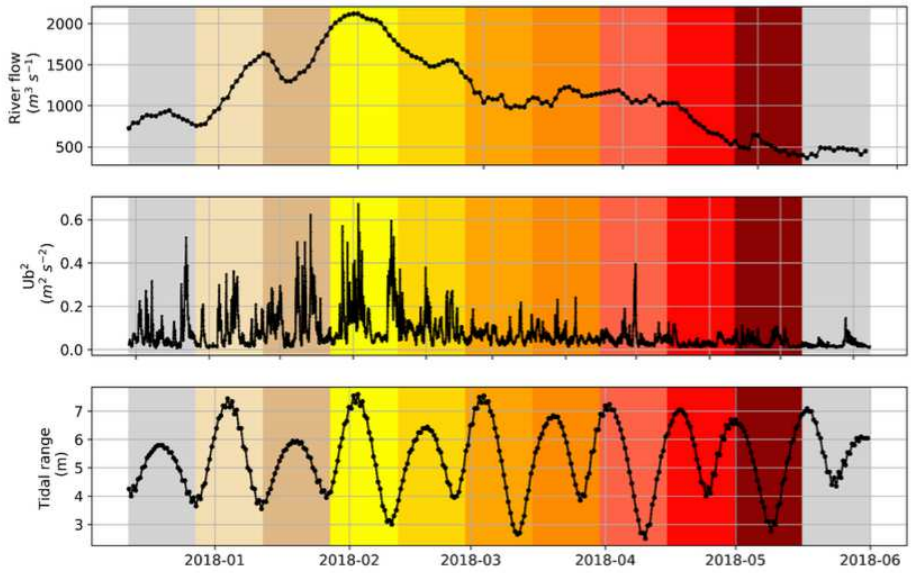
River flow
(m^3 s^{-1})
2000
1500
1000
500
Ub²
(m^2 s^{-2})
0.6
0.4
0.2
0.0
Tidal range
(m)
7
6
5
4
3
2018-01
2018-02
2018-03
2018-04
2018-05
2018-06

(c)

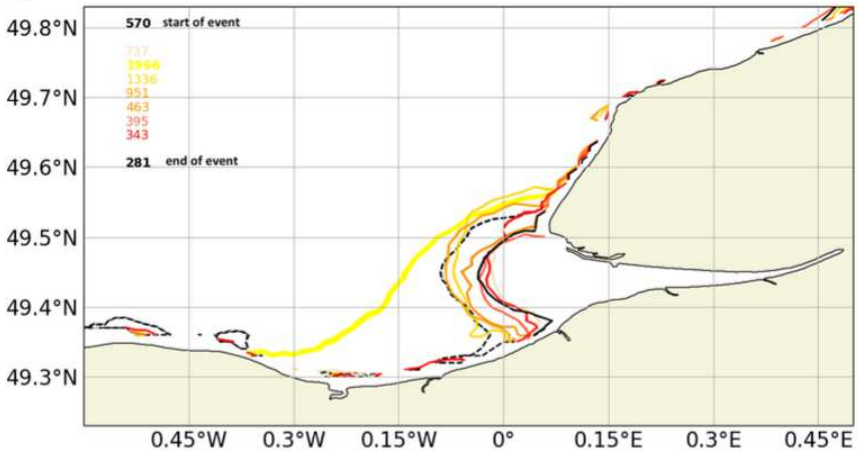
570 start of event
737
1966
1336
951
463
395
343
281 end of event
49.8°N
49.7°N
49.6°N
49.5°N
49.4°N
49.3°N
0.45°W
0.3°W
0.15°W
0°
0.15°E
0.3°E
0.45°E

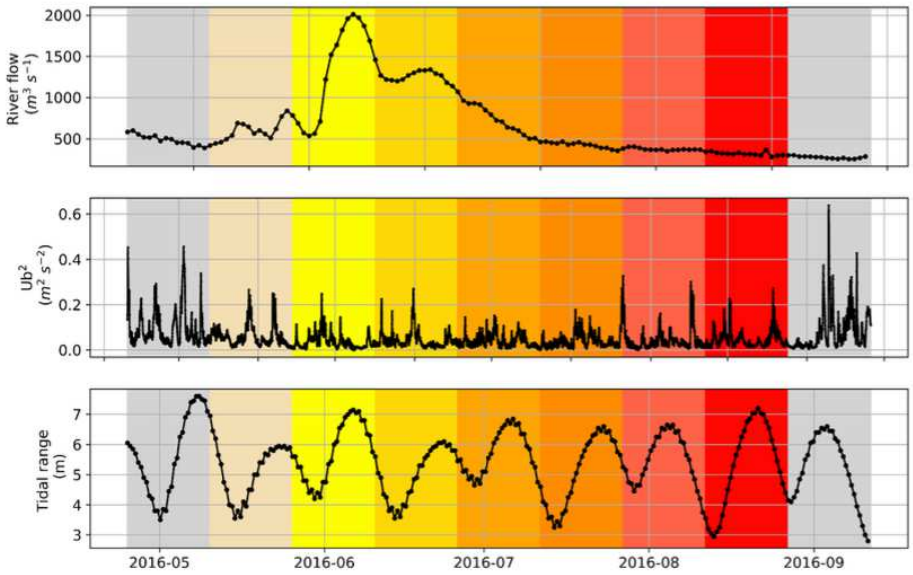

Figure 13: Evolution of the sediment plume represented by the 5 mg L^{-1} SPM contour every 15 days for three extreme river discharge events: (a) the weakest in early autumn 2008 (b) the strongest in winter 2018 and (c) the most rare in summer 2016. Start of the event (dotted black line), the end of the event (solid black line) and the maximum peak of the event (bold line) are indicated. Environmental conditions associated with these events are also represented for river flow, square wave orbital speed, and tidal amplitude. Values on the map represent the maximum river flow for each period of the event expressed in m^3 s^{-1}.

4. Discussion

4.1 Reversal of the extreme detection method: SPM extreme events

In this study the extreme forcings are detected and the associated SPM response is then analyzed. This is the usual strategy used in other studies to observe the impact of external hydro-meteorological forcings such as storms (Fettweis *et al.*, 2010) and floods (Tavora *et al.*, 2023) on SPM. Meanwhile, questions can arise if a direct cascade effect exists, and if an extreme event in the forcing necessarily implies an extreme event in SPM concentration anomalies. Both methods, (i) detection of extreme forcings and response in SPM and (ii) detection of extreme SPM are compared to analyze the possible similarities and discrepancies. This is tested on modeled (longest, continuous) SPM time series from 2006 to 2019 at the surface and at the bottom using the same methodology as applied for observations (Verney *et al.*, submitted, 2023). The results show a good agreement between both detection methods with a similar number of events. 210 extreme SPM events are found at the surface and 199 at the bottom against 200 extreme wave events detected over the same period. Also, differences are observed on the number of non-detected events (about a quarter) in a serie that appear however extreme on the other serie. There are 55 and 47 extreme SPM events detected in model data that do not correspond to extreme wave events, against 38 and 27 extreme wave events detected that do not correspond to extreme SPM anomalies at the surface and the bottom respectively. The

584 seasonality, with longer, more intense extreme events with more activity in winter than in other
585 seasons explain this variability in both cases, indicating higher sediment bottom stress in winter
586 than in summer. In the end, this study is significant and brings the same results whether forcing
587 is studied first or the parameter (SPM) itself to explain the role of extremes in the Bay of Seine.
588 This shows that both approaches are possible without bias in the conclusions.
589
590 4.2 Robustness of the extreme detection method: the threshold question
591
592 In a second step, the robustness of our method is questioned as well as the definition of
593 extreme events. SPM response to wave extreme forcing is often investigated for specific events
594 and generally during the winter season when storms are strongest (Warner *et al.*, 2008;
595 Lettmann *et al.*, 2009; Fettweis *et al.*, 2010). In this study 20 extreme river flows and 200
596 extreme waves are detected over less than 2 decades from 2006 to 2019 during all seasons.
597
598 We question if these extreme events are really extreme in the sense of rare and if the
599 percentile 90 as a threshold is the right choice. The percentile 90 remains the most used
600 threshold in the scientific community (McPhillips *et al.*, 2018), as used in marine heatwaves
601 studies (Hobday *et al.*, 2016). The percentile 95 is used to detect extreme events of river flows
602 and significant wave heights in the Bay of Seine by Grasso *et al.* (2021), or intense
603 hydrodynamic events in the mudflat of the Gironde region by Lamarque *et al.* (2022) and
604 extreme river flows and winds in the Scheldt estuary by Tavora *et al.* (2023). Our method seems
605 to be robust with both thresholds (percentile 90 versus percentile 95) giving similar results
606 (Figure 14 & 15). The same events are (generally) detected, while (10 to 25%) less events are
607 detected with a higher percentile 95, as expected. The threshold chosen will depend on the
608 scientific question, whether it concerns the determination of a trend of these extremes
609 considered as rare or whether, as in our case, the interannual variability and the processes
610 related to these extremes are studied.
611
612 Another aspect of this method is the temporal variability of the threshold which is also
613 to be taken into account according to the scientific question asked. In a (simple) physical study
614 context, it could be studied only during the winter period, for example, when storms are the
615 most important (Poppeschi *et al.,* 2021). On the other hand, if the study ambitions to investigate
616 different parts of the ecosystem, it will be necessary to extend the study over the year or over a
617 season that is more favorable to the observation of these biological processes. The threshold
618 can be either fixed to a standard value like for oxygen (threshold of 2 mg L^{-1} - Conley *et al.*,
619 2009) or variable in time (Stephenson, 2008). For the latter, thresholds can vary according to a
620 certain frequency : day, week, month or season (Figure 14 & 15). Marine heatwaves for
621 example are only studied in summer with a seasonal threshold calculated from a daily
622 climatology (Hobday *et al.*, 2016) but with climate change, these extreme phenomena studies
623 could probably be extended to months surrounding the summer season as well. Because of
624 global change, extremes are more and more present in unexpected periods, and it is mandatory
625 to study them using variable thresholds with the finest possible temporal resolution in order to
626 detect all extreme events all year long, as proposed in the present study.
627
628 The integration time period to calculate the threshold plays a role in detecting extremes.
629 Climate scientists recommend to estimate the threshold over a period of at least 30 years
630 (Hobday *et al.,* 2016; Oliver *et al.*, 2008). However, present *in situ* data rarely cover such long
631 periods of time, especially at high frequencies. Some series exceed 30 years like the Hawaii
632 ocean time-series (HOT, Karl and Lucas, 1996), but most are shorter than a decade or limited
633 to several years (Poppeschi *et al.,* 2022). The time series of forcing are often longer because

they have been taken by specialized organizations on strategic sites for years such as Météo-france for meteorological parameters or the Shom for tides in France. Therefore, tests are performed in this study on the Seine River flows over 10 to 60 years of data and for waves in the Bay of Seine over 5 to 25 years of data (Figure 14 & 15). The time period integration shows its importance in the consideration of the EE detection method on this signal is relatively weak, with thresholds very close to each other, compared to other setup conditions such as the percentile value or the threshold variability time scale. We also examine if splitting the signal in small time periods would not lead to the same conclusions as on a longer period (not shown), and results do not differ much as well.

Finally, the parameter variability also drives the scale to consider for detection events. In our case, the river flow is a continuous signal that follows a clear seasonal cycle, the floods are easily detected. In comparison, waves strongly and rapidly fluctuate and it is more complicated to separate the extremes from the signal. However, is this a realistic idea? It is perhaps necessary to sort the parameters according to their mathematical distributions in a first step as it has been highlighted here.

(a)

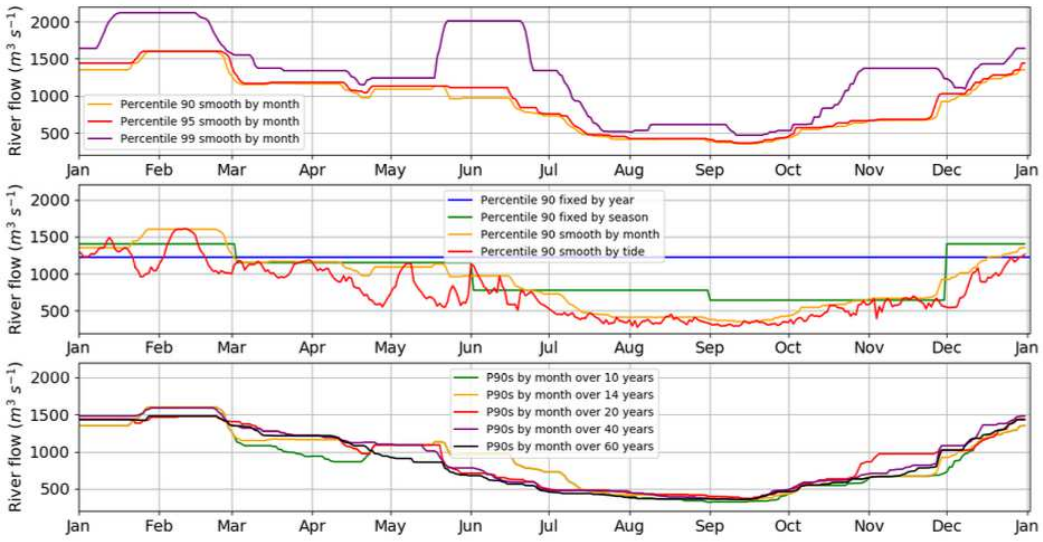

(b)

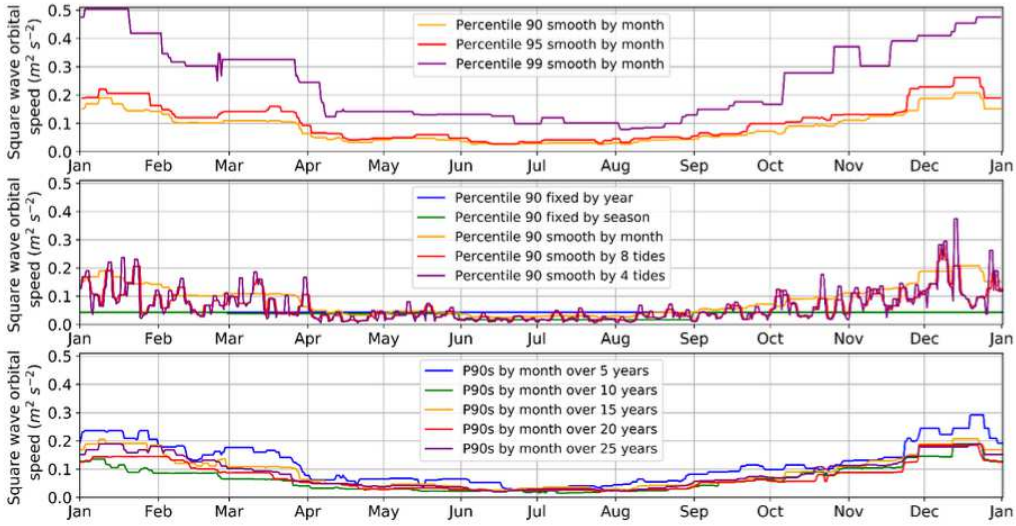

Figure 14. Analysis of thresholds for the extreme event detection method over percentiles, temporal variability and duration period on (a) river flow and (b) waves

(a)

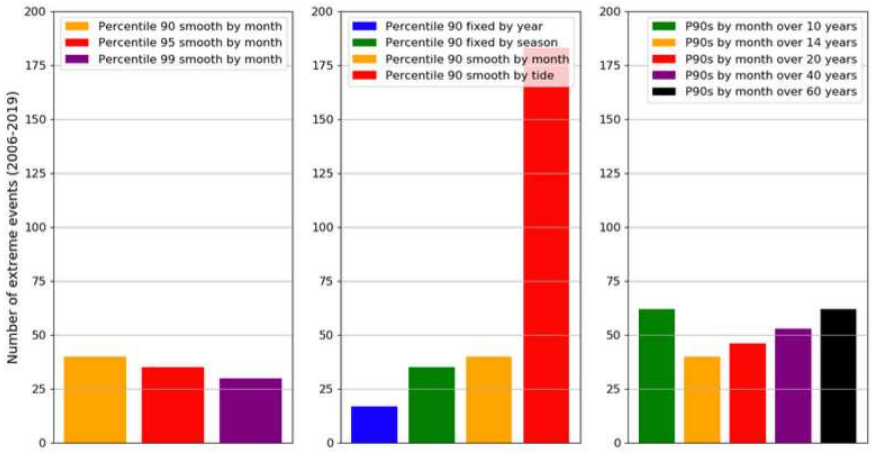

(b)

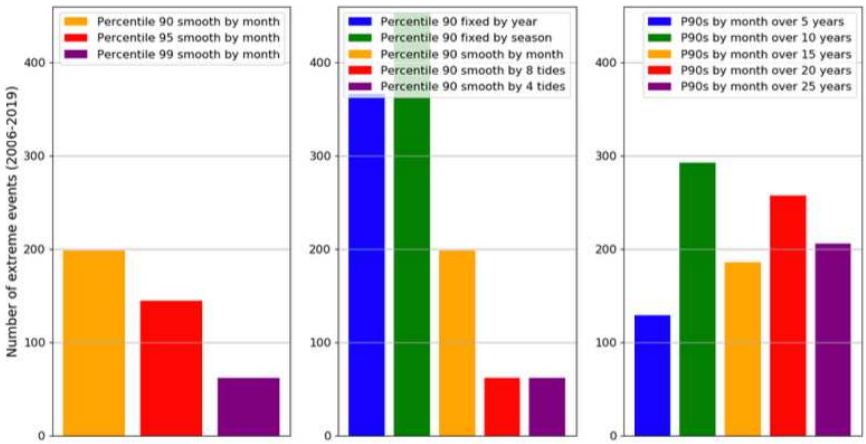

Figure 15. Number of extreme events detected over the period 2006 to 2019 for tests on thresholds over percentiles, temporal variability and duration period on (a) river flow and (b) waves

4.3 Characterization of extreme events and seasonal sediment dynamics

Is the impact of extremes on SPM different from the SPM variability related to non-extreme events ? The response of SPM to extreme forcings show strong links such as a similar seasonality with higher SPM concentrations in winter, explained by the stronger presence of storms in winter that resuspend the sediment in the water column in accordance with Lee *et al.* 2012. The proportional intensity between intensity of forcings and intensity of SPM explain also the similar evolution. However, this seasonality is also reflected in sediment dynamics outside extreme events. Extreme events for both flood and wave forcing do not appear to explain the most significant sediment response. In fact, the extremes are occuring in the same turbidity range as the sediment dynamics outside events (Figure 16).

(a)

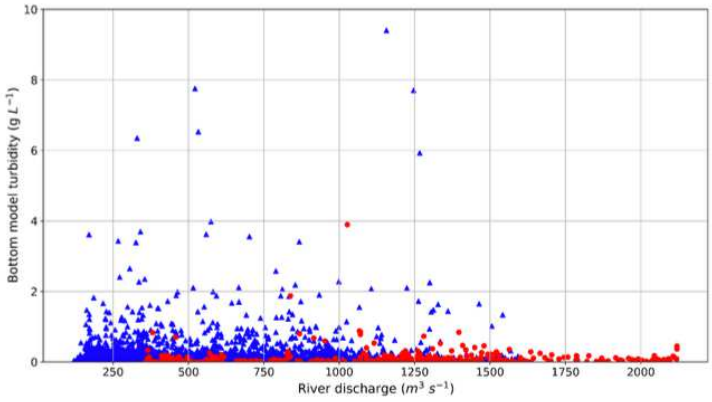

(b)

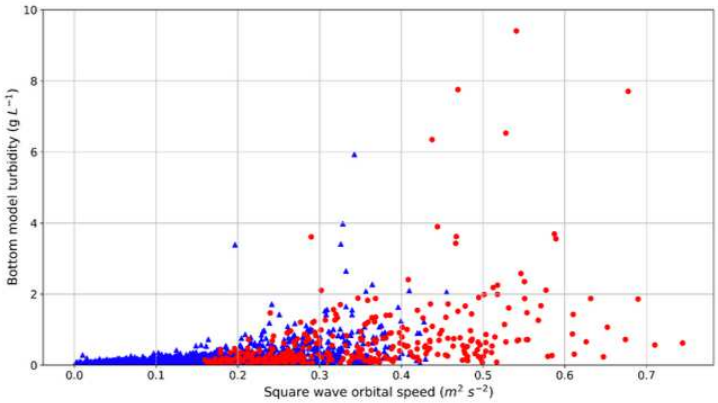

Figure 16. Comparison between forcings, (a) river flows and (b) square wave orbital speed, and the SPM response during extreme events (red) and outside extreme periods (blue).

4.4 Variability and trend of extreme forcings

Extreme hydro-meteorological events tend to intensify worldwide but also to become more and more frequent implying important consequences for coastal ecosystems (Breitburg *et al.*, 2018; Ibrahim *et al.*, 2021; IPCC, 2021).

For river flows analyses with the percentile 90 yearly from 1946 to 2020, yearly statistics reveal an increase of the extremes (Figure 17a). The extremes detected present a similar variability as the median river flows with a shared slight increase. The slope of the linear regression between the median and percentiles mean mobile values is not negligible +1.72 m^3 s^{-1} over the 72 years analyzed.

For waves using the percentile 90 yearly from 2006 to 2019, a particular year, 2007, is highlighted as intense with values up to 0.06 m^2 s^{-2} (Figure 17b). After 2010 a slight increase in intensity is shown with values around 0.035 to 0.05 m^2 s^{-2} for extremes (Figure 17b). In the yearly median there is no significant visible evolution (<0.005 m^2 s^{-2}). The slope of the linear regression between the median and percentiles mean mobile values shows an evolution even of this short period analysed (12 years) with +0.03 m^2 s^{-2}.

Several assumptions are also confronted, notably on the evolution of the mean discharge of French rivers, with some studies predicting lower mean river discharges part of the year (Gohin *et al.,* 2019) and others showing that river flows will be higher due to higher precipitations (Jalon-Rojas and Castelle, 2021). Median Seine river flow is calculated over the 60 years of available daily data. An increase of river flow is seen through a comparison between the last decade 2010-2020 and the first decade studied 1950-1960 with an increase of +84 m^3 s^{-1} for extreme values and +52 m^3 s^{-1} for median values. So, between 6 decades from 1950 to 2020 the Seine river flow extremes have increased 1.5 more than the median. Regarding the waves a slight increase is observed between 2010-2014 and 2015-2019 of +0.014 m^2 s^{-2} but there is no evolution of the median value corresponding.

In the last decade, the intensity of river flow extremes are increasing depending on the median whereas wave extremes are increasing also but without following wave median signal.

(a)

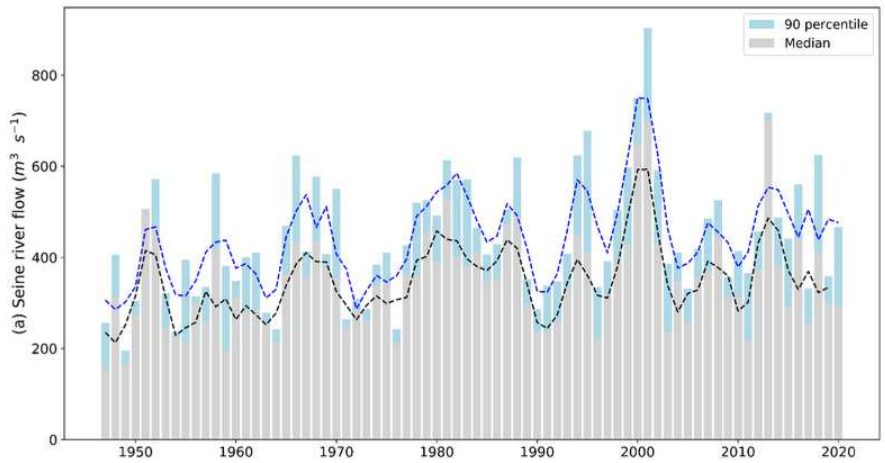

(b)

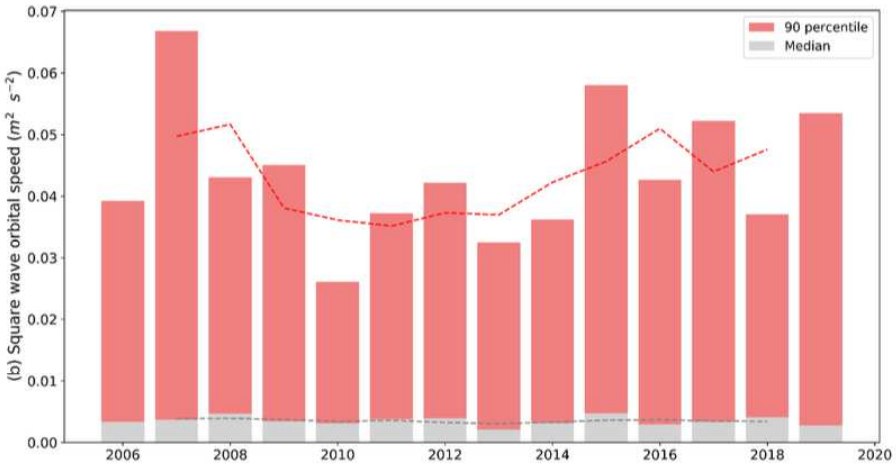

Figure 17: Interannual variability represented by the percentile 90 (blue or red bars) and the mean (grey bars) with for both an average mean over 3 years (dashed line) for (a) Seine river flow data from 1946 to 2020 and (b) square wave orbital speed data from 2006 to 2019.

5 Conclusion

Extreme forcings playing a role in sediment dynamics in the mouth of the Seine estuary have been detected using an innovative detection method applied to long term high frequency time series. This method investigates extreme forcings occurrence throughout the year, can be easily transposed to other coastal and estuarine sites, and its robustness has been validated in this study. A strong seasonality of these extreme forcings is highlighted with highest intensity and many successions of events in winter. The SPM response to extreme events is analyzed through tidal anomalies time series and satellite ocean color SPM surface concentration data.

Extreme wave events are the most impacting, generating large anomalies (stronger near the bottom than close to surface) caused by storm season induced by bottom sediment erosion. During summer, the average lower intensity of extreme wave events leads to lower SPM anomalies. River discharge extreme events also generate positive but weaker SPM anomalies compared to waves, mainly induced by the shift of the estuarine turbidity maximum toward the mouth. Similarly to wave events, low intensity river discharge anomalies do not imply a strong shift in ETM location and hence yield lower SPM anomalies.

Hence, based on the annual SPM anomaly distribution, extreme events do not necessarily induce extreme SPM anomalies. Nevertheless, exceptional extreme events during summer periods are such as the extreme flood event in June 2016, reported as the second highest SPM anomaly event over the 2015-2019 study period.

The importance of adapting the method for studying extremes to the parameter is developed. The various tests carried out have shown that the choice of threshold, its variability and the duration of its application are parameters to be considered and adapted according to the study.

Finally, an interesting aspect of this study is that it highlights the possible difference between the evolution of median and extreme values. This has been the case for flow and wave forcing in recent years.

It would be interesting to extend this study by considering the impact of SPM on phytoplankton in the Bay of Seine. Thus the classification of extreme events could be reviewed with events outside the winter season showing a stronger impact on the ecosystem (Fettweis *et al.*, 2014; Poppeschi *et al.*, 2022). Extreme forcing such as waves linked to storms often govern the entire English Channel dynamics and it could be considered to compare the SPM response between different coastal ecosystems along the French, English and Belgian coasts.

6 Acknowledgments

This study is part of the Contrat Plan Etat-Region ObsOcean / ROEC-ILICO and the COXTCLIM project funded by the Loire-Brittany Water Agency, the Brittany region, and Ifremer. This study also contributes to the RUNTIME project, co-funded by the EC2CO program and OFB.

We would like to acknowledge the COAST-HF (http://www.coast-hf.fr) national observing network component of the National Research Infrastructure ILICO. We would like to thank the Shom for tidal data and Météo-France for wind products. Finally, we are grateful to Anne Daniel of the Pelagos laboratory at Ifremer in Brest, France for her constructive comments and her attentive review of this article.

7 References

Abarnou, A., Avoine, J., Dupont, J. P., Lafite, R., Simon, S., 1987. Role of suspended sediments on the distribution of PCB in the Seine Estuary (France). Cont. Shelf Res., 7(11-12), 1345-1350. https://doi.org/10.1016/0278-4343(87)90038-0.

Aminot, A., Guillaud, J-F., Kerouel, R., 1997. La baie de Seine : hydrologie, nutriments, chlorophylle (1978-1994). Repères océans, 14, 151.

803 Andersen, T.J., Pejrup, M., 2001. Suspended sediment transport on a temperate, microtidal
804 mudflat, the Danish Wadden Sea. Marine Geology, 173(1-4), 69-85.
805 https://doi.org/10.1016/S0025-3227(00)00164-X.
806
807 Artelia, 2019. Définition des périodes de retour des forçages et des niveaux de pleines mers en
808 estuaire de Seine pour la gestion du risque inondation. Rapport réalisé pour le GIP Seine-Aval
809 et la DREAL Normandie, 99.
810
811 Breitburg, D., Levin, L.A., Oschlies, A., Grégoire, M., Chavez, F.P., Conley, D.J., Garçon, V.,
812 Gilbert, D., Gutiérrez, D., Isensee, K., Jacinto, G.S., Limburg, K.E., Montes, I., Naqvi, S.W.A.,
813 Pitcher, G.C., Rabalais, N.N., Roman, M.R., Rose, K.A., Seibel, B.A., Telszewski, M.,
814
815 Burchard, H., Schuttelaars, H.M., Ralston, D.K., 2018. Sediment trapping in estuaries. Annu.
816 Rev. Mar. Sci., 10, 371-95. https://doi.org/10.1146/annurev-marine-010816-060535.
817
818 Cailleaud, K., Forget-Leray, J., Souissi, S., Hilde, D., LeMenach, K., Budzinski, H., 2007.
819 Seasonal variations of hydrophobic organic contaminant concentrations in the water-column of
820 the Seine Estuary and their transfer to a planktonic species Eurytemora affinis (Calanoïda,
821 copepoda). Part 1: PCBs and PAHs. Chemosphere, 70(2), 270-280.
822 https://doi.org/10.1016/j.chemosphere.2007.05.095.
823
824 Cocquempot, L., Delacourt, C., Paillet, J., Riou, P., Aucan, J., Castelle, B., Charria, G., Claudet,
825 J., Conan, P., Coppola, L., Hocdé, R., Planes, S., Raimbault, P., Savoye, N., Testut, L.,
826 Vuillemin, R., 2019. Coastal ocean and nearshore observation: A French case study. Front.
827 Mar. Sci., 6, 324. https://doi.org/10.3389/fmars.2019.00324.
828 Conley, D.J., Carstensen, J., Vaquer-Sunyer, R., Duarte, C. M., 2009. Ecosystem thresholds
829 with hypoxia. In Eutrophication in Coastal Ecosystems: Towards better understanding and
830 management strategies Selected Papers from the Second International Symposium on Research
831 and Management of Eutrophication in Coastal Ecosystems, (20–23), 21-29.
832 https://doi.org/10.1007/s10750-009-9764-2.
833 Deloffre, J., Lafite, R., Lesueur, P., Lesourd, S., Verney, R., Guézennec, L., 2005. Sedimentary
834 processes on an intertidal mudflat in the upper macrotidal Seine estuary, France. *Estuar. Coast.*
835 *Shelf Sci.*, *64*(4), 710-720. https://doi.org/10.1016/j.ecss.2005.04.004.
836
837 Dufois, F., Verney, R., Le Hir, P., Dumas, F., Charmasson, S., 2014. Impact of winter storms
838 on sediment erosion in the rhone river prodelta and fate of sediment in the gulf of lion (north
839 western Mediterranean sea). Cont. Shelf Res., 72, 57-72.
840 https://doi.org/10.1016/j.csr.2013.11.004.
841 Dupont, N., Aksnes, D. L., 2013. Centennial changes in water clarity of the Baltic Sea and the
842 North Sea. Estuar. Coast. Shelf Sci., 131, 282-289. https://doi.org/10.1016/j.ecss.2013.08.010.
843
844 Farcy, P., Durand, D., Charria, G., Painting, S. J., Tamminen, T., Collingridge, K., Gremare,
845 A., Delauney, L., Puillat, I., 2019. Toward a European coastal observing network to provide
846 better answers to science and to societal challenges; the JERICO research infrastructure. Front.
847 Mar. Sci., 6, 529. https://doi.org/10.3389/fmars.2019.00529.
848
849 Fettweis, M., Francken, F., Van den Eynde, D., Verwaest, T., Janssens, J., Van Lancker, V.,
850 2010. Storm influence on SPM concentrations in a coastal turbidity maximum area with high
851 anthropogenic impact (southern North Sea). Cont. Shelf Res., 30(13), 1417-1427.
852 https://doi.org/10.1016/j.csr.2010.05.001.
853

Fettweis, M., Baeye, M., Van der Zande, D., Van den Eynde, D., Joon Lee, B., 2014. Seasonality of floc strength in the southern North Sea. J. Geophys. Res. Oceans, 119(3), 1911-1926. https://doi.org/10.1002/2013JC009750.

Gangloff, A., Verney, R., Doxaran, D., Ody, A., Estournel, C., 2017. Investigating Rhône River plume (Gulf of Lions, France) dynamics using metrics analysis from the MERIS 300 m Ocean Color archive (2002-2012). Cont. Shelf Res., 144, 98-111. https://dx.doi.org/10.1016/j.csr.2017.06.24

Garnaud, S., Lesueur, P., Clet, M., Lesourd, S., Garlan, T., Lafite, R., Brun-Cottan, J.C., 2003. Holocene to modern fine-grained sedimentation on a macrotidal shoreface-to-inner-shelf setting (eastern Bay of the Seine, France). Mar. Geol., 202(1-2), 33-54. https://doi.org/10.1016/S0025-3227(03)00266-4.

Gohin, F., Loyer, S., Lunven, M., Labry, C., Froidefond, J. M., Delmas, D., Huret, M., Herbland, A., 2005. Satellite-derived parameters for biological modelling in coastal waters: Illustration over the eastern continental shelf of the Bay of Biscay. Remote Sens. Environ., 95(1), 29-46.

Gohin, F., 2011. Annual cycles of chlorophyll-a, non-algal suspended particulate matter, and turbidity observed from space and in-situ in coastal waters. Ocean Sci., 7(5), 705-732. https://doi.org/10.5194/os-7-705-2011.

Gohin, F., Van der Zande, D., Tilstone, G., Eleveld, M. A., Lefebvre, A., Andrieux-Loyer, F., Blauw, A. N., Bryère, P., Devreker, D., Garnesson, P., Hernandez Farinas, T., Lamaury, Y., Lampert, L., Lavigne, H., Menet-Nedelec, F., Pardo, S., Saulquin, B., 2019. Twenty years of satellite and in situ observations of surface chlorophyll-a from the northern Bay of Biscay to the eastern English Channel. Is the water quality improving?. Remote Sens.Environ., 233, 111343. https://doi.org/10.1016/j.rse.2019.111343.

Grasso, F., Le Hir, P., Bassoullet, P., 2015. Numerical modelling of mixed-sediment consolidation. Ocean Dyn., 65(4), 607-616. https://doi.org/10.1007/s10236-015-0818-x.

Grasso, F., Verney, R., Le Hir, P., Thouvenin, B., Schulz, E., Kervella, Y., Khojasteh Pour Fard, I., Lemoine, J.-P., Dumas, F., Garnier, V., 2018. Suspended sediment dynamics in the macrotidal Seine Estuary (France): 1. Numerical modeling of turbidity maximum dynamics. J. Geophys. Res. Oceans, 123(1), 558-577. https://doi.org/10.1002/2016JC012638.

Grasso, F., Le Hir, P., 2019. Influence of morphological changes on suspended sediment dynamics in a macrotidal estuary: diachronic analysis in the Seine Estuary (France) from 1960 to 2010. Ocean Dyn., 69(1), 83-100. https://doi.org/10.1007/s10236-018-1233-x.

Grasso, F., Bismuth, E., Verney, R., 2021. Unraveling the impacts of meteorological and anthropogenic changes on sediment fluxes along an estuary-sea continuum. Sci. rep., 11(1), 1-11. https://doi.org/10.1038/s41598-021-99502-7.

Hobday, A. J., Alexander, L. V., Perkins, S. E., Smale, D. A., Straub, S. C., Oliver, E. C. J., Benthuysen, J. A., Burrows, M. T., Donat, M. G., Feng, M., Holbrook, N. J., Moore, P. J., Scannell, H. A., Sen Gupta, A., Wernberg, T., 2016. A hierarchical approach to defining marine heatwaves. Prog. Oceanogr., 141, 227–238. https://doi.org/10.1016/j.pocean.2015.12.014

Ibrahim, O., Mohamed, B., Nagy, H., 2021. Spatial variability and trends of marine heat waves in the eastern mediterranean sea over 39 years. Journal of Marine Science and Engineering, 9(6), 643. https://doi.org/10.3390/jmse9060643.

IPCC, Masson-Delmotte, V., Zhai, P., Pirani, A., Connors, S. L., Peìan, C., Berger, S., Caud, N., Chen, Y., Goldfarb, L., Gomis, M. I., Huang, M., Leitzell, K., Lonnoy, E., Matthews, J. B. R., Maycock, T. K., Waterfield, T., Yelekçi, O., Yu, R., Zhou, B., 2021. Climate change 2021: the physical science basis. Contribution of working group I to the sixth assessment report of the intergovernmental panel on climate change, Cambridge University Press, 2, 2391 pp.

Izquierdo, P., Rico, J. M., Taboada, F. G., González-Gil, R., Arrontes, J., 2022. Characterization of marine heatwaves in the Cantabrian Sea, SW Bay of Biscay. Estuar. Coast. Shelf Sci., 274. https://doi.org/10.1016/j.ecss.2022.107923.

Jalón-Rojas, I., Castelle, B., 2021. Climate control of multidecadal variability in river discharge and precipitation in western Europe. Water, 13(3), 257. https://doi.org/10.3390/w13030257.

Karl, D.M., Lukas, R., 1996. The Hawaii Ocean Time-series (HOT) program: Background, rationale and field implementation. Deep Sea Research Part II: Topical Studies in Oceanography, 43(2-3), 129-156.

Lamarque, B., Deflandre, B., Schmidt, S., Bernard, G., Dubosq, N., Diaz, M., Lavesque, N., Garabetian, F., Grasso, F., Sottolichio, A., Rigaud, S., Romero-Ramirez, A., Cordier, M.-A., Poirier, D., Danilo, M., Grémare, A., 2022. Spatiotemporal dynamics of surface sediment characteristics and benthic macrofauna compositions in a temperate high-energy River-dominated Ocean Margin. Cont. Shelf Res., 247, 104833. https://doi.org/10.1016/j.csr.2022.104833.

Landemaine, V., 2016. Érosion des sols et transferts sédimentaires sur les bassins versants de l'Ouest du Bassin de Paris: analyse, quantification et modélisation à l'échelle pluriannuelle. University of Rouen. https://hal-normandie-univ.archives-ouvertes.fr/tel-01937208 S.

Lazure, P., Dumas, F., 2008. An external–internal mode coupling for a 3D hydrodynamical model for applications at regional scale (MARS). Adv. water resour., 31(2), 233-250. https//doi.org/10.1016/j.advwatres.2007.06.010.

Lee, B. J., Fettweis, M., Toorman, E., Molz, F. J., 2012. Multimodality of a particle size distribution of cohesive suspended particulate matters in a coastal zone. J. Geophys. Res. Oceans, 117(C3). https://doi.org/10.1029/2011JC007552.

Le Gall, M., Ayrault, S., Evrard, O., Laceby, J. P., Gateuille, D., Lefèvre, I., Mouchel, J.-M., Meybeck, M., 2018. Investigating the metal contamination of sediment transported by the 2016 Seine River flood (Paris, France). Environ. Pollut., 240, 125-139. https://doi.org/10.1016/j.envpol.2018.04.082.

Le Hir, P., Ficht, A., Jacinto, R. S., Lesueur, P., Dupont, J. P., Lafite, R., Brenon, I., Thouvenin, B., Cugier, P., 2001. Fine sediment transport and accumulations at the mouth of the Seine estuary (France). Estuaries, 24(6), 950-963.

Le Hir, P., Cayocca, F., Waeles, B., 2011. Dynamics of sand and mud mixtures: A multiprocess-based modelling strategy. Cont. Shelf Res., 31(10), S135-S149. http://dx.doi.org/10.1016/j.csr.2010.12.009.

Lesourd, S., Lesueur, P., Brun-Cottan, J. C., Garnaud, S., Poupinet, N., 2003. Seasonal variations in the characteristics of superficial sediments in a macrotidal estuary (the Seine inlet, France). Estuar., Coast. Shelf Sci., 58(1), 3-16. https://doi.org/10.1016/S0272-7714(02)00340-2.

Lettmann, K.A., Wolff, J.O., Badewien, T.H., 2009. Modeling the impact of wind and waves on suspended particulate matter fluxes in the East Frisian Wadden Sea (southern North Sea). Ocean Dyn. 59, 239–262. https://doi.org/10.1007/s10236-009-0194-5.

McPhillips, L. E., Chang, H., Chester, M. V., Depietri, Y., Friedman, E., Grimm, N. B., Kominoski, J.S., McPhearson, T., Mendez-Lazaro, P., Rosi, E.J., Shafiei Shiva, J., 2018. Defining extreme events: A cross-disciplinary review. Earth's Future, 6(3), 441-455. https://doi.org/10.1002/2017EF000686.

Méar, Y., Poizot, E., Murat, A., Beryouni, K., Baux, N., Dauvin, J.C., 2018. Improving the monitoring of a dumping site in a dynamic environment. Example of the Octeville site (Bay of Seine, English Channel). Mar. Pollut. Bull., 129(2), 425-437. https://doi.org/10.1016/j.marpolbul.2017.10.011.

Paladini de Mendoza, F., Bonamano, S., Martellucci, R., Melchiorri, C., Consalvi, N., Piermattei, V., Marcelli, M., 2018. Circulation during storms and dynamics of suspended matter in a sheltered coastal area. Remote Sensing, 10(4), 602. https://doi.org/10.3390/rs10040602.

Muylaert, K., Vyverman, W., 2006. Impact of a flood event on the planktonic food web of the Schelde estuary (Belgium) in spring 1998. *Hydrobiologia*, *559*, 385-394. https://doi.org/10.1007/s10750-005-1081-9.

Poppeschi, C., Charria, G., Goberville, E., Rimmelin-Maury, P., Barrier, N., Petton, S., Unterberger, M., Grossteffan, E., Repecaud, M., Quemener, L., Theetten, S., Le Roux, J.-F., Tréguer, P., 2021. Unraveling salinity extreme events in coastal environments: a winter focus on the Bay of Brest. Front. Mar. Sci., 966. https://doi.org/10.3389/fmars.2021.705403.

Poppeschi, C., Charria, G., Daniel, A., Verney, R., Rimmelin-Maury, P., Retho, M., Goberville, E., Grossteffan, E., Plus, M., 2022. Interannual variability of the initiation of the phytoplankton growing period in two French coastal ecosystems. *Biogeosciences*, *19*(24), 5667-5687. https://doi.org/10.5194/bg-19-5667-2022.

Répécaud, M., Quemener, L., Charria, G., Pairaud, I., Rimmelin, P., Claquin, P., Jacqueline, F., Lefebvre, A., Facq, J.V., Retho, M., Verney, R., 2019. National observation infrastructure: an example of a fixed-plateforms network along the French Coast: COAST HF. Oceans, 1-6. https://doi.org/ 10.1109/OCEANSE.2019.8867451.

Roland, A., Ardhuin, F., 2014. On the developments of spectral wave models: numerics and parameterizations for the coastal ocean. Ocean Dyn., 64(6), 833-846. https://doi.org/10.1007/s10236-014-0711-z.

Rossignol-Strick, M., 1985. A marine anoxic event on the Brittany coast, July 1982. *J. Coast. Res.*, 11-20. https://www.jstor.org/stable/4297005.

Salomon, J.-C., Breton, M., 1991. Courants résiduels de marée dans la Manche. Oceanologica Acta, Special issue. 11, 47-53.

Salomon, J.C., Breton, M., 1991. Courants résiduels de marée dans la Manche. *Oceanol. Acta, Special issue*.

Schulz, E., Grasso, F., Le Hir, P., Verney, R., Thouvenin, B., 2018. Suspended sediment dynamics in the macrotidal Seine Estuary (France): 2. Numerical modeling of sediment fluxes and budgets under typical hydrological and meteorological conditions. J. Geophys. Res. Oceans, 123(1), 578-600. https://doi.org/10.1002/2017JC013185.

Simon, A., Poppeschi, C., Plecha, S., Charria, G., Russo, A., 2023. Coastal and regional marine heatwaves and cold-spells in the Northeast Atlantic. *EGUsphere*, *2023*, 1-25.

Soulsby, R. L., Hamm, L., Klopman, G., Myrhaug, D., Simons, R.R., Thomas, G.P., 1993. Wave-current interaction within and outside the bottom boundary layer. Coastal engineering, 21(1-3), 41-69.

Stephenson, D., 2008. Definition, diagnosis, and origin of extreme weather and climate events. Clim. extremes soc., 340, 11-23.

Tavora, J., Salama, M., Penning de Vries, M., Mannaerts, C. M., van der Wal, D., 2023. Detecting the Effects of Extreme Events on Estuarine Suspended Particulate Matter Using Satellite Remote Sensing (Scheldt Estuary): Challenges and Opportunities. Remote Sens., 15(3), 670. https://doi.org/10.3390/rs15030670.

Uncles, R. J., Stephens, J. A., 1989. Distributions of suspended sediment at high water in a macrotidal estuary. J. Geophys. Res.Oceans, 94(C10), 14395-14405.

Verney, R., Le Berre, D., Repecaud, M., Bocher, A., Poppeschi, C., Grasso, F., 2023. Suspended particulate matter dynamics at the interface between an estuary and its adjacent coastal sea: unravelling the impact of tides, waves and river discharge from 2015-2022 *in situ* high-frequency observations. Marine Geology.

Warner, J.C., Butman, B., Soupy Dalyander, P., 2008. Storm-driven sediment transport in Massachusetts bay. Cont. Shelf Res., 28, 257-282. https://doi.org/10.1016/j.csr.2007.08.008.

Wilson, R.J., Heath, M.R., 2019. Increasing turbidity in the North Sea during the 20th century due to changing wave climate. Ocean Sci., 15(6), 1615-1625. https://doi.org/10.5194/os-15-1615-2019.

Yasuhara, M., Zhang, J. (2018). Declining oxygen in the global ocean and coastal waters. Science, 359(6371), eaam7240. https://doi.org/10.1126/science.aam7240.

7 Appendix

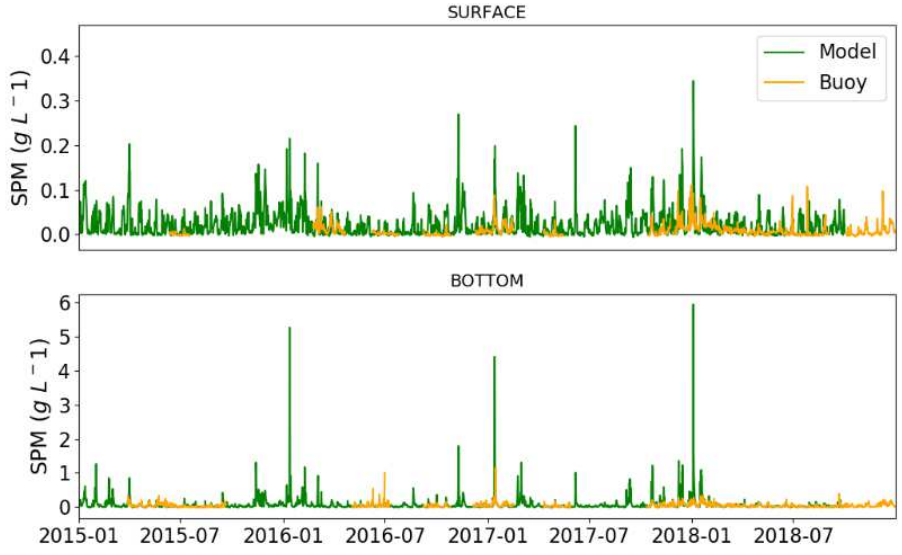

1048

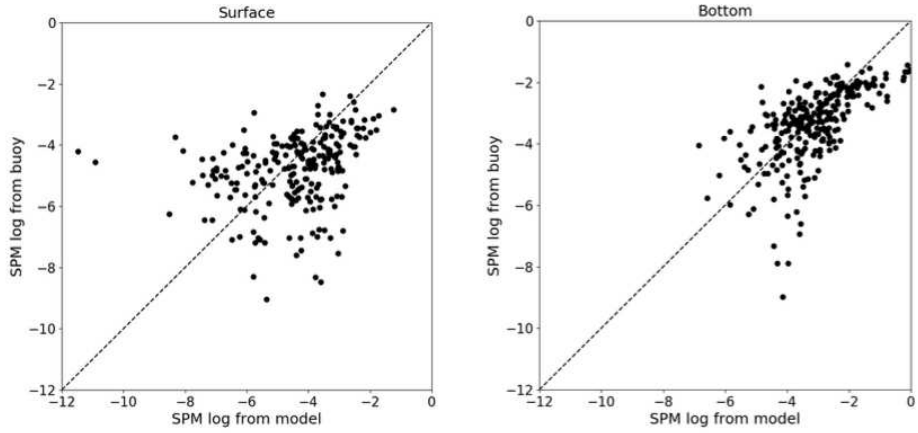

1049
1050
1051 Figure S1. Validation of SPM data from the model via surface and bottom observations from
1052 the SCENES buoy
1053

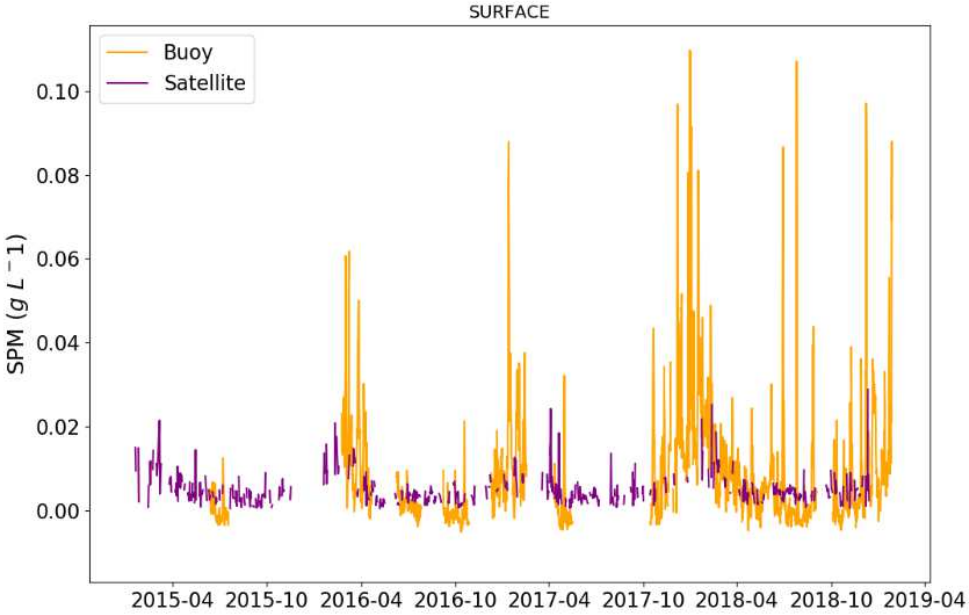

Figure S2. Validation of SPM data from the satellite MODIS via surface observations from the SCENES buoy

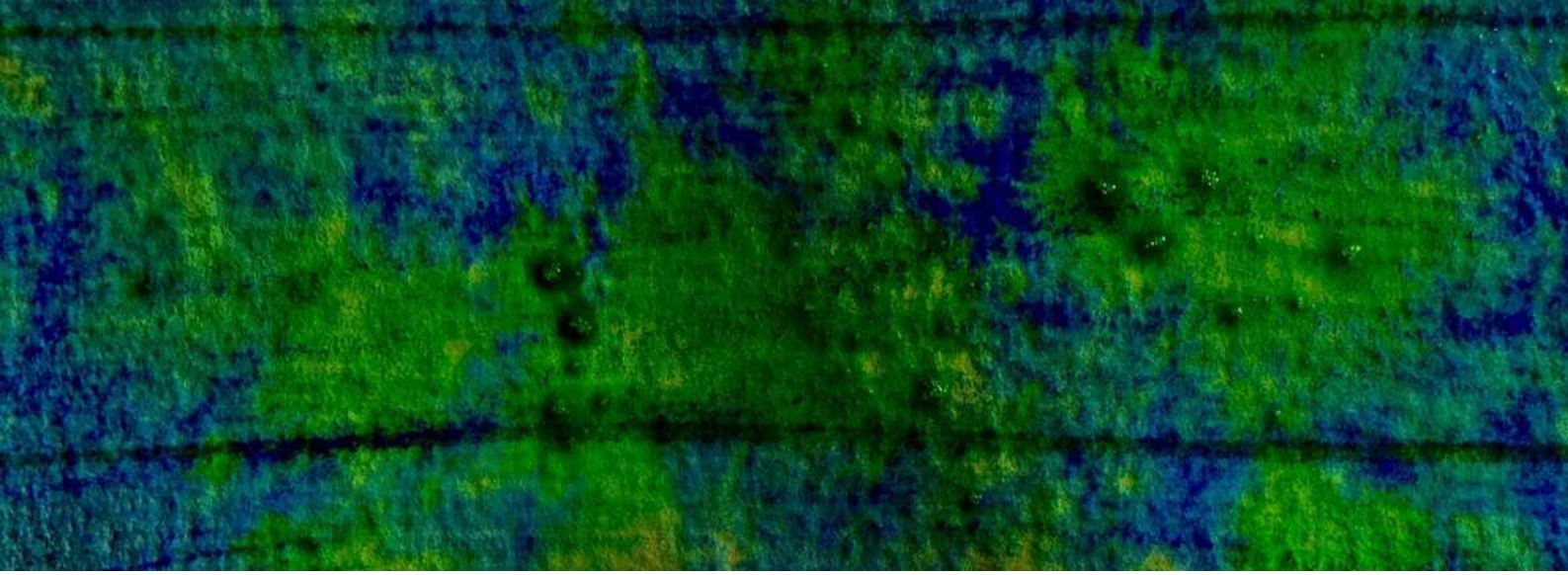

Chapitre 6 Évolution de l'initiation de la période productive du phytoplancton en zone côtière face aux évènements extrêmes

Dans ce chapitre, le compartiment de l'écosystème lié au vivant est exploré au travers de la biogéochimie. L'impact des EE sur la biomasse phytoplanctonique est analysé. L'effet cumulé des vagues marines de froid, des crues et des rafales de vent sont explorés en baie de Vilaine et en rade de Brest.

6.1 Résumé

L'étude se concentre sur les processus induisant des variations interannuelles dans l'initiation de la période productive du phytoplancton (IPGP - Initiation of Phytoplankton Growing Period) au début du printemps. L'IPGP est spécifiquement détaillée dans deux écosystèmes côtiers tempérés contrastés sous l'influence de rivières riches en nutriments : la rade de Brest et la baie de Vilaine. Dans ces deux écosystèmes côtiers, une grande variabilité interannuelle de l'IPGP est observée, influencée par la température de la mer, les apports fluviaux, la disponibilité de la lumière (modulée par le rayonnement solaire et la turbidité de l'eau), le mélange turbulent généré par les courants de marée, le vent et les courants induits par les panaches des fleuves.

La mise en place d'un modèle vertical unidimensionnel couplant l'hydrodynamique, la biogéochimie et la dynamique des sédiments, permet de tester plusieurs scénarios d'EE et d'estimer leur dominance sur l'IPGP. L'effet cumulé des EE est également exploré.

Le résultat principal de cette étude est que l'IPGP est retardé d'environ 30 jours dans l'espace d'une décennie (2010 à 2019) dans les deux baies. Les observations et le modèle montrent que l'IPGP ne dépend généralement pas d'un facteur environnemental spécifique mais de l'interaction entre plusieurs facteurs environnementaux. Dans ces deux baies, l'IPGP est principalement liée à la température de la surface de la mer et aux conditions de lumière disponible, contrôlées par la turbidité du système avant les premières efflorescences algales. Bien que l'étude soit réalisée dans deux environnements hydrodynamiquement contrastés, les processus qui modulent l'IPGP sont similaires. L'IPGP réagit aux événements extrêmes tels que

les vagues marines de froid et les crues à la fin de l'hiver. Si ces événements extrêmes durent plusieurs jours, un retard de l'IPGP est alors observé. L'effet cumulé des paramètres environnementaux jouant sur l'IPGP, via l'utilisation du modèle numérique, est mis en évidence.

Ce travail a fait l'objet d'une publication dans le journal Biogeosciences en 2022 (https://doi.org/10.5194/bg-19-5667-2022) et les détails de l'étude sont présentés dans la partie suivante.

6.2 Article : Interannual variability of the initiation of the phytoplankton growing period in two French coastal ecosystems

Biogeosciences, 19, 5667–5687, 2022
https://doi.org/10.5194/bg-19-5667-2022

Biogeosciences Open Access EGU

Interannual variability of the initiation of the phytoplankton growing period in two French coastal ecosystems

Coline Poppeschi[1], Guillaume Charria[1], Anne Daniel[2], Romaric Verney[3], Peggy Rimmelin-Maury[4], Michaël Retho[5], Eric Goberville[6], Emilie Grossteffan[4], and Martin Plus[2]

[1]Ifremer, Univ. Brest, CNRS, IRD, Laboratory for Ocean Physics and Satellite remote sensing (LOPS), IUEM, 29280 Brest, France
[2]Ifremer, DYNECO, Pelagic Ecology Laboratory (PELAGOS), 29280 Brest, France
[3]Ifremer, DYNECO, Hydrosedimentary Dynamics Laboratory (DHYSED), 29280 Brest, France
[4]OSU-European University Institute of the Sea (IUEM), UMS3113, 29280 Plouzané, France
[5]Ifremer, Morbihan-Pays de Loire Environment Resources Laboratory (LERMPL), 56100 Lorient, France
[6]Unité Biologie des Organismes et Ecosystèmes Aquatiques (BOREA), Muséum National d'Histoire Naturelle, CNRS, IRD, Sorbonne Université, Université de Caen Normandie, Université des Antilles, Paris, France

Correspondence: Coline Poppeschi (coline.poppeschi@ifremer.fr)

Received: 29 March 2022 – Discussion started: 14 April 2022
Revised: 14 November 2022 – Accepted: 16 November 2022 – Published: 14 December 2022

Abstract. Decadal time series of chlorophyll *a* concentrations sampled at high and low frequencies are explored to study climate-induced impacts on the processes inducing interannual variations in the initiation of the phytoplankton growing period (IPGP) in early spring. We specifically detail the IPGP in two contrasting coastal temperate ecosystems under the influence of rivers highly rich in nutrients: the Bay of Brest and the Bay of Vilaine. In both coastal ecosystems, we observed a large interannual variation in the IPGP influenced by sea temperature, river inputs, light availability (modulated by solar radiation and water turbidity), and turbulent mixing generated by tidal currents, wind stress, and river runoff. We show that the IPGP is delayed by around 30 d in 2019 in comparison with 2010. In situ observations and a one-dimensional vertical model coupling hydrodynamics, biogeochemistry, and sediment dynamics show that the IPGP generally does not depend on one specific environmental factor but on the interaction between several environmental factors. In these two bays, we demonstrate that the IPGP is mainly caused by sea surface temperature and available light conditions, mostly controlled by the turbidity of the system before first blooms. While both bays are hydrodynamically contrasted, the processes that modulate the IPGP are similar. In both bays, the IPGP can be delayed by cold spells and flood events at the end of winter, provided that these extreme events last several days.

1 Introduction

Although studied for 70 years (Sverdrup, 1953), the optimal conditions that trigger the initiation of phytoplankton growing period (IPGP) in ocean waters in early spring are not well understood (Sathyendranath et al., 2015). Three main theories are proposed to date: the critical depth hypothesis (Sverdrup, 1953), the critical turbulence hypothesis (Huisman et al., 1999), and the disturbance-recovery hypothesis (Banse, 1994; Behrenfeld, 2010; Behrenfeld et al., 2013). For Sverdrup (1953), phytoplankton blooms occur when the surface mixed layer shoals to a depth shallower than the critical depth, according to light conditions. While Huisman et al. (1999) agreed with Sverdrup, they proposed that relaxation of turbulent mixing allows the bloom to develop if it occurs below a critical turbulence rate. Behrenfeld (2010) observed blooms in the absence of spring mixed layer shoaling and declared that the initiation of bloom is controlled by a balance between phytoplankton growth and grazing rate and suggested a seasonal control of this balance by physical processes. No consensus emerges among these hypotheses – es-

Published by Copernicus Publications on behalf of the European Geosciences Union.

pecially because most of these concepts have been defined at specific temporal and spatial scales (Caracciolo et al., 2021; Chiswell et al., 2015), and the debate is still open, in particular due to the use of more efficient models, the availability of new observations, and the ensuing collection of large in situ datasets (Boss and Behrenfeld, 2010; Rumyantseva et al., 2019). Coastal waters remain highly dynamic and productive ecosystems at the interface between land and sea and are distinguished from the waters of the open sea (Gohin et al., 2019; Liu et al., 2019). Because coastal systems are directly influenced by anthropogenic inputs from rivers, no nutrient limitation is observed in late winter. A myriad of factors and mechanisms can then affect the IPGP in coastal areas (Townsend et al., 1994; Cloern, 1996), but the incident light at the air–sea interface (Glé et al., 2007) and sea surface temperature (SST) (Trombetta et al., 2019) are regarded as the main forcings. Low water turbidity also plays an important role and allows deeper light penetration (Iriarte and Purdie, 2004). This occurs in low vertical mixing conditions in shallow waters (Ianson et al., 2001), i.e. limited advective exchanges, weak wind (Tian et al., 2011), neap tide (Ragueneau et al., 1996), and in the absence of flooding events (Peierls et al., 2012). Depending on the morphology and hydrodynamics of coastal zones (estuaries, bays, lagoons), the importance of controlling factors can be variable (Cloern, 1996). Temporal variation in the IPGP is of great importance in coastal ecosystems because it impacts not only phytoplankton by changing species composition or the succession of species (Ianson et al., 2001; Edwards and Richardson, 2004; Chivers et al., 2020) but also several other biological compartments, such as zooplankton and fish, by species replacements (Sommer et al., 2012).

By amplifying or modifying environmental forcings, it is now well-documented that global climate change may influence the IPGP in coastal areas (Smetacek and Cloern, 2008; Barbosa et al., 2010; Paerl et al., 2014; IPCC, 2021). Heat waves – as opposed to cold spells – have become more frequent in recent years and can advance or delay the IPGP (Gomez and Souissi, 2008). Wind storms, by inducing vertical mixing and sediment resuspension, can have a significant effect on water turbidity, which in turn limits light penetration and therefore influences the IPGP. Floods, following heavier rainfall, may increase continental erosion and ultimately nutrient inputs to coastal ecosystems. Because coastal ecosystems are strongly influenced by human activities such as changes in land use, quantifying the contribution related to long-term climate-induced signals is challenging (Kromkamp and Van Engeland, 2010).

Our study is based on two geographically close, but hydrodynamically different, nearshore ecosystems: (1) the Bay of Brest, a shallow semi-enclosed bay with well-mixed waters (Le Pape and Menesguen, 1997), and (2) the Bay of Vilaine, a shallow open bay with long water residence times (Chapelle et al., 1994). These two coastal ecosystems are strongly impacted by anthropogenic pressures, such as intensive agriculture (Ragueneau et al., 2018; Ratmaya et al., 2019), which induces highly rich nutrient waters.

In this study, we aim to better understand interannual local changes in the IPGP in coastal temperate ecosystems in the current context of global climate change over the last 20 years. As most studies dealing with the IPGP are mainly based on discrete water sampling (Iriarte et al., 2004; Tian et al., 2011) or modelling (Townsend et al., 1994; Philippart et al., 2010), we focus here on the use of long-term high-frequency observations to assess interannual variability of the IPGP and to identify the triggering and controlling factors. We detect and analyse the temporal variability of the IPGP and quantify how environmental forcings influence its dynamics. To detect and analyse the IPGP in coastal environments, we develop a numerical framework that combines high-frequency decadal in situ observations and a one-dimensional vertical (1DV) hydro-sedimentary and biogeochemical coupled numerical model. The potential impact of hydro-meteorological extreme events, such as cold spells, flood events, and wind bursts, on the IPGP is then investigated.

2 Data and methods

2.1 Study areas

Our study focuses on two northwestern French coastal temperate ecosystems located in the Bay of Biscay: the Bay of Brest and the Bay of Vilaine, two ecosystems impacted by excessive nutrient inputs from watersheds but exposed to different hydrodynamic conditions.

The Bay of Biscay is a region with a complex system of coastal currents influenced by the combined effects of seasonal wind regimes and important river discharges modulated by large-scale gyre circulation patterns (Isemer and Hasse, 1985; Pingree and Le Cann, 1989; Lazure and Jégou, 1998; Lazure et al., 2006; Lazure and Dumas, 2008; Ferrer et al., 2009; Le Boyer et al., 2013; Charria et al., 2013). In the Iroise Sea, at spring tide close to the islands and capes, tidal currents can reach $4\,m\,s^{-1}$ (Muller et al., 2010). This tidal circulation combined with meteorological forcings and sharp thermal gradients generates a strongly variable local circulation. In the vicinity of the Loire estuary, the freshwater discharges in the surface layers induce important density gradients driving a poleward circulation (about $10\,cm\,s^{-1}$) modulated by wind forcings (Lazure and Jégou, 1998; Lazure et al., 2006). The river plumes can propagate towards the southwest under specific conditions.

Under these hydrodynamic conditions, the Bay of Brest is a semi-enclosed bay ($180\,km^2$) with 50 % of the surface shallower than 5 m depth. The bay is connected with the Atlantic Ocean (Iroise sea) through a narrow and shallow strait. Tidal variation reaches 8 m during spring tides, which represents an oscillating volume of 40 % of the high tide volume.

Freshwater inputs come from the Aulne River (catchment area 1875 km^2, mean river flow 26 $m^3 s^{-1}$) and two smaller rivers: the Elorn (catchment area 385 km^2, mean river flow 6 $m^3 s^{-1}$) and the Mignonne (catchment area 111 km^2, mean river flow 1.5 $m^3 s^{-1}$). Due to the macrotidal regime, associated with a strong vertical mixing, the high nitrate concentrations do not generate important green tides (Le Pape et al., 1997). Strong decreases in the Si : N and Si : P ratios did not exhibit dramatic phytoplankton community shifts from diatoms to non-siliceous species in spring (Del Amo et al., 1997) because of the high Si recycling (Ragueneau et al., 2002; Beucher et al., 2004).

The Bay of Vilaine is a mesotidal open bay (69 km^2) under the influence of the Vilaine (catchment area 10 500 km^2, mean river flow 70 $m^3 s^{-1}$) and the Loire (catchment area 117 000 km^2, mean river flow 850 $m^3 s^{-1}$) river discharges, with tidal ranges varying between 4 and 6 m (Merceron, 1985). The Loire River plume tends to spread northwestward, with a dilution of 20- to 100-fold by the time it reaches the Bay of Vilaine (Ménesguen et al., 2018). The Vilaine River plume tends to spread throughout the bay before moving westward (Chapelle et al., 1994). The water residence time varies seasonally between 10 and 20 d (Chapelle et al., 1994). The water circulation is mainly driven by tides, winds and river flows (Lazure and Jegou, 1998). This bay is well known as one of the European Atlantic coastal ecosystems most sensitive to eutrophication (Ménesguen et al., 2019). The Bay of Vilaine has undergone eutrophication over recent decades mainly due to high nutrient inputs from the Vilaine and Loire rivers (Rossignol-Strick, 1985; Ratmaya et al., 2019).

2.2 In situ observations

COAST-HF-Iroise (Rimmelin-Maury et al., 2020) and COAST-HF-Molit (Retho et al., 2022) are two high-frequency monitoring buoys of the French national observation network COAST-HF[1] (Répécaud et al., 2019; Farcy et al., 2019; Cocquempot et al., 2019; Poppeschi et al., 2021) located, respectively, in the Bay of Brest (48.357° N, 4.582° W) and in the Bay of Vilaine (47.434° N, 2.660° W) (Fig. 1). COAST-HF-Iroise has been operating in the strait between the Bay of Brest and the Iroise sea since 2000. The COAST-HF-Molit buoy has been sampling the plume of the Vilaine River since 2008. Buoys are deployed during the whole year except for COAST-HF-Molit, which is only available for part of the year prior to 2018 (from mid-February to early September, i.e. from day 50 to 250 for the period 2008–2017). Depending on the tide, the depth at the mooring sites ranges from 11 to 17 m for both COAST-HF buoys. Environmental parameters (SST, salinity, turbidity, dissolved oxygen, and Chl *a* fluorescence) are measured at 1 to 2 m below the surface every 20 min (COAST-HF-Iroise) or every hour (COAST-HF-Molit). The Chl *a* fluorescence, a proxy for phytoplankton biomass (FFU units), is measured by a Turner CYCLOPS-7 sensor (precision ± 5 %).

Sub-surface Chl *a* concentrations are provided by two French marine monitoring networks, the SOMLIT coastal observation network and the REPHY (French Observation and Monitoring programme for Phytoplankton and Hydrology in coastal waters).[2] Samples are collected bimonthly at the SOMLIT-Brest (48.358° N, 4.552° W) and the REPHY-Loscolo (47.496° N, 2.445° W) stations, which are close to the COAST-HF stations. Chl *a* concentrations are measured with either spectrophotometric or fluorimetric methods (Aminot and Kérouel, 2004).

Daily river flows are measured at gauging stations (French hydrology Banque Hydro database[3]), located close to the main river mouths (Aulne-Gouezec (48.205° N, 4.093° W), Loire-Montjean (47.106° N, 1.78° W)). The Vilaine River flow is controlled by a dam, and data are provided by the Vilaine Public Territorial Basin Organization (Fig. 1).[4]

The tide gauge stations (Shom[5]) at Brest (48.382° N, 4.495° W) and Crouesty (47.542° N, 2.895° W) record the sea level every minute.

Precipitation, air temperature, wind direction and intensity, and the solar flux data are retrieved every 6 min from two meteorological stations from the Météo-France observation network:[6] Guipavas (48.440° N, 4.410° W) and Vannes-Séné (47.362° N, 2.425° W) (Fig. 1). We use the solar flux as a proxy for subsurface PAR (photosynthetically available radiation).

2.3 MARS3D-1DV modelling experiments

2.3.1 MARS3D-1DV model

A 1DV (one-dimensional vertical) model configuration is implemented to simulate changes in biogeochemical variables due to hydrodynamics and sediment dynamics in both bays.

The hydrodynamical model is based on the code developed for MARS3D (3D hydrodynamics Model for Applications at Regional Scale; Lazure and Dumas, 2008). This model is a primitive equation model with a free surface and uses the Boussinesq and hydrostatic pressure assumptions. We use the 1DV configuration of the model, with 10 vertical sigma levels for 15 m depth and a time step of 30 s.

The sediment model (MUSTANG – Le Hir et al., 2011; Grasso et al., 2015; Mengual et al., 2017) is designed to sim-

[1] http://www.coast-hf.fr, last access: 20 March 2022, data available at https://www.coriolis-cotier.org, last access: 20 March 2022.

[2] For the SOMLIT network, see https://somlit.fr, last access: 20 March 2022. For the REPHY programme, see https://doi.org/10.17882/47248.

[3] https://www.hydro.eaufrance.fr/, last access: 20 March 2022

[4] https://www.eptb-vilaine.fr/, last access: 20 March 2022.

[5] http://data.shom.fr, last access: 20 March 2022.

[6] https://donneespubliques.meteofrance.fr/, last access: 20 March 2022.

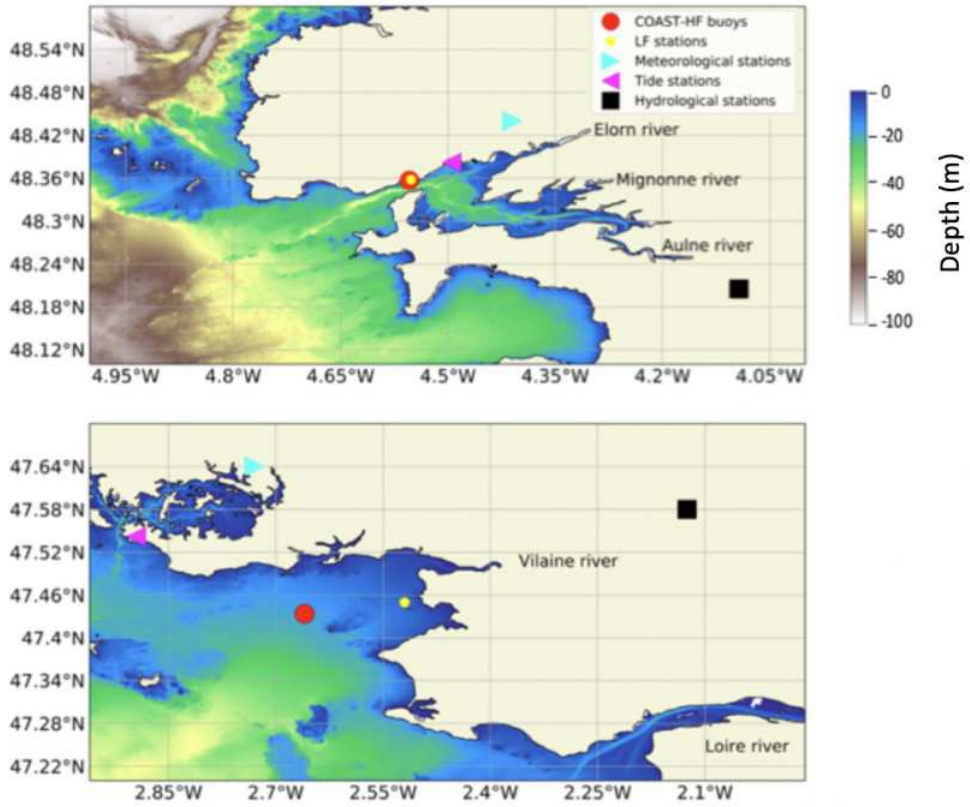

Figure 1. Location of the sampling sites: COAST-HF-Iroise and COAST-HF-Molit buoys (red circles); SOMLIT-Brest and REPHY-Loscolo sampling stations (yellow circles); Brest and Crouesty tide gauge stations (blue triangles); Guipavas and Vannes-Séné meteorological stations (purple triangles); hydrological stations of the Aulne and Vilaine rivers (black squares), with the Loire station off the map.

ulate the transport and changes in different sediment mixtures. In the sediment, 50 layers (refined near the surface) for a total thickness of 40 cm are implemented. Four sediment classes are considered: muds (diameter 10 µm), fine sand (diameter 100 µm), medium sand (diameter 200 µm), and coarse sand (diameter 400 µm). The sediment dynamics (transport in the water column, exchanges at the water–sediment interface, erosion/deposition processes) are driven by an advection/dispersion equation for each sediment class (refer to Le Hir et al., 2011, for a detailed description of the sediment model).

The biogeochemical model BLOOM (BiogeochemicaL cOastal Ocean Model) is derived from the ECO-MARS model (Cugier et al., 2005; Ménesguen et al., 2019) adding major processes of early diagenesis. Nitrogen, phosphorus, and silica cycles are studied considering four nutrients: nitrate, ammonium, soluble reactive phosphorus, and silicic acid (sorption/desorption of phosphate on suspended sediment and precipitation/dissolution of phosphate with iron processes are also included). The model is also represented by three phytoplankton classes (microphytoplankton, dinoflagellates, pico-nano-phytoplankton), two zooplankton classes (micro- and meso-zooplankton), and exchanges at the water–sediment interface and inside the sediment compartment.

2.3.2 MARS3D-1DV model sensitivity experiments

These three models (hydrodynamical, sediment, and biogeochemical) are coupled online during simulations and allow the nutrient and phytoplankton dynamics in both bays to be reproduced. The simulation for the Bay of Brest does not include nutrient inputs from the sediment because they are considered to be negligible around the COAST-HF-Iroise station.

Dissolved and particulate variables are defined in the water column and in the sediment. Initial values for both bays are uniform over the initial vertical profile (Table 1) and are based on a 3D realistic coupled simulation during the year 2015. Values for the 15 February are extracted at the position of COAST-HF-Iroise for the Bay of Brest and at the position of the COAST-HF-Molit station for the Bay of Vilaine (Plus et al., 2021).

To evaluate the sensitivity of the biogeochemical dynamics to environmental conditions, sensitivity experiments are then performed using the coupled MARS3D/BLOOM/MUSTANG 1DV model configuration.

Table 1. Initial conditions in the water column for the MARS-1DV model for the beginning of the simulation on the 15 February.

Parameters	Bay of Brest	Bay of Vilaine
Dissolved O_2 ($mg\,L^{-1}$)	9	10
Mesozooplankton ($\mu molN\,L^{-1}$)	0.05	0.1
Microzooplankton ($\mu molN\,L^{-1}$)	0.05	0.05
Dinoflagellates ($\mu molN\,L^{-1}$)	0.05	0.1
Diatoms ($\mu molN\,L^{-1}$)	0.5	0.5
Soluble reactive phosphorus ($\mu mol\,L^{-1}$)	0.5	0.8
Silicic acid ($\mu mol\,L^{-1}$)	10	30
Nitrate ($\mu mol\,L^{-1}$)	16	30
Ammonium ($\mu mol\,L^{-1}$)	0.5	0.25
Coarse sand ($g\,L^{-1}$)	0	0
Fine sand ($g\,L^{-1}$)	0	0
Mud ($g\,L^{-1}$)	0.03	0.05

All simulations are started at the end of winter (15 February) and run until the end of the year. The range of values used in the sensitivity experiments are derived from the minimum and maximum observed in situ data. Each parameter is tested with a constant value for the whole simulation.

Three parameters are individually explored in both bays:

- The air temperature in sensitivity experiments ranges from 4 to 14 °C and is controlled by the intensity of solar radiations. Air temperature represents the main controlling parameter of SST in the 1DV model. This parameter drives the radiative fluxes in the model and then constrains SST.
- Wind intensity effect on the IPGP is explored for values between 0 and $10\,m\,s^{-1}$. In the 1DV model, wind is a source of vertical mixing in the simulation.
- The cloud coverage (CC) sensitivity experiments ranged in value between 0 % CC and 100 % CC. This parameter is a driver of photosynthetic available radiation (PAR) in the ocean. For the formulation of radiative fluxes in the 1DV MARS3D model, 100 % cloud coverage allows an inflow of 38 % of the total solar radiation into the water column. Each individual experiment is associated with a constant CC applied to the seasonal solar radiation.

In the Bay of Vilaine, the sediment plays a role in light penetration and acts as an active source of nutrients: we therefore explored the influence of mud erosion rate (values between 2.10^{-5} and $2.10^{-7}\,kg\,m^{-2}\,s^{-1}$) in that bay (sand erosion rate fixed to $0.0001\,kg\,m^{-2}\,s^{-1}$). For the sensitivity experiments, it drives a mass of sediment that is eroded and resuspended and a bottom input of nutrients in the water column.

A second set of experiments is conducted by combining the individual effect of environmental parameters in order to explore possible cumulative or opposite effects on the IPGP. The upper and lower bounds of the range of environmental parameters are taken into account. Experiments are detailed in Table 5.

2.4 Data processing

2.4.1 Chl *a* fluorescence data

To analyse high-frequency time series of in situ Chl *a* fluorescence, the quenching effect (Lehmuskero et al., 2018) – a decrease in fluorescence in the presence of light (Fig. 2) – is removed by analysing only nighttime data, as reported in Carberry et al. (2019). Chl *a* fluorescence data are studied on a daily basis, i.e. averaged from 22:00 to 05:00. Years with less than 75 % of valid data are not considered in our analyses: for the Bay of Brest, these are the years 2005, 2006, 2008, 2009, and 2018.

2.4.2 Detection of the IPGP

On the basis of the literature, we first apply three methods to determine the annual IPGP dates:

1. set an arbitrary beginning and end of the phytoplankton growing period at 20 % and 80 % of the cumulative Chl *a* fluorescence measured from 1 January to 31 December (Kromkamp et al., 2010),
2. consider a threshold of 5 % above the yearly median chlorophyll (Brody et al., 2013),
3. consider the beginning of the growing period as the maximum daily difference in Chl *a* fluorescence (Philippart et al., 2010).

Because none of these methods allowed us to obtain a valid IPGP detection – with too late (method 1) or too early (method 2) a detection or multiple IPGP dates (method 3) – we elaborate on a detection method based on discontinuities of the Chl *a* fluorescence signal (Fig. 3): daily FFU slopes

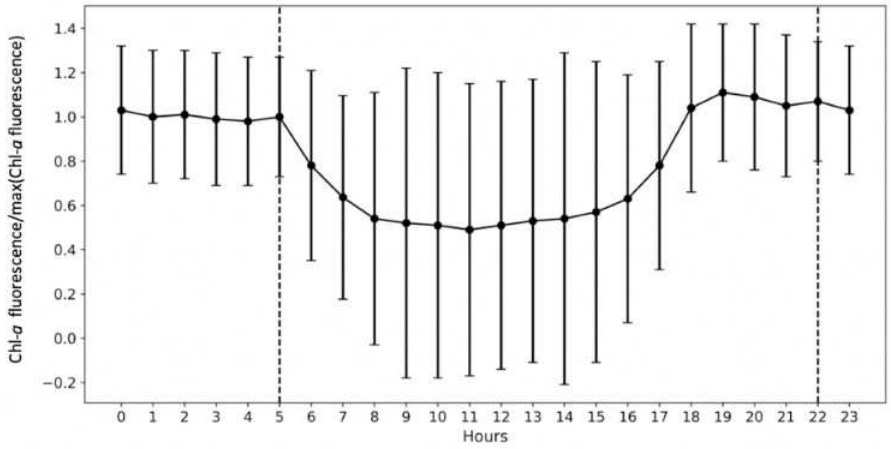

Figure 2. The importance of the quenching effect on Chl *a* fluorescence is represented by COAST-HF-Iroise data from 2000 to 2019. The standard deviation is represented by vertical black bars. The dashed lines represent the beginning and end of the selected values for the rest of the study from 22:00 to 05:00.

are calculated based on a linear regression over a ± 2 d window for each day, from 1 January to 31 December, and each year. The IPGP date is identified when the slope exceeds a threshold value – defined as the median of the daily slopes – for the first time in the year for at least 20 d. The end of the phytoplankton growing period is determined when the slope stabilizes below the threshold for at least 20 d for the last time in the year. The cumulative Chl *a* fluorescence corresponds to the duration of the growing period.

2.4.3 Pattern of the phytoplankton growing period

The *k*-means method (Hartigan and Wong, 1979) is used to characterize the annual patterns of the phytoplankton growing period.

We exclude the year 2013 from the analysis of the Bay of Vilaine because of a large number of missing data. When the interval over which consecutive data are missing is no longer than 1 week, we perform a linear interpolation to replace the missing data. A 5 d running average is applied to the Chl *a* fluorescence signal, and data are then normalized by the maximum value. We analyse Chl *a* fluorescence every year for 150 d after the IPGP.

Time series from both bays are merged before application of the *k*-means and the number of clusters (or centroids) is set to two to distinguish the dominant patterns of the phytoplankton growth period at both sites. The use of a larger number of clusters is investigated and does not produce a pattern representing a large number of observed growing periods.

2.4.4 Detection of extreme events

The peak over threshold method (see Oliver et al., 2018, and Poppeschi et al., 2021, for further details) is used to detect hydro-meteorological extreme events such as cold spells, flood events, and wind bursts. An event is regarded as extreme if values are higher than a given statistical threshold for at least 3 consecutive days. In the present study, the 90-percentile threshold is selected to detect floods and wind bursts, and the 10-percentile threshold is used to detect cold spells. Seasonal anomalies are calculated over at least 20 years, by subtracting raw data from the winter average value (for cold spells) or from the spring average value (wind bursts and floods).

3 Results

3.1 Characterization of the phytoplankton growing period

The high-frequency Chl *a* fluorescence time series at both sites show an intense seasonal cycle with low values from November to February and high values from March to October (Fig. 4). Focusing on the period from 2010 to 2019 in the Bay of Brest, the minimum Chl *a* fluorescence is observed during the years 2012 and 2013 and does not exceed 7 FFU. In contrast, some years show Chl *a* fluorescence values above 15 FFU but can be up to 20 FFU (such as 2010, 2014, 2015 or 2019). In the Bay of Vilaine, a similar seasonal pattern is observed with higher values reaching 50 FFU in 2013. Small (< 20 FFU) and high (> 35 FFU) Chl *a* fluorescence amplitudes are observed occasionally (in 2014 and 2017 and in 2013 and 2016, respectively). The Chl *a* fluorescence is higher, almost double, in the Bay of Vilaine compared to the Bay of Brest with a mean cumulative Chl *a* fluorescence of around 580 and 360 FFU, respectively (Table 2). The high phytoplankton biomass of the Bay of Vilaine is corroborated by the concentrations measured by low-frequency observation programmes (SOMLIT and REPHY).

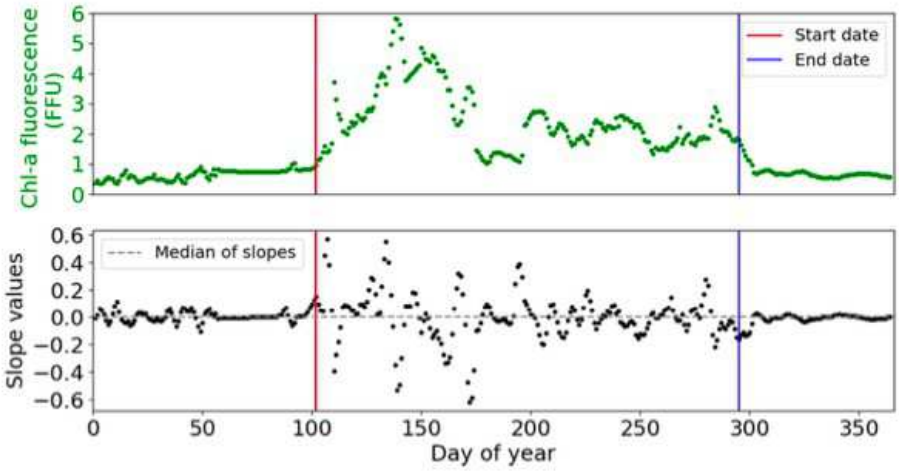

Figure 3. Example of detection of the start (red line) and end (blue line) of the phytoplankton growing period in 2001 at COAST-HF-Iroise. The threshold value – the median of slopes – is represented by a dotted grey line.

Table 2. Global characteristics of the phytoplankton growing period in the Bay of Brest and in the Bay of Vilaine.

	Start date (day of year)	End date (day of year)	Duration (days)	Cumulative Chl *a* fluorescence (FFU)
	Min–median–max	Min–median–max	Min–median–max	Min–median–max
Bay of Brest (2001–2019)	50–69–102	253–274–308	165–200–256	217–364–567
Bay of Vilaine (2011–2019)	53–68–93	218–269–316	165–179–239	276–582–1406

The phytoplankton growing period ranges from approximately 10 March to 30 September in both regions (Table 2). The average duration of the phytoplankton growing period is 179 d in the Bay of Vilaine and 200 d in the Bay of Brest (Table 2). The phytoplankton growing period is characterized by successive blooms, whose number and intensity are variable from year to year (Fig. 4).

The main patterns of the phytoplankton growing period are identified by two clusters (Fig. 5). Cluster 0 includes the phytoplankton growing period with two successive marked blooms in early spring and in summer, the intensity of the second bloom being highly variable. Cluster 1 is characterized by a plateau during the first 2 months of the phytoplankton growing period. Most of the patterns of the Bay of Vilaine are in cluster 0, while those of the Bay of Brest are in cluster 1 (Table 3). The years that stand out in the Bay of Brest (2002, 2010, 2014) correspond to years with the highest cumulative Chl *a* fluorescence (≥ 450 FFU). The atypical years in the Bay of Vilaine (2011, 2017 and 2019) show the lowest cumulative Chl *a* fluorescence (≤ 450 FFU).

3.2 Variability of the initiation of the phytoplankton growing period (IPGP)

Calculations performed to determine the IPGP for high- and low-frequency data yield comparable results (Fig. 6). The mean differences between the IPGP calculated with the high- and low-frequency data are 5 and 8 d for the Bay of Brest and the Bay of Vilaine, respectively. A difference of only 4 and 6 d between the model simulations (reference year: 2015) and the high-frequency in situ data are observed in the Bay of Brest and the Bay of Vilaine, respectively.

A decadal variability of the IPGP is recorded from mid-February to mid-April in both ecosystems (day 50 to day 102 in the Bay of Brest and day 53 to day 93 in the Bay of Vilaine; Fig. 6). In the Bay of Brest, early IPGPs (day < 53) are observed in 2010 and 2013, whereas late IPGPs (day > 93) are observed in 2001, 2017 and 2019. In the Bay of Vilaine, the earliest IPGP is detected in 2012 (day 53) and the latest in 2019 (day 93).

The variability of the IPGP in the Bay of Brest shows two linear trends (Fig. 6a), with a decrease of 52 d from 2001 to 2010 (observed in both high- and low-frequency datasets), followed by an increase (+48 d) from 2011 to 2019, a decline also observed in the Bay of Vilaine (Fig. 6b). Over the period

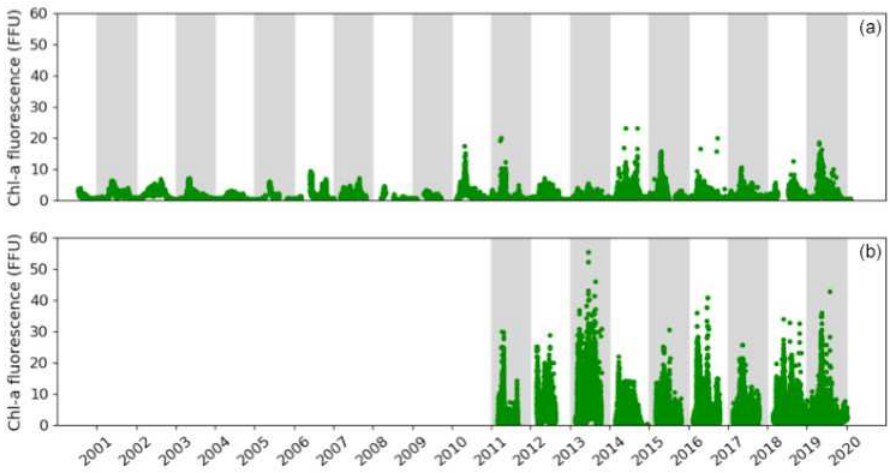

Figure 4. Temporal changes in the in situ Chl *a* fluorescence measured in the Bay of Brest **(a)** and the Bay of Vilaine **(b)**.

Table 3. Cluster group assigned to each annual phytoplankton growing period at both sites. The "–" dash represent years with missing data. The cross represents the year 2013 of the Bay of Vilaine, which was not considered.

Year	2001	2002	2003	2004	2005	2006	2007	2008	2009	2010	2011	2012	2013	2014	2015	2016	2017	2018	2019
Bay of Brest COAST-HF-Iroise	1	0	1	1	–	–	1	–	–	0	1	1	1	0	1	1	1	–	1
Bay of Vilaine COAST-HF-Molit	–	–	–	–	–	–	–	–	–	–	1	0	X	0	0	0	1	0	1

2011–2019, the IPGP is shifted towards a later date by +3.5 d per year in the Bay of Vilaine and +3.7 d per year in the Bay of Brest.

3.3 Analysis of environmental conditions driving the IPGP

3.3.1 Impact of environmental conditions on the IPGP

We next quantify the influence of environmental drivers on the date of the IPGP (Fig. 7). These drivers represent the major limiting factors of the phytoplankton growth and comprise input of nutrients (river flow), PAR (incident light), SST (air temperature, incident light), and turbidity in the water column (river flow, wind intensity, tidal range).

The median values of the environmental drivers observed at the date of each annual IPGP are very close in both bays (Table 4): temperate SST (10 °C), weak wind (3 m s^{-1}), a medium PAR (1360 W m^{-2}), a low turbidity (7 NTU), and a weak tidal amplitude (semi-amplitude of 1.6 m in the Bay of Brest and 0.9 m in the Bay of Vilaine). The IPGP occurs mainly during neap tides at 68 % in the Bay of Brest and 77 % in the Bay of Vilaine. The river flow is low during the IPGP with a runoff of 46 m^3 s^{-1} for the Aulne, 96 m^3 s^{-1} for the Vilaine, and 1196 m^3 s^{-1} for the Loire. These values are considered to be the favourable environmental conditions for this study.

To assess how environmental drivers may impact (i.e. advance or delay) the IPGP, we focus on the 15 d before the mean day of the IPGP (day 68) and of each annual IPGP. The considered 15 d length is related to the typical water residence time in both bays (Frère et al., 2017, and Poppeschi et al., 2021, for the Bay of Brest; Chapelle et al., 1994, and Ratmaya et al., 2019, for the Bay of Vilaine).

The earliest IPGP dates (IPGP < day 55) are associated with earlier occurrence of favourable environmental conditions than the other years. The earliest IPGP in 2010 and 2013 in the Bay of Brest and in 2012 in the Bay of Vilaine occurred before day 55 (Figs. 1f, 7c–2a). Early IPGPs between day 55 to 60, also associated with favourable environmental conditions, are found in 2002 and 2016 in the Bay of Brest (Fig. 1b, j).

The latest IPGP dates (IPGP > day 90) are associated with unfavourable environmental conditions until the date of the IPGP. The latest IPGPs occurring after day 90 are observed in 2001, 2003, 2017, and 2019 in the Bay of Brest and in 2019 in the Bay of Vilaine (Figs. S1a, c, k, l–S2g). For example, the delay detected in 2017 in both bays is due to strong wind and a lack of PAR until the day of the IPGP (Figs. S1k–S2e). Late IPGPs between day 70 to 90 are recorded in 2004, 2007, and 2012 in the Bay of Brest and in 2014, 2017, and 2018 in the Bay of Vilaine (Figs. S1d, e, g, 7d–2e, f).

The interannual variability of the date of the IPGP is therefore not controlled by a unique environmental driver. When

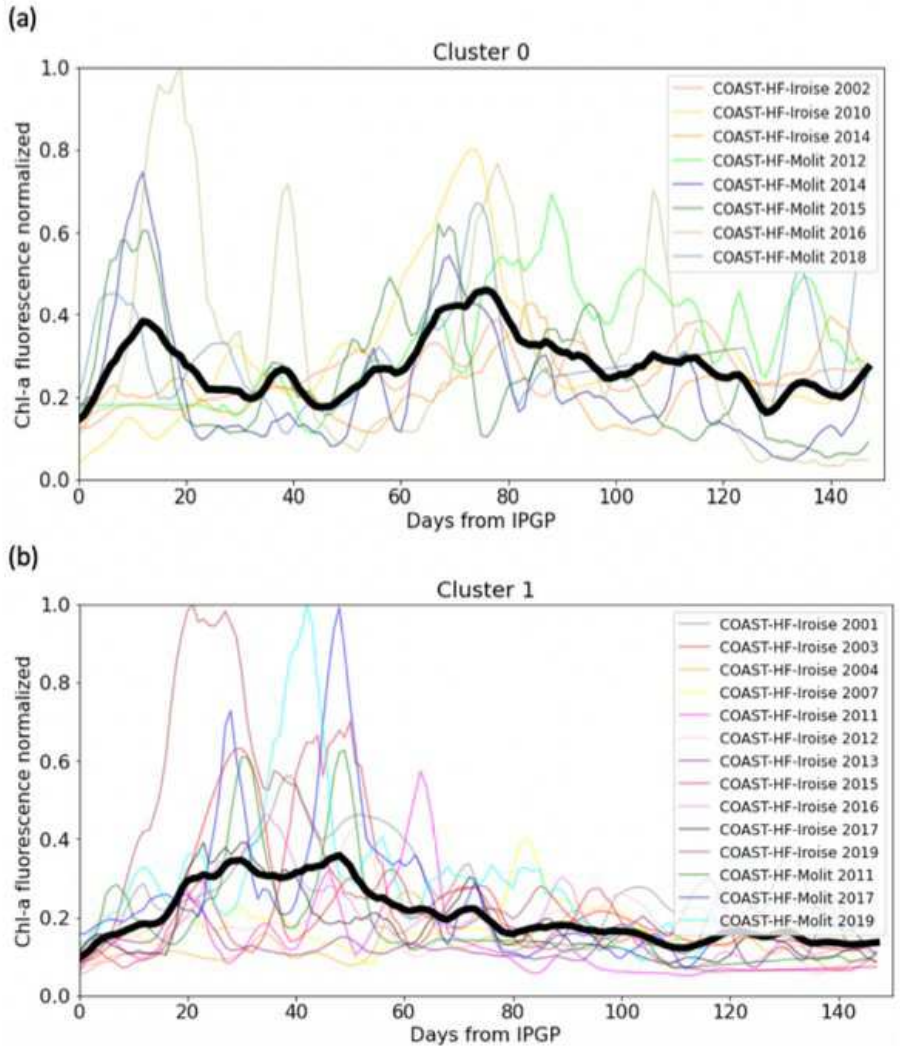

Figure 5. **(a)** Cluster 0 and **(b)** cluster 1 representative of the patterns of the phytoplankton growing period observed in both bays. The median pattern is drawn in bold.

Table 4. Characteristics of environmental drivers at the date of the IPGP except for nutrients from January to March in the Bay of Brest and in the Bay of Vilaine.

	Bay of Brest (2001–2019)	Bay of Vilaine (2011–2019)
	Min–median–max	Min–median–max
River flow ($m^3\ s^{-1}$)	13–46–100	36–96–205
SST (°C)	8–10–12	8–10–11
Wind intensity ($m\ s^{-1}$)	1–3–6	1–3–4
PAR ($W\ m^{-2}$)	915–1373–2220	814–1341–1939
Turbidity (NTU)	1–7–21	0–7–22
Sea level (m)	0.5–1.6–2.9	0.6–0.9–1.6
PO_4 ($\mu mol\ L^{-1}$)	0.1–0.4–0.6	0.1–0.8–1.4
Dissolved inorganic nutrients (DINs; $\mu mol\ L^{-1}$)	8–20–38	25–57–244
$Si(OH)_4$ ($\mu mol\ L^{-1}$)	4–8–16	8–38–112

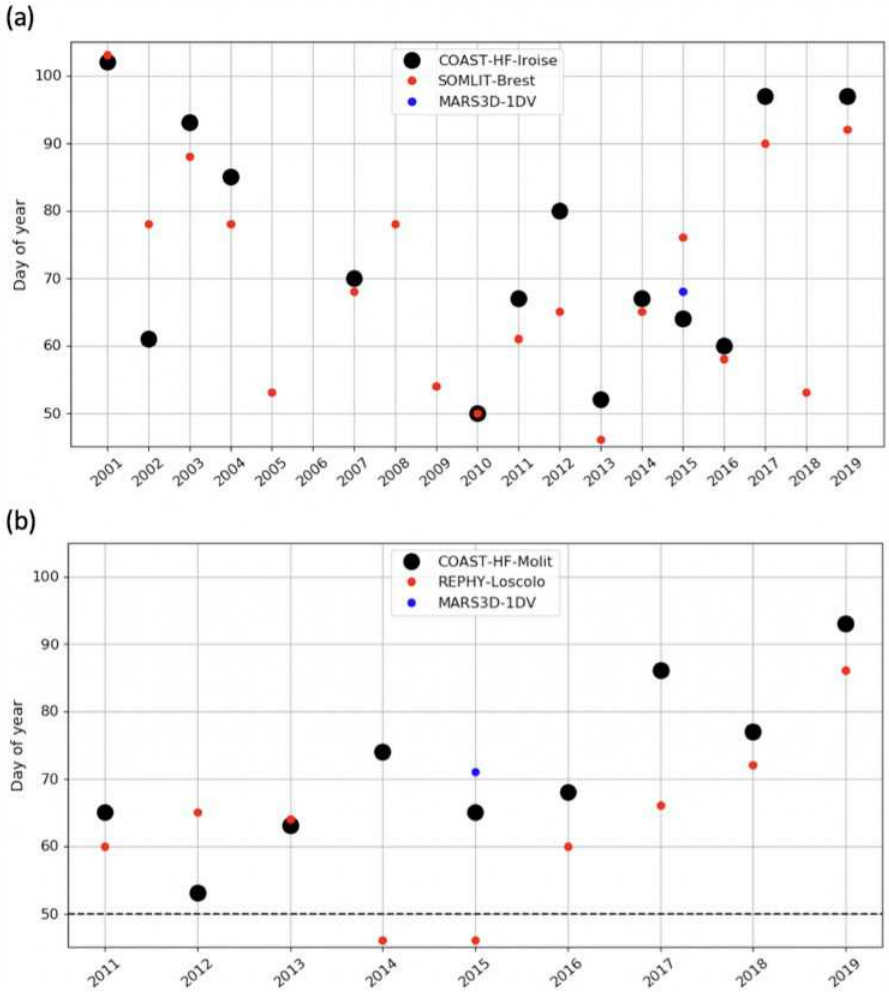

Figure 6. Changes in the IPGP date in **(a)** the Bay of Brest and **(b)** the Bay of Vilaine are determined with high-frequency time series (black circles), low-frequency time series (red circles), and with the model (blue circle). The dotted black line represents the date of the COAST-HF-Molit buoy deployment.

the values of the environmental drivers responsible for the IPGP (Table 4) are compared to the mean values of the environmental drivers over a period of 30 d around the IPGP (Table S1), threshold values are observed in both bays: river flow is lower than usual (between 10 and 30 $m^3 s^{-1}$), temperature is close to the expected value (10 °C), wind is weak (0.5 to 1.5 $m s^{-1}$), PAR is stronger (> 300 $W m^{-2}$), and turbidity is low (about 1.5 NTU). The IPGP starts around day 68 (± 3 d) on average (Fig. 7a, b).

3.3.2 Modelling the importance of the environmental drivers

The relative contribution of each environmental driver on the IPGP is determined by MARS-1DV simulations starting on 1 February (Fig. 8). Environmental drivers tested in the model control the following:

- sea temperature, explored in the model through air temperature (SST proxy),
- the level of water turbulence, through wind intensity,
- the available light, controlled by cloud coverage (CC, as a sea surface PAR proxy) and the erosion rate (turbidity proxy) limiting light penetration in the water column.

Model results show that early IPGPs are associated with an air temperature higher than 9 °C (resulting in SST higher than 8 °C), low wind intensity, weak CC, and low erosion rate. Environmental drivers responsible for early or late IPGPs are similar in both bays. Air temperature is the main driver with a potential deviation from the mean IPGP of 25 d in the Bay of Brest and 40 d in the Bay of Vilaine (Fig. 8). Wind, CC, and erosion rate have a lower impact on the IPGP (around 6 d in the Bay of Brest and 13 d in the Bay of Vi-

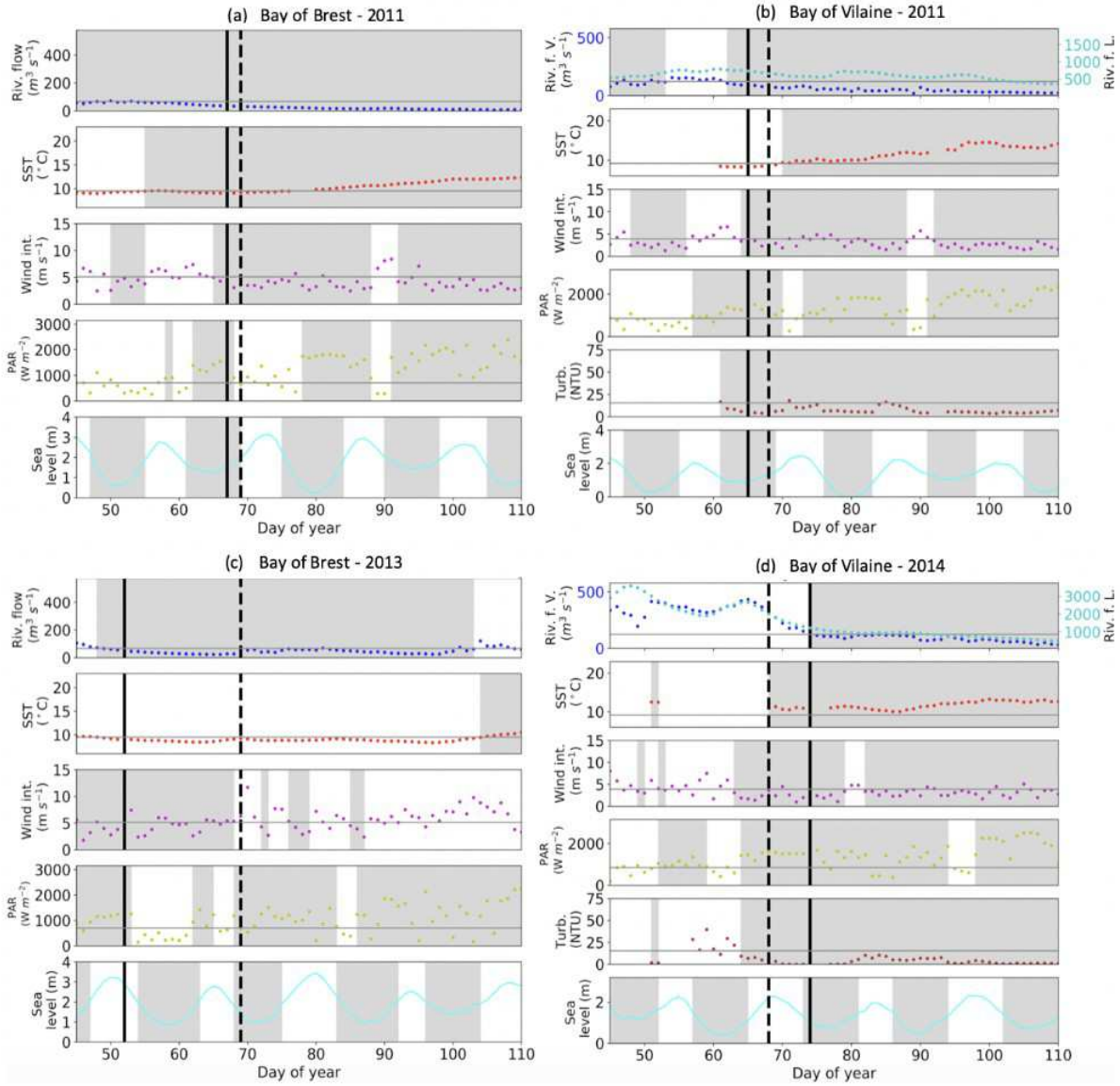

Figure 7. IPGP dates and environmental drivers: flow of the Aulne, Vilaine, and Loire rivers, sea surface temperature, wind intensity, PAR, turbidity, and sea level at high tide. Illustrations for a mean IPGP date in **(a)** the Bay of Brest and **(b)** the Bay of Vilaine in 2011; for an early IPGP date in **(c)** the Bay of Brest in 2013; for a late IPGP date in **(d)** the Bay of Vilaine in 2014. The mean IPGP date of each bay is represented by a dashed black line, and the IPGP date of the year is represented by a solid black line. Thresholds of each environmental driver are represented by grey horizontal lines corresponding to the mean conditions calculated 30 d around the IPGP date. Grey areas are time periods favourable to the IPGP.

laine). In the Bay of Vilaine, the environmental drivers can simulate a later IPGP than in the Bay of Brest.

In the Bay of Brest (Fig. 8a), only variations in air temperature have a real impact on the IPGP. If air temperature is low (< 8 °C), the IPGP is not triggered before day 74 (Table 5, Exp 1). If air temperature is high (> 13 °C), the IPGP can start on day 49 (Table 5, Exp 2).

In the Bay of Vilaine, air temperature and the erosion rate are the two main drivers impacting the IPGP (Fig. 8b). As in the Bay of Brest, if air temperature is low (< 6 °C), the IPGP is late and appears only after day 80 (Table 5, Exp 1). If temperature is equal or above 13 °C, the IPGP is early and appears on day 45 (Table 5, Exp 2). If the erosion rate is low (2.10^{-7} kg m^{-2} s^{-1}), the IPGP takes place on day 76 (Table 5, Exp 7). If the erosion rate is high (2.10^{-5} kg m^{-2} s^{-1}), the IPGP occurs late after day 87 (Table 5, Exp 8).

Even if variations in wind and CC induce weaker shifts in the date of the IPGP, i.e. about 1 week at most (Table 5,

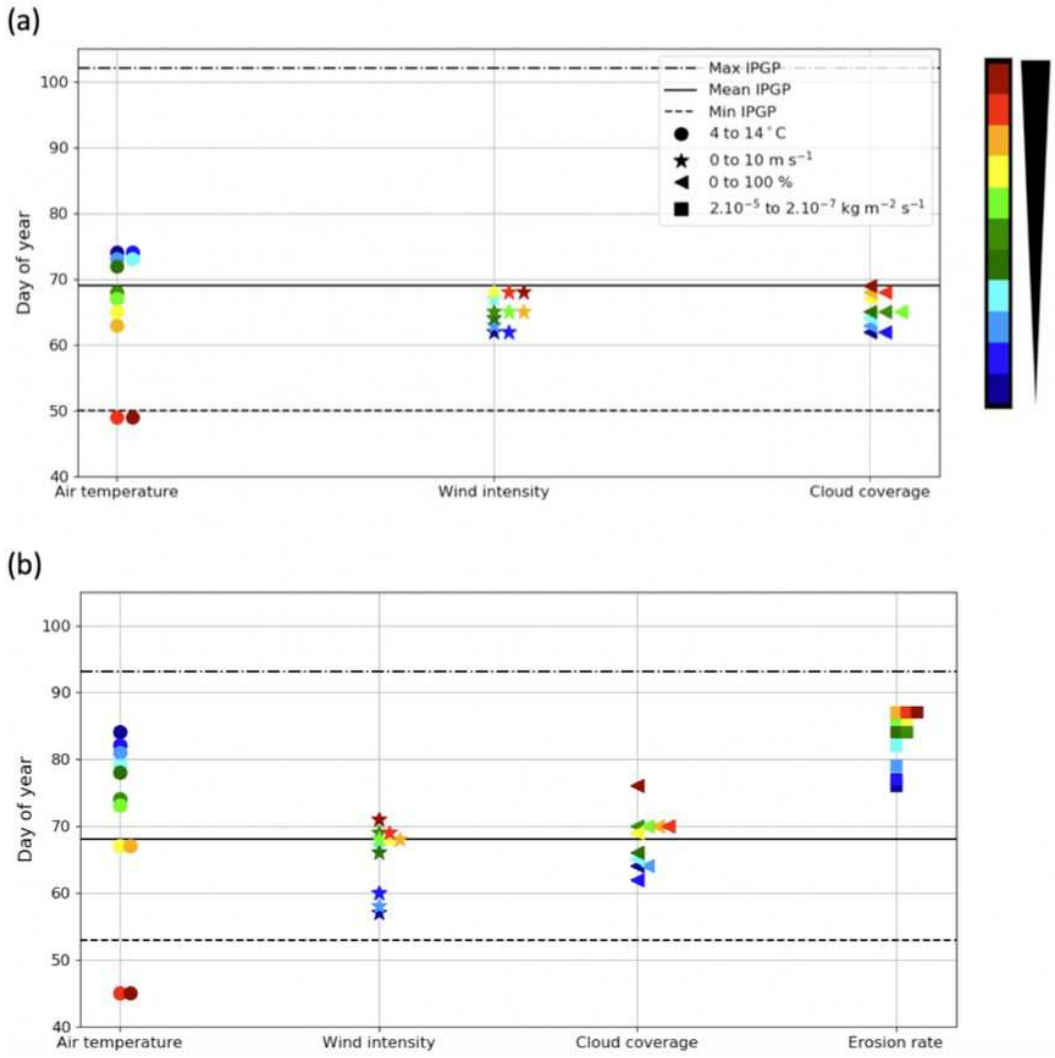

Figure 8. Impact of the variation in environmental drivers on the date of the IPGP in **(a)** the Bay of Brest and **(b)** the Bay of Vilaine. Steps of 1 °C for the air temperature, 1 m s^{-1} for the wind intensity, 10 % for the cloud coverage, and 0.0000036 kg m^{-2} s^{-1} for the erosion rate equivalent to a variation in suspended matter between 0.02 and 0.08 mg L^{-1} at the IPGP.

Exp 3, 4, 5, 6), they can however explain some variations in the IPGP. For example, the fact that the early IPGPs, observed in 2010 in the Bay of Brest and in 2012 in the Bay of Vilaine, are due to low wind conditions (around 2 m s^{-1}, Figs. S2a–S1f) are confirmed by both in situ measurements and the model (Fig. 8b).

The combined effect of the environmental factors can also be explored from the MARS-1DV model simulations (Fig. 9). The modelling conditions (hereafter called "Exp") are detailed in Table 5 and compared to the mean IPGP date (day 68).

The simulations confirm the observations: late IPGPs correspond to the most extreme unfavourable combined environmental values (temperature of 4 °C, wind intensity of 10 m s^{-1}, CC of 100 %, and erosion rate of 2.10^{-5} kg m^{-2} s^{-1} – Exp A). Due to the most unfavourable conditions, the IPGP occurs 9 and 64 d later in the Bay of Brest and in the Bay of Vilaine, respectively. A late IPGP can also be linked to the combined effect of only two factors such as "temperature and wind" and "temperature and CC" with a delay of 5 and around 22 d, respectively (Exp B and C). In contrast, no delay is observed for the combination "wind and CC" (Exp D) in both bays.

Early IPGP events are found in the model simulations and in the in situ observations when conditions correspond to a high temperature (14 °C), no wind intensity and CC, and a low erosion rate (2.10^{-7} kg m^{-2} s^{-1}) – Exp K. All the combined scenarios allow the occurrence of an earlier IPGP (by at least 5 additional days) compared to experiments that consider a single modified parameter.

This analysis enables environmental parameters to be classified with respect to their impact on the IPGP. In both bays,

Table 5. Assumptions are explored in the 1DV model for environmental parameters independently (1–8) and with a combined effect (A–N) with the modified values (grey background) and text in bold for the Bay of Brest only (+ for a later IPGP, − for an earlier IPGP, = for an equal IPGP) with the IPGP equal to the mean observed IPGP of day 68.

Experiment	Air temperature (°C)	Wind intensity ($m\ s^{-1}$)	Cloud coverage (%)	Erosion rate ($kg\ m^{-2}\ s^{-1}$)	Simulated IPGP Bay of Brest (days)	Simulated IPGP Bay of Vilaine (days)
1	**4**	**3**	**70**	2.10^{-6}	+5	+16
2	**14**	**3**	**70**	2.10^{-6}	−20	−23
3	**10**	**0**	**70**	2.10^{-6}	−1	−11
4	**10**	**10**	**70**	2.10^{-6}	−7	+3
5	**10**	**3**	**0**	2.10^{-6}	=	−4
6	**10**	**3**	**100**	2.10^{-6}	−7	+8
7	10	3	70	2.10^{-7}		+8
8	10	3	70	2.10^{-5}		+19
A	**4**	**10**	**100**	2.10^{-5}	+9	+64
B	**4**	**10**	**70**	2.10^{-6}	+5	+17
C	**4**	**3**	**100**	2.10^{-6}	+5	+28
D	**10**	**10**	**100**	2.10^{-6}	=	+6
E	4	10	70	2.10^{-5}		+48
F	4	3	100	2.10^{-5}		+46
G	10	10	100	2.10^{-5}		+34
H	10	3	100	2.10^{-5}		+19
I	10	10	70	2.10^{-5}		+29
J	4	3	70	2.10^{-5}		+36
K	**14**	**0**	**0**	2.10^{-7}	−20	−11
L	**14**	**0**	**70**	2.10^{-7}	−21	−11
M	**14**	**3**	**0**	2.10^{-7}	−20	−11
N	**10**	**0**	**0**	2.10^{-7}	−11	−11

the temperature appears to be the key factor driving the IPGP. By combining the environmental drivers, the IPGP can occur even later or earlier than with a single forcing. In both bays, the combination of wind and CC has no impact on the IPGP, which occurs near the median day (Exp D and N). The extreme couplings of Exp A, E, F, G, and J delay the date of the IPGP later than detected in the observations for the Bay of Vilaine. All simulations show a higher impact on the date of the IPGP in the Bay of Vilaine than in the Bay of Brest (Fig. 9, Table 5).

3.4 Impact of extreme hydro-meteorological events on the IPGP

3.4.1 Cold spells

The impact of cold spells on the IPGP is simulated with the MARS-1DV model based on two criteria: (i) the period of occurrence of the event, set in the middle or end of February; (ii) the duration and intensity of the cold spell, which can be either short and weak (8 d, 7 °C) or long and intense (20 d, 5 °C) (Fig. 10).

In both bays, when the cold spell appears in mid-February, the IPGP is not impacted. However, it is delayed by about 15 d when occurring at the end of February. The duration of the cold spell, when longer than 15 d, also has an impact on the IPGP, with a delay of 13 and 12 d in the Bay of Brest and in the Bay of Vilaine, respectively.

Eight cold spells are detected in February in both bays between 2001 and 2019. In 2011, both sites are impacted simultaneously with cold spells. Long cold spells (30 d) are observed in 2009 and 2018, leading to an anomaly of more than −1.9 °C.

The cold spell observed in 2018 in the Bay of Vilaine may explain the later IPGP. There is no change in the IPGP in 2011 and 2013, despite the cold spell, the period of occurrence being too early during winter 2011 and the duration too short in 2013 (only 10 d).

In the Bay of Brest, the cold spells in 2003 and 2004 may explain the delay in the IPGP (respectively, days 93 and 85). The presence of long and intense cold spells in 2010 and 2011 does not shift the IPGP (days 50 and 67) because they occur too early (before day 20).

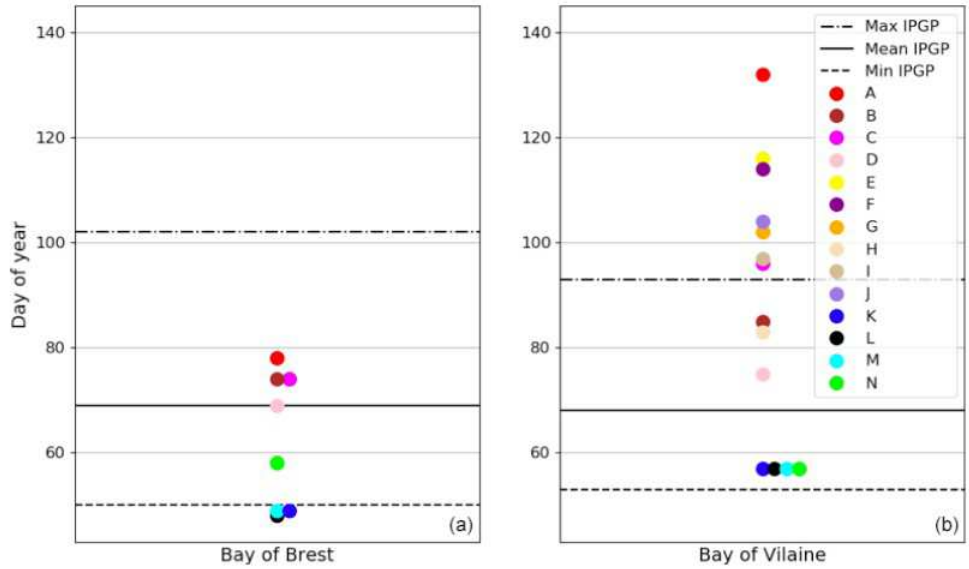

Figure 9. Influence of combined environmental parameters for the MARS-1DV model in both bays (Bay of Brest, **a**, and Bay of Vilaine, **b**) with detailed experiments in Table 2.

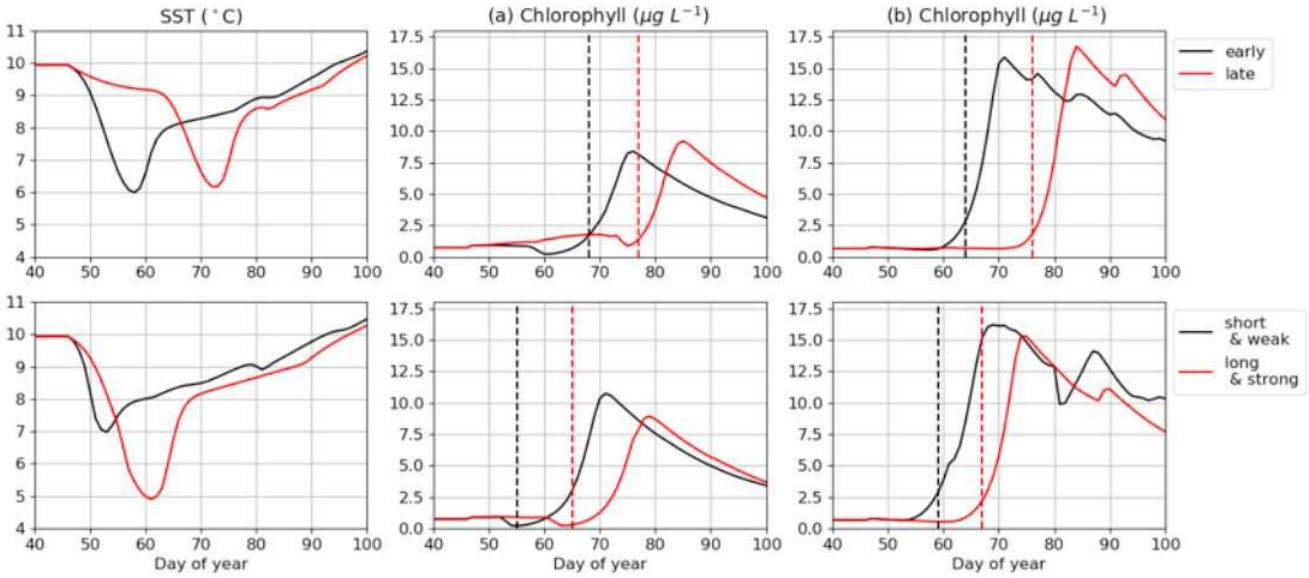

Figure 10. Impact of cold spells on the IPGP date simulated in **(a)** the Bay of Brest and **(b)** the Bay of Vilaine. Four conditions of cold spells are explored: early (mid-February), late (end of February), short (8 d), and long (20 d). The IPGP dates are represented by dashed lines.

3.4.2 Wind bursts

Based on our model simulations, the wind bursts that occur during at least 3 continuous days have no impact on the IPGP in both bays, whatever the duration, the period, and the intensity ($\pm$ 1 d). In the Bay of Vilaine, only one wind event is detected in 2018 (3 d long and 6 m s^{-1}). In the Bay of Brest, several events are detected, but no significant impact is observed on the IPGP.

3.4.3 Flood events

River floods can delay the IPGP by resuspending sediment in the water column and therefore limiting light penetration in the water column. Inputs of nutrients have no impact during the late winter period because nutrient concentrations are maximal, with no limitation on phytoplankton growth. Flood events are analysed with observation data collected in the month prior to the IPGP date because the 1DV modelling approach does not allow the sensitivity to hydrological events

to be simulated (i.e. it is necessary to simulate horizontal advection processes).

In the Bay of Brest, the impact of flood events depends on their duration and intensity: when the flood exceeds 15 d, a delay in the IPGP is detected. Shorter and more intense floods ($> 300\,m^3\,s^{-1}$) do not impact the IPGP.

In the Bay of Vilaine, only two flood events are observed close to the IPGP date in 2014 and 2015. The 2015 flood event, which is 10 d longer and more intense ($> 100\,m^3\,s^{-1}$) than the 2014 one, delays the IPGP date by 10 d.

4 Discussion

4.1 Comparison of the phytoplankton growing period in both bays

Despite their contrasting hydrodynamics (e.g. Petton et al., 2020; Poppeschi et al., 2021; Lazure and Jegou, 1998; Ratmaya et al., 2019; Ménesguen et al., 2019), the median dates of the start and the end of the phytoplankton growing period are the same in the Bay of Brest and in the Bay of Vilaine, whether they are calculated from high- and low- frequency datasets or model simulations. The phytoplankton growing period occurs from March to September and lasts about 190 d in both bays. This concordance is related to a similar seasonality of the environmental drivers.

The observed cumulative fluorescence is almost double in the Bay of Vilaine compared with the Bay of Brest. This difference in the amount of chlorophyll produced in surface waters from both bays is also recorded by the low-frequency observation programmes and satellite observations (Ménesguen et al., 2019). It can be explained by the difference between the hydrodynamics and the influence of different watersheds. The Bay of Brest is a semi-enclosed bay with a macrotidal regime influenced by two local rivers (Aulne and Elorn), whereas the Bay of Vilaine has a weaker tidal regime, is open on the continental shelf and is widely influenced by a large river (Loire River).

Two different patterns of the phytoplankton growing period are identified by the *k*-means classification in both bays. The flattened, weak, and long bloom highlighted in the Bay of Brest can be explained by assuming that nutrients are not limiting the phytoplankton growth during spring. The maintenance of the diatom succession throughout spring since the 1980s (Quéguiner 1982; Del Amo et al., 1997) can be explained by the combination of increasing N and P loads, intense Si recycling and a macrotidal regime (Ragueneau et al., 2019). The phytoplankton growing period in the Bay of Vilaine is characterized by several successive peaks including two main ones. Nutrients drive the seasonal evolution of the phytoplankton growing period through periods of nutrient-limited conditions. These fluctuations are governed by phosphorus and nitrate loads from Vilaine and Loire rivers (Ratmaya et al., 2019) but probably also by the stoichiometry of recycled elements in the water and at the water–sediment interface (Ratmaya et al., 2022). At the beginning of the phytoplankton growing period (IPGP), however, the system is not nutrient-limited in terms of nitrate, phosphorus, and silicate (Table 4).

4.2 Validation of the method for IPGP detection

The method that we developed to detect the IPGP in both high-frequency and low-frequency in situ observations shows comparable results and detects similar initiation dates for some years, while a time lag between high- and low-frequency observations can be observed for other years. This difference is mainly explained by the difference in the sampling frequency. The late deployment of the buoy in the Bay of Vilaine (i.e. not deployed until mid-February before 2018) can also explain some differences between both sites. High-frequency data provide a more accurate detection of the day of the IPGP, while an uncertainty of about ± 7 d is observed with low-frequency observations. This comparison between high- and low-frequency-based IPGP detection highlights the sensitivity of sampling strategy in the observation of phytoplankton growing periods (Bouman et al., 2005; Serre-Fredj et al., 2021) related to the response of the ecosystem within a few hours after an environmental change (Lefort and Gasol, 2014; Thyssen et al., 2008).

The modelled IPGP, based on the year 2015, is coherent with high-frequency observations (around 5 d of difference between modelled and observed IPGP). Considering the idealized framework for modelling computations (1DV model instead of a realistic 3D model configuration), the agreement between observations and simulations validates the 1DV approach to explore IPGP dynamics. With the 1DV configuration, the vertical dynamics in the water column, coupled with biogeochemistry and sediment dynamics are reproduced well. Atmospheric forcings and interactions with the bottom layer are the main environmental drivers. The full range of impacts related to the horizontal advection (e.g. in the considered regions, river-advected plumes can change the hydrodynamics and the nutrient fluxes) are not evaluated, however. In the Bay of Brest and in the Bay of Vilaine, such advected sources exist (Poppeschi et al., 2021; Lazure and Jegou, 1998). But inputs from rivers are not the main drivers of the IPGP in nutrient-rich environments. Nutrient loads advected by rivers may impact the phytoplankton community later during the growing period rather than at the IPGP (Ratmaya et al., 2019).

4.3 Identification of the environmental conditions supporting the IPGP

The main theories to explain the initiation of phytoplankton blooms (Sverdrup, 1953; Huisman et al., 1999; Banse, 1994) are not relevant in the context of shallow and well-mixed coastal waters under the influence of river plumes.

In the studied region, the ecosystem does not evolve with mixed layer dynamics, as observed in deeper environments. Both bays are permanently vertically mixed mainly by tides, and vertical stratification only occurs in a thin surface layer due to river runoffs at short timescales. However, the IPGP is mainly driven and limited by similar local environmental conditions in both bays. The ideal temperature ($> 10\,°C$) and PAR ($1300\,W\,m^{-2}$) for the IPGP are in agreement with those from previous studies conducted in similar coastal ecosystems (e.g. Glé et al., 2007; Townsend et al., 1994; Trombetta et al., 2019). Neap tidal conditions, weak wind (lower than $3\,m\,s^{-1}$), and weak river flow can also play a positive role in observations of earlier IPGPs according to previous studies (Ragueneau et al., 1996; Tian et al., 2011). The impact of wind direction on the IPGP is negligible.

Local changes in temperature, incident radiation, tidal conditions, wind conditions, and river flow induce differences in detected IPGPs. In this coastal temperate ecosystem, we observe that the beginning of the growing period is limited by light (controlled by incident radiation, turbidity in this season) and water temperature. The IPGP also occurs during low vertical mixing conditions.

The comparison of the individual importance of each environmental driver shows that temperature and light penetration are the key environmental drivers in both bays. When light penetration is reduced by a combined effect of PAR and turbidity (sediment resuspension), the delay in the IPGP can be amplified, especially in the Bay of Vilaine. The importance of light availability in the timing and intensity of the spring bloom is also highlighted in the North Sea (Wiltshire et al., 2015), in the German Bight (Tian et al., 2009), and along the UK south coast (Iriarte and Purdie, 2004).

4.4 Interannual evolutions of the IPGP

The IPGP in these two bays shows a strong interannual variability with initiation dates varying from late winter to spring, depending on the environmental conditions. A mean difference of 50 d between the earliest and latest IPGP dates is observed. It is important to note that the phytoplankton population during the IPGP is always dominated in both bays by the same centric diatoms, the genera *Chaetoceros* and *Skeletonema*, whose abundance varies from year to year depending on climatic conditions (REPHY, 2021). None of the nutrients limits the growing of phytoplankton at the IPGP (Table 4).

The earliest IPGPs are observed and related to favourable environmental conditions early in the year. For example, the IPGP can occur before day 50, associated with exceptionally weak wind and river flow in addition to a sufficient PAR and a near-optimal temperature of around 10 °C (e.g. 2010 in the Bay of Brest and 2012 in the Bay of Vilaine). But if the environmental conditions are not favourable (e.g. 2017 and 2019 in both bays), the IPGP is delayed. This can be due to (1) strong wind for several days (not a single wind burst) combined with a weak PAR and sometimes enhanced by high-turbidity events which further limits the light penetration and (2) low SST.

The IPGP appears to be more controlled by local environmental drivers than by regional environmental drivers, the IPGP being earlier at one site than in the other during half of the studied years: for example, the 2012 IPGP is early in the Bay of Vilaine (day 53) but late in the Bay of Brest (day 80), related to strong wind activity and low PAR in the last bay. The offshore regional dynamics will induce limited impacts on local hydrodynamical features that will change the IPGP.

Changes in the IPGP over the last 2 decades have highlighted its evolution through two trends: it occurs earlier each year until 2010, when the trend is reversed. Changes in environmental conditions over the last 20 years were then studied to seek a possible concordance with one of the environmental drivers, but no significant trend was detected. Because of global warning, earlier phytoplankton blooms are expected (Friedland et al., 2018) but not a later IPGP as observed in our study regions. However, the mechanisms that trigger blooms in coastal ecosystems – especially eutrophic ones – are not similar to the processes that influence blooms in the open ocean. No link between trends in the IPGP and environmental drivers has been identified in the southern California Bight from 1983 to 2000 (Kim et al., 2009). By investigating long-term (1975–2005) daily data, Wiltshire et al. (2008) also observed later phytoplankton blooms in the German bight, but no link to global warming was detected. Henson et al. (2018) modelled a bloom shift of 5 d per decade from 2006 to 2025, with later blooms. A possible explanation of these later IPGPs may involve a lower spring SST (Hunter-Cervera et al., 2016).

4.5 Extreme events

We show that a cold spell is likely to delay the IPGP if it occurs at the end of winter (after 20 February) and/or if the cold spell lasts long enough (> 15 d). The drop in temperature related to the cold spell prevents the IPGP in both bays. This is in accordance with the study of Gomez and Souissi (2008) in the English Channel where cold spells can delay the date of the IPGP, as a result of an increase in water column mixing. Cold spells may also drive local patterns by influencing the phytoplankton communities (Gomez and Souissi, 2008; Schlegel et al., 2021).

Flood events have an influence on the phytoplankton biomass when they occur in spring, due to the supply of nutrients. When they occur in late winter, nutrients are already at their maximum. The impact of floods on the IPGP is then due to the increase in the water turbulence and to the limitation of light by increasing the turbidity. The IPGP can be delayed only if floods are at least 15 d long. This scheme was also observed by Saeck et al. (2013) along a river–estuary–bay continuum and explained by a shortened water residence

time and limited light due to flood-induced turbidity in the coastal zone.

No relationship is observed between wind events and the IPGP in either bay because they are weakly stratified, contrary to open seas (i.e. Black Sea, Mikaelyan et al., 2017). In coastal stratified regions (e.g. under the influence of river plumes), strong wind and tidal mixing can enhance the mixing and break down stratification, which does not favour phytoplankton growth (Joordens et al., 2021). During the IPGP, except during floods, both regions are weakly stratified and are then less sensitive to combined wind/tidal short events.

5 Conclusions

This study provides a new understanding of the IPGP dynamics in coastal temperate areas by using both high- and low-frequency in situ data, in combination with simulations from a 1DV model. Strong similarities are found in both bays. An important interannual variability of the IPGP is observed, with a trend towards a later IPGP over the last decade (2010–2020). We quantify the importance of environmental conditions on the IPGP. When we compare observed IPGPs with favourable environmental conditions and following sensitivity experiments with the 1DV model, water temperature and turbidity (limiting light penetration in the water column) appear as the main drivers explaining interannual IPGP variability. The IPGP is a complex mechanism, usually triggered by more than one environmental parameter. The analysis of the influence of extreme events reveals that cold spells and floods have a strong impact by delaying the IPGP when episodes are long enough and occur after winter. No effect of wind bursts is detected.

While this study shows comparable IPGP dynamics when based on 1DV model simulations or in situ observations, we will next investigate the effect on phytoplankton dynamics of a fully realistic hydrodynamics (including horizontal and vertical advections; mixing processes; remote sources of nutrients from rivers) 3D model. We will focus on exploring the variability of phytoplankton communities during the IPGP to assess whether community change is occurring, as observed in other studies and for other ecosystems (Ianson et al., 2001; Edwards and Richardson, 2004; Chivers et al., 2020). When interannual evolutions in the phytoplankton growth are explored, the detection and the understanding of harmful algal bloom dynamics can also be addressed based on similar approaches. Further studies will be dedicated to the simulation of the coastal ecosystem in the future based on numerical simulation through climate scenarios. The investigation of other contrasting coastal environments will allow us to better understand and anticipate the expected impact of global change on coastal phytoplankton dynamics.

Code availability. Code used in this paper can be found at Zenodo https://doi.org/10.5281/zenodo.7426540 (cocopom, 2022).

Data availability. Data sets used in this paper can be found at SEANOE https://doi.org/10.17882/46529 (Retho et al., 2022) and https://doi.org/10.17882/74004 (Rimmelin-Maury et al., 2020).

Supplement. The supplement related to this article is available online at: https://doi.org/10.5194/bg-19-5667-2022-supplement.

Author contributions. CP, GC, AD, RV, PRM, and ErG conceptualized the study. PRM, EmG, and MR collected data. MP and GC developed the model configuration. CP, GC, AD, and RV drafted the first versions of the paper. CP carried out all the analyses and wrote the final version of the paper. All authors contributed to the discussions and revisions of the study.

Competing interests. The contact author has declared that none of the authors has any competing interests.

Disclaimer. Publisher's note: Copernicus Publications remains neutral with regard to jurisdictional claims in published maps and institutional affiliations.

Special issue statement. This article is part of the special issue "Towards an understanding and assessment of human impact on coastal marine environments". It is not associated with a conference.

Acknowledgements. We would like to acknowledge the COAST-HF (http://www.coast-hf.fr, last access: 20 March 2022), SOMLIT (http://somlit.epoc.u-bordeaux1.fr, last access: 20 March 2022), and REPHY (https://doi.org/10.17882/47248) national observing networks for making data flux readily available. COAST-HF and SOMLIT are components of the National Research Infrastructure ILICO. We would like to thank the Shom for tidal data and also Météo-France for wind and solar flux products. We also thank Claire Labry for fruitful discussions and Sally Close for her proofreading. We thank the referees for their helpful and constructive comments.

Financial support. This study is part of the State-Region Plan Contract ROEC supported in part by the European Regional Development Funds and the COXTCLIM project funded by the Loire-Brittany Water Agency, the Brittany region, and Ifremer.

Review statement. This paper was edited by Ulrike Braeckman and reviewed by Jose Iriarte and two anonymous referees.

References

Aminot, A. and Kerouel, R.: Hydrologie des écosystèmes marins, Paramètres et analyses, Editions de l'Ifremer, Méthodes d'analyse en milieu marin, 336 pp., ISBN 2-84433-133-5, 2004.

Banse, K.: Grazing and zooplankton production as key controls of phytoplankton production in the open ocean, Oceanography, 7, 13–20, 1994.

Barbosa, A., Domingues, R., and GalvaÞo., H.: Environmental forcing of phytoplankton in a Mediterranean estuary (Guadiana estuary, south-western Iberia): A decadal study of anthropogenic and climatic influences, Estuar. Coast., 33, 324–341, https://doi.org/10.1007/s12237-009-9200-x, 2010.

Behrenfeld, M. J.: Abandoning Sverdrup's critical depth hypothesis on phytoplankton blooms, Ecology, 91, 977–989, 2010.

Behrenfeld, M. J., Doney, S. C., Lima, I., Boss, E. S., and Siegel, D. A.: Annual cycles of ecological disturbance and recovery underlying the subarctic Atlantic spring plankton bloom, Global Biogeochem. Cy., 27, 526–540, https://doi.org/10.1002/gbc.20050, 2013.

Beucher, C., Treguer, P., Corvaisier, R., Hapette, A. M., and Elskens, M.: Production and dissolution of biosilica, and changing microphytoplankton dominance in the Bay of Brest (France), Mar. Ecol. Prog. Ser., 267, 57–69, https://doi.org/10.3354/meps267057, 2004.

Boss, E. and Behrenfeld, M.: In situ evaluation of the initiation of the North Atlantic phytoplankton bloom, Geophys. Res. Lett., 37, 18, https://doi.org/10.1029/2010GL044174, 2010.

Bouman, H., Platt, T., Sathyendranath, S., and Stuart, V.: Dependence of light-saturated photosynthesis on temperature and community structure, Deep-Sea Res. Pt. I, 52, 1284–1299, https://doi.org/10.1016/j.dsr.2005.01.008, 2005.

Brody, S. R., Lozier, M. S., and Dunne, J. P.: A comparison of methods to determine phytoplankton bloom initiation, J. Geophys. Res.-Ocean., 118, 2345–2357, https://doi.org/10.1002/jgrc.20167, 2013.

Caracciolo, M., Beaugrand, G., Hélaouët, P., Gevaert, F., Edwards, M., Lizon, F., Kléparski, L., and Goberville, E.: Annual phytoplankton succession results from niche-environment interaction, J. Plank. Res., 43, 85–102, https://doi.org/10.1093/plankt/fbaa060, 2021.

Carberry, L., Roesler, C., and Drapeau, S.: Correcting in situ chlorophyll fluorescence time-series observations for nonphotochemical quenching and tidal variability reveals nonconservative phytoplankton variability in coastal waters, Limnol. Oceanogr.-Method., 17, 462–473, https://doi.org/10.1002/lom3.10325, 2019.

Chapelle, A., Lazure, P., and Ménesguen, A.: Modelling eutrophication events in a coastal ecosystem, Sensitivity analysis, Estuar. Coast. Shelf Sci., 39, 529–548, https://doi.org/10.1016/S0272-7714(06)80008-9, 1994.

Charria, G., Lazure, P., Le Cann, B., Serpette, A., Reverdin, G., Louazel, S., Batifoulier, F., Dumas, F., Pichon, A., and Morel, Y.: Surface layer circulation derived from Lagrangian drifters in the Bay of Biscay, J. Mar. Syst., 109, 60–76, https://doi.org/10.1016/j.jmarsys.2011.09.015, 2013.

Chiswell, S., Calil, P., and Boyd, P.: Spring blooms and annual cycles of phytoplankton: a unified perspective, J. Plank. Res., 37, 500–508, https://doi.org/10.1093/plankt/fbv021, 2015.

Chivers, W. J., Edwards, M., and Hays, G. C.: Phenological shuffling of major marine phytoplankton groups over the last six decades, Divers. Distrib., 26, 536–548, https://doi.org/10.1111/ddi.13028, 2020.

Cloern, J. E.: Phytoplankton bloom dynamics in coastal ecosystems: a review with some general lessons from sustained investigation of San Francisco Bay, California, Rev. Geophys., 34, 127–168, https://doi.org/10.1029/96RG00986, 1996.

cocopom: cocopom/ipgp-detection: IPGP-detection v1.0 (v1.0), Zenodo [code], https://doi.org/10.5281/zenodo.7426540, 2022.

Cocquempot, L., Delacourt, C., Paillet, J., Riou, P., Aucan, J., Castelle, B., Charria, G., Claudet, J., Conan, P., Coppola, L., Hocdé, R., Planes, S., Raimbault, P., Savoye, N., Testut, L., and Vuillemin, R.: Coastal Ocean and Nearshore Observation: A French Case Study, Front. Mar. Sci., 6, 1–17, https://doi.org/10.3389/fmars.2019.00324, 2019.

Cugier, P., Billen, G., Guillaud, J. F., Garnier, J., and Ménesguen, A.: Modelling the eutrophication of the Seine Bight (France) under historical, present and future riverine nutrient loading, J. Hydrol., 304, 381–396, https://doi.org/10.1016/j.jhydrol.2004.07.049, 2005.

Del Amo, Y., Le Pape, O., Tréguer, P., Quéguiner, B., Ménesguen, A., and Aminot, A.: Impacts of high-nitrate freshwater inputs on macrotidal ecosystems, I. Seasonal evolution of nutrient limitation for the diatom-dominated phytoplankton of the Bay of Brest (France), Mar. Ecol. Prog. Ser., 161, 213–224, 1997.

Edwards, M., and Richardson, A. J.: Impact of climate change on marine pelagic phenology and trophic mismatch, Nature, 430, 881–884, https://doi.org/10.1038/nature02808, 2004.

Farcy, P., Durand, D., Charria, G., Painting, S.J., Tamminem, T., Collingridge, K., Grémare, A. J., Delauney, L., and Puillat, I.: Toward a European coastal observing network to provide better answers to science and to societal challenges; the JERICO research infrastructure, Front. Mar. Sci., 6, 1–13, https://doi.org/10.3389/fmars.2019.00529, 2019.

Ferrer, L., Fontán, A., Mader, J., Chust, G., González, M., Valencia, V., Uriarte, A., and Collins, M. B.: Low-salinity plumes in the oceanic region of the Basque Country, Cont. Shelf Res., 29, 970–984, https://doi.org/10.1016/j.csr.2008.12.014, 2009.

Frère, L., Paul-Pont, I., Rinnert, E., Petton, S., Jaffré, J., Bihannic, I., Soudant, P., Lambert, C., and Huvet, A.: Influence of environmental and anthropogenic factors on the composition, concentration and spatial distribution of microplastics: a case study of the Bay of Brest (Brittany, France), Environ. Pollut., 225, 211–222, https://doi.org/10.1016/j.envpol.2017.03.023, 2017.

Friedland, K. D., Mouw, C. B., Asch, R. G., Ferreira, A. S. A., Henson, S., Hyde, J. W., Morse, R., Thomas, A., and Braddy, D.: Phenology and time series trends of the dominant seasonal phytoplankton bloom across global scales, Glob. Ecol. Biogeogr., 27, 551–569, https://doi.org/10.1111/geb.12717, 2018.

Glé, C., Del Amo, Y., Bec, B., Sautour, B., Froidefond, J. M., Gohin, F., Maurer, D., Plus, M., Laborde, P., and Chardy, P.: Typology of environmental conditions at the onset of winter phytoplankton blooms in a shallow macrotidal coastal ecosystem, Arcachon Bay (France), J. Plank. Res., 29, 999–1014, https://doi.org/10.1093/plankt/fbm074, 2007.

Gohin, F., Van der Zande, D., Tilstone, G., Eleveld, M. A., Lefebvre, A., Andrieux-Loyer, F., Blauw, A. N., Bryère, P., Devreker, D., Garnesson, P., Hernández Fariñas, T., Lamaury, Y., Lam-

pert, L., Lavigne, H., Menet-Nedelec, F., Pardo, S., and Saulquin, B.: Twenty years of satellite and in situ observations of surface chlorophyll *a* from the northern Bay of Biscay to the eastern English Channel. Is the water quality improving?, Remote Sens. Environ., 233, 111343, https://doi.org/10.1016/j.rse.2019.111343, 2019.

Gomez, F. and Souissi, S.: The impact of the 2003 heat wave and the 2005 cold wave on the phytoplankton in the northeastern English Channel, Compt. Rend. Biol., 331, 678–685, https://doi.org/10.1016/j.crvi.2008.06.005, 2008.

Grasso F., Le Hir P., and Bassoullet P.: Numerical modelling of mixed-sediment consolidation, Ocean Dynam., 65, 607–616, https://doi.org/10.1007/s10236-015-0818-x, 2015.

Hartigan, J. and Wong, M.: Algorithm AS 136: A K-Means Clustering Algorithm, J. Roy. Stat. Soc. Ser. C, 28, 100–108, 1979.

Henson, S. A., Cole, H. S., Hopkins, J., Martin, A. P., and Yool, A.: Detection of climate change-driven trends in phytoplankton phenology, Glob. Change Biol., 24, 101–111, https://doi.org/10.1111/gcb.13886, 2018.

Huisman, J. E. F., van Oostveen, P., and Weissing, F. J.: Critical depth and critical turbulence: two different mechanisms for the development of phytoplankton blooms, Limnol. Oceanogr., 44, 1781–1787, https://doi.org/10.4319/lo.1999.44.7.1781, 1999.

Hunter-Cevera, K. R., Neubert, M. G., Olson, R. J., Solow, A. R., Shalapyonok, A., and Sosik, H. M.: Physiological and ecological drivers of early spring blooms of a coastal phytoplankter, Science, 354, 326–329, https://doi.org/10.1126/science.aaf8536, 2016.

Ianson, D., Pond, S., and Parsons, T.: The spring phytoplankton bloom in the coastal temperate ocean: growth criteria and seeding from shallow embayments, J. Oceanogr., 57, 723–734, https://doi.org/10.1023/A:1021288510407, 2001.

IPCC, Masson-Delmotte, V., Zhai, P., Pirani, A., Connors, S. L., Pei`an, C., Berger, S., Caud, N., Chen, Y., Goldfarb, L., Gomis, M. I., Huang, M., Leitzell, K., Lonnoy, E., Matthews, J. B. R., Maycock, T. K., Waterfield, T., Yelekcj, O., Yu, R., and Zhou, B.: Climate change 2021: the physical science basis. Contribution of working group I to the sixth assessment report of the intergovernmental panel on climate change, Cambridge University Press, 2, 2391 pp., 2021.

Iriarte, A. and Purdie, D. A.: Factors controlling the timing of major spring bloom events in an UK south coast estuary, Estuar. Coast. Shelf Sci., 61, 679–690, https://doi.org/10.1016/j.ecss.2004.08.002, 2004.

Isemer, H.-J. and Hasse, L.: The Bunker Climate Atlas of the North Atlantic Ocean, Vol. 2, Springer, Berlin, 218–252, ISBN-10: 0387155686, 1985.

Joordens, J. C. A., Souza, A. J., and Visser, A.: The influence of tidal straining and wind on suspended matter and phytoplankton distribution in the Rhine outflow region, Cont. Shelf Res., 21, 301–325, https://doi.org/10.1016/S0278-4343(00)00095-9, 2001.

Kromkamp, J. C. and Van Engeland, T.: Changes in phytoplankton biomass in the western Scheldt estuary during the period 1978–2006, Estuar. Coast., 33, 270–285, https://doi.org/10.1007/s12237-009-9215-3, 2010.

Kim, H. J., Miller, A. J., McGowan, J., and Carter, M. L.: Coastal phytoplankton blooms in the Southern California Bight, Prog. Oceanogr., 82, 137–147, https://doi.org/10.1016/j.pocean.2009.05.002, 2009.

Lazure, P., Jégou, A.-M., and Kerdreux, M. Analysis of salinity measurements near islands on the French continental shelf of the Bay of Biscay, Sci. Marina, 70, 7–14, 2006.

Lazure, P. and Dumas, F.: An external–internal mode coupling for a 3D hydrodynamical model for applications at regional scale (MARS), Adv. Water Res., 31, 233–250, https://doi.org/10.1016/j.advwatres.2007.06.010, 2008.

Lazure, P. and Jégou, A. M.: 3D modelling of seasonal evolution of Loire and Gironde plumes on Biscay Bay continental shelf, Oceanol. Acta, 21, 165–177, https://doi.org/10.1016/S0399-1784(98)80006-6, 1998.

Le Boyer, A., Charria, G., Le Cann, B., Lazure, P., and Marié, L. Circulation on the shelf and the upper slope of the Bay of Biscay, Cont. Shelf Res., 55, 97–107, https://doi.org/10.1016/j.csr.2013.01.006, 2013.

Lefort, T. and Gasol, J. M.: Short-time scale coupling of picoplankton community structure and single-cell heterotrophic activity in winter in coastal NW Mediterranean Sea waters, J. Plank. Res., 36, 243–258, https://doi.org/10.1093/plankt/fbt073, 2014.

Le Hir P., Cayocca F., and Waeles B.: Dynamics of sand and mud mixtures: A multiprocess-based modelling strategy, Cont. Shelf Res., 31, 135–149, https://doi.org/10.1016/j.csr.2010.12.009, 2011.

Lehmuskero, A., Skogen Chauton, M., and Boström, T.: Light and photosynthetic microalgae: A review of cellular- and molecular-scale optical processes, Prog. Oceanogr., 168, 43–56, https://doi.org/10.1016/j.pocean.2018.09.002, 2018.

Le Pape, O. and Menesguen, A.: Hydrodynamic prevention of eutrophication in the Bay of Brest (France), a modelling approach, J. Mar. Syst., 12, 171–186, https://doi.org/10.1016/S0924-7963(96)00096-6, 1997.

Liu, X., Dunne, J. P., Stock, C. A., Harrison, M. J., Adcroft, A., and Resplandy, L.: Simulating water residence time in the coastal ocean: A global perspective, Geophys. Res. Lett., 46, 13910–13919, https://doi.org/10.1029/2019GL085097, 2019.

Ménesguen, A., Dussauze, M., and Dumas, F.: Designing optimal scenarios of nutrient loading reduction in a WFD/MSFD perspective by using passive tracers in a biogeochemical-3D model of the English Channel/Bay of Biscay area, Ocean Coast. Manag., 163, 37–53, https://doi.org/10.1016/j.ocecoaman.2018.06.005, 2018.

Ménesguen, A., Dussauze, M., Dumas, F., Thouvenin, B., Garnier, V., Lecornu, F., and Répécaud, M.: Ecological model of the Bay of Biscay and English Channel shelf for environmental status assessment part 1: Nutrients, phytoplankton and oxygen, Ocean Modelling, 133, 56–78, https://doi.org/10.1016/j.ocemod.2018.11.002, 2019.

Mengual B., Le Hir P., Cayocca F., and Garlan T.: Modelling fine sediment dynamics: Towards a common erosion law for fine sand, mud and mixtures, Water, 9, 564, https://doi.org/10.3390/w9080564, 2017.

Merceron, M.: Impact du barrage d'Arzal sur la qualité des eaux de l'estuaire de la baie de Vilaine, 31 pp., Ifremer, Brest, France, 1985 (in French).

Mikaelyan, A., Chasovnikov, V., Kubryakov, A., and Stanichny, S.: Phenology and drivers of the winter-spring phytoplankton bloom in the open Black Sea: The application of Sverdrup's hypothesis and its refinements, Prog. Oceanogr., 151, 163–176, https://doi.org/10.1016/j.pocean.2016.12.006, 2017.

Muller, H., Blanke, B., Dumas, F., and Mariette, V.: Identification of typical scenarios for the surface Lagrangian residual circulation in the Iroise Sea, J. Geophys. Res., 115, 1–14, https://doi.org/10.1029/2009JC005834, 2010.

Oliver, E., Donat, M., Burrows, M., Moore, P., Smale, D., Alexanda, L., Benthuysen, J., Feng, M., Sen Gupta, A., Hobday, A., Holbrook, N., Perkins-Kirkpatrick, S., Scannell, H., Straub, S., and Wernberg, T.: Longer and more frequent marine heatwaves over the past century, Nat. Commun., 9, 1324, https://doi.org/10.1038/s41467-018-03732-9, 2018.

Paerl, H. W., Hall, N. S., Peierls, B. L., and Rossignol, K. L.: Evolving paradigms and challenges in estuarine and coastal eutrophication dynamics in a culturally and climatically stressed world, Estuar. Coast., 37, 243–258, https://doi.org/10.1007/s12237-014-9773-x, 2014.

Peierls, B. L., Hall, N. S., and Paerl, H. W.: Non-monotonic responses of phytoplankton biomass accumulation to hydrologic variability: a comparison of two coastal plain North Carolina estuaries, Estuar. Coast., 35, 1376–1392, https://doi.org/10.1007/s12237-012-9547-2, 2012.

Petton, S., Pouvreau, S., and Dumas, F. Intensive use of Lagrangian trajectories to quantify coastal area dispersion, Ocean Dynam., 70, 541–559, https://doi.org/10.1007/s10236-019-01343-6, 2020.

Philippart, C. J. M., van Iperen, J. M., Cadée, G. C., and Zuur, A. F.: Long-term field observations on seasonality in chlorophyll-a concentrations in a shallow coastal marine ecosystem, the Wadden Sea, Estuar. Coast., 33, 286–294, https://doi.org/10.1007/s12237-009-9236-y, 2010.

Pingree, R. D. and Le Cann, B.: Celtic and Armorican slope and shelf residual currents, Prog. Oceanogr., 23, 303–338, https://doi.org/10.1016/0079-6611(89)90003-7, 1989.

Plus, M., Thouvenin, B., Andrieux, F., Dufois, F., Ratmaya, W., and Souchu, P.: Diagnostic étendu de l'eutrophisation (DIETE), Modélisation biogéochimique de la zone Vilaine-Loire avec prise en compte des processus sédimentaires, Description du modèle Bloom (BiogeochemicaL coastal Ocean Model), RST/LER/MPL/21.15, https://archimer.ifremer.fr/doc/00754/86567/ (last access: 20 March 2022), 2021.

Poppeschi, C., Charria, G., Goberville, E., Rimmelin-Maury, P., Barrier, N., Petton, S., Unterberger, M., Grossteffan, E., Repeccaud, M., Quéméner, L., Le Roux, J.-F., and Tréguer, P.: Unraveling salinity extreme events in coastal environments: a winter focus on the bay of Brest, Front. Mar. Sci., 8, 705403, https://doi.org/10.3389/fmars.2021.705403, 2021.

Quéguiner, B. and Tréguer, P.: Studies on the Phytoplankton in the Bay of Brest (Western Europe), Seasonal Variations in Composition, Biomass and Production in Relation to Hydrological and Chemical Features (1981—1982), Bot. Mar., 27, 449–459, 1984.

Ragueneau, O., Quéguiner, B., and Tréguer, P.: Contrast in biological responses to tidally-induced vertical mixing for two macrotidal ecosystems of western Europe, Estuar. Coast. Shelf Sci., 42, 645–665, https://doi.org/10.1006/ecss.1996.0042, 1996.

Ragueneau, O., Chauvaud, L., Leynaert, A., Thouzeau, G., Paulet, Y. M., Bonnet, S., Lorrain, A., Grall, J., Corvaisier, R., Le Hir, M., Jean, F., and Clavier, J.: Direct evidence of a biologically active coastal silicate pump: ecological implications, Limnol. Oceanogr., 47, 1849–1854, https://doi.org/10.4319/lo.2002.47.6.1849, 2002.

Ragueneau, O., Raimonet, M., Mazé, C., Coston-Guarini, J., Chauvaud, L., Danto, A., Grall, J., Jean, F., Paulet Y.-M., and Thouzeau, G.: The impossible sustainability of the Bay of Brest? Fifty years of ecosystem changes, interdisciplinary knowledge construction and key questions at the science-policy-community interface, Front. Mar. Sci., 5, 124, https://doi.org/10.3389/fmars.2018.00124, 2018.

Ratmaya, W., Soudant, D., Dalmon-Monviola, J., Plus, M., Cochennec-Laureau, N., Goubert, E., Andrieux-Loyer, F., Barillé, L., and Souchu, P.: Reduced phosphorus loads from the Loire and Vilaine rivers were accompanied by increasing eutrophication in the Vilaine Bay (south Brittany, France), Biogeosciences, 16, 1361–1380, https://doi.org/10.5194/bg-16-1361-2019, 2019.

Ratmaya, W., Laverman, A. M., Rabouille, C., Akbarzadeh, Z., Andrieux-Loyer, F., Barillé, L., Barillé, A.-L., Le Merrer, Y., and Souchu, P.: Temporal and spatial variations in benthic nitrogen cycling in a temperate macro-tidal coastal ecosystem: Observation and modeling, Cont. Shelf Res., 235, https://doi.org/10.1016/j.csr.2022.104649, 2022.

Répécaud, M., Quemener, L., Charria, G., Pairaud, I., Rimmelin, P., Claquin, P., Jacqueline, F., Lefebvre, A., Facq, J. V., Retho, M., and Verney, R.: National observation infrastructure: an example of a fixed-platforms network along the French Coast: COAST HF, OCEANS 2019, Marseille, IEEE, 1–6, https://doi.org/10.1109/OCEANSE.2019.8867451, 2019.

REPHY: French Observation and Monitoring program for Phytoplankton and Hydrology in coastal waters, REPHY dataset – French Observation and Monitoring program for Phytoplankton and Hydrology in coastal waters, Metropolitan data, SEANOE, https://doi.org/10.17882/47248, 2021.

Retho, M., Quemener, L., Le Gall, C., Repecaud, M., Souchu, P., Gabellec, R., and Manach, S.: COAST-HF – data and metadata from the MOLIT buoy in the Vilaine Bay, SEANOE [data set], https://doi.org/10.17882/46529, 2022.

Rimmelin-Maury, P., Charria, G., Repecaud, M., Quemener, L., Beaumont, L., Guillot, A., Gautier, L., Prigent, S., Le Becque, T., Bihannic, I., Bonnat, A., Le Roux, J.-F., Grossteffan, E., Devesa, J., Bozec, Y.: Iroise buoy s data from Coriolis data center as core parameter support for Brest Bay and Iroise sea studies, SEANOE [data set], https://doi.org/10.17882/74004, 2020.

Rossignol-Strick, M.: A marine anoxic event on the Brittany coast, July 1982, J. Coast. Res., 11–20, https://www.jstor.org/stable/4297005 (last access: 20 March 2022), 1985.

Rumyantseva, A., Henson, S., Martin, A., Thompson, A. F., Damerell, G. M., Kaiser, J., and Heywood, K. J.: Phytoplankton spring bloom initiation: The impact of atmospheric forcing and light in the temperate North Atlantic, Ocean, Prog. Oceanogr., 178, 102202, https://doi.org/10.1016/j.pocean.2019.102202, 2019.

Saeck, E. A., Hadwen, W. L., Rissik, D., O'Brien, K. R., and Burford, M. A.: Flow events drive patterns of phytoplankton distribution along a river–estuary–bay continuum, Mar. Freshw. Res., 64, 655–670, https://doi.org/10.1071/MF12227, 2013.

Sathyendranath, S., Ji, R., and Browman, H. I.: Revisiting Sverdrup's critical depth hypothesis, ICES J. Mar. Sci., 72, 1892–1896, https://doi.org/10.1093/icesjms/fsv110, 2015.

Schlegel, R. W., Darmaraki, S., Benthuysen, J. A., Filbee-Dexter, K., and Oliver, E. C.: Marine cold-spells, Prog. Oceanogr., 198, 102684, https://doi.org/10.1101/2021.10.18.464880, 2021.

Serre-Fredj, L., Jacqueline, F., Navon, M., Izabel, G., Chasselin, L., Jolly, O., Repecaud, M., and Claquin, P.: Coupling high frequency monitoring and bioassay experiments to investigate a harmful algal bloom in the Bay of Seine (French-English Channel), Mar. Pollut. Bull., 168, 112387, https://doi.org/10.1016/j.marpolbul.2021.112387, 2021.

Smetacek, V. and Cloern, J. E.: On phytoplankton trends, Science, 319, 1346–1348, https://doi.org/10.1126/science.1151330, 2008.

Sommer, U., Adrian, R., De Senerpont Domis, L., Elser, J. J., Gaedke, U., Ibelings, B., Jeppesen, E., Lürling, M., Molinero, J. C., Mooij, W. M., van Donk, E., and Winder, M.: Beyond the Plankton Ecology Group (PEG) model: mechanisms driving plankton succession, Ann. Rev. Ecol. Evolut. Syst., 43, 429–448, https://doi.org/10.1146/annurev-ecolsys-110411-160251, 2012.

Sverdrup, H.: On vernal blooming of phytoplankton, Conseil Exp. Mer, 18, 287–295, 1953.

Thyssen, M., Tarran, G. A., Zubkov, M. V., Holland, R. J., Grégori, G., Burkill, P. H., and Denis, M.: The emergence of automated high-frequency flow cytometry: revealing temporal and spatial phytoplankton variability, J. Plank. Res., 30, 333–343, https://doi.org/10.1093/plankt/fbn005, 2008.

Tian, T., Merico, A., Su, J., Staneva, J., Wiltshire, K., and Wirtz, K.: Importance of resuspended sediment dynamics for the phytoplankton spring bloom in a coastal marine ecosystem, J. Sea Res., 62, 214–228, https://doi.org/10.1016/j.seares.2009.04.001, 2009.

Tian, T., Su, J., Flöser, G., Wiltshire, K., and Wirtz, K.: Factors controlling the onset of spring blooms in the German Bight 2002–2005: light, wind and stratification, Cont. Shelf Res., 31, 1140–1148, https://doi.org/10.1016/j.csr.2011.04.008, 2011.

Townsend, D. W., Cammen, L. M., Holligan, P. M., Campbell, D. E., and Pettigrew, N. R.: Causes and consequences of variability in the timing of spring phytoplankton blooms, Deep-Sea Res. Pt. I, 41, 747–765, https://doi.org/10.1016/0967-0637(94)90075-2, 1994.

Trombetta, T., Vidussi, F., Mas, S., Parin, D., Simier, M., and Mostajir, B.: Water temperature drives phytoplankton blooms in coastal waters, PloS One, 14, e0214933, https://doi.org/10.1371/journal.pone.0214933, 2019.

Wiltshire, K. H., Malzahn, A. M., Wirtz, K., Greve, W., Janisch, S., Mangelsdorf, P., Manly, B., and Boersma, M.: Resilience of North Sea phytoplankton spring bloom dynamics: An analysis of long-term data at Helgoland Roads, Limnol. Oceanogr., 53, 1294–1302, https://doi.org/10.4319/lo.2008.53.4.1294, 2008.

Wiltshire, K. H., Boersma, M., Carstens, K., Kraberg, A. C., Peters, S., and Scharfe, M.: Control of phytoplankton in a shelf sea: determination of the main drivers based on the Helgoland Roads Time Series, J. Sea Res.h, 105, 42–52, https://doi.org/10.1016/j.seares.2015.06.022, 2015.

Chapitre 7 Conclusions

Dans cette thèse, les principaux objectifs étaient d'identifier, de caractériser et de comprendre les processus associés aux EE à l'échelle de l'océan côtier français sur les dernières décennies.

7.1 Identifier les évènements extrêmes

Pour détecter les EE côtiers, j'ai pu montrer au travers d'études de différents systèmes côtiers que la méthode de seuil permet d'identifier et de comprendre la dynamique des évènements extrêmes en milieu côtier. La méthode de seuil permet de prendre en compte la variabilité temporelle de l'évènement et est facilement adaptable selon la région étudiée à n'importe quel extrême que ce soit les extrêmes environnementaux (extrême d'une variable océanique) ou les forçages extrêmes (extrême d'un forçage atmosphérique).

Le seuil est associé à un percentile qui doit être adapté pour que les extrêmes considérés représentent des évènements rares (percentile 5, 10, 15 ou 85, 90, 95) et pas seulement exceptionnels (percentile 1 ou 99) afin d'exploiter des statistiques représentatives du milieu et de caractériser les EE. Le percentile peut être choisi selon la distribution statistique du paramètre. Le percentile doit être extrême (percentile 5 à 10 ou 90 à 95) si la distribution du paramètre a une faible amplitude et avec un écart-type élevé, c'est à dire des valeurs dispersées par rapport à la moyenne (cas des paramètres tels que le débit des fleuves, la température de surface de la mer et la turbidité). Si la distribution du paramètre présente une forte amplitude et un faible écart-type, le percentile pourra être moins extrême (percentile 10 à 15 ou 85 à 90, cas de la salinité, la fluorescence et l'oxygène dissous). De plus, certains paramètres ont une tolérance au seuil plus ou moins importante. Par exemple, une faible variation du nombre de détection des EE entre les percentiles 80 à 99 (ou de 1 à 20 pour l'oxygène) est observée pour la fluorescence et la concentration en oxygène dissous alors qu'elle est très élevée pour le débit et la turbidité. Le choix de la valeur du percentile est donc capital le nombre d'EE détectés.

La période temporelle utilisée pour la méthode de seuil est également cruciale. La durée d'application du seuil a un rôle important si le paramètre a une variance importante (cas du débit et de la salinité). Par contre, si la variance est faible (cas de la température, la salinité, la fluorescence), une période d'application du seuil qu'elle soit de 10 ou 30 ans n'a que très peu, voire pas du tout, d'influence.

Enfin, pour tous les paramètres étudiés dans cette thèse, la variabilité temporelle du seuil est importante à prendre en compte dans la détection des EE. Une variabilité mensuelle du seuil peut être appliquée à tout type d'extrême et permettra une analyse approfondie et précise des EE.

Des méthodes innovantes ont été testées, discutées et validées au cours de la thèse:

- Pour l'étude des vagues marines de chaleur et de froid, un paramètre intégrateur regroupant l'intensité, la durée et l'étendue spatiale (nommé activité, Simon et al., 2022) a été utilisé pour décrire la dynamique des EE.

- Une nouvelle méthode de détection de l'initiation de la période productive du phytoplancton en milieu côtier a été développée à partir de données *in situ* haute fréquence pour comprendre l'impact des EE. Un modèle 1DV a été mis en place pour mieux comprendre les processus en jeu.

- Une méthode de détection originale des forçages extrêmes des vagues et des crues a été élaborée à partir d'un seuil variable tout au long de l'année. Ces forçages extrêmes ont aussi été analysés sous forme d'évènements concomitants.

Le développement de l'ensemble de ces méthodes a répondu à une nécessité d'adapter les approches selon les évènements analysés et les dynamiques des systèmes considérés.

7.2 Caractériser les évènements extrêmes

Les caractéristiques des évènements extrêmes

Les EE peuvent être caractérisés par leur nombre, leur intensité, leur durée, leur étendue spatiale, leur période d'occurrence, leur succession et leur période de retour. L'ensemble de ces caractéristiques permet de définir chaque EE. Mes analyses montrent que la classification des EE est rarement prise en compte alors que c'est un outil intéressant à mettre en place surtout pour des évènements uniques et historiques tels que les tempêtes.

J'ai ainsi pu montrer une intensification des évènements extrêmes en termes de fréquence et de durée. Les MHW observées en Atlantique Nord-Est sont plus fréquentes, plus longues et avec des étendues spatiales plus importantes et inversement pour les MCS. La Manche est une zone où les caractéristiques des EE de MHW et MCS évoluent encore plus rapidement que dans le Golfe de Gascogne. Les années 2018 dans le Golfe de Gascogne et 2022 en Manche sont associées à des EE très importants. Les MCS de 1986 et 1987 en Manche présentent les valeurs d'activité les plus intenses. Les dessalures extrêmes en rade de Brest sont plus nombreuses et plus longues cette dernière décennie au regard de la période analysée (1982-2022).

La succession des tempêtes reliées aux extrêmes de vagues et de crues n'a pas d'impact significatif sur les MES en baie de Seine. Les forçages extrêmes en baie de Seine montrent une réponse saisonnière des MES. Ainsi, les pics de turbidité sont observés essentiellement en hiver quand les forçages sont forts et les pics de turbidité sont moins intenses face aux forçages extrêmes du printemps, été et automne. Nous avons cependant observé des exceptions avec, par exemple, la crue de juillet 2016 en baie de Seine, qui est un EE très intense pour une période

temporelle estivale. Lors de cette crue qui a atteint les 2000 m^3 s^{-1}, le panache sédimentaire s'est propagé loin dans la baie jusqu'à 0.3°W alors qu'il est plutôt proche de l'embouchure lors de conditions calmes (vers 0°W).

Une inflexion dans l'activité des EE: 2010

Les évolutions des EE sont rapides, et même si les séries temporelles *in situ* étudiées au cours de cette thèse sont courtes, de nombreuses variations sont observées. Un point de bascule autour de 2010 ressort particulièrement des études réalisées pendant cette thèse. Les MHW augmentent depuis 2000 avec une accentuation en 2010 en Atlantique Nord-Est. De même, les MCS diminuent avec plus d'évènements après 2000. Les dessalures sont plus présentes en rade de Brest cette dernière décennie. Les crues de la Seine sont plus fortes cette dernière décennie, mais l'évolution des EE en hydrodynamique sédimentaire et des vagues n'est pas détectable. L'initiation de la période productive du phytoplancton a été de plus en plus précoce entre 2000 et 2010 en rade de Brest, puis de plus en plus tardive entre 2010 et 2020 en rade de Brest et en baie de Vilaine. Cette inflexion observée en 2010 n'a pas pu être expliquée par des évolutions des conditions atmosphériques et reste à documenter.

7.3 Comprendre les évènements extrêmes

Une réponse régionale en lien avec l'hydrodynamique

Les MHW, MCS et les dessalures dans l'océan côtier sont des EE qui présentent des signaux comparables à ceux de l'océan ouvert. Les MHW et MCS comme les dessalures sont contrôlées par les variations atmosphériques de grandes échelles cycloniques et anticycloniques. Les MHW se développent plus favorablement lors de la phase positive de l'oscillation Nord-Atlantique dans l'Atlantique Nord-Est, tandis que les conditions de basse pression dominantes sur l'Europe du Nord et un anticyclone au large de la péninsule ibérique en hiver favorisent la présence de MCS. Les dessalures sont contrôlées par la phase positive de l'oscillation Nord-Atlantique et les périodes de faible occurrence du régime météorologique de la dorsale Atlantique.

Ces variations grandes échelles engendrent des modifications extrêmes au niveau local concernant les crues des rivières, les précipitations, le vent et l'ensoleillement qui vont agir sur la température et la salinité dans l'océan côtier et provoquer ces extrêmes environnementaux. Toutefois, des processus locaux agissent sur les vagues marines de froid et de chaleur comme sur les dessalures qui vont être favorisées ou défavorisées selon le type d'environnement côtier étudié tel que les baies, estuaires, lagunes, étangs. J'ai exposé le fait qu'une baie semi-fermée comme la rade de Brest, desservie par trois rivières, présente une réponse importante aux précipitations générant des dessalures.

Une réponse saisonnière pour la dynamique sédimentaire

Les panaches turbides contrôlés par le débit des rivières et les vagues en zone côtière présentent une forte saisonnalité. L'étude de ces forçages extrêmes révèle une faible réponse de l'hydrodynamique sédimentaire face à ces EE. L'hydrodynamique sédimentaire est contrôlée avant tout par un seuil de remise en suspension du sédiment correspondant à une certaine tension sur le fond liée au débit et aux vagues. La réponse des matières en suspensions aux forçages extrêmes se traduit dans l'intensité et la durée des EE. L'intensité des MES est proportionnelle à l'intensité des vagues. La durée des MES est proportionnelle à la durée des crues. Les MES varient en fonction des forçages extrêmes mais aussi par rapport aux variations saisonnières, aux marées, à l'intensité du vent, des vagues et du débit du fleuve. L'étude de la variabilité interannuelle des forçages extrêmes de vagues et de crues sur plusieurs années a révélé une légère augmentation cette dernière décennie (2010-2020) en lien avec leurs augmentations moyennes.

Une réponse locale du compartiment biologique

La variabilité interannuelle du début de la période de croissance du phytoplancton (IPGP) sur les deux dernières décennies montre des évolutions fortes avec des dates d'IPGP qui varient jusqu'à 30 jours entre deux décennies consécutives. Ces évolutions d'IPGP précoces ou tardives au printemps sont liées à de multiples paramètres locaux, principalement la température et la turbidité. L'IPGP a lieu lorsque la SST atteint une température minimale de 10°C et une turbidité maximale de 7 NTU. Les phénomènes extrêmes comme les crues et les MCS retardent l'IPGP alors que les coups de vent n'ont pas d'impact. L'étude menée à l'échelle interannuelle montre que, pour chaque année analysée, la nature des EE est différente. L'IPGP peut aussi être influencée par un seul EE comme, par exemple, une MCS d'au moins 15 jours en fin d'hiver.

7.4 Les évènements extrêmes, un enjeu scientifique en pleine évolution

L'identification des EE reste sensible aux approches considérées. Selon la méthode utilisée, j'ai pu constater que les résultats diffèrent en termes de nombre, d'intensité voir de durée de l'EE. La méthode de détection des EE est souvent dépendante de l'EE étudié. Certaines méthodes de détection d'EE, comme celles des MHW ou les hypoxies ont abouti à un consensus scientifique mais elles nécessitent une révision en raison de l'évolution des effets du changement climatique. Le changement global évoluant rapidement, les études portant sur l'ensemble de l'année sont à favoriser par rapport à celles menées sur une saison de l'année. Les vagues marines de chaleur et de froid pourraient être explorées avec un seuil de détection variant aux alentours de leur saison favorable d'apparition (mai à septembre) au lieu d'un seuil fixe de juin à août. L'étendue spatiale de l'ensemble des EE évolue et leur dynamique nécessite une étude sur tous les écosystèmes.

Les extrêmes environnementaux (MHW, MCS, dessalures) et les forçages extrêmes (précipitations, vagues, crues, vent) présentent une augmentation en termes d'activité ces deux

dernières décennies avec une accentuation cette dernière décennie. J'ai montré l'intensification de ces EE dans le milieu côtier et mis en évidence un point d'inflexion en 2010.

Enfin, la compréhension des EE reste complexe du fait des cascades d'impacts qui en découlent. J'ai observé que les EE sont multiples et dépendent des forçages locaux comme globaux. Les impacts des EE englobent tous les compartiments de l'océan côtier, c'est-à-dire l'hydrodynamique, la dynamique sédimentaire, la biologie et la biogéochimie. La crue extrême détectée en baie de Seine en juillet 2016 est un exemple type de potentiel début de cascade dans l'environnement par un EE car elle a provoqué de façon inhabituelle une forte réponse en intensité et en durée des MES pendant l'été.

Chapitre 8 Perspectives

Suite à ces travaux de thèse, certaines interrogations sont posées et de nouvelles pistes de recherche sont établies. Des perspectives sur l'analyse des différents EE étudiés dans la thèse (MHW, les MCS, les dessalures extrêmes, la réponse de la turbidité face aux tempêtes et l'impact des extrêmes sur l'IPGP) sont présentées ainsi qu'une analyse préliminaire de phénomènes d'hypoxie en baie de Vilaine.

8.1 Vers des indicateurs d'évènements extrêmes en milieu côtier

Extrêmes de température dans la colonne d'eau

J'ai montré que la dynamique des extrêmes de température de la mer tend vers une augmentation des épisodes de MHW et une diminution des épisodes de MCS dans l'océan côtier comme dans l'océan ouvert. Cependant, mon étude est limitée par le fait que seules des données de surface ont été utilisées alors que l'ensemble de la colonne d'eau doit être prise en compte pour connaître l'impact des MHW sur les échelons trophiques. Il convient donc d'étendre les analyses afin de quantifier la propagation des vagues de températures extrêmes dans la colonne d'eau et de se préparer à leurs impacts (Smith et al., 2023). Cette pénétration de chaleur dans la colonne d'eau peut être quantifiée au travers de différents bilans et études de flux. Par exemple, les données de stratification de la colonne d'eau sont intéressantes à prendre en compte pour évaluer l'extension en profondeur des MHW et MCS. D'une part, certains produits *in situ* permettraient une première exploration comme les campagnes océanographiques côtières, les mesures d'opportunités (telles que celles issues des Fishery Observing Systems) ainsi que les profils établis par les réseaux de mesure basse fréquence comme SOMLIT et REPHY à la côte. Plus largement, des simulations existent dans la colonne d'eau (marc.ifremer.fr - data.shom.fr - les simulations issues du service marin de Copernicus - CMEMS) mais leurs couvertures temporelles (plusieurs décennies consécutives) et les résolutions spatiales (quelques dizaines de m) doivent être étendues afin de mieux étudier la dynamique des EE et leur évolution dans le temps.

Enfin, pour mieux prédire l'occurrence des MHW et MCS dans l'océan côtier, il convient de mettre en place des suivis de mesures et/ou des modèles numériques pouvant permettre d'évaluer plus précisément le temps de réponse entre les vagues de chaleur et de froid atmosphériques et celles de l'océan. A cela devrait être ajouté un calcul de coefficient de mélange des masses d'eau, à partir d'observations, qui peut empêcher la propagation de ces extrêmes dans la colonne d'eau. Ce coefficient de mélange devra prendre en compte les courants produits par le vent, les vagues, la marée et le débit des fleuves côtiers. A partir d'une meilleure compréhension des processus, il peut être envisagé de déterminer un facteur d'impact des MHW sous forme d'indicateur. Ce facteur d'impact pourrait combiner l'intensité des MHW et les conditions de mélange de la zone océanique étudiée pendant une période précise afin de mieux estimer l'impact et la probable étendue des MHW.

Dessalures extrêmes sous influence des fleuves

Les régimes de temps Nord-Atlantique régissent les précipitations extrêmes sur les bassins versants qui en remplissant le lit des rivières se déversent dans l'océan côtier et sont à l'origine de dessalures extrêmes, comme par exemple en rade de Brest. Dans ma thèse, l'étude a été réalisée uniquement lors de la période hivernale ce qui ne permet pas d'évaluer son impact sur la biologie lors de la période productive au printemps et en été. Pour pallier ces limitations et pour comprendre au mieux ces dessalures extrêmes, il faut s'interroger sur deux points cruciaux :

- Quel est l'impact des dessalures extrêmes dans l'environnement côtier ? Les dessalures extrêmes jouent un rôle important sur la stratification des eaux côtières en déversant un panache d'eau douce important et de façon soudaine dans le milieu côtier marin. Il est donc nécessaire d'effectuer cette étude tout au long de l'année pour voir l'impact de ces dessalures extrêmes sur le compartiment biologique lors de la période productive. Cette stratification, lorsqu'elle intervient après une importante efflorescence algale, peut entraîner des phénomènes d'hypoxie, voire d'anoxie, comme cela est évoqué en perspective de cette thèse (cf. section 8.2). Les dessalures extrêmes peuvent engendrer à elles seules des effets néfastes pour l'environnement comme la mortalité soudaine d'huîtres (La Peyre et al., 2013). Ces études doivent donc être étendues à d'autres milieux côtiers sous influence de fleuves.

- Quel est l'indicateur clé à prendre en compte pour la détection de dessalures extrêmes ? Les précipitations extrêmes contrôlent les dessalures extrêmes dans le cas de bassins versants aux sols imperméables ou saturés en eau. Pour une meilleure prédiction, la planification des tempêtes pluvieuses enregistrées par Météo-France via des calculs de période de retour basés sur des jeux de données historiques pourrait être un excellent indicateur. Le fait d'avoir un indicateur météorologique, plutôt qu'océanique, est un avantage car il permet une prédiction anticipée et plus précise. Enfin, le développement de modèles numériques, qui intègrent le continuum terre-mer pour calculer de manière fiable l'écoulement d'une particule d'eau depuis sa chute dans le bassin versant jusqu'à son arrivée dans l'océan côtier, est primordial. Pour suivre le devenir des précipitations extrêmes dans l'océan côtier, il faudrait coupler des modèles de cycle de l'eau au niveau atmosphérique, au niveau de chaque bassin versant et au niveau océanique. Ce couplage devra prendre en compte la morphologie du bassin versant et la nature des sols.

Réponse de la turbidité face aux extrêmes dans d'autres environnements côtiers

Les forçages extrêmes détectés en baie de Seine sont représentatifs des tempêtes qui s'abattent dans la Manche. D'autres sites très turbides de la Manche sont soumis à ces forçages extrêmes. Les réponses obtenues en baie de Seine pourraient être comparées à celles observées sur les côtes belges au niveau de la rencontre entre la Manche et la mer du Nord (Fettweis et al., 2010). L'intérêt serait d'analyser la réponse en MES lors d'une tempête et de comparer

plusieurs sites d'étude placés sur sa trajectoire. Est-ce que les MES évoluent selon leurs emplacements vis-à-vis du forçage sur la côte en prenant en compte la géographie de la zone ?

Le lien entre crue extrême et variabilité moyenne du débit doit encore être exploré sur les trois façades maritimes françaises car des différences significatives pourraient être trouvées régionalement (Madsen et al., 2014 ; Jalon-Rojas et Castelle, 2021). Est-ce que les vagues extrêmes liées aux tempêtes présentent une augmentation selon les façades maritimes avec au nord, plus de tempêtes dans la Manche et au sud, moins de tempêtes dans le Golfe de Gascogne et la Méditerranée (Feser et al., 2015) ? Les outils de modélisation actuels permettent-ils de prévoir les forçages extrêmes ?

Evolution des écosystèmes côtiers: initiation de la période productive phytoplanctonique

La limite majeure de cette étude réside dans l'utilisation d'un modèle à une dimension verticale qui ne prend pas en compte l'hydrodynamique des zones d'études. Des simulations en trois dimensions doivent être exécutées sur ces zones côtières pour simuler l'importance de l'arrivée des flux de rivière, de la marée sur la circulation de la zone étudiée. L'IPGP requiert un faible mélange des masses d'eau pour pouvoir débuter. Différents modèles (MARS3D, CROCO) existent et permettraient de réaliser cette analyse.

8.2 Phénomènes d'hypoxie en baie de Vilaine

J'ai étudié les EE dans le milieu côtier en partant du compartiment physique avec les MHW, MCS et les dessalures extrêmes. Puis je me suis intéressée à la dynamique sédimentaire et sa réponse aux tempêtes pour finir avec le compartiment biologique et la modification de la période de l'IPGP lors d'EE. Pour faire suite à cette logique, après avoir analysé le phytoplancton en terme de biomasse dans le milieu côtier, la dynamique de l'oxygène dissous est étudiée à travers l'observation des phénomènes d'hypoxie et d'anoxie.

L'océan global présente une baisse de la teneur en oxygène et cette diminution est encore plus marquée dans l'océan côtier (Breitburg et al., 2018). Ces phénomènes de désoxygénation ont des conséquences dramatiques sur l'environnement comme des mortalités de masse de mollusques et de poissons (Andersen et Hepner-Medina, 2020) qui engendrent des impacts économiques dans l'aquaculture et la pêche, ou encore des modifications de taille et de reproduction de certaines espèces benthiques et pélagiques.

En suivant la démarche mise en place pendant la thèse (Chapitre 2), les phénomènes de désoxygénation sont évalués à partir de la bouée MOLIT du réseau COAST-HF qui mesure la concentration en oxygène dissous en surface et au fond (**Figure 8-1**). La baie de Vilaine (Chapitre 6) est connue pour l'apparition fréquente d'hypoxies, voire d'anoxies, qui ont conduit à des mortalités de masses de poissons et d'huîtres (Rossignol-Strick, 1985; Chapelle et al., 1994).

Des systèmes de mesure de fond MASTODON Oxygène, dont le système de largage a été décrit par Lazure et al. (2015, 2019), ont été déployés de mai à octobre entre 2020 et 2023 sur six sites de la baie de Vilaine (**Figure 8-1**) pour mesurer la concentration en oxygène dissous à 15 cm au-dessus du sédiment toutes les 10 minutes. Les sites ont été choisis pour décrire le gradient de dilution de la Vilaine et certains ont été placés stratégiquement au niveau de zones conchylicoles.

Des données de salinité et de température ont été obtenues avec le modèle MARS3D dans sa configuration MANGA (Yelekçi et al., 2017) pour établir la densité de l'eau et calculer la stratification de la colonne d'eau.

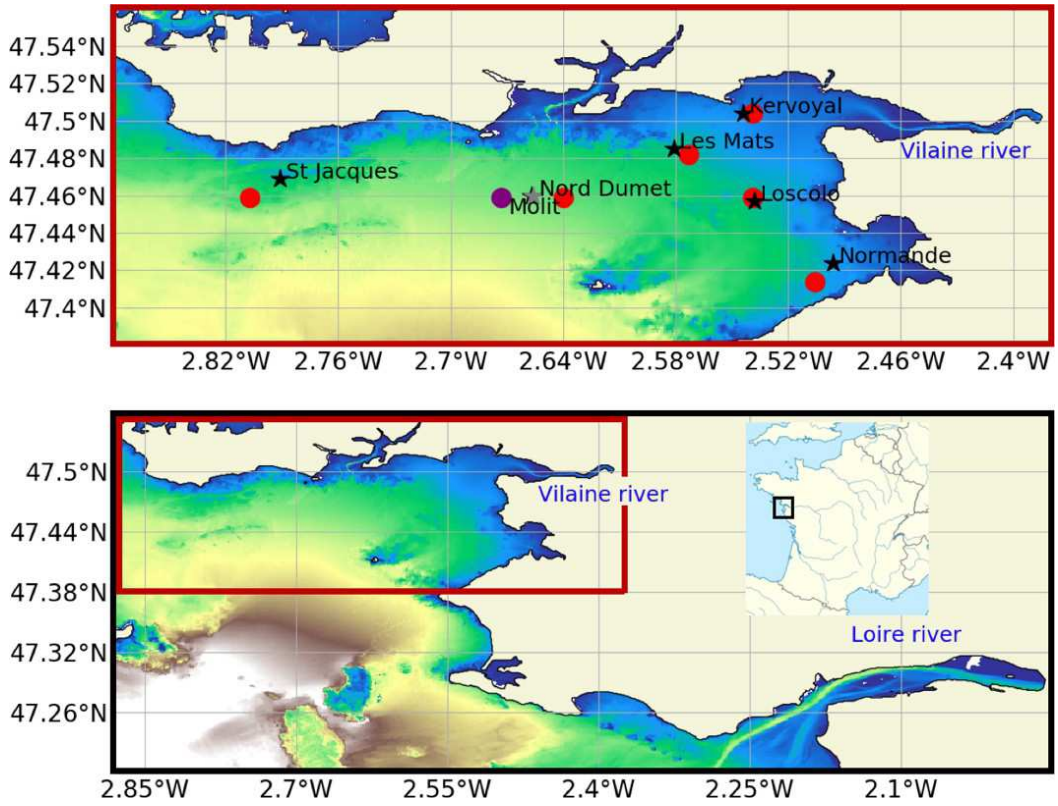

Figure 8-1 Carte de présentation de la baie de Vilaine avec la bouée MOLIT (rond violet), les mastodons déployés (ronds rouges) et les points de grille du modèle associés (étoiles noires)

La variabilité interannuelle est analysée à partir d'évènements de désoxygénation par rapport au seuil établi par la communauté scientifique de 5 mg L^{-1}.

Le nombre de désoxygénations observé à MOLIT a diminué en passant de 7 à 4 de 2020 à 2022 (**Tableau 8-1**). Cependant, le nombre d'évènements doit être analysé avec prudence car si on utilise le percentile 5, l'évolution est inverse avec 2 désoxygénations en 2020 détectées contre 1 en 2021 et 4 en 2022. La variabilité saisonnière est intéressante à observer avec des désoxygénations en 2021 et 2022 uniquement en juin et juillet alors qu'en 2020 celles-ci étaient présentes de mai à septembre. En revanche, l'évolution vers des désoxygénations plus longues dans le temps n'apparaît pas au cours de ces trois années.

Année	2020	2021	2022
Nombre de désoxygénation	7	6	4
Mois d'occurrence	Mai à Septembre	Juin à Juillet	Juin à Juillet
Pic minimal (mg L^{-1})	2.96	2.60	2.24
Pic médian (P10)	3.44	3.42	2.60
Durée maximale (jours)	13	6	10
Durée médiane (P10)	4.57	3.83	6

Tableau 8-1 Caractéristiques interannuelles des désoxygénations détectées à la bouée Molit de 2020 à 2022

(a)

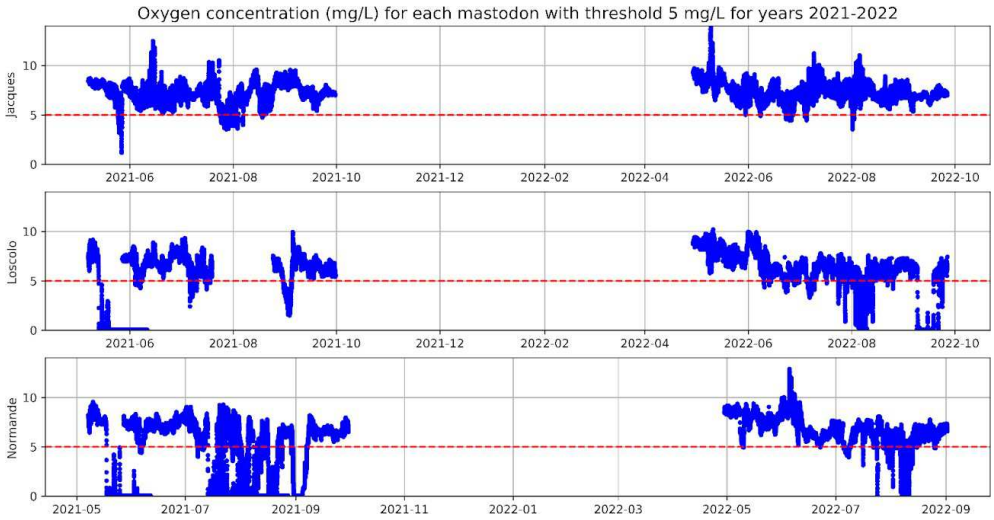

(b)

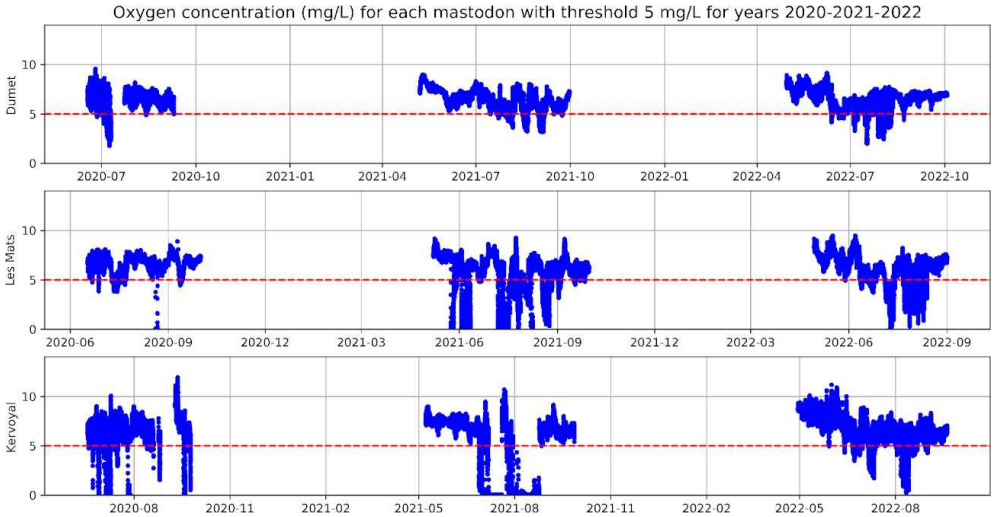

Figure 8-2 Oxygène dissous de fond enregistré par les MASTODON (a) de 2021 à 2022 aux stations St Jacques, Loscolo et Normande et (b) de 2020 à 2022 aux stations Dumet, Les Mats et Kervoyal

Les signaux d'oxygène dissous mesurés au fond par les 6 MASTODON mettent en évidence 3 évènements particuliers (Figure 8-2 & Tableau 8-2) qui sont brièvement décrits pour illustrer les processus expliquant les EE observés en oxygène en Baie de Vilaine.

- Le premier évènement du 27 juin 2020 est également observé à la bouée Molit et est en lien avec une crue de la Vilaine du 10 au 30 juin avec des valeurs de débit fortes pour la saison estivale (maximum à 120 m^3 s^{-1}, **Annexe 2**). Cet évènement a eu lieu en période de mortes eaux (coefficients de 63 et 66) et s'observe sur le gradient côte/large : quatre évènements anoxiques (0.03 mg L^{-1}) sont observéss à Kervoyal, (site proche de l'embouchure de la Vilaine), trois évènements hypoxiques (3.84 mg L^{-1}) à la station Les Mats puis un signal faible à la station Dumet (4.71 mg L^{-1}).

- Le deuxième évènement est observé en août 2021 et dure 6 jours. Il est lié à une crue de la Vilaine entre mi-juin à mi-août (max. 100 m^3 s^{-1}) et à une crue de la Loire (**Annexe 2**). Il s'est déroulé en période de mortes eaux (coefficients de 48 à 72).

- Le troisième évènement s'est déroulé le 28 juillet 2022. Cet évènement n'est lié à aucune crue de la Vilaine ou de la Loire (**Annexe 2**) mais il se déroule de nouveau en période de mortes eaux (coefficients de 67 et 69).

Cas n°1 : 27/06/2020	**Durée (h)**	**Minimum (mg L^{-1})**	**Nombre d'évènement**
Dumet	1.45	4.71	1
Les Mâts	0.40	3.84	3
Kervoyal	4.40	0.03	4

Cas n°2 : 08/2021	**Durée (h)**	**Minimum (mg L^{-1})**	**Nombre d'évènements**
St Jacques	24	4.74	1
Dumet	96	3.2	1
Les Mâts	144	0.4	1
Kervoyal	288	0	1
Loscolo	x	x	x
Normande	144	0	1

Cas n°3 : 28/07/2022	**Durée (h)**	**Minimum (mg L^{-1})**	**Nombre d'évènements**
St Jacques	X	X	X
Dumet	7	2.65	1
Les Mâts	12	2.18	1
Kervoyal	X	X	X
Loscolo	14	0.84	1
Normande	1.40	4.8	1

Tableau 8-2 Caractéristiques des trois événements de désoxygénation enregistrés par les MASTODON en baie de Vilaine. Si la désoxygénation n'a pas été enregistrée par le mastodon par

(arrêt du capteur) alors elle est marquée par un x par contre si la donnée d'oxygène est présente mais n'est pas assez importante pour être considérée comme une désoxygénation alors elle est marquée d'un X

L'hypothèse que la stratification des eaux joue un rôle important sur les phénomènes de désoxygénation dans la baie de Vilaine est émise. On observe, par exemple, que les évènements de désoxygénation se produisent généralement en mortes eaux. De plus, ces évènements sont plus nombreux et intenses à la côte qu'au large, avec un étalement spatial lors des crues. La stratification des eaux est régulée par la salinité lors de crues et/ou via des changements de température de surface de l'eau. Les analyses sont en cours et la stratification des eaux lors des désoxygénations sera calculée à l'aide du modèle MARS3D. La stratification des eaux côtières pourrait être envisagée comme un indicateur de détection des phénomènes hypoxiques et anoxiques.

8.3 Mesures des EE en milieu côtier

Les EE sont des phénomènes qui restent complexes à observer car il est, par exemple, difficile d'anticiper leur occurrence. Mes travaux de thèse, basés sur la compréhension des processus et les études saisonnières des EE, permettent de mieux les comprendre et d'identifier des stratégies de mesure pour les observer. Un des aspects réside dans l'adaptation de l'échantillonnage des mesures aux processus observés. Il est, par exemple, envisageable d'explorer l'adaptabilité en temps réel de l'observation à une fréquence *in situ* permettant d'observer les EE. La mesure des EE devrait être à fréquence variable et comprise entre la haute (10 min) et la basse fréquence (15 jours) avec des instruments tel que le COSTOF2 (Legrand et al., 2019) qui pourraient élever leur fréquence d'échantillonnage lors de l'occurrence des EE (approche de "smart observation" - intelligence de l'observation par connexion entre processeur et capteur). L'échantillonnage des mesures reste à optimiser pour les capteurs dont l'autonomie est limitée mais aussi dans une démarche de sobriété. Comme les EE durent en moyenne plusieurs jours (e.g. en moyenne 3 jours pour une dessalure en rade de Brest), un signal journalier régulier n'est pas suffisant. Il serait souhaitable de tendre vers un système de mesure horaire qui pourrait déclencher une fréquence d'acquisition plus importante (ex :10 min) lorsque le signal passe en dessous d'un seuil critique.

Les EE sont en constante évolution et les zones spatiales ainsi que la période temporelle d'analyse doivent être élargies. Les EE sont désormais présents dans des zones dans lesquelles ils étaient faibles en intensité, peu nombreux, voire pas observés du tout. La récente MHW de juin 2023 dans la Manche a mis en évidence le manque d'études au niveau des côtes irlandaises. Une étude sur ce sujet a été initiée et est en cours (i.e. collaboration avec Maynooth University - Irlande et Instituto Dom Luiz - Portugal).

Il faut désormais analyser le EE en dehors de leurs périodes de prédilection, ainsi des dessalures se produisent en rade de Brest en automne et non pas exclusivement en hiver. Les études des EE sur l'année entière, ou du moins sur les mois autour des saisons de prédilections des EE, devront être privilégiées.

Enfin, les méthodes développées lors de ma thèse pour détecter les EE devront être automatisées et étendues aux échelles nationale (réseau COAST-HF) et européenne

(infrastructure de recherche – Jerico-RI) voir internationales (programme CoastPredict) afin que des études comparatives sur le long terme soient réalisables.

8.4 Evolution des EE côtiers et points d'inflexion

Les tendances des évolutions des EE côtiers sont difficiles à établir car les séries temporelles d'observations sont courtes et potentiellement incomplètes. Cependant, certains EE présentent toutefois des évolutions claires ces dernières décennies en milieu côtier. Le lien entre la variabilité du paramètre environnemental de l'océan côtier et la variabilité de la dynamique des EE (occurrence, intensité, durée) est couramment documenté. Par exemple, Oliver *et al.* (2019) et Simon et al. (2023) ont établi une relation entre l'évolution des MHW et le réchauffement des eaux. La question est donc de déterminer s'il est réellement possible de séparer les tendances globales du changement climatique des tendances liées uniquement à la dynamique des évènements extrêmes ? Certaines études proposent de retirer la tendance globale du réchauffement de l'océan via la comparaison d'un seuil de détection statique basé sur le cycle saisonnier climatologique contre un seuil dynamique incorporant une tendance linéaire au réchauffement (Oliver et al., 2021; Izquierdo et al., 2022; Amaya et al., 2023). Ces premiers développements ne permettent pas à ce stade de déterminer quelle approche permettra une meilleure identification de la dynamique des évènements extrêmes et reste sujet à discussion. De plus, le choix des climatologies utilisées doit être évalué selon les dynamiques et les paramètres analysés.

Une autre évolution remarquable dans les milieux côtiers français étudiés est un point d'inflexion en 2010. Ce point d'inflexion impacte la dynamique des EE comme les dessalures en rade de Brest, et les modifications de l'IPGP en rade de Brest et en baie de Vilaine. En effet, plusieurs scientifiques retrouvent ce point d'inflexion au niveau de la façade maritime française sur des données très différentes. Une analyse multidisciplinaire visant à regarder les paramètres des écosystèmes côtiers français sur les dernières décennies reliant la physique (les régimes de temps, la température, la salinité) à la biologie (le phytoplancton, le zooplancton, les mollusques) est envisagée. Dans des environnements très contrastés comme la lagune de Thau, la baie de Veys et le secteur de Marennes-Oléron, les traits de vie des huîtres juvéniles sur la période 1970 à 2018 marquent un changement de trajectoire entre 2010 et 2012. Cette évolution est synchrone avec des variables de l'environnement comme les températures atmosphériques maximales et l'intensité des vents (Guesdon et al., 2023). Une efflorescence exceptionnelle en intensité de l'algue toxique Pseudo nitzschia en 2010 est mise en avant. Une augmentation de la mortalité des huîtres le long des façades maritimes Manche et Atlantique depuis 2010 est corrélée avec l'occurrence de la NAO en hiver (Thomas et al., 2018). Un rapport sur 30 ans de données basse fréquence issues du réseau de mesure REPHY souligne une augmentation de la température de surface de l'eau en baie d'Audierne et au Croisic (Belin et Soudant, 2018). Une synthèse de toutes les études montrant un point d'inflexion autour de 2010 est nécessaire tout en explorant leur relation avec les régimes de temps. Enfin, Il serait souhaitable que les points d'inflexion soient pris en compte dans les méthodes de détection des futurs EE.

Bibliographie

Abarnou, A., Avoine, J., Dupont, J. P., Lafite, R., & Simon, S. (1987). Role of suspended sediments on the distribution of PCB in the Seine Estuary (France). *Continental Shelf Research*, *7*(11–12), 1345–1350. https://doi.org/10.1016/0278-4343(87)90038-0

Alosairi, Y., Alsulaiman, N., Petrov, P., & Karam, Q. (2019). Responses of salinity and chlorophyll-a to extreme rainfall events in the northwest Arabian Gulf: Emphasis on Shatt Al-Arab. *Marine Pollution Bulletin*, *149*(September), 110564. https://doi.org/10.1016/j.marpolbul.2019.110564

Amaya, D. J., Jacox, M. G., Fewings, M. R., Saba, V. S., Stuecker, M. F., Rykaczewski, R. R., Ross, A. C., Stock, C. A., Capotondi, A., Petrik, C. M., Bograd, S. J., Alexander, M. A., Cheng, W., Hermann, A. J., Kearney, K. A., & Powell, B. S. (n.d.). *so coastal communities can adapt*.

Anagnostopoulou, C., & Tolika, K. (2012). Extreme precipitation in Europe: Statistical threshold selection based on climatological criteria. *Theoretical and Applied Climatology*, *107*(3–4), 479–489. https://doi.org/10.1007/s00704-011-0487-8

Andersen, T. J., & Pejrup, M. (2001). Suspended sediment transport on a temperate, microtidal mudflat, the Danish Wadden Sea. *Marine Geology*, *173*(1–4), 69–85. https://doi.org/10.1016/S0025-3227(00)00164-X

Anderson, A., & Kostinski, A. (2011). Evolution and distribution of record-breaking high and low monthly mean temperatures. *Journal of Applied Meteorology and Climatology*, *50*(9), 1859–1871. https://doi.org/10.1175/JAMC-D-10-05025.1

Arena, F., Laface, V., Malara, G., Romolo, A., Viviano, A., Fiamma, V., Sannino, G., & Carillo, A. (2015). *Wave climate analysis for the design of wave energy harvesters in the Mediterranean Sea*. *77*.

ARES report, Recherche, R. D. E. (2020). *Projet Seine-Aval 6 « Analyse de Rejeux hydro-sédimentaires en* baie de Seine ».

Barrier, N., Cassou, C., Deshayes, J., & Treguier, A. M. (2014). Response of north atlantic ocean circulation to atmospheric weather regimes. *Journal of Physical Oceanography*, *44*(1), 179–201. https://doi.org/10.1175/JPO-D-12-0217.1

Belin, C., & Soudant, D. (2018). Trente années d'observation des micro-algues et des toxines d'algues sur le littoral. In *Trente années d'observation des micro-algues et des toxines d'algues sur le littoral*. https://doi.org/10.35690/978-2-7592-2941-3

Bell, J. E., Brown, C. L., Conlon, K., Herring, S., Kunkel, K. E., Lawrimore, J., Luber, G., Schreck, C., Smith, A., & Uejio, C. (2018). Changes in extreme events and the potential impacts on human health. *Journal of the Air and Waste Management Association*, *68*(4), 265–287. https://doi.org/10.1080/10962247.2017.1401017

Berrisford, P., Kâlberg, P., Kobayashi, S., Dee, D., Uppala, S., Simmons, A.J. et al. (2011). Atmospheric conservation properties in ERA-Interim. Q. J. R. Meteorol. Soc. 137, 1381-1399. https://doi.org/10.1002/qj.864

Biondi, F., Kozubowski, T. J., Panorska, A. K., & Saito, L. (2008). A new stochastic model of episode peak and duration for eco-hydro-climatic applications. *Ecological Modelling*, *211*(3–4), 383–395. https://doi.org/10.1016/j.ecolmodel.2007.09.019

Boss, E., & Behrenfeld, M. (2010). In situ evaluation of the initiation of the North Atlantic phytoplankton bloom. *Geophysical Research Letters*, *37*(18), 1–5. https://doi.org/10.1029/2010GL044174

Boyé, A., Gauthier, O., Becheler, R., Le Garrec, V., Hily, C., Maguer, M., & Grall, J. (2022). Drivers and limits of phenotypic responses in vulnerable seagrass populations: Zostera marina in the intertidal. *Journal of Ecology*, *110*(1), 144–161. https://doi.org/10.1111/1365-2745.13791

Breitburg, D. L., Hondorp, D. W., Davias, L. A., & Diaz, R. J. (2009). Hypoxia, nitrogen, and fisheries: Integrating effects across local and global landscapes. *Annual Review of Marine Science*, *1*, 329–349. https://doi.org/10.1146/annurev.marine.010908.163754

Breitburg, D., Levin, L. A., Oschlies, A., Grégoire, M., Chavez, F. P., Conley, D. J., Garçon, V., Gilbert, D., Gutiérrez, D., Isensee, K., Jacinto, G. S., Limburg, K. E., Montes, I., Naqvi, S. W. A., Pitcher, G. C., Rabalais, N. N., Roman, M. R., Rose, K. A., Seibel, B. A., … Zhang, J. (2018). Declining oxygen in the global ocean and coastal waters. *Science*, *359*(6371). https://doi.org/10.1126/science.aam7240

Broska, L. H., Poganietz, W. R., & Vögele, S. (2020). Extreme events defined—A conceptual discussion applying a complex systems approach. *Futures*, *115*(September 2019), 102490. https://doi.org/10.1016/j.futures.2019.102490

Brown, A., Lilley, M. K. S., Shutler, J., Widdicombe, C., Rooks, P., McEvoy, A., Torres, R., Artioli, Y., Rawle, G., Homyard, J., Tyler, C. R., & Lowe, C. (2022). Harmful Algal Blooms and their impacts on shellfish mariculture follow regionally distinct patterns of water circulation in the western English Channel during the 2018 heatwave. *Harmful Algae*, *111*(June 2020), 102166. https://doi.org/10.1016/j.hal.2021.102166

Burchard, H., Schuttelaars, H. M., & Ralston, D. K. (2018). Sediment trapping in estuaries. *Annual Review of Marine Science*, *10*, 371–395. https://doi.org/10.1146/annurev-marine-010816-060535

Caillaud, M., Petton, S. & Dumas, F. (2016). Hydrodynamic Hindcast at 500m resolution with MARS3D-AGRIF Model – Channel-Biscay Zone. Brest: Ifremer.

Cailleaud, K. (2007). Seasonal variation of hydrophobic organic contaminant concentrations in the water-column of the Seine Estuary and their transfer to a planktonic species Eurytemora affinis (Calanoı ¨ d , copepod). Part 2 : Alkylphenol-polyethoxylates. 70, 281–287. https://doi.org/10.1016/j.chemosphere.2007.06.012

Capuzzo, E., Lynam, C. P., Barry, J., Stephens, D., Forster, R. M., Greenwood, N., McQuatters-Gollop, A., Silva, T., van Leeuwen, S. M., & Engelhard, G. H. (2018). A decline in primary production in the North Sea over 25 years, associated with reductions in zooplankton abundance and fish stock recruitment. *Global Change Biology*, *24*(1), e352–e364. https://doi.org/10.1111/gcb.13916

Caracciolo, M., Beaugrand, G., Hélaouët, P., Gevaert, F., Edwards, M., Lizon, F., Kléparski, L., & Goberville, E. (2021). Annual phytoplankton succession results from niche-environment interaction. *Journal of Plankton Research*, *43*(1), 85–102. https://doi.org/10.1093/plankt/fbaa060

Cariolet, J. M., Use of high water marks and eyewitness accounts to delineate flooded coastal areas: The case of Storm Johanna (10 March 2008) in Brittany, France, Ocean & Coastal Management, Volume 53, Issue 11, 2010, Pages 679-690, ISSN 0964-5691, https://doi.org/10.1016/j.ocecoaman.2010.09.002.

Castelle, B., Guillot, B., Marieu, V., Chaumillon, E., Hanquiez, V., Bujan, S., & Poppeschi, C. (2018). Spatial and temporal patterns of shoreline change of a 280-km high-energy disrupted sandy coast from

1950 to 2014: SW France. *Estuarine, Coastal and Shelf Science*, *200*, 212–223. https://doi.org/10.1016/j.ecss.2017.11.005

Cassou, C., Minvielle, M., Terray, L., & Périgaud, C. (2011). A statistical-dynamical scheme for reconstructing ocean forcing in the Atlantic. Part I: Weather regimes as predictors for ocean surface variables. *Climate Dynamics*, *36*(1), 19–39. https://doi.org/10.1007/s00382-010-0781-7

Ceccaldi, H.-J., Hénocque, Y., Komatsu, T., Prouzet, P., Benoit, ·, Jiro, S. ·, & Editors, Y. (n.d.). *Evolution of Marine Coastal Ecosystems under the Pressure of Global Changes Proceedings of Coast Bordeaux Symposium and of the 17th French-Japanese Oceanography Symposium*.

Chapelle, A., Lazure, P., & Ménesguen, A. (1994). Modelling eutrophication events in a coastal ecosystem. Sensitivity analysis. *Estuarine, Coastal and Shelf Science*, *39*(6), 529–548. https://doi.org/10.1016/S0272-7714(06)80008-9

Charria, G., Theetten, S., Vandermeirsch, F., Yeleki, Z., & Audiffren, N. (2017). Interannual evolution of (sub)mesoscale dynamics in the Bay of Biscay. *Ocean Science*, *13*(5), 777–797. https://doi.org/10.5194/os-13-777-2017

Chiswell, S. M., Calil, P. H. R., & Boyd, P. W. (2014). Spring blooms and annual cycles of phytoplankton: A unified perspective. *Journal of Plankton Research*, *37*(3), 500–508. https://doi.org/10.1093/plankt/fbv021

Chivers, W. J., Edwards, M., & Hays, G. C. (2020). Phenological shuffling of major marine phytoplankton groups over the last six decades. *Diversity and Distributions*, *26*(5), 536–548. https://doi.org/10.1111/ddi.13028

Christidis, N., Jones, G. S., & Stott, P. A. (2015). Dramatically increasing chance of extremely hot summers since the 2003 European heatwave. *Nature Climate Change*, *5*(1), 46–50. https://doi.org/10.1038/nclimate2468

Chust, G., Allen, J. I., Bopp, L., & Schrum, C. (2014). *Biomass changes and trophic amplification of plankton in a warmer ocean*. *2010*, 2124–2139. https://doi.org/10.1111/gcb.12562

Claquin Pascal, Jacqueline Franck, Repecaud Michel, Riou Philippe (2018). MAREL SMILE buoy data and metadata from coriolis Data Centre. SEANOE. https://doi.org/10.17882/53689

Cloern, J. E. (1996). Phytoplankton bloom dynamics in coastal ecosystems: A review with some general lessons from sustained investigation of San Francisco Bay, California. *Reviews of Geophysics*, *34*(2), 127–168. https://doi.org/10.1029/96RG00986

Cocquempot, L., Delacourt, C., Paillet, J., Riou, P., Aucan, J., Castelle, B., Charria, G., Claudet, J., Conan, P., Coppola, L., Hocdé, R., Planes, S., Raimbault, P., Savoye, N., Testut, L., & Vuillemin, R. (2019). Coastal ocean and nearshore observation: A French case study. *Frontiers in Marine Science*, *6*(JUN), 1–17. https://doi.org/10.3389/fmars.2019.00324

Coles, S. (2001). An Introduction to Statistical Modeling of Extreme. In *Journal of Chemical Information and Modeling* (Vol. 53, Issue 9).

Cook, B. I., Smerdon, J. E., Cook, E. R., Williams, A. P., Anchukaitis, K. J., Mankin, J. S., Allen, K., Andreu-Hayles, L., Ault, T. R., Belmecheri, S., Coats, S., Coulthard, B., Fosu, B., Grierson, P., Griffin, D., Herrera, D. A., Ionita, M., Lehner, F., Leland, C., … Wise, E. K. (2022). Megadroughts in the Common Era and the Anthropocene. *Nature Reviews Earth and Environment*, *3*(11), 741–757. https://doi.org/10.1038/s43017-022-00329-1

Coumou, D., & Rahmstorf, S. (2012). A decade of weather extremes. *Nature Climate Change*, *2*(7), 491–496. https://doi.org/10.1038/nclimate1452

Darmaraki, S., Somot, S., Sevault, F., & Nabat, P. (2019). Past Variability of Mediterranean Sea Marine Heatwaves. *Geophysical Research Letters*, *46*(16), 9813–9823. https://doi.org/10.1029/2019GL082933

Del Amo, Y., Le, O., Treguer, P., & Queguinerl, B. (1997). *Impacts of high-nitrate freshwater inputs on macrotidal ecosystems . I . Seasonal evolution of nutrient limitation for the diatom-dominated phytoplankton of the Bay of Brest (France). 161*.

Deloffre, J., Lafite, R., Lesueur, P., Verney, R., Lesourd, S., Cuvilliez, A., & Taylor, J. (2005). Controlling factors of rhythmic sedimentation processes on an intertidal estuarine mudflat - Role of the turbidity maximum in the macrotidal Seine estuary, France. *Marine Geology*, *235*(1-4 SPEC. ISS.), 151–164. https://doi.org/10.1016/j.margeo.2006.10.011

Deser, C., Alexander, M. A., Xie, S. P., & Phillips, A. S. (2010). Sea surface temperature variability: Patterns and mechanisms. In *Annual Review of Marine Science* (Vol. 2, Issue 1). https://doi.org/10.1146/annurev-marine-120408-151453

Diego-Feliu, M., Rodellas, V., Alorda-Kleinglass, A., Saaltink, M., Folch, A., & Garcia-Orellana, J. (2022). Extreme precipitation events induce high fluxes of groundwater and associated nutrients to coastal ocean. *Hydrology and Earth System Sciences*, *26*(18), 4619–4635. https://doi.org/10.5194/hess-26-4619-2022

Domeisen, D. I. V., Eltahir, E. A. B., Fischer, E. M., Knutti, R., Perkins-Kirkpatrick, S. E., Schär, C., Seneviratne, S. I., Weisheimer, A., & Wernli, H. (2023). Prediction and projection of heatwaves. *Nature Reviews Earth and Environment*, *4*(1), 36–50. https://doi.org/10.1038/s43017-022-00371-z

Dufois, F., Verney, R., Le Hir, P., Dumas, F., & Charmasson, S. (2014). Impact of winter storms on sediment erosion in the Rhone River prodelta and fate of sediment in the Gulf of Lions (North Western Mediterranean Sea). *Continental Shelf Research*, *72*(January), 57–72. https://doi.org/10.1016/j.csr.2013.11.004

Dupont, N., & Aksnes, D. L. (2013). Centennial changes in water clarity of the baltic sea and the north sea. *Estuarine, Coastal and Shelf Science*, *131*, 282–289. https://doi.org/10.1016/j.ecss.2013.08.010

Dzwonkowski, B., Coogan, J., Fournier, S., Lockridge, G., Park, K., & Lee, T. (2020). Compounding impact of severe weather events fuels marine heatwave in the coastal ocean. *Nature Communications*, *11*(1), 1–10. https://doi.org/10.1038/s41467-020-18339-2

Esteves, K., Hervio-Heath, D., Mosser, T., Rodier, C., Tournoud, M., Jumas-Bilak, E., Colwell, R. R., & Monfort, P. (2015). *Vibrio cholerae* during freshwater flash floods in french mediterranean coastal lagoons. *Frontiers in Microbiology*, *81*, 7600–7609. https://doi.org/10.1128/AEM.01848-15.Editor

Etcheber, H., Taillez, A., Abril, G., Garnier, J., Servais, P., Moatar, F., & Commarieu, M. V. (2007). Particulate organic carbon in the estuarine turbidity maxima of the Gironde, Loire and Seine estuaries: Origin and lability. *Hydrobiologia*, *588*(1), 245–259. https://doi.org/10.1007/s10750-007-0667-9

Farcy, P., Durand, D., Charria, G., Painting, S. J., Tamminem, T., Collingridge, K., Grémare, A. J., Delauney, L., & Puillat, I. (2019). Toward a European coastal observing network to provide better answers to science and to societal challenges; the JERICO research infrastructure. *Frontiers in Marine Science*, *6*(SEP), 1–13. https://doi.org/10.3389/fmars.2019.00529

Feng, M., Caputi, N., Chandrapavan, A., Chen, M., Hart, A., & Kangas, M. (2021). Multi-year marine cold-spells off the west coast of Australia and effects on fisheries. *Journal of Marine Systems*, *214*(October 2020), 103473. https://doi.org/10.1016/j.jmarsys.2020.103473

Feser, F., Barcikowska, M., Krueger, O., Schenk, F., Weisse, R., & Xia, L. (2015). Storminess over the North Atlantic and northwestern Europe-A review. *Quarterly Journal of the Royal Meteorological Society*, *141*(687), 350–382. https://doi.org/10.1002/qj.2364

Fettweis, M., Francken, F., Van den Eynde, D., Verwaest, T., Janssens, J., & Van Lancker, V. (2010). Storm influence on SPM concentrations in a coastal turbidity maximum area with high anthropogenic impact (southern North Sea). *Continental Shelf Research*, *30*(13), 1417–1427. https://doi.org/10.1016/j.csr.2010.05.001

Fettweis, M., Toorman, E., Verney, R., Chapalain, M., Legrand, S., Lurton, X., Montereale-Gavazzi, G., Roche, M., Shen, X., Van den Eynde, D., & Van Lancker, V. (2020). *INDI 67. Developments of Indicators to improve monitoring of MSFD descriptors 6 and 7 (INDI67): final report. June*, SP2901. https://archimer.ifremer.fr/doc/00634/74632/

Folland, C. K., Knight, J., Linderholm, H. W., Fereday, D., Ineson, S., & Hurrel, J. W. (2009). The summer North Atlantic oscillation: Past, present, and future. *Journal of Climate*, *22*(5), 1082–1103. https://doi.org/10.1175/2008JCLI2459.1

Frölicher, T. L., Fischer, E. M., & Gruber, N. (2018). Marine heatwaves under global warming. *Nature*, *560*(7718), 360–364. https://doi.org/10.1038/s41586-018-0383-9

Frölicher, T. L., & Laufkötter, C. (2018). Emerging risks from marine heat waves. *Nature Communications*, *9*(1), 2015–2018. https://doi.org/10.1038/s41467-018-03163-6

Gailhard, I., Gros, P., Durbec, J. P., Beliaeff, B., Belin, C., Nézan, E., & Lassus, P. (2002). *Variability patterns of microphytoplankton communities along the French coasts*. *242*, 39–50.

Garnaud, S., Lesueur, P., Clet, M., Lesourd, S., Garlan, T., Lafite, R., & Brun-Cottan, J. C. (2003). Holocene to modern fine-grained sedimentation on a macrotidal shoreface-to-inner-shelf setting (eastern Bay of the Seine, France). *Marine Geology*, *202*(1–2), 33–54. https://doi.org/10.1016/S0025-3227(03)00266-4

Garrabou, J., Gómez-Gras, D., Medrano, A., Cerrano, C., Ponti, M., Schlegel, R., Bensoussan, N., Turicchia, E., Sini, M., Gerovasileiou, V., Teixido, N., Mirasole, A., Tamburello, L., Cebrian, E., Rilov, G., Ledoux, J. B., Souissi, J. Ben, Khamassi, F., Ghanem, R., … Harmelin, J. G. (2022). Marine heatwaves drive recurrent mass mortalities in the Mediterranean Sea. *Global Change Biology*, *28*(19), 5708–5725. https://doi.org/10.1111/gcb.16301

Glé, C., Del Amo, Y., Bec, B., Sautour, B., Froidefond, J. M., Gohin, F., Maurer, D., Plus, M., Laborde, P., & Chardy, P. (2007). Typology of environmental conditions at the onset of winter phytoplankton blooms in a shallow macrotidal coastal ecosystem, Arcachon Bay (France). *Journal of Plankton Research*, *29*(11), 999–1014. https://doi.org/10.1093/plankt/fbm074

Goberville, E., Beaugrand, G., Sautour, B., & Tréguer, P. (2010). Climate-driven changes in coastal marine systems of western Europe. *Marine Ecology Progress Series*, *408*, 129–147. https://doi.org/10.3354/meps08564

Goberville, E., Beaugrand, G., & Edwards, M. (2014). Synchronous response of marine plankton ecosystems to climate in the Northeast Atlantic and the North Sea. *Journal of Marine Systems*, *129*, 189–202. https://doi.org/10.1016/j.jmarsys.2013.05.008

Gohin, F., Loyer, S., Lunven, M., Labry, C., Froidefond, J. M., Delmas, D., Huret, M., & Herbland, A. (2005). Satellite-derived parameters for biological modelling in coastal waters: Illustration over the eastern continental shelf of the Bay of Biscay. *Remote Sensing of Environment*, *95*(1), 29–46. https://doi.org/10.1016/j.rse.2004.11.007

Gohin, F. (2011). Annual cycles of chlorophyll-a, non-algal suspended particulate matter, and turbidity observed from space and in-situ in coastal waters. *Ocean Science*, *7*(5), 705–732. https://doi.org/10.5194/os-7-705-2011

Gohin, F., Van der Zande, D., Tilstone, G., Eleveld, M. A., Lefebvre, A., Andrieux-Loyer, F., Blauw, A. N., Bryère, P., Devreker, D., Garnesson, P., Hernández Fariñas, T., Lamaury, Y., Lampert, L., Lavigne, H., Menet-Nedelec, F., Pardo, S., & Saulquin, B. (2019). Twenty years of satellite and in situ observations of surface chlorophyll-a from the northern Bay of Biscay to the eastern English Channel. Is the water quality improving? *Remote Sensing of Environment*, *233*(December 2018), 111343. https://doi.org/10.1016/j.rse.2019.111343

Gómez, F., & Souissi, S. (2008). The impact of the 2003 summer heat wave and the 2005 late cold wave on the phytoplankton in the north-eastern English Channel. *Comptes Rendus - Biologies*, *331*(9), 678–685. https://doi.org/10.1016/j.crvi.2008.06.005

Grassi, K., Caillault, E. P., & Lefebvre, A. (2019). Multilevel spectral clustering for extreme event characterization. *OCEANS 2019 - Marseille, OCEANS Marseille 2019*, *2019-June*(1), 1–7. https://doi.org/10.1109/OCEANSE.2019.8867261

Grasso Florent, Le Hir Pierre, Bassoullet Philippe (2015). Numerical modelling of mixed-sediment consolidation. Ocean Dynamics, 65(4), 607-616. Publisher's official version : https://doi.org/10.1007/s10236-015-0818-x

Grasso, F., Verney, R., Le Hir, P., Thouvenin, B., Schulz, E., Kervella, Y., Khojasteh Pour Fard, I., Lemoine, J. P., Dumas, F., & Garnier, V. (2018). Suspended Sediment Dynamics in the Macrotidal Seine Estuary (France): 1. Numerical Modeling of Turbidity Maximum Dynamics. *Journal of Geophysical Research: Oceans*, *123*(1), 558–577. https://doi.org/10.1002/2017JC013185

Guillou, N., Chapalain, G., & Petton, S. (2022). Predicting sea surface salinity in a tidal estuary with machine learning. *Oceanologia*, *xxxx*. https://doi.org/10.1016/j.oceano.2022.07.007

Guinaldo, T., Voldoire, A., Waldman, R., Saux Picart, S., & Roquet, H. (2023). Response of the sea surface temperature to heatwaves during the France 2022 meteorological summer. *Ocean Science*, *19*(3), 629–647. https://doi.org/10.5194/os-19-629-2023

Guesdon, S., Derolez, V., Gangnery, A., & Soudant, D. (2020). Co-évolution de traits de vie d' huîtres juvéniles et de forçages environnementaux au sein de trois écosystèmes côtiers français Co-evolution of cultivated oyster biological traits and their environmental drivers in three French coastal ecosystems (bay . 2, 4–5.

Halawi Ghosn, R., Poisson-Caillault, É., Charria, G., Bonnat, A., Repecaud, M., Facq, J.-V., Quéméner, L., Duquesne, V., Blondel, C., and Lefebvre, A.: MAREL Carnot data and metadata from Coriolis Data Center, Earth Syst. Sci. Data Discuss. [preprint], https://doi.org/10.5194/essd-2023-8, in review, 2023.

Hallin, M., Paindaveine, D., & Šiman, M. (2010). Multivariate quantiles and multiple-output regression quantiles: From L1 optimization to halfspace depth. *Annals of Statistics*, *38*(2), 635–669. https://doi.org/10.1214/09-AOS723

Harris, R. M. B., Beaumont, L. J., Vance, T. R., Tozer, C. R., Remenyi, T. A., Perkins-Kirkpatrick, S. E., Mitchell, P. J., Nicotra, A. B., McGregor, S., Andrew, N. R., Letnic, M., Kearney, M. R., Wernberg,

T., Hutley, L. B., Chambers, L. E., Fletcher, M. S., Keatley, M. R., Woodward, C. A., Williamson, G., … Bowman, D. M. J. S. (2018). Biological responses to the press and pulse of climate trends and extreme events. *Nature Climate Change*, *8*(7), 579–587. https://doi.org/10.1038/s41558-018-0187-9

Henocque, Y. (2003). Development of process indicators for coastal zone management assessment in France. *Ocean and Coastal Management*, *46*(3–4), 363–379. https://doi.org/10.1016/S0964-5691(03)00013-9

Hersbach, H., Bell, B., Berrisford, P., Hirahara, S., Horányi, A., Nicolas, J., Peubey, C., Radu, R., Bonavita, M., Dee, D., Dragani, R., Flemming, J., Forbes, R., Geer, A., Hogan, R. J., Janisková, H. M., Keeley, S., Laloyaux, P., Cristina, P. L., & Thépaut, J. (2020). *The ERA5 global reanalysis*. *March*, 1999–2049. https://doi.org/10.1002/qj.3803

Hobday, A. J., Alexander, L. V., Perkins, S. E., Smale, D. A., Straub, S. C., Oliver, E. C. J., Benthuysen, J. A., Burrows, M. T., Donat, M. G., Feng, M., Holbrook, N. J., Moore, P. J., Scannell, H. A., Sen Gupta, A., & Wernberg, T. (2016). A hierarchical approach to defining marine heatwaves. *Progress in Oceanography*, *141*, 227–238. https://doi.org/10.1016/j.pocean.2015.12.014

Hodapp, D., Roca, I. T., Fiorentino, D., Garilao, C., Kaschner, K., Kesner-Reyes, K., Schneider, B., Segschneider, J., Kocsis, Á. T., Kiessling, W., Brey, T., & Froese, R. (2023). Climate change disrupts core habitats of marine species. *Global Change Biology*, *29*(12), 3304–3317. https://doi.org/10.1111/gcb.16612

Howell, P., & Simpson, D. (1994). Abundance of marine resources in relation to dissolved oxygen in Long Island Sound. *Estuaries*, *17*(2), 394–402. https://doi.org/10.2307/1352672

Huang, Q., Li, N., & Li, Y. (2021). Long-term trend of heat waves and potential effects on phytoplankton blooms in Lake Qiandaohu, a key drinking water reservoir. *Environmental Science and Pollution Research*, *28*(48), 68448–68459. https://doi.org/10.1007/s11356-021-15414-z

Hughes, T. P., Kerry, J. T., Álvarez-Noriega, M., Álvarez-Romero, J. G., Anderson, K. D., Baird, A. H., Babcock, R. C., Beger, M., Bellwood, D. R., Berkelmans, R., Bridge, T. C., Butler, I. R., Byrne, M., Cantin, N. E., Comeau, S., Connolly, S. R., Cumming, G. S., Dalton, S. J., Diaz-Pulido, G., … Wilson, S. K. (2017). Global warming and recurrent mass bleaching of corals. *Nature*, *543*(7645), 373–377. https://doi.org/10.1038/nature21707

Hurrell, J. W., Kushnir, Y., Ottersen, G., & Visbeck, M. (2003). An overview of the North Atlantic oscillation, *Geophysical Monograph-American Geophysical Union*, *134*, 1-36, https://doi.org/10.1029/134GM01

Imran, J., & Syvitski, J. P. M. (2000). Impact of extreme river events on the coastal ocean. *Oceanography*, *13*(SPL. ISS. 3), 85–92. https://doi.org/10.5670/oceanog.2000.17

Iriarte, A., & Purdie, D. A. (2004). Factors controlling the timing of major spring bloom events in an UK south coast estuary. *Estuarine, Coastal and Shelf Science*, *61*(4), 679–690. https://doi.org/10.1016/j.ecss.2004.08.002

Izquierdo, P., Rico, J. M., Taboada, F. G., González-Gil, R., & Arrontes, J. (2022a). Characterization of marine heatwaves in the Cantabrian Sea, SW Bay of Biscay. *Estuarine, Coastal and Shelf Science*, *274*(June). https://doi.org/10.1016/j.ecss.2022.107923

Izquierdo, P., Taboada, F. G., González-Gil, R., Arrontes, J., & Rico, J. M. (2022b). Alongshore upwelling modulates the intensity of marine heatwaves in a temperate coastal sea. *Science of the Total Environment*, *835*(February). https://doi.org/10.1016/j.scitotenv.2022.155478

Jalón-Rojas, I., & Castelle, B. (2021). Climate control of multidecadal variability in river discharge and precipitation in western europe. *Water (Switzerland)*, *13*(3). https://doi.org/10.3390/w13030257

Joint, I., & Smale, D. A. (2017). Marine heatwaves and optimal temperatures for microbial assemblage activity. *FEMS Microbiology Ecology*, *93*(2), 1–9. https://doi.org/10.1093/femsec/fiw243

Juza, M., Fernández-Mora, A., & Tintoré, J. (2022). Sub-Regional Marine Heat Waves in the Mediterranean Sea From Observations: Long-Term Surface Changes, Sub-Surface and Coastal Responses. *Frontiers in Marine Science*, *9*(March). https://doi.org/10.3389/fmars.2022.785771

Kim, D., Park, D. S. R., Chang, M., Cha, D. H., & Lee, M. (2023). Reanalyzing the Relationship of Tropical Cyclone Frequency and Intensity Affecting South Korea with the Pacific Decadal Oscillation. *Journal of Climate*, *36*(9), 2847–2855. https://doi.org/10.1175/JCLI-D-22-0302.1

Labry, C., Herbland, A., Delmas, D., Laborde, P., Lazure, P., Froidefond, J. M., Jegou, A. M., & Sautour, B. (2001). Initiation of winter phytoplankton blooms within the Gironde plume waters in the Bay of Biscay. *Marine Ecology Progress Series*, *212*, 117–130. https://doi.org/10.3354/meps212117

Lamy, E., & Lassabatere, L. (2010). *Hydrologie urbaine*. *6368*, 86–92. https://doi.org/10.1051/lhb

Lazure, P., & Dumas, F. (2008). An external-internal mode coupling for a 3D hydrodynamical model for applications at regional scale (MARS). *Advances in Water Resources*, *31*(2), 233–250. https://doi.org/10.1016/j.advwatres.2007.06.010

Lazure, P., Garnier, V., Dumas, F., Herry, C., & Chifflet, M. (2009). Development of a hydrodynamic model of the Bay of Biscay. Validation of hydrology. *Continental Shelf Research*, *29*(8), 985–997. https://doi.org/10.1016/j.csr.2008.12.017

Lazure, P., Le Berre, D., Gautier, L. (2015). Mastodon mooring system to measure seabed temperature data logger with ballast, release device at European continental shelf. Sea Technology 56(10), 19-21. Open Access version: https://archimer.ifremer.fr/doc/00292/40319/

Lazure, P., Pairaud, I., Leizour, S., Puillat, I. (2019). Report on the mastodon2D mooring system. JERICO-NEXT-WP3-D3.5-190719-V1.1. https://archimer.ifremer.fr/doc/00630/74245/

La Peyre, M. K., Eberline, B. S., Soniat, T. M., & La Peyre, J. F. (2013). Differences in extreme low salinity timing and duration differentially affect eastern oyster (Crassostrea virginica) size class growth and mortality in Breton Sound, LA. *Estuarine, Coastal and Shelf Science*, *135*, 146–157. https://doi.org/10.1016/j.ecss.2013.10.001

Leckebusch, G. C., Koffi, B., Ulbrich, U., Pinto, J. G., Spangehl, T., & Zacharias, S. (2006). Analysis of frequency and intensity of European.pdf. *Climate Research*, *31*, 59–74.

Ledger, M. E., & Milner, A. M. (2015). Extreme events in running waters. *Freshwater Biology*, *60*(12), 2455–2460. https://doi.org/10.1111/fwb.12673

Le Grix, N., Zscheischler, J., Laufkötter, C., Rousseaux, C. S., & Frölicher, T. L. (2021). Compound high-temperature and low-chlorophyll extremes in the ocean over the satellite period. *Biogeosciences*, *18*(6), 2119–2137. https://doi.org/10.5194/bg-18-2119-2021

Lehmann, J., Coumou, D., & Frieler, K. (2015). Increased record-breaking precipitation events under global warming. *Climatic Change*, *132*(4), 501–515. https://doi.org/10.1007/s10584-015-1434-y

Lehmuskero, A., Skogen Chauton, M., & Boström, T. (2018). Light and photosynthetic microalgae: A review of cellular- and molecular-scale optical processes. *Progress in Oceanography*, *168*(August), 43–56. https://doi.org/10.1016/j.pocean.2018.09.002

Le Hir, P., Cayocca, F., Waeles, B. (2011). Dynamics of sand and mud mixtures: a multiprocess-based modelling strategy. Continental Shelf Research, 31(10), S135-S149. Publisher's official version : https://doi.org/10.1016/j.csr.2010.12.009

Le Pape, O., Del Amo, Y., Menesguen, A., Aminot, A., Quequiner, B., & Treguer, P. (1996). Resistance of a coastal ecosystem to increasing eutrophic conditions: the Bay of Brest (France), a semi-enclosed zone of Western Europe. *Continental Shelf Research*, *16*(15), 1885–1907. https://doi.org/10.1016/0278-4343(95)00068-2

Lesourd, S., Lesueur, P., Brun-Cottan, J. C., Garnaud, S., & Poupinet, N. (2003). Seasonal variations in the characteristics of superficial sediments in a macrotidal estuary (the Seine inlet, France). *Estuarine, Coastal and Shelf Science*, *58*(1), 3–16. https://doi.org/10.1016/S0272-7714(02)00340-2

Lettmann, K. A., Wolff, J. O., & Badewien, T. H. (2009). Modeling the impact of wind and waves on suspended particulate matter fluxes in the East Frisian Wadden Sea (southern North Sea). *Ocean Dynamics*, *59*(2), 239–262. https://doi.org/10.1007/s10236-009-0194-5

Lheureux, A., Savoye, N., Amo, Y. Del, Goberville, E., Bozec, Y., Breton, E., Conan, P., L'Helguen, S., Mousseau, L., Raimbault, P., Rimelin-Maury, P., Seuront, L., Vuillemin, R., Caparros, J., Cariou, T., Cordier, M. A., Corre, A. M., Costes, L., Crispi, O., … David, V. (2021). Bi-decadal variability in physico-biogeochemical characteristics of temperate coastal ecosystems: From large-scale to local drivers. *Marine Ecology Progress Series*, *660*, 19–35. https://doi.org/10.3354/meps13577

Lima, F. P., & Wethey, D. S. (2012). Three decades of high-resolution coastal sea surface temperatures reveal more than warming. *Nature Communications*, *3*. https://doi.org/10.1038/ncomms1713

Liu, H., Nie, X., Cui, C., & Wei, Z. (2023). Compound marine heatwaves and low sea surface salinity extremes over the tropical Pacific Ocean. *Environmental Research Letters*, *18*(6). https://doi.org/10.1088/1748-9326/acd0c4

Losada, J., Nicholls, R. J., Dalrymple, R. A., Marcel, J., & Toimil, A. (2020). *Addressing the challenges of climate change risks and adaptation in coastal areas : A review*. Coastal Engineering, *156*(November 2019). https://doi.org/10.1016/j.coastaleng.2019.103611

Machado, K. B., Andrade, A. T. de, Almeida, M. F. de, & Nabout, J. C. (2023). Systematic mapping of phytoplankton literature about global climate change: revealing temporal trends in research. *Hydrobiologia*, *850*(1), 167–182. https://doi.org/10.1007/s10750-022-05052-y

Madsen, H., Lawrence, D., Lang, M., Martinkova, M., & Kjeldsen, T. R. (2014). Review of trend analysis and climate change projections of extreme precipitation and floods in Europe. *Journal of Hydrology*, *519*(PD), 3634–3650. https://doi.org/10.1016/j.jhydrol.2014.11.003

Mann, M. E., Rahmstorf, S., Kornhuber, K., Steinman, B. A., Miller, S. K., & Coumou, D. (2017). Influence of Anthropogenic Climate Change on Planetary Wave Resonance and Extreme Weather Events. *Scientific Reports*, *7*(1), 45242. https://doi.org/10.1038/srep45242

Marcos, M., Rohmer, J., Vousdoukas, M. I., Mentaschi, L., Le Cozannet, G., & Amores, A. (2019). Increased Extreme Coastal Water Levels Due to the Combined Action of Storm Surges and Wind Waves. *Geophysical Research Letters*, *46*(8), 4356–4364. https://doi.org/10.1029/2019GL082599

Masson-Delmotte, V., Zhai, P., Pirani, A., Connors, S. L., Péan, C., Berger, S., Caud, N., Chen, Y., Goldfarb, L., Gomis, M. I., Huang, M., Leitzell, K., Lonnoy, E., Matthews, J. B. R., Maycock, T. K., Waterfield, T., Yelekçi, O., Yu, R., Zhou, B., & (eds.). (2021). IPCC: Summary for Policymakers. In Press. *Climate Change 2021: The Physical Science Basis. Contribution of Working Group I to the Sixth Assessment Report of the Intergovernmental Panel on Climate Change*, 1–42. https://www.ipcc.ch/report/ar6/wg1/

Mateos, R. M., Sarro, R., Díez-Herrero, A., Reyes-Carmona, C., López-Vinielles, J., Ezquerro, P., Martínez-Corbella, M., Bru, G., Luque, J. A., Barra, A., Martín, P., Millares, A., Ortega, M., López, A., Galve, J. P., Azañón, J. M., Pereira, S., Santos, P. P., Zêzere, J. L., … Monserrat, O. (2023). Assessment of the Socio-Economic Impacts of Extreme Weather Events on the Coast of Southwest Europe during the Period 2009–2020. *Applied Sciences (Switzerland)*, *13*(4). https://doi.org/10.3390/app13042640

Matzinger, A., Schmid, M., Veljanoska-Sarafiloska, E., Patceva, S., Guseska, D., Wagner, B., Müller, B., Sturm, M., & Wüest, A. (2007). Eutrophication of ancient Lake Ohrid: Global warming amplifies detrimental effects of increased nutrient inputs. *Limnology and Oceanography*, *52*(1), 338–353. https://doi.org/10.4319/lo.2007.52.1.0338

Méar, Y., Poizot, E., Murat, A., Beryouni, K., Baux, N., & Dauvin, J. C. (2018). Improving the monitoring of a dumping site in a dynamic environment. Example of the Octeville site (Bay of Seine, English Channel). *Marine Pollution Bulletin*, *129*(2), 425–437. https://doi.org/10.1016/j.marpolbul.2017.10.011

McPhillips, L. E., Chang, H., Chester, M. V., Depietri, Y., Friedman, E., Grimm, N. B., Kominoski, J. S., McPhearson, T., Méndez-Lázaro, P., Rosi, E. J., & Shafiei Shiva, J. (2018). Defining Extreme Events: A Cross-Disciplinary Review. *Earth's Future*, *6*(3), 441–455. https://doi.org/10.1002/2017EF000686

Méar, Y., Poizot, E., Murat, A., Beryouni, K., Baux, N., & Dauvin, J. C. (2018). Improving the monitoring of a dumping site in a dynamic environment. Example of the Octeville site (Bay of Seine, English Channel). *Marine Pollution Bulletin*, *129*(2), 425–437. https://doi.org/10.1016/j.marpolbul.2017.10.011

Meehl, G. A., & Tebaldi, C. (2004). More intense, more frequent, and longer lasting heat waves in the 21st century. *Science*, *305*(5686), 994–997. https://doi.org/10.1126/science.1098704

Mendoza, F. P., Bonamano, S., Martellucci, R., Melchiorri, C., Consalvi, N., Piermattei, V., & Marcelli, M. (2018). Circulation during storms and dynamics of suspended matter in a sheltered coastal area. *Remote Sensing*, *10*(4), 1–27. https://doi.org/10.3390/rs10040602

Ménesguen, A., Dussauze, M., Dumas, F., Thouvenin, B., Garnier, V., Lecornu, F., & Répécaud, M. (2019). Ecological model of the Bay of Biscay and English Channel shelf for environmental status assessment part 1: Nutrients, phytoplankton and oxygen. *Ocean Modelling*, *133*(December 2017), 56–78. https://doi.org/10.1016/j.ocemod.2018.11.002

Mengual, B., Hir, P. Le, Cayocca, F., & Garlan, T. (2017). Modelling fine sediment dynamics: Towards a common erosion law for fine sand, mud and mixtures. *Water (Switzerland)*, *9*(8). https://doi.org/10.3390/w9080564

Mentaschi, L., Vousdoukas, M. I., Voukouvalas, E., Dosio, A., & Feyen, L. (2017). Global changes of extreme coastal wave energy fluxes triggered by intensified teleconnection patterns. *Geophysical Research Letters*, *44*(5), 2416–2426. https://doi.org/10.1002/2016GL072488

Mertens, K. N., Retho, M., Manach, S., Zoffoli, M. L., Doner, A., Schapira, M., Bilien, G., Séchet, V., Lacour, T., Robert, E., Duval, A., Terre-Terrillon, A., Derrien, A., & Gernez, P. (2023). An

unprecedented bloom of Lingulodinium polyedra on the French Atlantic coast during summer 2021. *Harmful Algae*, *125*(March). https://doi.org/10.1016/j.hal.2023.102426

Milkoreit, M., Hodbod, J., Baggio, J., Benessaiah, K., Calderón-Contreras, R., Donges, J. F., Mathias, J. D., Rocha, J. C., Schoon, M., & Werners, S. E. (2018). Defining tipping points for social-ecological systems scholarship - An interdisciplinary literature review. *Environmental Research Letters*, *13*(3). https://doi.org/10.1088/1748-9326/aaaa75

Molines, J., Barnier, B., Penduff, T., Treguier, A.-M., and Le Sommer, J. (2014). ORCA12.L46 Climatological and Interannual Simulations Forced With DFS4.4: GJM02 and MJM88. Drakkar Group Experiment Report GRI-DRAKKAR-2014-03-19. Available online at: https://www.drakkar-ocean.eu/publications/reports/orca12_reference_experiments_2014

Msadek, R., & Frankignoul, C. (2009). Atlantic multidecadal oceanic variability and its influence on the atmosphere in a climate model. *Climate Dynamics*, *33*(1), 45–62. https://doi.org/10.1007/s00382-008-0452-0

Muh Aris, M., Lorenz, M. Æ., Junun, K. Æ., & Sudrajat, S. Æ. (2008). *The impact of tidal flooding on a coastal community in Semarang , Indonesia*. 237–248. https://doi.org/10.1007/s10669-007-9134-4

Najjar, R. G., Walker, H. A., Anderson, P. J., Barron, E. J., Bord, R. J., Gibson, J. R., Kennedy, V. S., Knight, C. G., Megonigal, J. P., Connor, R. E. O., Polsky, C. D., Psuty, N. P., Richards, B. A., Sorenson, L. G., Steele, E. M., & Swanson, R. S. (2000). *The potential impacts of climate change on the mid-Atlantic coastal region*. *14*, 219–233.

Nicholls, N. (1995). Long-term climate monitoring and extreme events. *Climatic Change*, *31*(2–4), 231–245. https://doi.org/10.1007/BF01095148

Oliver, E. C. J., Donat, M. G., Burrows, M. T., Moore, P. J., Smale, D. A., Alexander, L. V., Benthuysen, J. A., Feng, M., Sen Gupta, A., Hobday, A. J., Holbrook, N. J., Perkins-Kirkpatrick, S. E., Scannell, H. A., Straub, S. C., & Wernberg, T. (2018). Longer and more frequent marine heatwaves over the past century. *Nature Communications*, *9*(1), 1–12. https://doi.org/10.1038/s41467-018-03732-9

Oliver, E. C. J., Burrows, M. T., Donat, M. G., Sen Gupta, A., Alexander, L. V., Perkins-Kirkpatrick, S. E., Benthuysen, J. A., Hobday, A. J., Holbrook, N. J., Moore, P. J., Thomsen, M. S., Wernberg, T., & Smale, D. A. (2019). Projected Marine Heatwaves in the 21st Century and the Potential for Ecological Impact. *Frontiers in Marine Science*, *6*(December), 1–12. https://doi.org/10.3389/fmars.2019.00734

Oliver, E. C. J., Benthuysen, J. A., Darmaraki, S., Donat, M. G., Hobday, A. J., Holbrook, N. J., Schlegel, R. W., & Sen Gupta, A. (2021). Marine Heatwaves. *Annual Review of Marine Science*, *13*, 313–342. https://doi.org/10.1146/annurev-marine-032720-095144

Olsen, J. R., Lambert, J. H., & Haimes, Y. Y. (1998). Risk of extreme events under nonstationary conditions. *Risk Analysis*, *18*(4), 497-510. https://doi.org/10.1111/j.1539-6924.1998.tb00364.x

Opdal, A. F., Lindemann, C., & Aksnes, D. L. (2019). Centennial decline in North Sea water clarity causes strong delay in phytoplankton bloom timing. *Global Change Biology*, *25*(11), 3946–3953. https://doi.org/10.1111/gcb.14810

Paladini de Mendoza, F. P., Bonamano, S., Martellucci, R., Melchiorri, C., Consalvi, N., Piermattei, V., & Marcelli, M. (2018). Circulation during storms and dynamics of suspended matter in a sheltered coastal area. *Remote Sensing*, *10*(4), 1–27. https://doi.org/10.3390/rs10040602

Paskoff, A., Roland, P., & Paskoff, R. P. (2023). *Potential Implications of Sea-Level Rise for France Potential Implications of Sea-Level Rise for France*. *20*(2), 424–434.

Peierls, B. L., Hall, N. S., & Paerl, H. W. (2012). Non-monotonic responses of phytoplankton biomass accumulation to hydrologic variability: A comparison of two coastal plain north carolina estuaries. *Estuaries and Coasts*, *35*(6), 1376–1392. https://doi.org/10.1007/s12237-012-9547-2

Petton, S., Pouvreau, S., & Dumas, F. (2020). Intensive use of Lagrangian trajectories to quantify coastal area dispersion. *Ocean Dynamics*, *70*(4), 541–559. https://doi.org/10.1007/s10236-019-01343-6

Petton, S., Le Roy, V., Pouvreau, S. (2021). SMART Daoulas data from coriolis Data Centre in the Bay of Brest. SEANOE. https://doi.org/10.17882/86020

Petton, S., Garnier, V., Caillaud, M., Debreu, L., & Dumas, F. (2023). Using the two-way nesting technique AGRIF with MARS3D V11.2 to improve hydrodynamics and estimate environmental indicators. *Geoscientific Model Development*, *16*(4), 1191–1211. https://doi.org/10.5194/gmd-16-1191-2023

Philippart, C. J. M., van Iperen, J. M., Cadée, G. C., & Zuur, A. F. (2010). Long-term field observations on seasonality in chlorophyll-a concentrations in a shallow coastal marine ecosystem, the Wadden Sea. *Estuaries and Coasts*, *33*(2), 286–294. https://doi.org/10.1007/s12237-009-9236-y

Pineau-Guillou, L., Delouis, J. M., & Chapron, B. (2023). Characteristics of Storm Surge Events Along the North-East Atlantic Coasts. *Journal of Geophysical Research: Oceans*, *128*(4), 1–16. https://doi.org/10.1029/2022JC019493

Piver, D. Le, Gautier, L., Coail, J. Y., & Moreau, B. (2019). COSTOF2 , a smart solution for multisensor marine observations. *OCEANS 2019 - Marseille*, 1–5.

Plecha, S. M., & Soares, P. M. M. (2020). Global marine heatwave events using the new CMIP6 multi-model ensemble: From shortcomings in present climate to future projections. *Environmental Research Letters*, *15*(12). https://doi.org/10.1088/1748-9326/abc847

Plecha, S. M., Soares, P. M. M., Silva-Fernandes, S. M., & Cabos, W. (2021). On the uncertainty of future projections of Marine Heatwave events in the North Atlantic Ocean. *Climate Dynamics*, *56*(7–8), 2027–2056. https://doi.org/10.1007/s00382-020-05529-3

Plus Martin, Thouvenin Benedicte, Andrieux Francoise, Dufois Francois, Ratmaya Widya, Souchu Philippe (2021). Diagnostic étendu de l'eutrophisation (DIETE). Modélisation biogéochimique de la zone Vilaine-Loire avec prise en compte des processus sédimentaires . Description du modèle Bloom (BiogeochemicaL cOastal Ocean Model). RST/LER/MPL/21.15 . https://archimer.ifremer.fr/doc/00754/86567/

Poblete, B., Guzman, J., Maldonado, J., & Tobar, F. (2018). Robust Detection of Extreme Events Using Twitter: Worldwide Earthquake Monitoring. *IEEE Transactions on Multimedia*, *20*(10), 2551–2561. https://doi.org/10.1109/TMM.2018.2855107

Poppeschi, C., Charria, G., Goberville, E., Rimmelin-maury, P., Barrier, N., Petton, S., Unterberger, M., Grossteffan, E., Repecaud, M., Quéméner, L., Theetten, S., & Roux, J. Le. (2021). *Unraveling Salinity Extreme Events in Coastal Environments : A Winter Focus on the Bay of Brest*. *8*(July). https://doi.org/10.3389/fmars.2021.705403

Poppeschi Coline, Charria Guillaume, Daniel Anne, Verney Romaric, Rimmelin-Maury Peggy, Retho Michael, Goberville Eric, Grossteffan Emilie, Plus Martin (2022). Interannual variability of the initiation of the phytoplankton growing period in two French coastal ecosystems. Biogeosciences , 19(24), 5667-5687 . Publisher's official version : https://doi.org/10.5194/bg-2022-86

Ragueneau, O., Quéguiner, B., & Tréguer, P. (1996). Contrast in biological responses to tidally-induced vertical mixing for two macrotidal ecosystems of western Europe, Estuar. Coast. Shelf Sci., 42, 645–665. https://doi.org/10.1006/ecss.1996.0042

Rahmstorf, S., & Coumou, D. (2011). Increase of extreme events in a warming world. *Proceedings of the National Academy of Sciences of the United States of America*, *108*(44), 17905–17909. https://doi.org/10.1073/pnas.1101766108

Ren, F. M., Trewin, B., Brunet, M., Dushmanta, P., Walter, A., Baddour, O., & Korber, M. (2018). A research progress review on regional extreme events. *Advances in Climate Change Research*, *9*(3), 161–169. https://doi.org/10.1016/j.accre.2018.08.001

Retho Michael, Quemener Loic, Le Gall Christian, Repecaud Michel, Souchu Philippe, Gabellec Raoul, Manach Soazig (2022). COAST-HF - data and metadata from the MOLIT buoy in the Vilaine Bay. SEANOE. https://doi.org/10.17882/46529

Reynolds, R. W., Smith, T. M., Liu, C., Chelton, D. B., Casey, K. S., & Schlax, M. G. (2007). Daily high-resolution-blended analyses for sea surface temperature. *Journal of Climate*, *20*(22), 5473–5496. https://doi.org/10.1175/2007JCLI1824.1

Rimmelin-Maury Peggy, Charria Guillaume, Repecaud Michel, Quemener Loic, Beaumont Laurence, Guillot Antoine, Gautier Laurent, Prigent Sebastien, Le Becque Thierry, Bihannic Isabelle, Bonnat Armel, Le Roux Jean-Francois, Grossteffan Emilie, Devesa Jérémy, Bozec Yann, Gautier de Charnacé Corentin (2023). COAST-HF-Marel-Iroise buoy's time series (French Research Infrastructure ILICO) : long-term high-frequency monitoring of the Bay of Brest and Iroise sea hydrology. SEANOE. https://doi.org/10.17882/74004

Roland, A., & Ardhuin, F. (2014). On the developments of spectral wave models: Numerics and parameterizations for the coastal ocean Topical Collection on the 7th International Conference on Coastal Dynamics in Arcachon, France 24-28 June 2013. *Ocean Dynamics*, *64*(6), 833–846. https://doi.org/10.1007/s10236-014-0711-z

Rosa, F., Bloesch, J., & Rathke, D. E. (1994). Sampling the settling and suspended particulate matter (SPM). *Handbook of techniques for aquatic sediments sampling. CRC*, 97-129.

Ross Brown, A., Lilley, M. K. S., Shutler, J., Widdicombe, C., Rooks, P., McEvoy, A., Torres, R., Artioli, Y., Rawle, G., Homyard, J., Tyler, C. R., & Lowe, C. (2022). Harmful Algal Blooms and their impacts on shellfish mariculture follow regionally distinct patterns of water circulation in the western English Channel during the 2018 heatwave. *Harmful Algae*, *111*(December 2021), 102166. https://doi.org/10.1016/j.hal.2021.102166

Rumyantseva, A., Henson, S., Martin, A., Thompson, A. F., Damerell, G. M., Kaiser, J., & Heywood, K. J. (2019). Phytoplankton spring bloom initiation: The impact of atmospheric forcing and light in the temperate North Atlantic Ocean. *Progress in Oceanography*, *178*(September), 102202. https://doi.org/10.1016/j.pocean.2019.102202

Ruthrof, K. X., Breshears, D. D., Fontaine, J. B., Froend, R. H., Matusick, G., Kala, J., Miller, B. P., Mitchell, P. J., Wilson, S. K., van Keulen, M., Enright, N. J., Law, D. J., Wernberg, T., & Hardy, G. E. S. J. (2018). Subcontinental heat wave triggers terrestrial and marine, multi-taxa responses. *Scientific Reports*, *8*(1), 1–9. https://doi.org/10.1038/s41598-018-31236-5

Saulquin, B., Gohin, F., & Garrello, R. (2011). *Regional Objective Analysis for Merging and SeaWiFS Chlorophyll- a Data From 1998 to 2008 on the European Atlantic Shelf*. *49*(1), 143–154. https://doi.org/10.1109/TGRS.2010.2052813

Schlegel, R. W., & Smit, A. J. (2016). Climate change in coastal waters: Time series properties affecting trend estimation. *Journal of Climate*, *29*(24), 9113–9124. https://doi.org/10.1175/JCLI-D-16-0014.1

Schlegel, R., & Smit, A. (2018). heatwaveR: A central algorithm for the detection of heatwaves and cold-spells. *Journal of Open Source Software*, *3*(27), 821. https://doi.org/10.21105/joss.00821

Schlegel, R. W., Oliver, E. C. J., Hobday, A. J., & Smit, A. J. (2019). Detecting Marine Heatwaves With Sub-Optimal Data. *Frontiers in Marine Science*, *6*(November), 1–14. https://doi.org/10.3389/fmars.2019.00737

Schlegel, R. W., Darmaraki, S., Benthuysen, J. A., Filbee-dexter, K., & Oliver, E. C. J. (2021). Progress in Oceanography Marine cold-spells. *Progress in Oceanography*, *198*(September), 102684. https://doi.org/10.1016/j.pocean.2021.102684

Schmidt, R., & Stadtmüller, U. (2006). Non-parametric estimation of tail dependence. *Scandinavian Journal of Statistics*, *33*(2), 307–335. https://doi.org/10.1111/j.1467-9469.2005.00483.x

Schmitt, F., Schertzer, D., & Lovejoy, S. (1999). Multifractal analysis of foreign exchange data. *Applied Stochastic Models and Data Analysis*, *15*(1), 29–53. https://doi.org/10.1002/(SICI)1099-0747(199903)15:1<29::AID-ASM357>3.0.CO;2-Z

Seneviratne, S. I., Zhang, X., Adnan, M., Badi, W., Dereczynski, C., Di Luca, A., Ghosh, S., Iskandar, I., Kossin, J., Lewis, S., Otto, F., Pinto, I., Satoh, M., Vicente-Serrano, S. M., Wehner, M., & Zhou, B. (2021). Weather and Climate Extreme Events in a Changing Climate. In *Climate Change 2021: The Physical Science Basis. Contribution of Working Group I to the Sixth Assessment Report of the Intergovernmental Panel on Climate Change*. https://doi.org/10.1017/9781009157896.013

Serre-Fredj, L., Jacqueline, F., Navon, M., Izabel, G., Chasselin, L., Jolly, O., Repecaud, M., & Claquin, P. (2021). Coupling high frequency monitoring and bioassay experiments to investigate a harmful algal bloom in the Bay of Seine (French-English Channel). *Marine Pollution Bulletin*, *168*(January). https://doi.org/10.1016/j.marpolbul.2021.112387

Seuront, L., Nicastro, K. R., Zardi, G. I., & Goberville, E. (2019). Decreased thermal tolerance under recurrent heat stress conditions explains summer mass mortality of the blue mussel Mytilus edulis. *Scientific Reports*, *9*(1), 1–14. https://doi.org/10.1038/s41598-019-53580-w

Shi, J., Cui, L., Ma, Y., Du, H., & Wen, K. (2018). Trends in temperature extremes and their association with circulation patterns in China during 1961–2015. *Atmospheric Research*, *212*(May), 259–272. https://doi.org/10.1016/j.atmosres.2018.05.024

Simon, A., Plecha, S. M., Russo, A., Teles-Machado, A., Donat, M. G., Auger, P. A., & Trigo, R. M. (2022). Hot and cold marine extreme events in the Mediterranean over the period 1982-2021. *Frontiers in Marine Science*, *9*(August), 1–12. https://doi.org/10.3389/fmars.2022.892201

Simon, A., Poppeschi, C., Plecha, S., Charria, G., & Russo, A. (2023). Coastal and regional marine heatwaves and cold-spells in the Northeast Atlantic. *EGU Sphere*, *March*, 1–25. https://doi.org/10.5194/egusphere-2023-430

Smith, K. E., Burrows, M. T., Hobday, A. J., King, N. G., Moore, P. J., Sen Gupta, A., Thomsen, M. S., Wernberg, T., & Smale, D. A. (2023). Biological Impacts of Marine Heatwaves. *Annual Review of Marine Science*, *15*, 119–145. https://doi.org/10.1146/annurev- marine-032122-121437

Sims, D. W., Wearmouth, V. J., Genner, M. J., Southward, A. J., & Hawkins, S. J. (2004). Low-temperature-driven early spawning migration of a temperate marine fish. *Journal of Animal Ecology*, *73*(2), 333–341. https://doi.org/10.1111/j.0021-8790.2004.00810.x

Smale, D. A., & Wernberg, T. (2013). Extreme climatic event drives range contraction of a habitat-forming species. *Proceedings of the Royal Society B: Biological Sciences*, *280*(1754). https://doi.org/10.1098/rspb.2012.2829

Smale, D. A., Wernberg, T., Oliver, E. C. J., Thomsen, M., Harvey, B. P., Straub, S. C., Burrows, M. T., Alexander, L. V., Benthuysen, J. A., Donat, M. G., Feng, M., Hobday, A. J., Holbrook, N. J., Perkins-Kirkpatrick, S. E., Scannell, H. A., Sen Gupta, A., Payne, B. L., & Moore, P. J. (2019). Marine heatwaves threaten global biodiversity and the provision of ecosystem services. *Nature Climate Change*, *9*(4), 306–312. https://doi.org/10.1038/s41558-019-0412-1

Smith, M. D. (2011). The ecological role of climate extremes: Current understanding and future prospects. *Journal of Ecology*, *99*(3), 651–655. https://doi.org/10.1111/j.1365-2745.2011.01833.x

Smith, K. E., Burrows, M. T., Hobday, A. J., King, N. G., Moore, P. J., Sen Gupta, A., Thomsen, M. S., Wernberg, T., & Smale, D. A. (2023). Biological Impacts of Marine Heatwaves. *Annual Review of Marine Science*, *15*, 119–145. https://doi.org/10.1146/annurev-marine-032122-121437

Stephenson, D. B. (2008). Definition, diagnosis, and origin of extreme weather and climate events. *Climate Extremes and Society*, *9780521870*, 11–23. https://doi.org/10.1017/CBO9780511535840.003

Su, H., Wei, Y., Lu, W., Yan, X. H., & Zhang, H. (2023). Unabated Global Ocean Warming Revealed by Ocean Heat Content from Remote Sensing Reconstruction. *Remote Sensing*, *15*(3). https://doi.org/10.3390/rs15030566

Sura, P. (2011). A general perspective of extreme events in weather and climate. *Atmospheric Research*, *101*(1–2), 1–21. https://doi.org/10.1016/j.atmosres.2011.01.012

Tavora, J., Fernandes, E. H. L., Thomas, A. C., Weatherbee, R., & Schettini, C. A. F. (2019). The influence of river discharge and wind on Patos Lagoon, Brazil, Suspended Particulate Matter. *International Journal of Remote Sensing*, *40*(12), 4506–4525. https://doi.org/10.1080/01431161.2019.1569279

Tavora, J., Salama, M. S., Penning de Vries, M., Mannaerts, C. M., & van der Wal, D. (2023). Detecting the Effects of Extreme Events on Estuarine Suspended Particulate Matter Using Satellite Remote Sensing (Scheldt Estuary): Challenges and Opportunities. *Remote Sensing*, *15*(3). https://doi.org/10.3390/rs15030670

Thibault, K. M., & Brown, J. H. (2008). Impact of an extreme climatic event on community assembly. *Proceedings of the National Academy of Sciences of the United States of America*, *105*(9), 3410–3415. https://doi.org/10.1073/pnas.0712282105

Thomas, Y., Cassou, C., Gernez, P., & Pouvreau, S. (2018). Oysters as sentinels of climate variability and climate change in coastal ecosystems. *Environmental Research Letters*, *13*(10). https://doi.org/10.1088/1748-9326/aae254

Thompson, D. A., Karunarathna, H., & Reeve, D. E. (2017). Modelling extreme wave overtopping at Aberystwyth promenade. *Water (Switzerland)*, *9*(9), 1–16. https://doi.org/10.3390/w9090663

Townsend, D. W., Cammen, L. M., Holligan, P. M., Campbell, D. E., & Pettigrew, N. R. (1994). Causes and consequences of variability in the timing of spring phytoplankton blooms. *Deep-Sea Research Part I*, *41*(5–6), 747–765. https://doi.org/10.1016/0967-0637(94)90075-2

Tréguer, P., Goberville, E., Barrier, N., L'Helguen, S., Morin, P., Bozec, Y., Rimmelin-Maury, P., Czamanski, M., Grossteffan, E., Cariou, T., Répécaud, M., & Quéméner, L. (2014). Large and local-

scale influences on physical and chemical characteristics of coastal waters of Western Europe during winter. *Journal of Marine Systems*, *139*, 79–90. https://doi.org/10.1016/j.jmarsys.2014.05.019

Trenberth, K. E., Fasullo, J. T., & Shepherd, T. G. (2015). Attribution of climate extreme events. *Nature Climate Change*, *5*(8), 725–730. https://doi.org/10.1038/nclimate2657

Trombetta, T., Vidussi, F., Mas, S., Parin, D., Simier, M., & Mostajir, B. (2019). Water temperature drives phytoplankton blooms in coastal waters. *PLoS ONE*, *14*(4), 1–28. https://doi.org/10.1371/journal.pone.0214933

Trouet, V., Babst, F., & Meko, M. (2018). Recent enhanced high-summer North Atlantic Jet variability emerges from three-century context. *Nature Communications*, *9*(1), 1–9. https://doi.org/10.1038/s41467-017-02699-3

UICN. (n.d.). *Désoxygénation des océans : le problème de chacun décideurs*.

Ummenhofer, C. C., & Meehl, G. A. (2017). Extreme weather and climate events with ecological relevance: A review. *Philosophical Transactions of the Royal Society B: Biological Sciences*, *372*(1723). https://doi.org/10.1098/rstb.2016.0135

Van Aalst, M. K. (2006). The impacts of climate change on the risk of natural disasters. *Disasters*, *30*(1), 5–18. https://doi.org/10.1111/j.1467-9523.2006.00303.x

Vaquer-Sunyer, R., & Duarte, C. M. (2008). Thresholds of hypoxia for marine biodiversity. *Proceedings of the National Academy of Sciences of the United States of America*, *105*(40), 15452–15457. https://doi.org/10.1073/pnas.0803833105

Walsh, J. E., Ballinger, T. J., Euskirchen, E. S., Hanna, E., Mård, J., Overland, J. E., Tangen, H., & Vihma, T. (2020). Extreme weather and climate events in northern areas: A review. *Earth-Science Reviews*, *209*(August), 103324. https://doi.org/10.1016/j.earscirev.2020.103324

Wang, A. jun, Ye, X., Xu, X. hui, Yin, X. jie, & Xu, Y. hang. (2018). Settling flux and origin of particulate organic carbon in a macro-tidal semi-enclosed embayment: Luoyuan Bay, Southeast China coast. *Estuarine, Coastal and Shelf Science*, *206*, 38–48. https://doi.org/10.1016/j.ecss.2017.03.023

Wang, Y., Kajtar, J. B., Alexander, L. V., Pilo, G. S., & Holbrook, N. J. (2022). Understanding the Changing Nature of Marine Cold-Spells. *Geophysical Research Letters*, *49*(6), 1–9. https://doi.org/10.1029/2021GL097002

Wasan, D. T., Nikolov, A. D., & Brenner, H. (2001). Droplets speeding on surfaces. *Science*, *291*(5504), 605–606. https://doi.org/10.1126/science.1058466

Wernberg, T., Smale, D. A., Tuya, F., Thomsen, M. S., Langlois, T. J., De Bettignies, T., Bennett, S., & Rousseaux, C. S. (2013). An extreme climatic event alters marine ecosystem structure in a global biodiversity hotspot. *Nature Climate Change*, *3*(1), 78–82. https://doi.org/10.1038/nclimate1627

Werners, S. E., Pfenninger, S., van Slobbe, E., Haasnoot, M., Kwakkel, J. H., & Swart, R. J. (2013). Thresholds, tipping and turning points for sustainability under climate change. *Current Opinion in Environmental Sustainability*, *5*(3–4), 334–340. https://doi.org/10.1016/j.cosust.2013.06.005

Werners, S. E., van Slobbe, E., Bölscher, T., Oost, A., Pfenninger, S., Trombi, G., Bindi, M., & Moriondo, M. (2015). Turning points in climate change adaptation. *Ecology and Society*, *20*(4). https://doi.org/10.5751/ES-07403-200403

Wilson, R. J., & Heath, M. R. (2019). Increasing turbidity in the North Sea during the 20th century due to changing wave climate. *Ocean Science*, *15*(6), 1615–1625. https://doi.org/10.5194/os-15-1615-2019

Winder, M., & Sommer, U. (2012). Phytoplankton response to a changing climate. *Hydrobiologia*, *698*(1), 5–16. https://doi.org/10.1007/s10750-012-1149-2

Wölz, J., Fleig, M., Schulze, T., Maletz, S., Lübcke-von Varel, U., Reifferscheid, G., Kühlers, D., Braunbeck, T., Brack, W., & Hollert, H. (2010). Impact of contaminants bound to suspended particulate matter in the context of flood events. *Journal of Soils and Sediments*, *10*(6), 1174–1185. https://doi.org/10.1007/s11368-010-0262-y

Yang, Y., Ni, J., Niu, D., Zheng, G., & Li, Y. (2022). Physiological response of the razor clam Sinonovacula constricta exposed to hyposalinity stress. *Aquaculture and Fisheries*, *October*, 1–11. https://doi.org/10.1016/j.aaf.2022.11.002

Yao, Y., & Wang, C. (2022). Marine heatwaves and cold-spells in global coral reef zones. *Progress in Oceanography*, *209*(October), 102920. https://doi.org/10.1016/j.pocean.2022.102920

Yelekçi, Ö., Charria, G., Capet, X., Reverdin, G., Sudre, J., & Yahia, H. (2017). Spatial and seasonal distributions of frontal activity over the French continental shelf in the Bay of Biscay. *Continental Shelf Research*, *144*, 65-79. https://doi.org/10.1016/j.csr.2017.06.015

Zou, X. Y., Peng, X. Y., Zhao, X. X., & Chang, C. P. (2023). The impact of extreme weather events on water quality: international evidence. *Natural Hazards*, *115*(1), 1–21. https://doi.org/10.1007/s11069-022-05548-9

Zscheischler, J., Mahecha, M. D., Harmeling, S., & Reichstein, M. (2013). Detection and attribution of large spatiotemporal extreme events in Earth observation data. *Ecological Informatics*, *15*, 66–73. https://doi.org/10.1016/j.ecoinf.2013.03.004

Annexes

Annexe 1

Suspended particulate matter dynamics at the interface between an estuary and its adjacent coastal sea: unravelling the impact of tides, waves and river discharge from 2015-2022 *in situ* high-frequency observations.

Verney, R.[1]; Le Berre, D.[1]; Repecaud, M.[2]; Bocher, A.[3]; Bescond, T.[3] ; Poppeschi, C.[4]; Grasso, F.[1]

1. Ifremer, DYNECO-DHYSED, CS10070, 29280 Plouzane, France
2. Ifremer, RDT-LBCM, CS10070, 29280 Plouzane, France
3. Ifremer, RDT-SIIM, CS10070, 29280 Plouzane, France
4. Ifremer, Univ. Brest, CNRS, IRD, Laboratory for Ocean Physics and Satellite remote sensing (LOPS), IUEM, 29280 Brest, France.

1. Abstract

Suspended particulate matter (SPM) dynamics and exchange fluxes at the interface between a macrotidal estuary and its adjacent coastal sea were investigated from long-term high-frequency *in situ* observations. Optical and acoustic measurements were coupled to calculate SPM concentration over the whole water column using an existing acoustic inversion algorithm. A method was developed to distribute over the water column the surface and bottom calibrated equivalent particle diameters based on complementary ship-based surveys. Surface and bottom SPM show similar patterns in response to main forcings (tide, river discharge and waves), but present significantly higher concentrations near the bed. Increasing tidal ranges were responsible for higher tidal-median SPM concentrations, with spring/neap SPMC ratio varying from 2 to 3. This increase is driven by local resuspension during flood phase at the bottom, and low salinity turbid water flushed out from the estuary from mid-ebb to low tide at the surface. Increasing river discharge implies a downward shift of the estuarine turbidity maximum from the inner estuary to the mouth, and yields a 2-fold increase in both surface and bottom tidal-median concentration. Waves generated strong resuspension, with the highest SPM concentration recorded both at the surface and near the bed. Analysing SPM residual fluxes highlighted large up-estuary fluxes from low to moderate tidal ranges (below 6m), and exporting seaward fluxes for higher tidal ranges, due to stronger mixing during spring tides. High river discharge enhanced stratification at the mouth and strengthened density circulation and up-estuary residual bottom circulation, resulting in larger up-estuary fluxes for all tidal ranges. Larger SPM concentrations along the tidal cycle during wave events yield high exporting fluxes.

2. Introduction

Estuary-coastal systems (ECS) represent one of the most critical areas in the land-sea continuum, providing essential functions and services for both the ecosystem and the society, and is meantime dramatically threatened by human activities and climate change (Costanza et al., 1997; Lotze et al., 2006; Worm et al., 2006). ECS are featured by strong morphological, hydrological and biogeochemical gradients, structuring a mosaic of habitats and hence sheltering rich biodiversity. For several decades, ECS faced multiple challenges, potentially conflicting with their sustainable management (Halpern et al., 2008; Worm et al., 2006): preserving their predominant ecological value, their healthy biodiversity and together with providing essential ecosystem services (e.g. fisheries, maritime traffic); improving water quality threatened by urban and industrial effluents (Rodrigues et al., 2020) together with adapting to climate change effects (Dunn et al., 2019; Nicholls and Cazenave, 2010).

In such a changing context, investigating suspended particulate matter (SPM) dynamics and fluxes in the ECS can contribute to understanding and anticipating future trajectories of these systems. Indeed, SPM are transported all along the land-sea continuum, linking catchments, rivers, estuaries and coastal

seas. Understanding mechanisms controlling these fluxes is essential to address multiple challenges: i) nutrients and pollutants of various origin are adsorbed on SPM, hence water quality issue is closely related to SPM dynamics; ii) SPM through turbidity and light penetration depth contributes to control primary production (Cloern, 1987; Wetsteyn and Kromkamp, 1994); iii) while transported downward, SPM accumulate in estuarine turbidity maximum (ETM) areas (Burchard et al., 2018), creating a typical environment where organic and mineral SPM can be intensively transformed (Garnier et al., 2010), with direct consequences on water quality (Etcheber et al., 2011). Moreover, SPM fluxes and predominantly their mineral content drive the morphological evolution and sediment budget of ECS: migration of subtidal banks, evolution of lateral intertidal flats, siltation in the main channel(s) (Cox et al., 2021; Schulz et al., 2018; Wang et al., 2018). The latter yield to nearly continuously extensive maintenance dredging works to keep navigable channels (Cox et al., 2021; Lemoine and Le Hir, 2021). Finally, modifications in SPM fluxes due to climate change effects are crucial for the fate of estuarine habitats, and the functions they support (Leuven et al., 2019).

Within ECS, the estuarine dynamics and its consequences on ETMs have been largely explored, from *in situ* measurements (Jalón-Rojas et al., 2016, 2015; Jay et al., 2015; McSweeney et al., 2016; Moskalski et al., 2020; Sommerfield and Wong, 2011; Sottolichio et al., 2011) and modelling studies (Burchard and Baumert, 1998; Gong et al., 2022; Grasso et al., 2018; Hesse et al., 2019; Liu et al., 2023), leading to consolidated review papers (Burchard et al., 2018; Geyer and MacCready, 2014). These studies highlighted the importance of tides and river discharge on key sediment transport mechanisms: tidal pumping and density circulation induced by longitudinal and vertical stratification inside estuaries. Moving seaward, the interface between estuary and coastal sea is much less observed while not less complex, due to the strong competition between tides, river discharge and waves, generating large vertical gradients due to low-salinity-turbid surface plumes or intense bottom resuspension by tidal currents and waves (Chapalain et al., 2019). Together with modelling studies (e.g. Diaz et al., 2020; Grasso et al., 2021; Schulz et al., 2018), most existing observations are mainly ship-based surveys or short-term deployments (from weeks to months), that focus on limited typical events (Chapalain et al., 2019; Figueroa et al., 2020; Liu et al., 2011; Schettini et al., 2013; Uncles et al., 1985). However, understanding sediment transport regimes at the mouth of estuaries and how waves, tides and river discharge interact and drive SPM dynamics and sediment exchange between estuaries and coastal seas is essential to anticipate the morphological evolutions of ECS, and at the ecosystem scale their capacity to maintain their functions and services.

In the present study, we aim to unravel the relative contribution of tides, river discharge and waves on SPM dynamics and SPM fluxes at the interface between the estuary and the coastal sea, investigating physical mechanisms mainly explored with numerical models (Diaz et al., 2020; Grasso et al., 2021; Schulz et al., 2018). This work is supported by a long-term observation time series (2015-2022) at the SCENES coastal observation station, providing multi-source observations (CTD, optical and acoustic sensors) for a wide range of hydro-meteorological conditions. This dataset is concurrently used to analyse the influence of extreme forcing events on the SPM dynamics at the interface between estuary and coastal sea (see Poppeschi et al., submitted).

3. Methods

3.1. Study site

The Seine Estuary-sea continuum connects a 170km-long macrotidal estuary (with simi-diurnal tides, tidal range (TR)>7m during highest spring tides, TR<3m during lowest neap tides) and a large bay (100x50km^2, 30m depth on average, and shallower than 45m). The main tributary is the Seine River, characterized by a mean discharge (Q) of ~410m^3/s and flood events exceeding 800m^3/s and reaching

up to 2000m^3/s, mainly during winter and early spring. During summer, Q reaches the lowest values, below 200m^3/s and down to 100m^3/s during the driest years.
The Bay of Seine is partly protected from Atlantic Ocean swells but storm winds blowing from west to north-east generate intense local wave events generally from October to April. At the mouth of the estuary (depth ~15m), waves can reach 3 to 4m and periods from ~8s to 10s.
This system is highly engineered, with the presence of Le Havre and Rouen harbours, submersible dikes channelizing the tidal flow at the mouth, and intense, continuous dredging to maintain or enhance navigability (Figure 1) (Avoine et al., 1981; Grasso and Le Hir, 2019; Lemoine and Le Hir, 2021).

The Seine system is a mixed-sediment environment, with both mud and sand. At the mouth, sand banks are present on each side of the main channel, and mud covers mainly lateral intertidal areas. Subtidal areas are featured by a mosaic of mud-sand facies (Lesourd et al., 2016) with sand offshore and muddy fine sand-mud facies in the mouth. The Seine Estuary is characterized by a strong estuarine turbidity maximum (near-bottom SPM concentration (SPMC)~1 to 4 g/l; Druine et al., 2018), on average located 20km upstream of the estuary mouth (i.e. ~kilometric point (kp) 350 - kilometric distance from Paris). Depending on tides and river discharge, the tidally-averaged ETM position can move from the mouth (kp 365 – Q>1500m^3/s) to 20 to 30km upstream of the estuary (i.e. kp 340) for Q<200m^3/s (Grasso et al., 2018).

The SCENES observatory is located in the north-western part of the Seine mouth, at the interface between estuary and bay (49°28.844 N; 0°01.908 E), by 15.8 m depth (mean sea level – percentile 1: 12m – percentile 99: 19m). From field surveys in 2016, Chapalain et al. (2019) observed neap and spring tidal dynamics at this location, showing intense flood currents during spring, exceeding 1m/s, and lower ebb currents (~0.5m/s). They also observed a strong subsurface stratification at low tide (from 20 to 30PSU at surface compared with marine salinity ranging from 31PSU to 33PSU) when the estuarine freshwater is flushed out from the estuary to the bay. These estuarine waters are associated with SPMC reaching 50mg/l during spring tide and 10mg/l during neap tide. Near bottom (2m above the bed), Chapalain et al. (2019) also observed strong resuspension mainly during the flood phase, with SPMC values reaching 150mg/l during spring tide, and below 30mg/l during neap tides.

3.2. Hydro-meteorological and tidal forcing parameters

The tidal gauge at Le Havre (mouth of the Seine Estuary) provides the tidal range time series (http://datashom.fr). The river discharge is measured daily at the Vernon gauging station, located upstream the estuary tidal limit (www.hydro.eaufrance.fr), 200km up the mouth. According to Artelia (2019), we consider that the propagation time of the river flow to the mouth is on average 5 days.
Wave data such as the significant wave height (Hs) could have been directly taken from SCENES observation (wave characteristics recorded every hour). However, the maintenance of the bottom station is complex, as it requires regular diver intervention and fair-weather conditions. As a consequence, gaps are observed in bottom data. To work with a continuous wave dataset, wave parameters are extracted from Wave Watch III® (WW3, Roland and Ardhuin, 2014) model simulations at the closest mesh point from the SCENES station. Hourly WW3 data are available from the MARC wave portal (https://marc.ifremer.fr). Wave model parameters were compared against *in situ* data and show very good agreement (see appendix 8.1). Wave statistics are calculated per tide to provide key metrics, such as the percentile 90 of significant wave height per tide (Hs_{P90}).

3.3. SCENES station

The SCENES station is part of the National Observation Service COAST-HF and the regional PHRESQUES monitoring network operating along the Seine River-Estuary-Bay continuum. It combines a surface buoy and a bottom station. The system was first deployed from January 2015 to June 2017, then slightly modified and redeployed from October 2017 until now (see details below).

3.3.1. *Surface buoy*

The surface buoy is instrumented with a CTD measuring salinity, temperature and dissolved oxygen; an optical turbidity and fluorescence sensor and a weather station. The CTD and optical sensors are both equipped with anti-fouling systems. CTD and optical sensors collect measurements between 1m and 1.5m below surface every 15min. Data are stored internally and available in real time using 4G transmission.

3.3.2. *Bottom station*

The bottom station is equipped with an Acoustic Doppler Profiler (ADP – Nortek AWAC), measuring the current velocity profile (first bin 1.4m above bed (mab), bin size 0.5m) and the acoustic backscatter profile, as well as wave parameters. Current measurements are collected every 30min, while wave measurements are collected every hour. The same type of ADP was used from 2015 until now, but 3 sensors are used for assuring the best measurement continuity.
An optical sensor is also deployed from the bottom station. From 2015 to June 2017, only turbidity was recorded, 1.4mab. As the sensor was damaged by trawling, the optical sensor was then deployed 0.5mab from October 2017 and protected by a station frame. From 2017 to now, turbidity and fluorescence are recorded. Optical measurements are collected every 30min together with the current velocity profile.

3.4. *Field campaigns*

In order to maintain the station, periodically replace sensors (optimally every ~3-4months) and inter-calibrate observations, regular field surveys were conducted close to the SCENES station. Field surveys were realized at least seasonally, except in 2016 when surveys were done every two months. Each survey consisted of at least one tidal cycle observation, and sometimes more. This results in a total of 47 tidal cycles, but only 19 complete cycles are available with the station fully operational.

The same protocol was applied for all field campaigns and is fully described in Chapalain et al. (2019). Every 15min or 30min, CTD and optical sensor (OBS3+) profiles were realized. Data are collected at 4Hz and binned every 0.5m using downward cast. Every hour, subsurface and bottom water samples were collected using a horizontal Niskin bottle equipped with an optical turbidity and fluorescence sensor (identical to the optical sensor deployed from the station), allowing an optimal co-location of samples and optical measurements for NTU to SPMC calibration. Water samples were filtered on pre-ash, pre-weighted GFF filters, rinsed with demineralized water to remove remaining salts, air-dried at 50° for 24h and re-weighted to measure SPMC. The mean OBS3+ calibration coefficient is found to reach 0.00165g/l/NTU and is used in this study to calculate SPM concentration from the OBS3+.

3.5. *Data processing*

3.5.1. *Vertical bottom turbidity alignment between deployment periods*

The elevation of the bottom turbidity measurements changed from the first deployment period (2015-June 2017; 1.4mab – $Turb_{1.4mab}$) to the second (Oct. 2017-now; 0.5mab – $Turb_{0.5mab}$). As turbidity is higher close to the bed, this implies that larger turbidity values have been observed since 2017. In order to process a coherent bottom turbidity dataset, and ultimately to evaluate SPMC from acoustic backscatter data, data from the second period are extrapolated to 1.4mab. We calculated intratidal average turbidity climatology for each period (see section 3.4.6 for climatology calculation). All intratidal turbidity values for each condition of tidal range, wave intensity and river discharge from the

two datasets are then compared using the ratio between $Turb_{1.4mab}$ and $Turb_{0.5mab}$ (Figure 2). Data are grouped by classes of climatology $Turb_{0.5mab}$ (every 10NTU from 0 to 100NTU, and one class from 100 to 200NTU), and corresponding ratio values are selected. For each class, the median and percentile 25 and 75 values are calculated. Based on these statistical datasets, an empirical relationship comparing $Turb_{1.4mab}$ and $Turb_{0.5mab}$ is finally computed such as:

$$Turb_{1.4mab} = max\left(0.7 * e^{\frac{10-Turb_{0.5mab}}{40}} + 0.3; 1\right) * Turb_{0.5mab} \qquad \text{(Eq. 1)}$$

Hence for turbidity values at 0.5mab below 10NTU, no correction is applied, next the extrapolation factor exponentially decreases to reach 50% for $Turb_{0.5mab}$ around 50NTU and a plateau at 30% above 150NTU.

3.5.2. SCENES optical turbidity sensor calibration

All samples from field surveys are compared with optical turbidity measurements to evaluate an NTU to SPMC calibration function for sensors deployed on the station. No significant differences were observed between surface and bottom data, then all are pooled together. The calibration method developed by Landemaine (2016) and applied by Druine et al. (2018) and Chapalain et al. (2019) is used. The dataset (450 samples) is divided into 30 classes of 15 elements (division based on increasingly sorted turbidity values). Then in each class, one sample is randomly drawn and the linear relationship minimizing root-mean-square error (RMSE) is found. This is repeated 40000 times to get a stable probability density function of the calibration relationship. From this analysis, we observe that a range of calibration coefficients (from 0.0013 to 0.0018 g/l/NTU) corresponds to very similar RMSE. Then the median value within the lowest range of RMSE is used, i.e. 0.00156g/l/NTU. However, the SPMC was underestimated by ~0.001g/l for very low turbidity values. We decided to apply an offset of 0.001g/l to the calibration function (Figure 3):

$$SPMC = 0.00156 * NTU + 0.001 \qquad \text{(Eq. 2)}$$

Hence, even if the RMSE on the global dataset remain unchanged, bias and RMSE on the lowest SPMC are reduced. Finally, considering the calibration function described above, bias per concentration classes is below 15% and RMSE below 50%. We can also note that 70% of samples fall between calibration coefficients 0.0013 to 0.0025, which informs about the overall uncertainty when calibrating SCENES optical sensors over long time periods.

3.5.3. Evaluating bottom SPMC from ADP backscatter data

When measuring bottom SPMC at 0.5mab, turbidity sensor often saturated during stormy periods, when turbidity exceeded 180NTU (i.e. 0.085g/l). In order to evaluate SPMC during this saturation regime, the acoustic backscatter signal can be calibrated and used. Moreover, inverting acoustic signal to SPMC over the whole water column is necessary to evaluate sediment fluxes. The acoustic inversion approach for calculating bottom SPMC is fully detailed in appendix 9.2, and is only briefly summarized below.

The Sonar equation is used to convert the raw acoustic backscatter into decibels and correct it for geometric and near-field corrections, spherical spreading and water attenuation, as detailed in Tessier et al. (2008) and Fettweis et al. (2019). The acoustic model developed by Thorne et al. (2014) is used

to evaluate the calibration factor as a function of an optimal acoustic diameter, based on unsaturated bottom optical SPMC. This tidal optimal acoustic diameter is then averaged per tidal range and wave conditions, generating a tidal $D50_{opt\text{-}acc}$ climatology. This climatology can be used directly or dynamically-adapted to calculate optimal-acoustic SPMC ($SPMC_{opt\text{-}acc}$). $SPMC_{opt\text{-}acc}$ are substituted for the saturated optical SPMC measurements to create the final bottom SPMC time series.

3.5.4. Calculating intratidal statistical parameters at tidal scale for Hs, salinity, SPMC and SPM fluxes

Similarly to the method applied on $D50_{opt\text{-}acc}$, Hs, surface salinity and surface and bottom SPMC time series are processed to evaluate intratidal and statistical parameters at tidal scale. The original time series for each parameter is separated tide by tide, between two following low tides. The mean and percentiles 10, 50 and 90 are calculated for each tidal cycle. Also, each tide is characterized by its tidal range, the Seine River discharge and the percentile 90 of Hs over the 3 previous tides. For each forcing, different classes are given: from 2 to 8m, every 1m or 0.5 for tidal range, five Q ranges ([0-300]; [300-500]; [500-700]; [700-1000]; [1000-2500]m^3/s) and five Hs_{P90} classes ([0-0.5]; [0.5-1.0]; [1.0-1.5]; [1.5-2]; [2.0-2.5]m). For each class of combined parameters, corresponding intratidal time series of surface or bottom SPMC are interpolated on a common time array. For each intratidal time period, values from all selected tides are averaged, producing an intratidal climatology.

4. Results

4.1. Forcings, surface salinity and SPM dynamics

The Seine River discharge shows a strong inter-annual variability from 2015 to 2022. Winter 2016-2017, 2018-2019 and 2021-2022 are characterized by low river inputs, rarely and very exceptionally exceeding 1000m^3/s (Figure 4). In 2019-2020 and 2020-2021, the river discharge follows the average dynamics, with high values (exceeding 1800m^3/s) in January-February. Year 2015-016 is particular as an exceptional flood was recorded in June, reaching 2000m^3/s as on average 400m3/s are usually expected at this period of the year. Winter 2017-2018 was also particular, with an intense and remarkably long flood event: the river discharge was continuously above 1000m^3/s from January to April 2018.

The wave activity also follows a well-identified seasonal dynamics, with storms mainly occurring from October to March: at this period, storms induce Hs_{P90} ranging from 1 to 2m. Strongest events reach Hs_{P90} value above 3m. Winter 2017-2018, 2019-2020 and 2021-2022 are the most intense periods.

Surface salinity ranges from 10 to 34 PSU at the interannual scale, and as the river discharge shows a strong seasonal variability, with lower salinity (~20PSU) during high river flow (>1000m^3/s). At the tidal scale (not shown), surface salinity is lower during ebb and around slack, when ebb currents flush out estuarine brackish water towards the bay.

Depth-average current velocity (Figure 5) also significantly changes at the tidal scale. Peak flood currents are the strongest 1h to 2h after low tide and are directed southeast, following the estuary mouth funnel shape. Next, the current direction turns northward between 3h after low tide and high tide, due to tide propagation into the English Channel, generating a strong northward current, and named as the Verhaule current. Ebb currents are the strongest 2h to 3h after high tide and orientated north-west to west. Current intensity generally increases with the tidal range, with peak flood currents ranging on average from 0.2m/s during neap tides to 0.9m/s during spring tides.

Surface and bottom SPMC significantly varies seasonally in response to forcings (Figure 4). In general, SPMC at surface and bottom are the highest during winter, ranging from 0.01 to 0.1g/l at surface and from 0.01 to 1g/l at 1.4mab. SPMC decreases seasonally from spring to summer, together with lower wave conditions. At the end of summer, surface SPMC ranges from 0.005 to 0.02g/l and bottom SPMC from 0.005 to 0.08g/l. Tides also affect the SPMC variability, but this effect is not easily visible at the interannual scale. It can be observed during summer, in absence of wave and when tides dominate the hydrodynamic forcing, with a neap-spring variability of the tidal-median SPMC, especially close to the bed. Further investigations on the influence of each forcings on SPMC dynamics are explored in the discussion section.

4.2. Examining density circulation at the estuary mouth

At the estuary mouth, estuarine hydrodynamics and sediment transport are mainly controlled by tidal current (and tidal pumping) and density circulation. The latter is driven by confronting marine salt waters and riverine freshwaters, and the resulting vertical and horizontal gradients. While tidal pumping is clearly observed from current ellipses (Figure 5), with peak flood barotropic velocities during flood twice larger than the ebb velocities, and larger SPMC during flood, examining density circulation intensity requires further analysis.

The vertical salinity gradient was first evaluated. As bottom salinity is not recorded at the SCENES station, bottom salinity was explored from CTD field surveys. Bottom salinity was shown to weakly vary between 31.5 and 33.5, and bottom salinity was then fixed to a mean constant value of 32.5 PSU. Salinity gradient was then calculated by subtracting mean bottom salinity to the recorded surface salinity, and salinity gradient per tidal range and river discharge conditions was calculated (for low wave conditions - Figure 6). As expected, the salinity gradient decreases with increasing tidal ranges (tidal mixing) and increases with increasing river discharge. For low river flow conditions ($Q<300m^3/s$), the vertical salinity gradient varies from -1.5 PSU (spring tide) to -4.5 PSU (neap tide), while it ranges from -5 PSU (spring) to -12 PSU (neap) for Q values above $1000m^3/s$.

The mean bottom velocities (averaged on the 9 first bins above the bed, i.e. from 1.4 to 4.9m) are next extracted from the ADP dataset, and residual velocities are calculated for low wave conditions. These residual bottom velocities are averaged by tidal range and river discharge classes (Figure 6). For low to moderate river flow conditions, residual velocities are the strongest for low to moderate tidal ranges, reaching 0.02m/s and directed upward, while the highest spring tides are associated with seaward residual flows (around -0.02m/s). As observed in Figure 4 and Figure 6, increasing river flow yields to a decrease in surface salinity, hence enhancing stratification and density circulation: higher river flows and enhanced stratification lead to increase the landward residual bottom velocities (for low tidal range) and to turn residual flow direction during spring tides: for tidal range between 6m to 7m, the bottom residual velocities for low river flow ($Q<300m^3/s$) reaches -0.025m/s (seaward), while for high to exceptional river flows ($Q>500m^3/s$) residual velocities are positive (upward) and reach 0.01m/s and 0.02m/s respectively. For moderate tidal ranges, bottom residual velocity values are stronger and range from 0.02 to 0.06m/s. These observations are in very good agreement with model results of Schulz et al. (2018) at a similar location in the estuary.

4.3. SPM fluxes

4.3.1. Evaluating SPM fluxes

Surface and bottom SPM fluxes are calculated from surface and bottom SPMC and current velocity (bin 1.5m below surface and 1st bin above the bed respectively). Calculating depth-integrated SPM fluxes is more challenging, as it requires evaluating SPMC over the whole water column using the acoustic

backscatter signal (Eq. 3). Similarly to acoustic bottom concentration (3.5.3.), the main issue is to evaluate the vertical and temporal D50 variability, essential for the acoustic inversion. Bottom and surface SPMC time series can be used to evaluate bottom and surface optimal D50, but evaluating D50 for all bins in the water column requires an extrapolation method. This method is fully detailed in appendix 9.3.

The SPM concentration at all times and all bins in the water column computed from ADP backscatter data can be compared with ship-based SPMC measurements (Figure 7). Calculated ADP SPMC data are in good agreement with ship-based SPMC, with median values per SPMC class less than 10% different from the reference, and percentile 25 and 75 always within the +/-50% interval. Main differences are observed below 0.003g/l (overestimation) and over 0.07g/l (underestimation by 20% to 40%).

SPM depth-integrated fluxes are finally computed using ADP SPMC and current velocity profiles, projected along the main flood current direction (see dashed line in Figure 5). SPM fluxes at bin 1 are extended from seabed to bin 1. In order to consider reliable SPMC and current velocity below surface, SPM fluxes 1.5below surface are also extended to the sea surface. Intratidal depth-integrated fluxes, surface and bottom fluxes are integrated over each tide to calculate respective residual fluxes.

4.3.2. SPM fluxes time series

SPM fluxes dynamics are illustrated for two contrasted meteorological conditions, i.e. for calm weather (Hs_{P90}<1m - Figure 8) and storm conditions (Hs_{P90}>2m - Figure 9).

During calm weather conditions, both bottom, surface and depth-integrated fluxes increase with tidal range, as more energetic conditions are associated with stronger current velocities and larger SPMC in the water column. Bottom fluxes are stronger than surface fluxes whatever the tidal range, with maximum values observed during flood phase, e.g. ranging from 0.008kg/m/s during neap tide (TR=3.8m) to 0.015 kg/m/s during moderate spring tide (TR=5.5m). During flood phase, surface fluxes reach 0.002 to 0.004 kg/m/s from neap to spring. During ebb, bottom and surface fluxes show similar values, ranging between 0.002kg/m/s to 0.004kg/m/s. Sheared fluxes are observed around low tide, with positive (upward) bottom fluxes and negative (seaward) surface fluxes.
Depth-integrated fluxes show similar behaviour as the sum of the surface and bottom fluxes, with increasing strong upward flood fluxes reaching 0.25kg/m/s during spring tide, and less than 0.1kg/m/s during neap tide.
Residual bottom fluxes are significantly larger than residual surface fluxes, and residual depth-integrated fluxes are all positive, sediment being imported to the estuary. The depth-integrated residual fluxes are increasing with tidal range, varying from 400 kg/m per tide for low tidal ranges to 800 kg/m per tide for moderate tidal ranges.

The situation during stormy conditions is definitively different (Figure 9). Moderate wave conditions (1m<Hs<2m – 01/10-01/12) show larger bottom fluxes compared with surface fluxes during flood phase, but depth-integrated flux intensities are similar during ebb and flood (around 0.1kg/m/s). From the 13th to 14th of January, Hs values are larger than 2m and reach up to 3m. Surface and bottom fluxes strongly increase, reaching 0.03 kg/m/s and 0.1 kg/m/s respectively, 4 to 6 times larger than during calm conditions. Depth-integrated fluxes also increase during storms, e.g. 2kg/m/s during flood and -2kg/m/s during ebb. These intense resuspension conditions, associated with strong mixing due to high tidal range (TR>6m) yield strongly negative seaward fluxes, both observed from raw and residual depth-integrated fluxes, often reaching -2000 to -5000 kg/m per tide. While Hs decreases (Hs<1m – 16/01/2017), residual depth-integrated fluxes still show negative values, highlighting an hysteresis-time lag effect on SPMC before the situation comes back to normal (calm) condition, up to 2 tides after strong wave condition (17/01/2017).

5. Discussion

5.1. Unravelling the impact of tides, waves and river discharge on SPM concentration

5.1.1. Q/TR/HS on SPM concentration

Tide, river discharge and storms play a significant role on the SPMC patterns along the year, but highlighting and unravelling their individual contribution is challenging, as these forcings are often superimposed. A first approach is to analyse the tidal-median SPMC variability per conditions of tidal range, river discharge and wave activity (Figure 10).

Surface and bottom tidal-median SPMC show similar trends, but different orders of magnitude, with higher SPMC being observed near the bottom. For a given river flow condition, the tidal-median SPMC increases with the tidal range. For instance, for average river flow conditions (300-500m^3/s) and low wave activity (Hs_{P90}<1m), tidal-median surface SPMC increases from 0.008g/l to 0.010g/l while tidal-median bottom SPMC ranges from 0.015 to 0.035g/l.

Increasing river discharge causes an increase in both surface and bottom SPMC, with a factor from 2 to 3. Hence, for tidal range values between 3 and 4m, median tidal-median surface SPMC increases from 0.005 to 0.013g/l and bottom values from 0.009 to 0.02g/l. Considering surface dynamics in response to river flow, confronting tidal median surface salinity and SPMC with tidal range provides clear insights for periods of low wave conditions (Figure 11): high river flows induce low surface salinity and stronger stratification at the mouth, especially during neap tide, and low salinity (<20PSU) is associated with high surface SPMC (up to 0.02g/l). Increasing tidal range induces intense vertical mixing and hence higher salinity values (~28PSU), but SPMC remains high.

Wave events significantly increase SPMC, and the stronger the wave event, the higher the SPMC. Figure 10 shows the impact of waves (Hs_{P90}=[1-2]m and Hs_{P90}=[2-3]m) for river discharge ranging from 300 to 500m^3/s. This effect is observed both for surface and bottom, but is larger near the bed, with median tidal-median concentration ranging from 0.04 to 0.08g/l for Hs_{P90} values above 2m. For a given tidal range condition, the variability in bottom tidal-median SPMC induced by wave events is large, ranging from 0.025 up to 0.2g/l.

5.1.2. Intratidal SPMC Climatology

As observed above, the SPMC tidal signal is strongly entangled with the contribution of wave and river discharge. In order to separate the tidal contribution from the raw high-frequency signal, an SPMC climatology, i.e. an intratidal-average signal, is computed from the raw data, representative of low wave (Hs_{P90}<1m) and mean river discharge (Q=[300-500]m^3/s) conditions. First, all tides corresponding to these criteria are extracted. Then selected tides are separated by tidal range (from 2 to 8m, every 1m) and tidal range gradient conditions (positive: neap to spring; negative: spring to neap) (refer to section 3.5.4. for the description of the methodology).

Contrary to median tidal SPMC patterns, which are similar for surface and bottom SPMC (see section above), intratidal SPMC patterns highlight the influence of the main forcing on the respective dynamics (Figure 12). Surface SPMC values are the highest around low tide, associated with low salinity conditions, while the lowest SPMC values are found around high tide (around 0.01g/l on average). This pattern is clearly visible from mid to high tidal ranges (TR>4m), and the magnitude of the maximum

SPMC value around low tide increases with the tidal range, from 0.015g/l for TR values between 5 to 6m up to 0.035g/l for TR values above 7m.

Bottom concentration follows a different pattern, with the highest SPMC observed 1h to 3h after low tide, during the flood phase. At the end of the flood phase, 4h to 5h after low tide, a second peak in SPMC can be observed associated with the Verhaule northward current, on average 20% lower than the main flood peak and advecting sediment from the main channel. Then SPMC decreases progressively until high tide and remains stable or weakly increases during the ebb phase. Similarly to surface SPMC, the magnitude of the bottom SPMC signal is correlated with the tidal range, the maximum bottom SPMC reaching 0.065g/l during high spring tide (TR>7m), and reaching still nearly 0.03g/l for low to moderate tidal ranges (TR =[4-5]m). Bottom SPMC during ebb is also modulated by the tidal range, ranging from 0.01g/l during the lowest neap tides to 0.03g/l during the highest spring tides.

Differences between fortnightly tidal phases are low for high tidal ranges, but more sensible for neap tides, especially near the bed: for tidal ranges between 4 to 5m, peak SPMC during flood is 30% larger from spring to neap than neap to spring (increasing from 0.028 to 0.037g/l). Similarly, the SPMC during ebb is larger, increasing from 0.01 to nearly 0.02g/l from positive to negative tidal range gradient, respectively.

These differences in SPMC patterns are related to different dominant processes for surface and bottom concentration. Bottom SPMC dynamics is driven by local resuspension, especially during flood phase when peak current velocity can reach up to 1m/s. Bottom sediments resuspended by tidal currents seem to weakly reach the surface. High SPMC around low tide is related to estuarine brackish water being flushed out the estuary towards the bay at the end of ebb tide and around low tide. The increase in SPMC with the tidal range is driven by ETM resuspension in the estuary and advected toward the mouth during ebb.

5.1.3. SPM concentration anomalies

The intratidal SPMC signal can then be used to evaluate the contribution of wave events and river discharge by analysing SPMC anomalies (i.e. subtracting the intratidal signal from the raw signal) (Figure 13). Both surface and bottom SPMC anomalies vary around 0, but anomalies are mainly positive. High positive surface SPMC anomalies (above 0.05g/l and up to 0.1g/l) are observed during intense wave events, and correspond to twice the maximum tidal-induced SPMC observed during spring tide. The role of river discharge is more difficult to evaluate from time series. Negative anomalies (around 0.01g/l maximum) are mainly observed during summer, when the river discharge is the lowest.

Bottom SPMC anomalies range between 0.05 and 0.5g/l, and are often associated with intense wave events, as observed at the surface. These positive anomalies can reach up to 10 times the maximum tidal-induced concentration during spring tide (Figure 12). Similarly to surface SPMC, negative anomalies are observed during summer and low river discharge conditions.

In order to further investigate the relative influence of river discharge and wave events on SPMC anomalies, tidal-median SPMC anomalies are computed and separated by Hs_{P90} and river discharge conditions, similarly to results shown in section 5.1.1. In agreement with Poppeschi et al. (submitted), Figure 14 confirms the dominant role of wave events on suspended sediment dynamics at the mouth of the estuary, with median anomalies during intense wave events that can reach 4 times the tidal median SPMC during spring tide, i.e. 0.1g/l. More interestingly, this figure highlights the weaker but sensible influence of the river discharge. In absence of wave (Hs_{P90}<1m) bottom and surface anomalies increase with river discharge, reaching 0.05 g/l and 0.02 g/l respectively during intense flood events

(Q>1000m^3/s). This contribution for high river discharge is on average twice the tidal contribution. The influence of river discharge is also observed during storms, while not as clear as in absence of wave. While the influence of wave events is associated with "local" resuspension (i.e. at the mouth), the contribution of river discharge is directly related to ETM dynamics: with increasing river discharge, the ETM is progressively shifted downstream until being centred nearly at the estuary mouth for large river discharge (Q>1000m^3/s) as shown by Grasso et al. (2018). This implies i) higher SPMC at the surface and arriving sooner during ebb phase due to enhanced vertical stratification and ii) an additional source of easily fresh erodible sediments by tidal currents and waves on the seafloor.

5.2. *Unravelling the impact of tides, waves and river discharge on residual SPM fluxes*

5.2.1. *Relative influence of forcings*

The influence of tides and waves on residual fluxes was first illustrated in 4.3.2. and highlighted that calm conditions are associated with an import of SPM to the estuary mouth with a modulation by the tidal range, while storms yield SPM export. The relative contribution of forcings to residual SPM fluxes at the estuary-sea interface is further examined in this section, grouping residual fluxes values per conditions of wave, tidal range and river discharge and calculating median values, as presented in Figure 15.

Surface residual fluxes are generally negative (directed seaward), increasing with tidal range (TR>6m) and wave intensity (Hs_{P90}>1.5m) and exceeding 50kg/m per tide. Increasing river discharge weakly increases surface residual fluxes, despite an increase in SPMC concentration for high river flow as observed in Figure 10. This is because the increase in SPMC span +/-3h around LT, and positive early flood phase fluxes partly compensate negative ebb phase fluxes.
Bottom residual fluxes are directed landward, also increase with increasing tidal range, and show higher values during high wave conditions. The impact of increasing river discharge is even more significant, with a 2-fold increase especially for moderate to high tidal range conditions (4m<TR<7m). This is first explained by higher and asymmetric SPMC during high river flow, proportionally larger during flood than ebb, due to the ETM shift toward the mouth (Grasso et al., 2018). Also, high river flow enhances vertical and longitudinal stratification at the mouth and strengthens density circulation (Figure 6), leading to landward bottom sediment fluxes (Burchard and Baumert, 1998; Diaz et al., 2020; Grasso et al., 2021; Grasso and Le Hir, 2019; Schulz et al., 2018).

Considering depth-integrated residual fluxes and low to moderate river discharge (Q<500m^3/s), sediments are globally imported to the estuary for low to moderate tidal ranges (TR<6) and low wave conditions (Hs_{P90}<1.5), and exported to the sea for high tidal range conditions and storm events (TR>6m or Hs_{P90}>1.5m), due to stronger mixing in the water column during both flood and ebb as observed by Sommerfield and Wong (2011) in the most downstream part of the Delaware Estuary. The export of sediments during wave events was already observed by Figueroa et al. (2020), although weaker as their study site was more protected from waves than the Seine mouth. High and exceptional river discharge (>500m^3/s) are associated with positive (landward) and higher residual fluxes, even for high tidal range or wave conditions, related to the significant increase in near-bottom density circulation (Figure 6). This competition between tidal pumping, stratification and density circulation was already pointed out by McSweeney et al. (2016).

The comparison with previous studies is uneasy as most of observations mainly focused on ETM dynamics, hence further in-estuary, with different settings in terms of SPMC, width and depth, and wave influence. However, results can be compared with numerical simulations from Schulz et al. (2018) and Grasso et al. (2021) in the Seine Estuary. Schulz et al. (2018) subdivided the estuary mouth into boxes and calculated fluxes at all boundaries, and along full cross-sections from south to north, one

offshore, common with Grasso et al. (2021) and one close to the mouth. The comparison between model and observations can only be qualitative as models integrate fluxes over segments or cross-sections while observations are local and not representative of the full cross-section exchange, with potential cross-estuary shear fluxes as illustrated by McSweeney et al. (2016). In addition, Diaz et al. (2020) show that simulated fluxes between estuaries and coastal seas are associated with large uncertainties due to the equifinality effects in sediment transport parameterisation. Observations and model results agree on the general patterns, i.e. landward residual fluxes increasing with tidal range, the export of sediment during storms and the import of sediment with increasing river discharge. Model results do not clearly show the inversion of residual fluxes seaward when tidal ranges exceed 6m for low wave conditions, but the simulation analysis did not separate results by wave conditions, which precludes direct comparisons.

Complementary cross-estuary observation at the mouth should be prioritized in the near future to improve sediment exchange understanding at the interface between the estuary and the coastal sea, and examine the interaction between the morphology of the mouth and sediment fluxes.

5.2.2. Residual fluxes: uncertainty and limitations

These median (or mean) residual fluxes $F_{res,50}$ values are associated with uncertainty estimation U_F (triangles in Figure 15), representing the spread of residual fluxes per forcing conditions. A given condition is flagged uncertain if the median residual flux is positive (negative) and the percentile 25 (75) is negative (positive). The intensity of the uncertainty is quantified as:

$$\begin{cases} U_F = \left| \frac{F_{res,50} - F_{res,25}}{F_{res,50}} \right| & if\ F_{res,50} > 0 \\ U_F = \left| \frac{-F_{res,50} + F_{res,75}}{F_{res,50}} \right| & if\ F_{res,50} < 0 \end{cases}$$

For forcing conditions at the interface between landward to seaward fluxes, U_F is the largest, meaning that raw residual fluxes can also be directed opposite to the median flux direction. Hence these forcing conditions represent transitional patterns. This uncertainty can be caused by: i) possible miscalculation of SPMC vertical profiles, mainly during wave events where the ADP calibration vertical extrapolation can be questioned as not validated by ship-based surveys; and ii) the low occurrence of observations for these hydro-meteorological conditions hence weakening the statistical significance. This demonstrates that maintaining coastal and estuarine observatories and improving the continuity in measurements for long-term periods (i.e. decades) is essential to consolidate our understanding of SPM dynamics and SPM fluxes in these critical and complex areas.

A weakness in the current dataset is gaps in surface or bottom data, sometimes for very long time periods such as in 2019-2020 for surface data. Integrating *in situ* observations and ocean colour satellite data based on the most recent algorithms could provide a relevant solution for filling gaps and extending the surface dataset (Ody et al., 2022; Tavora et al., 2020). Similarly, statistical and machine learning gap-filling techniques (Arriagada et al., 2021; Phan et al., 2020) could also be carefully explored to densify observations.

5.2.3. An attempt for calculating annual cumulative residual fluxes and sediment budget

Extending investigations to evaluate cumulative fluxes and hence analyse annual to pluriannual SPM exchange at the mouth of the estuary is more challenging. Observations in the present study are not continuous in time, and cannot be directly used to reach this objective. Median depth-integrated residual fluxes shown in Figure 15 can first be used, constituting residual fluxes times series by

associating the median residual flux to the corresponding forcing conditions (Figure 16), tide by tide. This approach concludes with a long-term sediment import to the estuary (+300ton/m over 7 years), which is not in agreement with Schulz et al. (2018), who find that this area mainly exports SPM. In this approach, calculating median fluxes per condition biases the results for conditions weakly observed (less than 10 tides from 2015 to 2022) and when raw fluxes values show strong and asymmetric (positive/negative) variability. Indeed, flux values are highly scattered when analysing the whole dataset, with far larger negative values than positive values. Then, using a median operator smooths these high negative values, and biases results toward positive, importing, fluxes. Using the mean operator instead also biases results but in the opposite direction: the mean operator gives more weight to extremely negative values. Hence cumulative fluxes calculated from mean flux values conclude to strong negative, exporting, fluxes (-250ton/m) in 7 years. If the flux direction is now in line with model results on the area obtained by Schulz et al. (2018), the cumulative flux intensity is also questionable, as most high energetic conditions are rarely observed in our dataset, and statistics might not be reliable. Increasing the amount of collected data with coming observations in the next year will certainly improve statistics reliability, and hence cumulative flux estimation, but a new approach can also be tested with the existing dataset.

It should be noted that, as observed Figure 15, using mean or median operators does not change the conclusions on the role of forcings on residual fluxes when forcing intensities are low to moderate. The impact is mainly visible for high wave conditions and high tidal ranges that were already flagged as uncertain, and for which mean or median values change from positive to negative or show strong negative values.

Considering the previous methods unsatisfactory, a new method directly using the probability density function (PDF) of observed fluxes per condition can be used, hence accounting for intra-condition residual fluxes scattering. For each tide, a residual flux is randomly drawn within the PDF corresponding to the tidal condition. The more frequent the flux value, the higher the probability of getting this value. This stochastic approach is repeated 300 times to create a consistent ensemble of possible cumulative residual fluxes (Figure 16), and the ensemble average is calculated. This approach also informs about the uncertainty in cumulative flux estimation. Cumulative residual fluxes calculated at the end of the study period range from weakly importing values (+50ton/m) to high exporting values (-200ton/m). The ensemble average residual flux reaches -80ton/m, far from the mean export value exceeding -250ton/m.

Annual local sediment budgets can also be estimated by separating each year (from October to October) and calculating annual cumulative residual fluxes, and compared with wave and river discharge annual statistics (Figure 17). Wet years (average Q>500m^3/s) mainly show positive residual fluxes. Year 2015-2016 show the highest positive residual flux as it combines annual high river discharge and low wave conditions. Year 2019-2020 is the stormiest year, and sediment budget is the most negative, exporting sediment. Other years highlight the competition between wave-driven export and density circulation-driven import. When annual wave conditions are similar, increasing river discharge yields to significant exportation reduction and even, for the largest river discharge, to import sediment to the estuary. Year 2016-2017 is atypical because it is characterized by the lowest wave conditions, but is also one of the most exporting years. This may be explained by exceptionally low river discharge conditions, hence weakening the density circulation contribution, and increasing the relative contribution of tidal-driven fluxes or wave-driven fluxes.

This method to evaluate sediment budgets shows promising results, but must be strengthened by i) increasing the length of the dataset; ii) improving measurement continuity; iii) consolidating SPM concentration calculation from ADP measurements during storm conditions.

5.3. *Combining acoustics and optics: insights about SPM composition*

Most studies using ADP to estimate vertical SPM concentration profile use an empirical linear relationship between the acoustic backscatter index BI and $\log_{10}$ of the SPM concentration (Dufois, 2014; Fettweis et al., 2019; Figueroa et al., 2020; McSweeney et al., 2016; Tessier et al., 2008). This method is convenient and easy to implement, but can show limitations for long-term deployments as calibration should be regularly updated. Moreover, as slope coefficient can significantly move far from 1 for each calibration, hence diverging from theory, these coefficients cannot be related to any physical SPM feature.

The approach developed in this study follows theoretical developments (Thorne et al., 2014), calculating an equivalent optimal acoustic diameter $D50_{opt\text{-}acc}$ for each acoustic profile. This $D50_{opt\text{-}acc}$ was first considered as a calibration parameter, but it could also be, with care, considered as qualitatively characterizing the near bed SPM composition, in terms of sand-mud content, as explored by Pearson et al. (2021) with the Sediment Composition Index (SCI). By analogy with their study, SCI is equivalent to $-f(D50_{opt\text{-}acc})=-10\log10(\sigma/(\rho*v))$ in Eq. 4; then when $D50_{opt\text{-}acc}$ increases, SCI decreases and sand content increases. However, the absolute $D50_{opt\text{-}acc}$ value calculated by the inversion algorithm cannot be considered as representative of the median SPM particle size, but only as a proxy for sand or mud content. Indeed, the acoustic backscatter intensity has not been fully calibrated, and the system constant still needs to be estimated. This absolute calibration requires further investigations and accurate knowledge on particles and/or flocs in suspension, which is out of the scope of this study.

Examining raw $D50_{opt\text{-}acc}$ time-series (Figure 18) and intratidal average $D50_{opt\text{-}acc}$ (Figure 20) illustrates the sand/mud content variability in response to tidal and wave forcing: low $D50_{opt\text{-}acc}$ values are observed during neap tides and around slacks at the tidal scale; and high values are found during spring tides and during flood phase at the tidal scale. For increasing tidal ranges, $D50_{opt\text{-}acc}$ increases during flood phase with an abrupt increase for the largest tidal range values, indicating a non-linear increase in sand content with tidal range. This is in agreement with literature and theory: current velocity increases and turbulence conditions are likely to erode and resuspend fine sand in suspension, and sand erosion fluxes are non-linearly correlated with current velocity (Soulsby, 1997). This would suggest a net import of sand toward the estuary. We can also note if waves on average are associated with higher $D50_{opt\text{-}acc}$ values (Figure 20), intense wave events do not always necessarily correspond to high $D50_{opt\text{-}acc}$ values (Figure 18). This might be explained by either uncertainty in the extrapolation of the near-bed SPMC to observation 1.4mab, or due to incomplete sediment attenuation correction.

Two populations of particles, sand grains and flocs, are assumed to be possibly found in suspension. It could be envisaged to process the acoustic inversion considering a bimodal sand/floc population, expanding from the work by Fromant et al. (2017) on flocs and using the coupled optical-acoustic sensors to evaluate sand/mud fraction and total concentration. Investigating further acoustic inversion, including accurate absolute instrument calibration and bimodal SPM population may improve our understanding of the SPM composition and hence the quantification of both sand and mud concentrations and fluxes.

6. Conclusions

In situ high-frequency optical and acoustic observations were analysed to evaluate suspended particulate matter concentration at the surface and near the bed. An iterative inversion technique was applied to calibrate long-term acoustic measurements using equivalent D50. A climatology of

equivalent D50 was computed as a function of intratidal and subtidal dynamics, highlighting the probability for sand particles to be resuspended during spring tide flood phases, and during wave events. An original method was proposed to extrapolate equivalent D50 along the water column from surface and bottom measurements and hence calculating SPM concentration everywhere in the water column and reducing uncertainty. Further developments on acoustic inversion including two populations of particles could be further investigated to potentially evaluate both sand and fine sediment in suspension.

Surface and bottom measurements were examined to evaluate hydrodynamics, SPM dynamics and exchange between estuary and coastal sea in response to tides, river discharge and waves. Surface dynamics was shown to be correlated with the tidal range, the river discharge and waves. Surface SPM concentrations during spring are twice the SPM concentrations observed during neap. For a given tidal range, increasing river discharge leads to increase SPM concentrations by a factor of 2 due to the shift of the estuarine turbidity maximum toward the mouth, and high waves again multiply by 2 SPM concentrations for a given tidal range and river discharge. At tidal scale, the same patterns are observed near the bottom, while SPM concentrations are on average twice the surface SPM concentrations. Moreover, the impact of storms on bottom SPM concentrations is more significant. These results highlight the cumulative impact of tidal and hydro-meteorological forcings on SPM concentration. The tidal-induced SPM concentration can possibly hide the impact of other forcings, hence an intratidal climatology of SPM concentration for low-wave conditions and mean river discharge ($300<Q<500 m^3/s$) was calculated for TR classes. Subtracting this climatology to high-frequency raw signal yields to evaluate SPM concentration anomalies, emphasizing the role of waves and river discharge.

Surface, bottom and depth-integrated SPM fluxes were evaluated, and residual fluxes were analysed by forcing conditions. Residual fluxes are directed upward, importing sediment to the estuary for moderate tidal ranges (TR=[3 6]m) and low wave conditions. For high tidal range, residual fluxes are directed seaward, due to higher SPM concentration along the tidal cycle. Waves and tides contribute to higher SPM concentration in the water column and hence residual fluxes are oriented seaward. In case of high and exceptional river discharge ($Q>500 m^3/s$), the density circulation is strengthened and induces stronger importing residual fluxes, even for high tidal ranges.

These analyses can be further compared with modelled fluxes to contribute to consolidating model calibration and reducing uncertainty. These results from long-term observation strategy are also valuable to evaluate future changes in sediment exchange at the interface between estuary and coastal sea induced by estuarine management and climate change.

7. Acknowledgments

This work was co-funded by Ifremer and the PHRESQUES project, coordinated by the GIP Seine Aval. PHRESQUES was funded by the CPIER « Vallée de Seine », the Seine Normandy Water Agency (AESN), and the Normandie and Ile de France Regions. This project is also supported by the eLTER « Zone Atelier Seine » . This study also contributes to the RUNTIME project, co-funded by the EC2CO program and OFB.

We would like to acknowledge the COAST-HF (http://www.coast-hf.fr) national observing network component of the National Research Infrastructure ILICO, as well as the CNFC and RV Thalia and Côtes de la Manche crews for their support in field surveys.

8. References

Arriagada, P., Karelovic, B., Link, O., 2021. Automatic gap-filling of daily streamflow time series in data-scarce regions using a machine learning algorithm. Journal of Hydrology 598, 126454. https://doi.org/10.1016/j.jhydrol.2021.126454

Artelia, 2019. Définition des périodes de retour des forçages et des niveaux de pleines mers en estuaire de Seine pour la gestion du risque inondation.

Avoine, J., Allen, G.P., Nichols, M., Salomon, J.C., Larsonneur, C., 1981. Suspended-sediment transport in the Seine estuary, France: Effect of man-made modifications on estuary—shelf sedimentology. Marine Geology 40, 119–137. https://doi.org/10.1016/0025-3227(81)90046-3

Burchard, H., Baumert, H., 1998. The Formation of Estuarine Turbidity Maxima Due to Density Effects in the Salt Wedge. A Hydrodynamic Process Study. Journal of Physical Oceanography 28, 309–321. https://doi.org/10.1175/1520-0485(1998)028<0309:TFOETM>2.0.CO;2

Burchard, H., Schuttelaars, H.M., Ralston, D.K., 2018. Sediment Trapping in Estuaries. Annu. Rev. Mar. Sci. 10, 371–395. https://doi.org/10.1146/annurev-marine-010816-060535

Chapalain, M., Verney, R., Fettweis, M., Jacquet, M., Le Berre, D., Le Hir, P., 2019. Investigating suspended particulate matter in coastal waters using the fractal theory. Ocean Dynamics 69, 59–81. https://doi.org/10.1007/s10236-018-1229-6

Cloern, J.E., 1987. Turbidity as a control on phytoplankton biomass and productivity in estuaries. Continental Shelf Research 7, 1367–1381. https://doi.org/10.1016/0278-4343(87)90042-2

Costanza, R., d'Arge, R., de Groot, R., Farber, S., Grasso, M., Hannon, B., Limburg, K., Naeem, S., O'Neill, R.V., Paruelo, J., Raskin, R.G., Sutton, P., van den Belt, M., 1997. The value of the world's ecosystem services and natural capital. Nature 387, 253–260. https://doi.org/10.1038/387253a0

Cox, J.R., Dunn, F.E., Nienhuis, J.H., van der Perk, M., Kleinhans, M.G., 2021. Climate change and human influences on sediment fluxes and the sediment budget of an urban delta: the example of the lower Rhine–Meuse delta distributary network. Anthropocene Coasts 4, 251–280. https://doi.org/10.1139/anc-2021-0003

Diaz, M., Thouvenin, B., Grasso, F., Le Hir, P., Sottolichio, A., Caillaud, M., 2020. Modeling mud and sand transfers between a macrotidal estuary and the continental shelf: influence of the sediment-transport parameterization. Journal Of Geophysical Research-oceans. https://doi.org/10.1029/2019JC015643

Druine, F., Verney, R., Deloffre, J., Lemoine, J.-P., Chapalain, M., Landemaine, V., Lafite, R., 2018. In situ high frequency long term measurements of suspended sediment concentration in turbid estuarine system (Seine Estuary, France): Optical turbidity sensors response to suspended sediment characteristics. Marine Geology 400, 24–37. https://doi.org/10.1016/j.margeo.2018.03.003

Dufois Francois, C.S., Verney Romaric, Le Hir Pierre, Dumas Franck, 2014. Impact of winter storms on sediment erosion in the Rhone River prodelta and fate of sediment in the Gulf of Lions (North Western Mediterranean Sea). Continental Shelf Research. https://doi.org/10.1016/j.csr.2013.11.004

Dunn, F.E., Darby, S.E., Nicholls, R.J., Cohen, S., Zarfl, C., Fekete, B.M., 2019. Projections of declining fluvial sediment delivery to major deltas worldwide in response to climate change and anthropogenic stress. Environmental Research Letters 14, 084034. https://doi.org/10.1088/1748-9326/ab304e

Etcheber, H., Schmidt, S., Sottolichio, A., Maneux, E., Chabaux, G., Escalier, J.-M., Wennekes, H., Derriennic, H., Schmeltz, M., Quéméner, L., Repecaud, M., Woerther, P., Castaing, P., 2011. Monitoring water quality in estuarine environments: lessons from the MAGEST monitoring program in the Gironde fluvial-estuarine system. Hydrology and Earth System Sciences 15, 831–840. https://doi.org/10.5194/hess-15-831-2011

Fettweis, M., Riethmüller, R., Verney, R., Becker, M., Backers, J., Baeye, M., Chapalain, M., Claeys, S., Claus, J., Cox, T., Deloffre, J., Depreiter, D., Druine, F., Flöser, G., Grünler, S., Jourdin, F., Lafite, R., Nauw, J., Nechad, B., Röttgers, R., Sottolichio, A., Van Engeland, T., Vanhaverbeke, W., Vereecken, H., 2019. Uncertainties associated with in situ high-frequency long-term observations of suspended particulate matter concentration using optical and acoustic sensors. Progress in Oceanography 178, 102162. https://doi.org/10.1016/j.pocean.2019.102162

Figueroa, S.M., Lee, G., Chang, J., Schieder, N.W., Kim, K., Kim, S.-Y., 2020. Evaluation of along-channel sediment flux gradients in an anthropocene estuary with an estuarine dam. Marine Geology 429, 106318. https://doi.org/10.1016/j.margeo.2020.106318

Fromant, G., Floc'h, F., Lebourges-Dhaussy, A., Jourdin, F., Perrot, Y., Le Dantec, N., Delacourt, C., 2017. In Situ Quantification of the Suspended Load of Estuarine Aggregates from Multifrequency Acoustic Inversions. Journal of Atmospheric and Oceanic Technology 34, 1625–1643. https://doi.org/10.1175/JTECH-D-16-0079.1

Garnier, J., Billen, G., Némery, J., Sebilo, M., 2010. Transformations of nutrients (N, P, Si) in the turbidity maximum zone of the Seine estuary and export to the sea. Estuarine, Coastal and Shelf Science 90, 129–141. https://doi.org/10.1016/j.ecss.2010.07.012

Geyer, W.R., MacCready, P., 2014. The Estuarine Circulation. Annu. Rev. Fluid Mech. 46, 175–197. https://doi.org/10.1146/annurev-fluid-010313-141302

Gong, W., Zhang, G., LirongYuan, Zhu, L., Zhang, H., 2022. Effects of swell waves on the dynamics of the estuarine turbidity maximum in an idealized convergent partially mixed estuary. Journal of Marine Systems 235, 103784. https://doi.org/10.1016/j.jmarsys.2022.103784

Grasso, F., Bismuth, E., Verney, R., 2021. Unraveling the impacts of meteorological and anthropogenic changes on sediment fluxes along an estuary-sea continuum. Scientific Reports 11, 20230. https://doi.org/10.1038/s41598-021-99502-7

Grasso, F., Le Hir, P., 2019. Influence of morphological changes on suspended sediment dynamics in a macrotidal estuary: diachronic analysis in the Seine Estuary (France) from 1960 to 2010. Ocean Dynamics 69, 83–100. https://doi.org/10.1007/s10236-018-1233-x

Grasso, F., Verney, R., Le Hir, P., Thouvenin, B., Schulz, E., Kervella, Y., Khojasteh Pour Fard, I., Lemoine, J.-P., Dumas, F., Garnier, V., 2018. Suspended Sediment Dynamics in the Macrotidal Seine Estuary (France): 1. Numerical Modeling of Turbidity Maximum Dynamics. Journal of Geophysical Research: Oceans 123, 558–577. https://doi.org/10.1002/2017JC013185

Halpern, B.S., Walbridge, S., Selkoe, K.A., Kappel, C.V., Micheli, F., D'Agrosa, C., Bruno, J.F., Casey, K.S., Ebert, C., Fox, H.E., Fujita, R., Heinemann, D., Lenihan, H.S., Madin, E.M.P., Perry, M.T., Selig, E.R., Spalding, M., Steneck, R., Watson, R., 2008. A Global Map of Human Impact on Marine Ecosystems. Science 319, 948–952. https://doi.org/10.1126/science.1149345

Hesse, R.F., Zorndt, A., Fröhle, P., 2019. Modelling dynamics of the estuarine turbidity maximum and local net deposition. Ocean Dynamics 69, 489–507. https://doi.org/10.1007/s10236-019-01250-w

Jalón-Rojas, I., Schmidt, S., Sottolichio, A., 2015. Turbidity in the fluvial Gironde Estuary (southwest France) based on 10-year continuous monitoring: sensitivity to hydrological conditions. Hydrology and Earth System Sciences 19, 2805–2819. https://doi.org/10.5194/hess-19-2805-2015

Jalón-Rojas, I., Schmidt, S., Sottolichio, A., Bertier, C., 2016. Tracking the turbidity maximum zone in the Loire Estuary (France) based on a long-term, high-resolution and high-frequency monitoring network. Continental Shelf Research 117, 1–11. https://doi.org/10.1016/j.csr.2016.01.017

Jay, D.A., Talke, S.A., Hudson, A., Twardowski, M., 2015. Chapter 2 - Estuarine turbidity maxima revisited: Instrumental approaches, remote sensing, modeling studies, and new directions, in: Ashworth, P.J., Best, J.L., Parsons, D.R. (Eds.), Developments in Sedimentology. Elsevier, pp. 49–109. https://doi.org/10.1016/B978-0-444-63529-7.00004-3

Landemaine, V., 2016. Erosion des sols et transferts sédimentaires sur les bassins versants de l'Ouest du Bassin de Paris: analyse, quantification et modélisation à l'échelle plurianuelle (French version). Rouen University.

Lemoine, J.P., Le Hir, P., 2021. Maintenance dredging in a macrotidal estuary: Modelling and assessment of its variability with hydro-meteorological forcing. Estuarine, Coastal and Shelf Science 258, 107366. https://doi.org/10.1016/j.ecss.2021.107366

Lesourd, S., Lesueur, P., Fisson, C., Dauvin, J.-C., 2016. Sediment evolution in the mouth of the Seine estuary (France): A long-term monitoring during the last 150years. Comptes Rendus Geoscience 348, 442–450. https://doi.org/10.1016/j.crte.2015.08.001

Leuven, J.R.F.W., Pierik, H.J., Vegt, M. van der, Bouma, T.J., Kleinhans, M.G., 2019. Sea-level-rise-induced threats depend on the size of tide-influenced estuaries worldwide. Nature Climate Change 9, 986–992. https://doi.org/10.1038/s41558-019-0608-4

Liu, G., Zhu, J., Wang, Y., Wu, H., Wu, J., 2011. Tripod measured residual currents and sediment flux: Impacts on the silting of the Deepwater Navigation Channel in the Changjiang Estuary. Estuarine, Coastal and Shelf Science 93, 192–201. https://doi.org/10.1016/j.ecss.2010.08.008

Liu, J., Li, Y., Pan, Q., Zhang, T., 2023. Suspended sediment transport and turbidity maximum in a macro-tidal estuary with mountain streams: A case study of the Oujiang Estuary. Continental Shelf Research 255, 104924. https://doi.org/10.1016/j.csr.2023.104924

Lotze, H.K., Lenihan, H.S., Bourque, B.J., Bradbury, R.H., Cooke, R.G., Kay, M.C., Kidwell, S.M., Kirby, M.X., Peterson, C.H., Jackson, J.B.C., 2006. Depletion, degradation, and recovery potential of estuaries and coastal seas. Science 312, 1806–1809. https://doi.org/10.1126/science.1128035

McSweeney, J.M., Chant, R.J., Sommerfield, C.K., 2016. Lateral variability of sediment transport in the Delaware Estuary. Journal of Geophysical Research: Oceans 121, 725–744. https://doi.org/10.1002/2015JC010974

Moskalski, S., Floc'h, F., Verney, R., 2020. Suspended sediment fluxes in a shallow macrotidal estuary. Marine Geology 419, 106050. https://doi.org/10.1016/j.margeo.2019.106050

Nicholls, R.J., Cazenave, A., 2010. Sea-Level Rise and Its Impact on Coastal Zones. Science 328, 1517–1520. https://doi.org/10.1126/science.1185782

Ody, A., Doxaran, D., Verney, R., Bourrin, F., Morin, G.P., Pairaud, I., Gangloff, A., 2022. Ocean Color Remote Sensing of Suspended Sediments along a Continuum from Rivers to River Plumes: Concentration, Transport, Fluxes and Dynamics. Remote Sensing 14. https://doi.org/10.3390/rs14092026

Pearson, S.G., Verney, R., van Prooijen, B.C., Tran, D., Hendriks, E.C.M., Jacquet, M., Wang, Z.B., 2021. Characterizing the Composition of Sand and Mud Suspensions in Coastal and Estuarine Environments Using Combined Optical and Acoustic Measurements. Journal of Geophysical Research: Oceans 126, e2021JC017354. https://doi.org/10.1029/2021JC017354

Phan, T.-T.-H., Poisson Caillault, É., Lefebvre, A., Bigand, A., 2020. Dynamic time warping-based imputation for univariate time series data. Pattern Recognition Letters 139, 139–147. https://doi.org/10.1016/j.patrec.2017.08.019

Poppeschi, C., Verney, R., Charria, G., submitted. Suspended particulate matter response to extreme forcings in the Bay of Seine. Submitted to Marine Geology.

Rodrigues, M., Cravo, A., Freire, P., Rosa, A., Santos, D., 2020. Temporal assessment of the water quality along an urban estuary (Tagus estuary, Portugal). Marine Chemistry 223, 103824. https://doi.org/10.1016/j.marchem.2020.103824

Roland, A., Ardhuin, F., 2014. On the developments of spectral wave models: numerics and parameterizations for the coastal ocean. Ocean Dynamics 64, 833–846. https://doi.org/10.1007/s10236-014-0711-z

Schettini, C.A.F., Duarte Pereira, M., Siegle, E., de Miranda, L.B., Silva, M.P., 2013. Residual fluxes of suspended sediment in a tidally dominated tropical estuary. Continental Shelf Research 70, 27–35. https://doi.org/10.1016/j.csr.2013.03.006

Schulz, E., Grasso, F., Le Hir, P., Verney, R., Thouvenin, B., 2018. Suspended Sediment Dynamics in the Macrotidal Seine Estuary (France): 2. Numerical Modeling of Sediment Fluxes and Budgets Under Typical Hydrological and Meteorological Conditions. Journal of Geophysical Research: Oceans 123, 578–600. https://doi.org/10.1002/2016JC012638

Sommerfield, C.K., Wong, K.-C., 2011. Mechanisms of sediment flux and turbidity maintenance in the Delaware Estuary. Journal of Geophysical Research: Oceans 116. https://doi.org/10.1029/2010JC006462

Sottolichio, A., Castaing, P., hetcheber, H., Maneux, E., Schmeltz, M., Schmidt, S., 2011. Observations of suspended sediment dynamics in a highly turbid macrotidal estuary, derived from continuous monitoring. Journal of Coastal Research 1579–1583.

Soulsby, R., 1997. Dynamics of marine sands. Thomas Telford Publishing. https://doi.org/10.1680/doms.25844

Stanton, T.K., Wiebe, P.H., Chu, D., 1998. Differences between sound scattering by weakly scattering spheres and finite-length cylinders with applications to sound scattering by zooplankton. The Journal of the Acoustical Society of America 103, 254–264. https://doi.org/10.1121/1.421135

Tavora, J., Boss, E., Doxaran, D., Hill, P., 2020. An Algorithm to Estimate Suspended Particulate Matter Concentrations and Associated Uncertainties from Remote Sensing Reflectance in Coastal Environments. Remote Sensing 12. https://doi.org/10.3390/rs12132172

Tessier, C., Le Hir, P., Lurton, X., Castaing, P., 2008. Estimation de la matière en suspension à partir de l'intensité rétrodiffusée des courantomètres acoustiques à effet Doppler (ADCP). Comptes Rendus Geoscience 340, 57–67. https://doi.org/10.1016/j.crte.2007.10.009

Thorne, P.D., MacDonald, I.T., Vincent, C.E., 2014. Modelling acoustic scattering by suspended flocculating sediments. Continental Shelf Research 88, 81–91. https://doi.org/10.1016/j.csr.2014.07.003

Uncles, R.J., Elliott, R.C.A., Weston, S.A., 1985. Observed fluxes of water, salt and suspended sediment in a partly mixed estuary. Estuarine, Coastal and Shelf Science 20, 147–167. https://doi.org/10.1016/0272-7714(85)90035-6

Wang, Z.B., Elias, E.P.L., van der Spek, A.J.F., Lodder, Q.J., 2018. Sediment budget and morphological development of the Dutch Wadden Sea: impact of accelerated sea-level rise and subsidence until 2100. Netherlands Journal of Geosciences 97, 183–214. https://doi.org/10.1017/njg.2018.8

Wetsteyn, L.P.M.J., Kromkamp, J.C., 1994. Turbidity, nutrients and phytoplankton primary production in the Oosterschelde (The Netherlands) before, during and after a large-scale coastal engineering project (1980–1990), in: Nienhuis, P.H., Smaal, A.C. (Eds.), The Oosterschelde Estuary (The Netherlands): A Case-Study of a Changing Ecosystem. Springer Netherlands, Dordrecht, pp. 61–78. https://doi.org/10.1007/978-94-011-1174-4_7

Worm, B., Barbier, E.B., Beaumont, N., Duffy, J.E., Folke, C., Halpern, B.S., Jackson, J.B.C., Lotze, H.K., Micheli, F., Palumbi, S.R., Sala, E., Selkoe, K.A., Stachowicz, J.J., Watson, R., 2006. Impacts of Biodiversity Loss on Ocean Ecosystem Services. Science 314, 787–790. https://doi.org/10.1126/science.1132294

9. Appendices

9.1. Evaluation of WW3 wave model at the SCENES Station

Hourly WW3 data are available from the MARC wave portal (wwww.marc.ifremer.fr). Wave parameters are extracted from WaveWatch3 model simulations at the closest mesh point from the SCENES station. Wave model parameters are compared against *in situ* data, and show very good agreement, except for the highest observed Hs values, underestimated by the model.

9.2. Evaluating bottom SPMC from ADP backscatter data

The Sonar equation is used to convert the raw acoustic backscatter into decibels and correct it for geometric and near-field corrections, spherical spreading and water attenuation, as detailed in Fettweis et al. (2019) and Tessier et al. (2008). As SPMC can be temporary higher than 0.1g/l close to the bed (i.e. below 1.5m), sediment attenuation is also taken into account, using an iterative method as described in Thorne et al. (2014). From the Sonar equation, a backscatter index (BI) is calculated such as:

$$N + K_c\,(E - E_0) = SL - 20\,log_{10}(\psi R^2) - 2\int_0^R (\alpha_w(r) + \alpha_s(r))dr + BI + 10log_{10}\left(\varphi R^2 \frac{WS}{2}\right) \quad \text{(Eq. 3)}$$

Where E is the echo amplitude recorded by the ADP, N and E_0 the noise and reference acoustic level, Kc the conversion constant from count to dB, SL the source level (dB), R the distance from transducer to cell, ψ the near-field correction factor, α_w and α_s the water and sediment attenuation respectively, WS the cell size, φ the solid angle and BI the backscatter index.

The raw echo amplitude signal E recorded by the ADP can be significantly lowered due to biofouling as well as decreasing battery level. During the first weeks of the deployment of brand-new ADP, the amplitude signal recorded for low turbidity values (between 2 to 5NTU) is measured on average around 150count. As a first step, an offset per tide is calculated such as the raw echo amplitude signal in count is 150count for turbidity values at 1.4mab ranging from 2 to 5NTU. However, this correction is not applicable to long periods when turbidity remains high above 5NTU over the tidal cycle, as observed during winter time. When applicable, the correction value is then interpolated.

BI is directly related to SPM characteristics (e.g. median diameter, D50), using acoustic/floc hybrid interaction model developed by Thorne et al. (2014):

$$BI = 10log_{10}\left(\frac{SSC\,\bar{\sigma}}{\rho_s\,\overline{v_s}}\right) = 10log_{10}(SSC) + f(D50_{opt-acc}) \quad \text{(Eq. 4)}$$

With σ the backscattering cross section, ρ_s and v_s the representative floc volume and density (Stanton et al., 1998; Thorne et al., 2014 – n_f=2; D_p=4μm). At this stage, this optimal $D50_{opt\text{-}acc}$ must be considered as an equivalent acoustic calibration parameter, and not necessary as an absolute physical characteristic of SPM.

The temperature is recorded close to the bed and considered constant over the water column. The salinity is not necessarily known, and first considered constant, at 34PSU.

In this section we only consider the acoustic backscatter at the first cell of the ADP, and calibrate it against the SPMC recorded 1.4mab, i.e. at the elevation of the first bin of the ADP. $D50_{opt\text{-}acc}$ is calculated to retrieve the optical-derived SPMC, outside the saturation regime. $D50_{opt\text{-}acc}$ strongly varies at the tidal scale and also fortnightly. In order to evaluate an appropriate $D50_{opt\text{-}acc}$ within the saturation regime, the $D50_{opt\text{-}acc}$ time series is tide-separated, from low tide to the following low tide, and classified by tidal range and wave conditions. The intratidal time series for a given tidal range are then averaged to produce a climatology for $D50_{opt\text{-}acc}$ (refer to section 3.5.4. for method). This $D50_{opt\text{-}acc}$ climatology (Figure 20) is used to estimate bottom SPMC when the optical sensor reaches the saturation regime.

From November 2021 and March 2022, a high-range (0-1000NTU) optical Wetlabs FLNTU turbidity meter was deployed, hence significantly limiting saturation. This period is used to evaluate our capacity to compensate for saturated data using acoustic measurements.

Applying $D50_{opt\text{-}acc}$ to evaluate saturated SPMC provides reasonable but still uncertain quantification of D50 and hence SPMC (Figure 21 left). This is probably due to incomplete correction of the biofouling effect by correcting the raw echo amplitude. The next step in postprocessing (detailed below) can be separated in two situations, depending if turbidity is fully or partly saturated over the tidal cycle. For each situation, the $D50_{opt\text{-}acc}$ tidal climatology is modulated by multiplying $D50_{opt\text{-}acc}$ with a correction factor k_{opt} ranging from 0 to 2.

If turbidity data are fully saturated over the whole tidal cycle, the optimal correction factor k_{opt} corresponds to calculated tidal acoustic SPMC with all N values per tide above the saturation concentration (0.085g/l) and the closer to 1, meaning the lowest compensation is applied.

$$\begin{cases} \sum_{1}^{N} \left(SSC_{opt-acc}(k_{opt}) > SSC_{saturation}\right) = N \\ \& \\ abs(k_{opt} - 1) = \min\left(abs(k-1)\right) \end{cases} \quad \text{(Eq. 5)}$$

If saturation is partial and only concern N_{sat} (N_{sat}<N) values per tidal cycle, the optimal correction factor k_{opt} is calculated from a cost function based on the combination of calculated acoustic SPMC values above the saturation concentration when saturated and a good fit with observed non saturated data:

$$\begin{cases} fac_{sat}(k) = \frac{1}{N_{sat}} \sum_{1}^{N_{sat}} \left(SSC_{opt-acc}(k) > SSC_{saturation}\right) \\ fac_{obs}(k) = abs\left(\left\langle \frac{(SSC_{opt-acc}(k) - SSC_{obs}}{SSC_{obs}} \right\rangle\right) \\ fac(k) = \min\left(fac_{obs}(k) * \left(1 - \frac{N_{sat}}{N}\right) + fac_{sat}(k) * \frac{N_{sat}}{N}\right) \\ fac\left(k_{opt}\right) = \min\left(fac(k)\right) \end{cases} \quad \text{(Eq. 6)}$$

Figure 21 illustrates the efficiency of the saturation compensation method from acoustic inversion using high-range turbidity measurements. Adapting climatology provides better SPMC estimation for low concentration values (0-0.1g/l), but also and more important in high SPMC ranges (>0.1g/l). While median acoustic SPMC values reach a threshold around the saturation value when using raw climatology, the compensation method provides far better SPMC estimation, while still underestimating SPMC for values above 0.1g/l. The latter can be explained by the absence of reference data available to contribute to scale the correction factor when all the tidal cycle is saturated. In such situation k_{opt} is chosen to compute SPMC just above the saturation concentration, but during intense energetic events (i.e. large resuspension events), the "real" concentration can be significantly larger.

9.3. Evaluating depth-varying SPM concentration from ADP measurements

ADP measurements are largely used to evaluate SPMC in the water column. Similarly to bottom SPMC, this requires to correctly calibrate the optimal D50 in each cell, without additional observation other than bottom and surface optical SPMC. This section details the method applied to retrieve SPMC concentration over the whole water column and for all acoustic profile over the 7year period.

Based on ship-based surveys and vertical SPMC profiles at the tidal cycle, it is possible to calculate this parameter for the 19 tidal cycles. The optimal D50 for each bin is estimated using the Sonar equation

to match the observed optical SPMC in the water column, as illustrated in Figure 22. The D50 vertical dynamics significantly changes at tidal scale: strong vertical D50 gradients are observed, during flood and ebb phases, at different relative depth, e.g. decreasing from ~110µm close to the bed to ~50µm in the top half of the water column in 2015. We can also note that the dynamics is different before and after October 2017, associated with a change in bottom deployments: while D50 generally decreases from bottom to surface before October 2017 (i.e. 2015) during flood phase, D50 is maximum in the middle of the water column after October 2017. This is possibly due to the extrapolation of the SPMC 1.4mab during the second phase, which contains uncertainties. This can imply larger $D50_{opt\text{-}acc}$, which are used to normalize the D50 vertical profile. Two different D50 extrapolation methods are then searched to estimate the vertical distribution of D50 for each period.

All ship-based tidal cycles available for each period are used and cast time recalculated with the local low-tide time as reference. Vertical bin depths are normalized with the corresponding water depth, hence varying from 0 (bottom) to 1 (surface). For each cast, D50(z) are normalized by the bottom $D50_{opt\text{-}acc}$ estimated from bottom SPMC. Finally, all normalized D50 casts for all tidal cycles per period are grouped hourly from low tide, and averaged to provide hourly mean normalized D50 vertical profile at the tidal scale (Figure 23) and noted $D50_{z\_norm}$. As subsurface acoustic data often interfere with sea surface and wave-generated bubbles, $D50_{z\_norm}$ values are frozen to the value calculated at 80% of the total depth, corresponding to the depth of the sub-surface optical turbidity sensor. Before October 2017, $D50_{z\_norm}$ decreases from bottom to surface by 20% to 40% compared to bottom $D50_{opt\text{-}acc}$. During the second period (after October 2017), $D50_{z\_norm}$ first increases by 20 to 30% in the bottom third of the water column and decreases above, except around low tide.

This method ensures that the calculated bottom SPM concentrations using the acoustic backscatter signal still compare exactly with the bottom $SPMC_{opt\text{-}acc}$ at all times. A last correction must be included to ensure that surface SPMC from the acoustic signal also compare with the surface SPMC derived from the optical turbidity sensors. Similarly to bottom SPMC, two equivalent D50 are calculated based on observed surface SPMC 1.5m (optical sensor level) and 2.5m below surface. Two D50 are calculated as the acoustic backscatter can be impacted by air bubbles generated by waves or by sea surface reflection, and the $D50_{1.5bs}$ calculated 1.5m below surface can be biased. A $D50_{2.5bs}$ (2.5m below surface) is also calculated from the observed surface SPMC, assuming low subsurface SPMC gradients. Next, a vertical surface correction (cor_{surf_z}) is computed. Below mid-depth, cor_{surf_z} equals 1, and no correction is applied. At 80% of the water depth, the $D50_{2.5m}$ is forced to coincide with the optimal D50, and at 85% of the water column and higher, $D50_{1.5bs}$ is forced. From mid depth to 80% of the total depth, a linear interpolation is applied such as:

$$\begin{cases} \mathrm{cor}_{\mathrm{surf_z}}\left(\frac{z}{h}\right) = 1 \quad \text{if} \quad \frac{z}{h} \leq 0.5 \\ \mathrm{cor}_{\mathrm{surf\_z}}\left(\frac{z}{h}\right) = \mathrm{linear\_interp}\left(\left[\mathrm{cor}_{\mathrm{surf\_z}}\left(\frac{z}{h}=0.5\right)\ ;\ \mathrm{cor}_{\mathrm{surf\_z}}\left(\frac{z}{h}=0.8\right)\right], \frac{z}{h}\right) \quad \text{if} \quad 0.5 < \frac{z}{h} < 0.80 \\ \mathrm{cor}_{\mathrm{surf\_z}}\left(\frac{z}{h}\right) = \frac{\mathrm{D50_{2.5bs}}}{D50_{opt-acc} * D50_{z\_norm}\left(\frac{z}{h}\right)} \quad if \ \frac{z}{h} = 0.8 \\ \mathrm{cor}_{\mathrm{surf\_z}}\left(\frac{z}{h}\right) = \frac{\mathrm{D50_{1.5bs}}}{D50_{opt-acc} * D50_{z\_norm}\left(\frac{z}{h}\right)} \quad if \ \frac{z}{h} \geq 0.85 \end{cases} \qquad \text{(Eq. 7)}$$

Finally, the vertical D50 array at each time is calculated such as:

$$D50\left(\frac{z}{h}\right) = \mathrm{cor}_{\mathrm{surf\_z}}\left(\frac{z}{h}\right) * D50_{opt-acc} * D50_{z\_norm}\left(\frac{z}{h}\right)$$

(Eq. 8)

Using Eq. 3 and Eq. 4 solving the Sonar equation, the SPM concentration at all times and all bins in the water column can be computed from ADP backscatter data and compared with ship-based SPMC measurements.

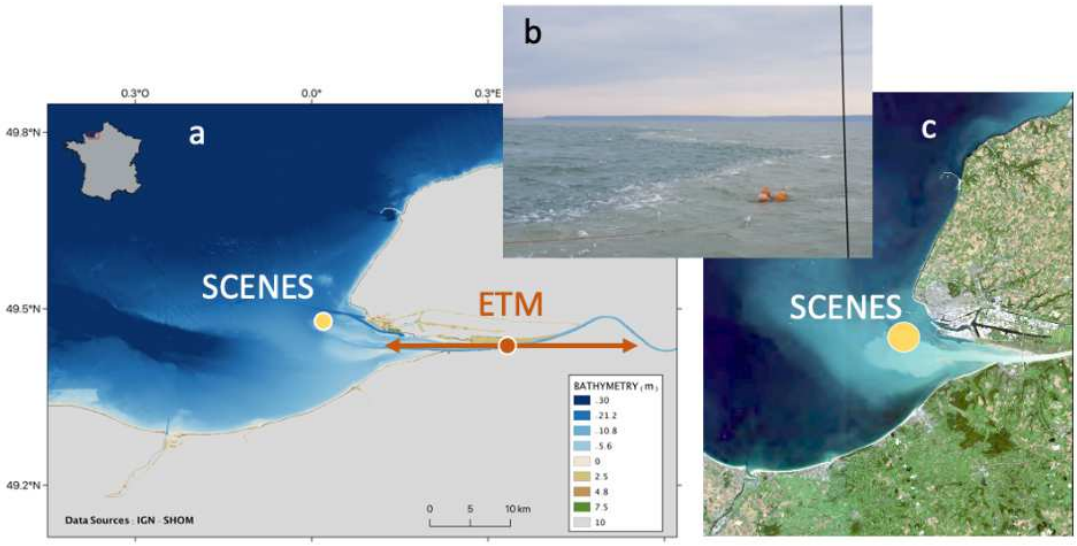

Figure 1: Seine estuary and bay: bathymetry and location of the SCENES station (a), picture of the frontal structure of the turbid plume at SCENES (b) and Landsat 8 images of surface turbidity plume(c).

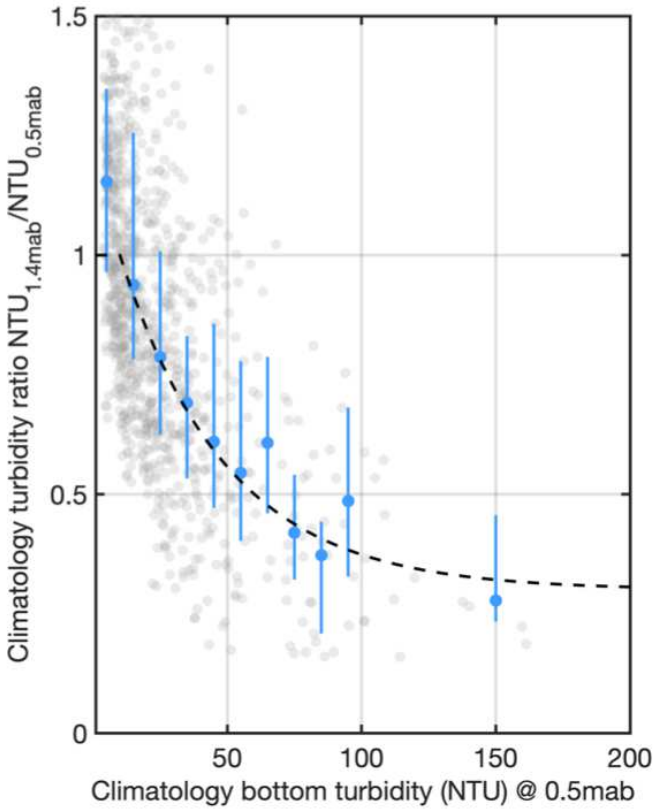

Figure 2: Evolution of intratidal turbidity climatology ratio between 2015-2017/06 (measured at 1.4mab) and 2017/10-2022 (measured at 0.5mab) as a function of turbidity at 0.5mab. Raw data are marked by grey dots, blue dots represent median values per turbidity classes and vertical bars the percentiles 25 and 75.

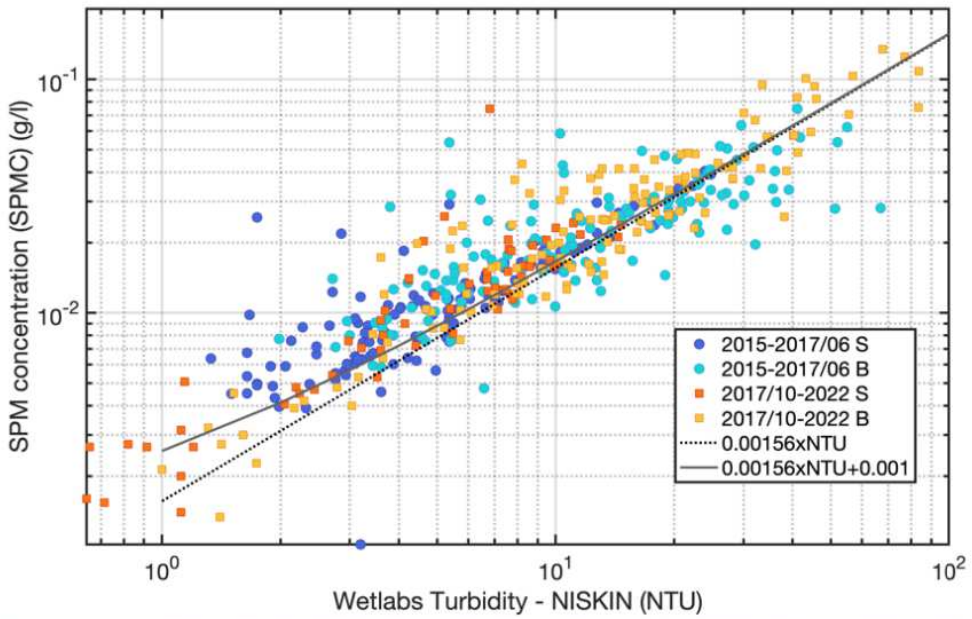

Figure 3: Wetlabs turbidity sensor calibration over in situ samples collected during field campaigns. In the legend, S refers to surface samples and B to bottom samples.

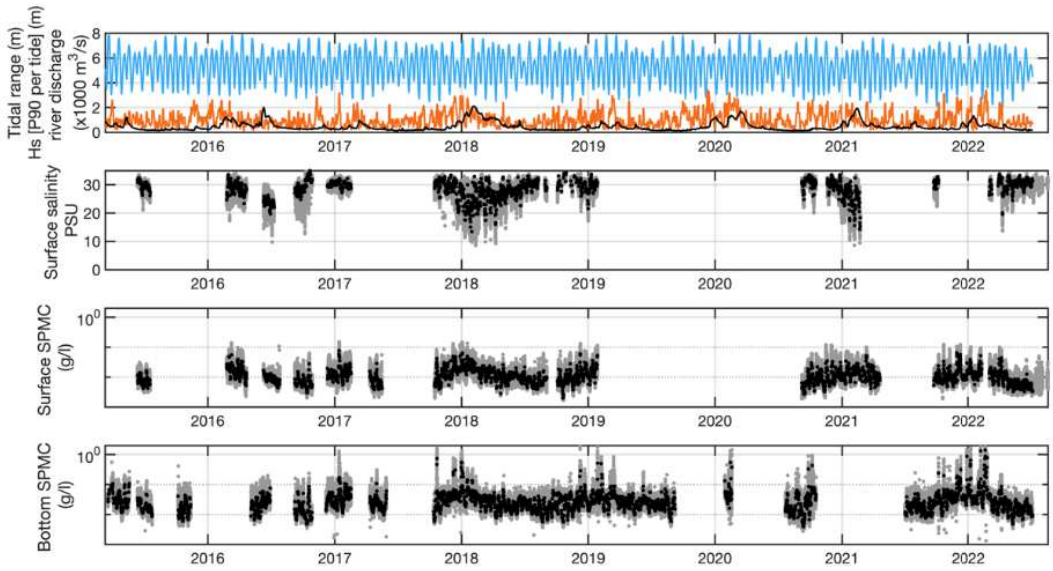

Figure 4: Hydro-meteorological and tidal forcing and SPM concentration dynamics from 2015 to 2022 at the mouth of the Seine Estuary. Top: River discharge, tidal range and waves (Hs_{P90}); middle: surface SPMC; bottom: bottom SPMC. (grey dots: raw high-frequency concentration; black dots: tidal-median SPMC).

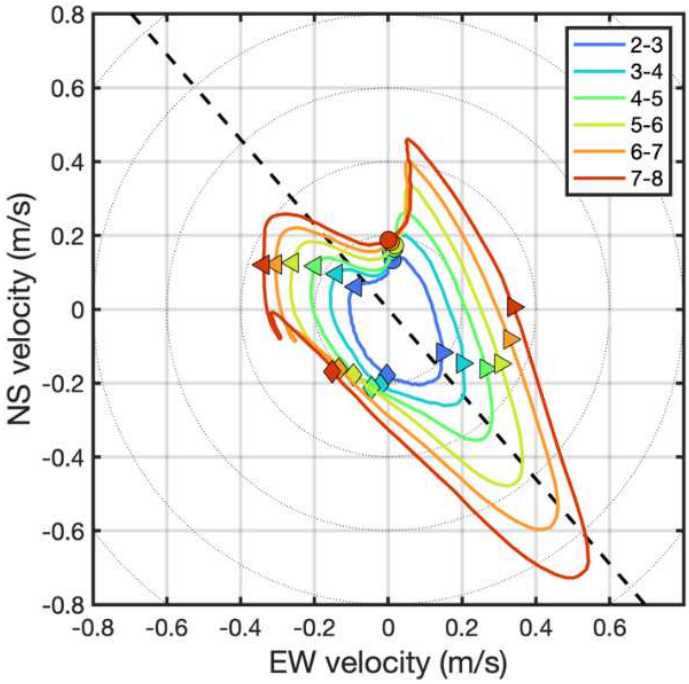

Figure 5: Average barotropic current velocity ellipses per tidal range classes (line colour) (Eastward and Northward positive). Diamonds represent low tide, circles high tide, right and left triangles +3h and -3h after low tide respectively. Grey circles represent velocity magnitude. Dashed line indicates the current direction during flood.

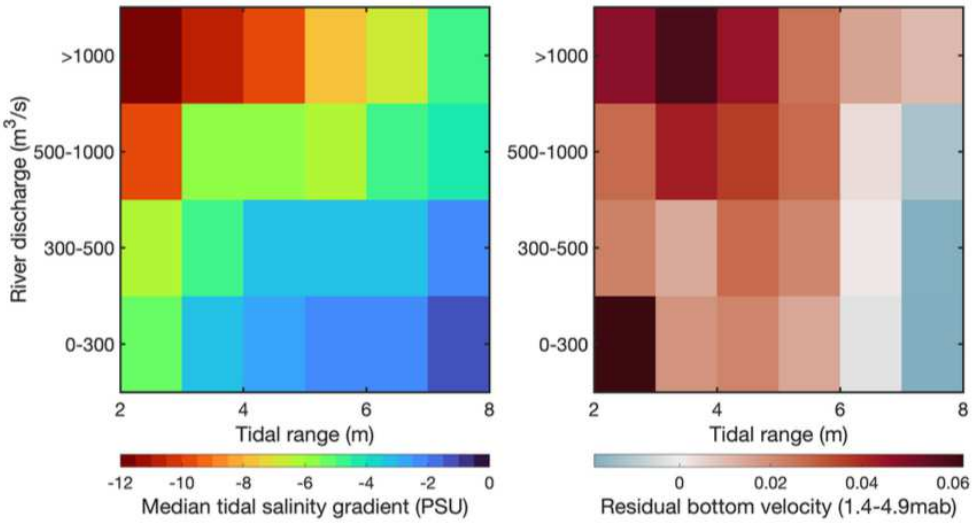

Figure 6: Tidal median vertical salinity gradient (Surface-Bottom) (left) and residual bottom (1.4-4.9m above bed) velocities (right) as a function of river discharge and tidal range classes, for low wave conditions (Hs_{P90}<1m)

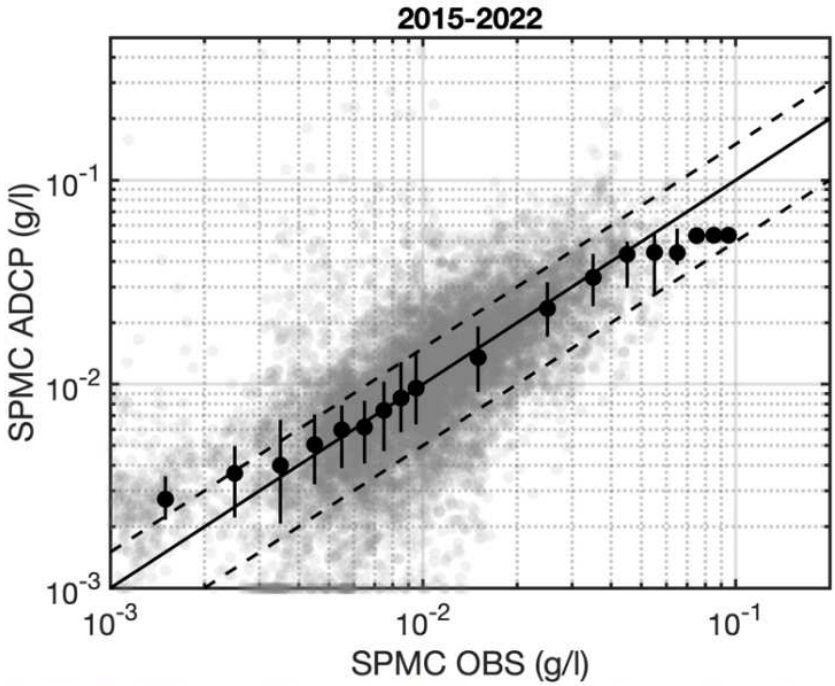

Figure 7: Comparison between ship-based SCC cast data and ADP SPMC data for 19 tidal cycles from 2015 to 2022. Grey points show raw data, black points the median per SPMC classes (every 0.01g/l below 0.1g/l; every 0.1g/l above 0.1g/l). Vertical bars show percentiles 25 and 75 per SPMC class. Black line is the 1:1 line, and the dashed lines represent +/-50% interval

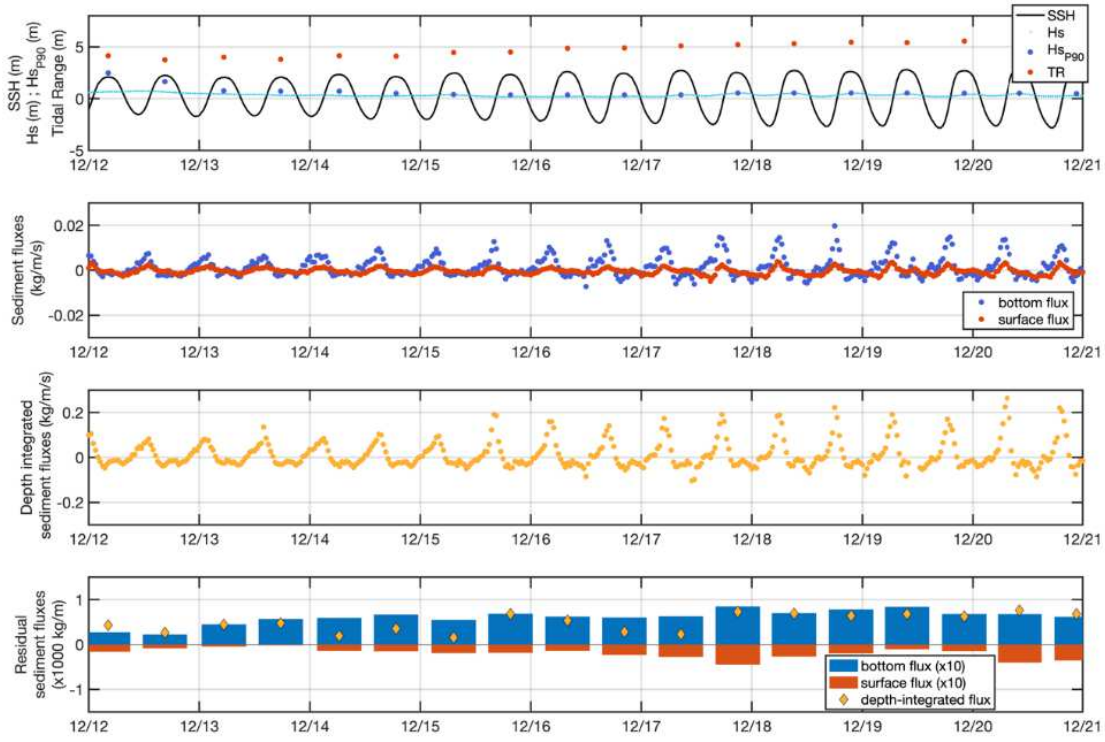

Figure 8: Tidal range, sea surface height, significant wave height (raw and tidal P90) (a) and SPM fluxes during calm weather conditions (Hs_{P90}<1m) (12/12/2021-20/12/2021): Surface and bottom fluxes (b); depth-integrated fluxes (c) and residual (surface, bottom and depth-integrated) fluxes (d).

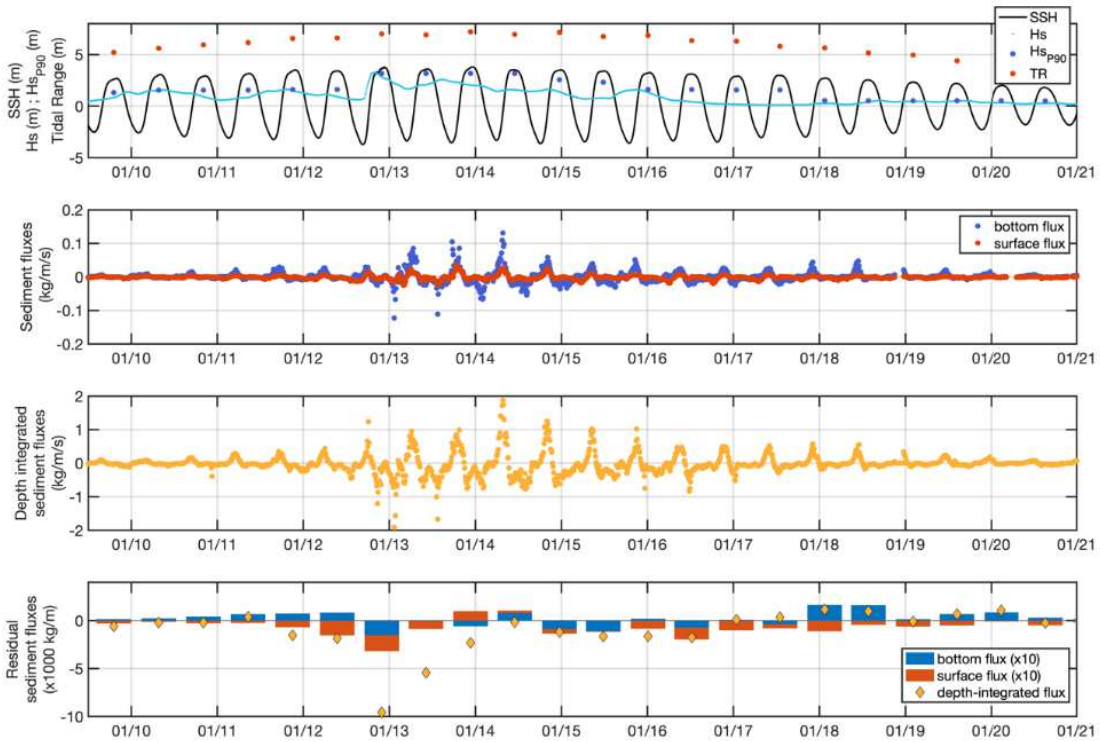

Figure 9: Tidal range, sea surface height, significant wave height (raw and tidal P90) (a) and SPM fluxes during stormy conditions (Hs_{P90}>2m) (9/1/2017-21/1/2017): Surface and bottom fluxes (b); depth-integrated fluxes (c) and residual (surface, bottom and depth-integrated) fluxes (d).

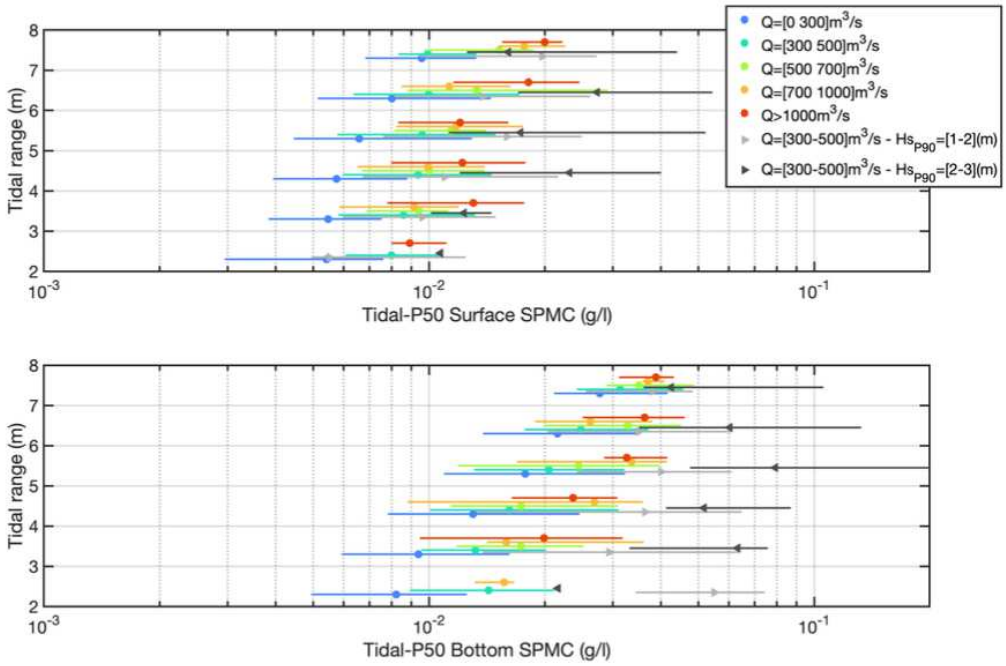

Figure 10: Variability of the tidal-median SPMC concentration at surface (top) and bottom (bottom) for different conditions of tidal range, river discharge (colour), and Hs_{P90} (triangles). Markers represent the median value per condition, and lines the extension between the percentile 10 and 90. Wave conditions are only shown for river discharge conditions from 300m³/s to 500m³/s.

1182

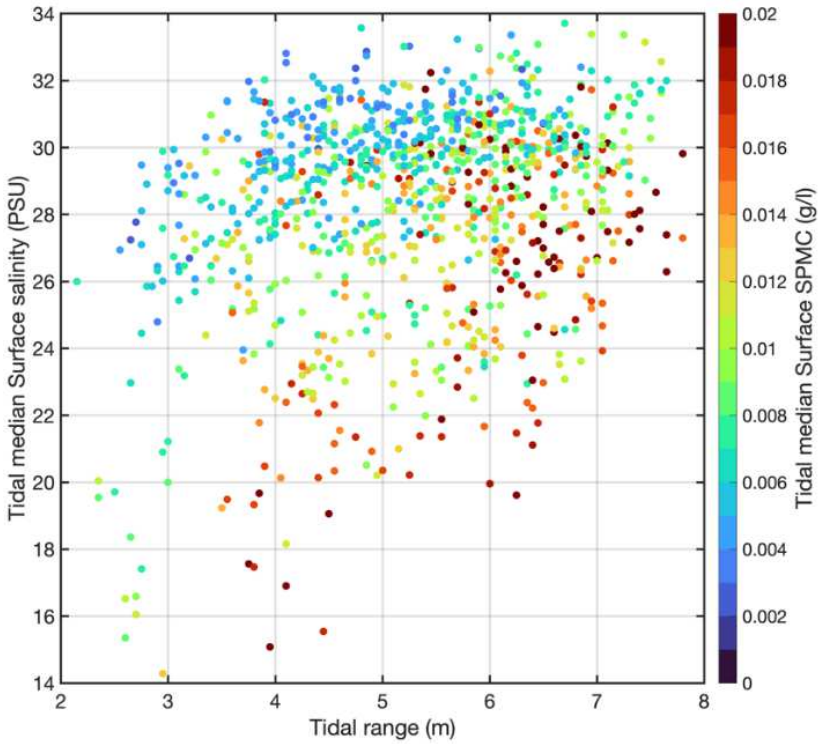

1183
1184 *Figure 11: Tidal-median surface salinity and SPMC function of tidal range, for low wave condition (Hs_{P90}<1m)*

1185
1186

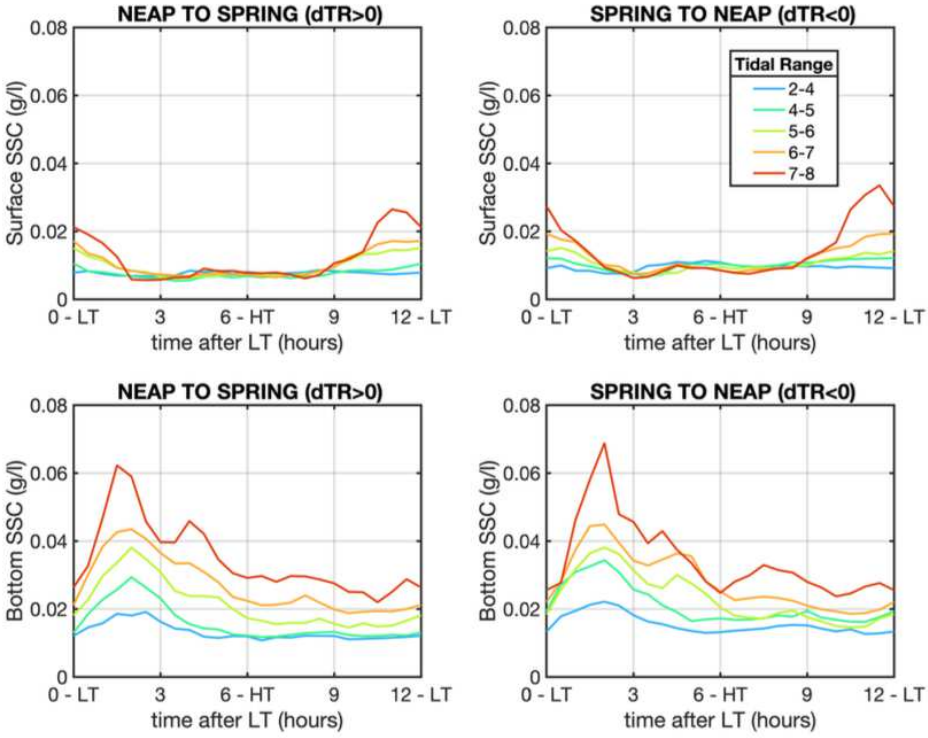

Figure 12: Intratidal SPMC climatology for different conditions of tidal range and tidal range gradients. Climatologies are computed for low wave conditions (Hs_{P90}<1m) and average river discharge conditions ([300-500]m^3/s). Top: surface intratidal SPMC; Bottom: bottom intratidal SPMC; Left: positive tidal range gradients (from neap to spring); Right: negative tidal range gradients (from spring to neap).

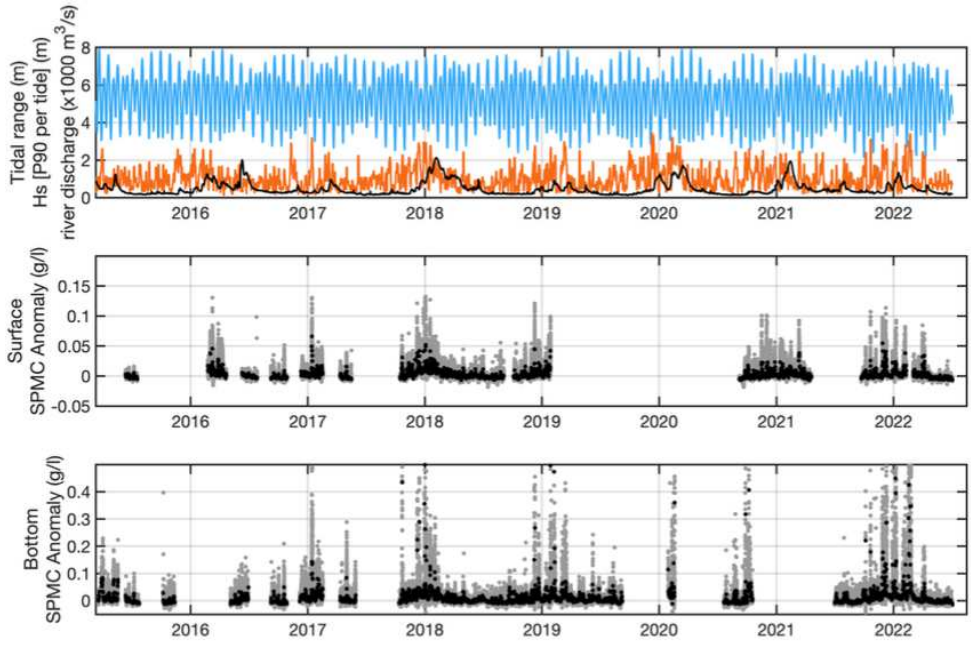

Figure 13: Hydro-meteorological and tidal forcing and SPM concentration anomalies from 2015 to 2022 at the mouth of the Seine Estuary. Top: River discharge (black line), tidal range (blue line) and waves (HsP90) (orange line); Middle: surface SPMC anomaly; Bottom: bottom SPMC anomaly (grey dots: raw high-frequency SPMC anomaly; black dots: tidal-median SPMC anomaly).

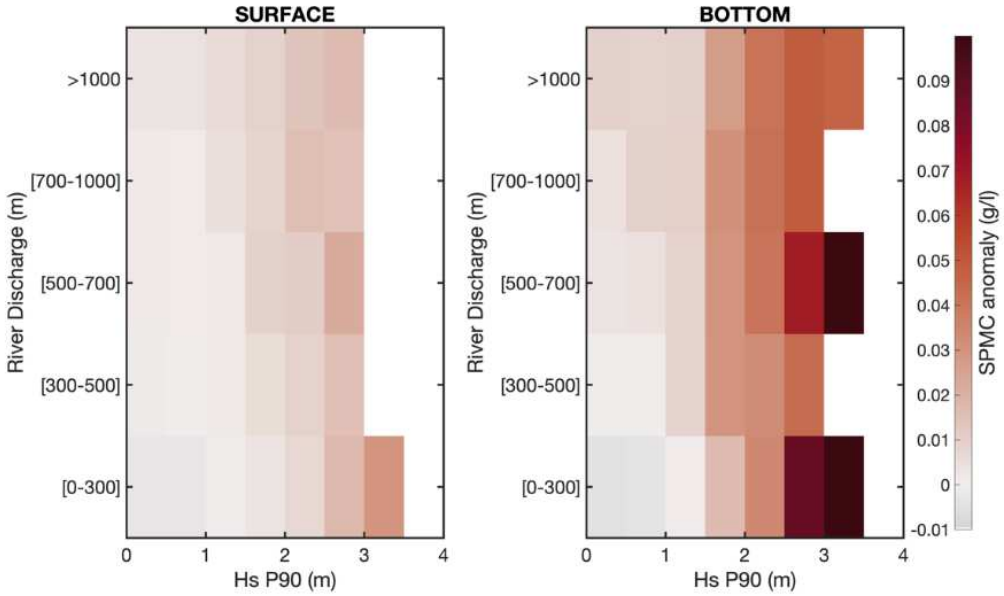

Figure 14: Tidal-median SPMC anomaly as a function of river discharge and wave (Hs_{P90}) conditions. Left: surface; Right: bottom.

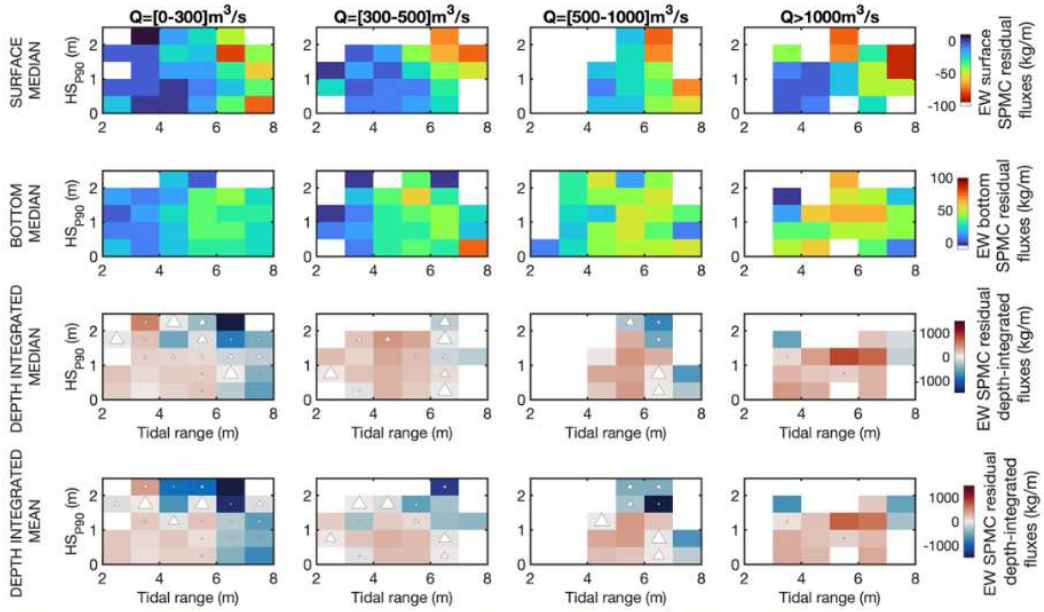

Figure 15: Median (row 1-3) and mean (row 4) residual fluxes per wave, tidal range and river discharge conditions. Different fluxes are evaluated: Surface, bottom and depth-integrated fluxes (at least 5 tides per hydro-meteorological conditions). White triangles represent the uncertainty U_F of the median depth-integrated residual fluxes (percentile 25 or 75 with an opposite sign as the median). The triangle size indicates uncertainty intensity.

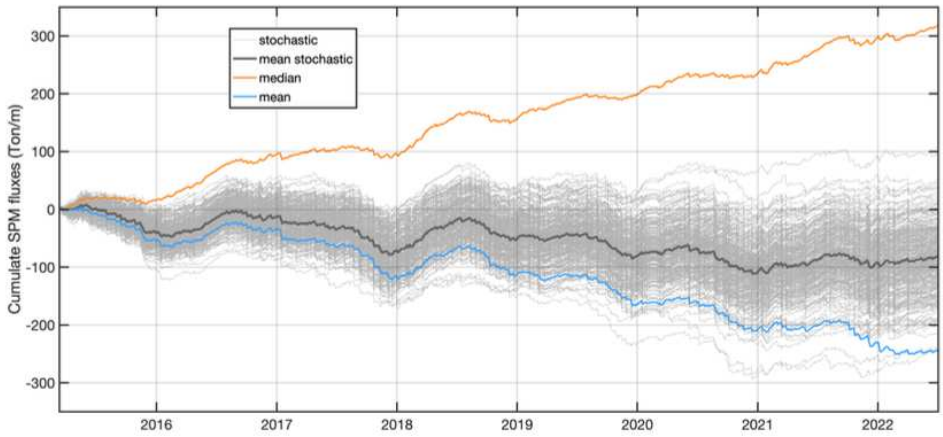

Figure 16: SPM cumulative residual fluxes over the period 2015-2022. Thin grey lines represent fluxes estimated from stochastic analysis using the residual flux probability density function for each river discharge, wave and tidal condition. Thick dark grey line shows the mean of the stochastic fluxes. Blue and orange lines represent cumulative fluxes using mean and median residual flux calculation per conditions.

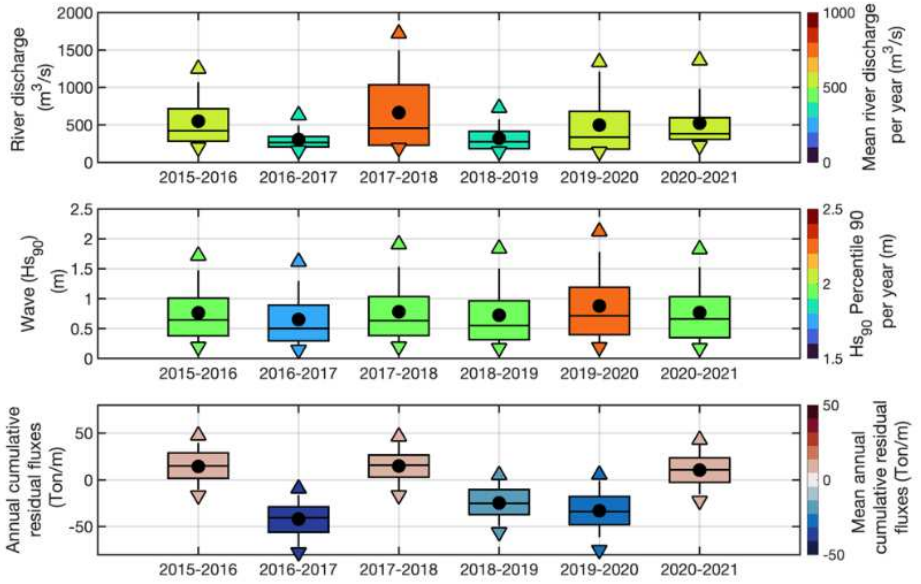

Figure 17: Annual statistics of river discharge (top), tidal percentile 90 of significant wave height (middle) and cumulative residual fluxes (bottom) from 2015 to 2021. Hydrological years are considered to separate annual time series, i.e. from October to October.

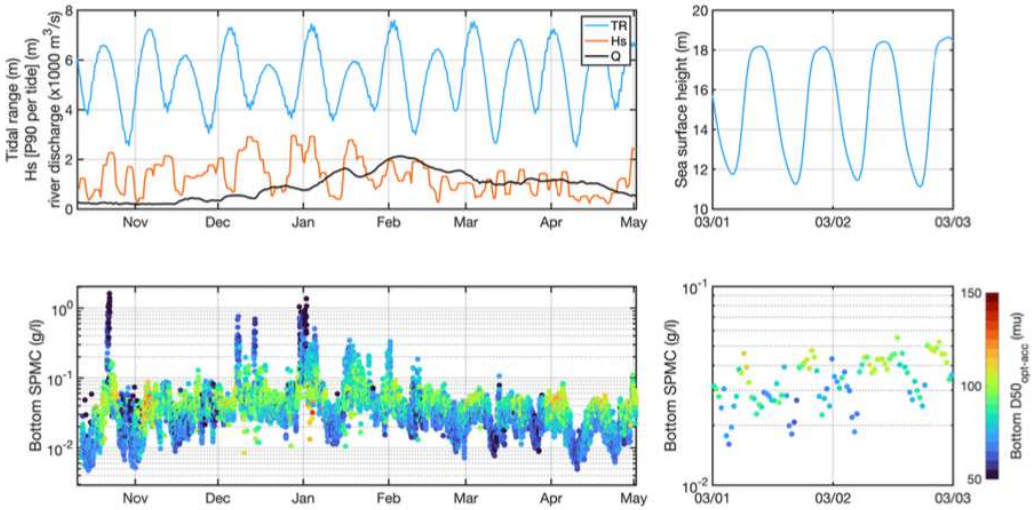

Figure 18: Hydro-meteorological and tidal forcing and bottom SPM concentration from October 2017 to may 2018 at the mouth of the Seine Estuary. Top left: River discharge, tidal range and waves (HsP90); Bottom left: bottom SPMC and $D50_{opt-acc}$ (colour); Top right: water level – focus from march 1st to march 3rd, 2018 (red rectangle); Bottom right: bottom SPMC and $D50_{opt-acc}$ (colour)

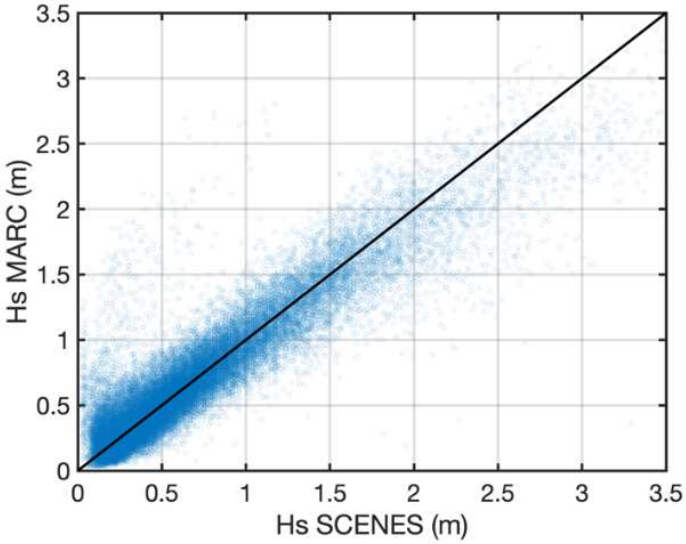

Figure 19: Comparison of simulated (WW3 – MARC data) and observed significant wave height at the SCENES station

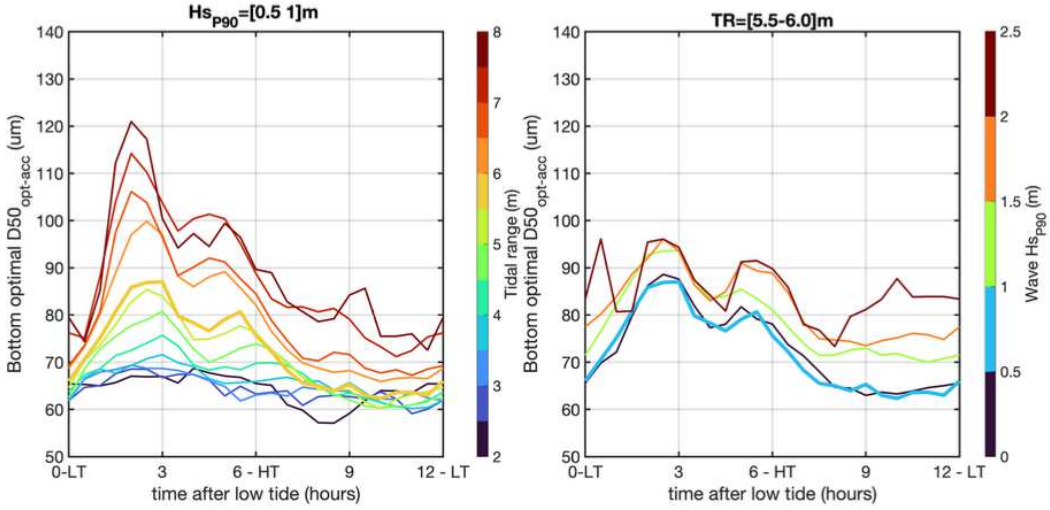

Figure 20: Intratidal D50$_{opt-acc}$ climatology calculated over the period 2015-2022. Left: intratidal D50$_{opt-acc}$ over tidal range (for low wave activity: Hs$_{P90}$=[0.5-1]m). Right: intratidal D50opt-acc over wave Hs$_{P90}$ range (for TR=[5.5-6]m)

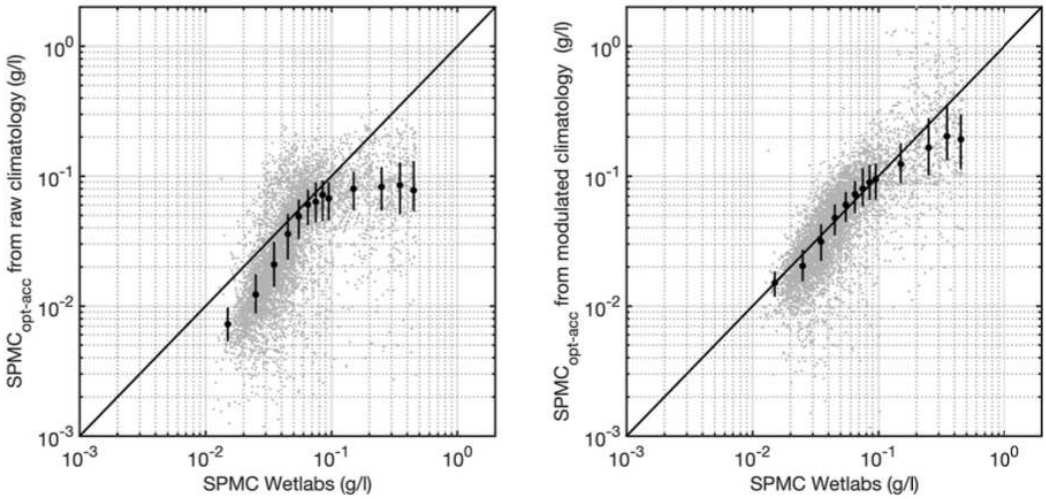

Figure 21: Comparison of non-saturated observed SPMC data (from November 2021 to March 2022) with SPMC calculated from acoustic inversion, using the raw $D50_{opt-acc}$ climatology (left) and the modulated $D50_{opt-acc}$ climatology (right). Gray dots show raw data, black dots median $SPMC_{opt-acc}$ data per SPMC Wetlabs classes, and vertical bars show percentile 25 and 75 values.

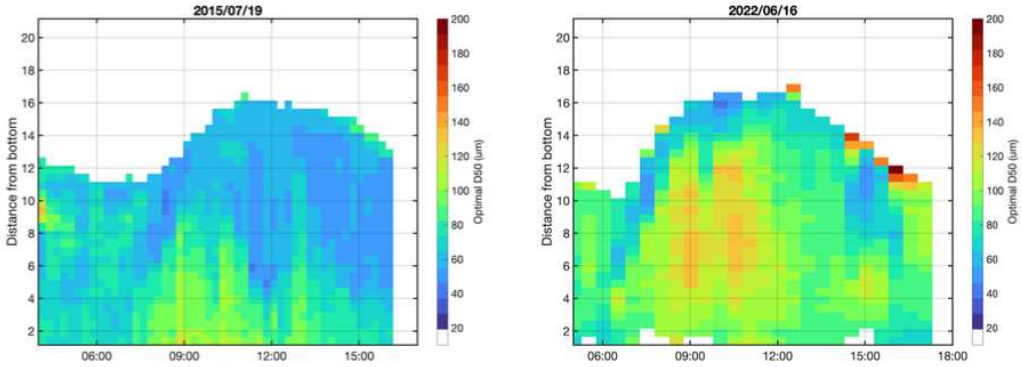

Figure 22: Optimal acoustic D50 from the inversion of the acoustic backscatter signal and ship-based SPMC profiles during two tidal cycles (left: 19th July 2015; right: 16th June 2022).

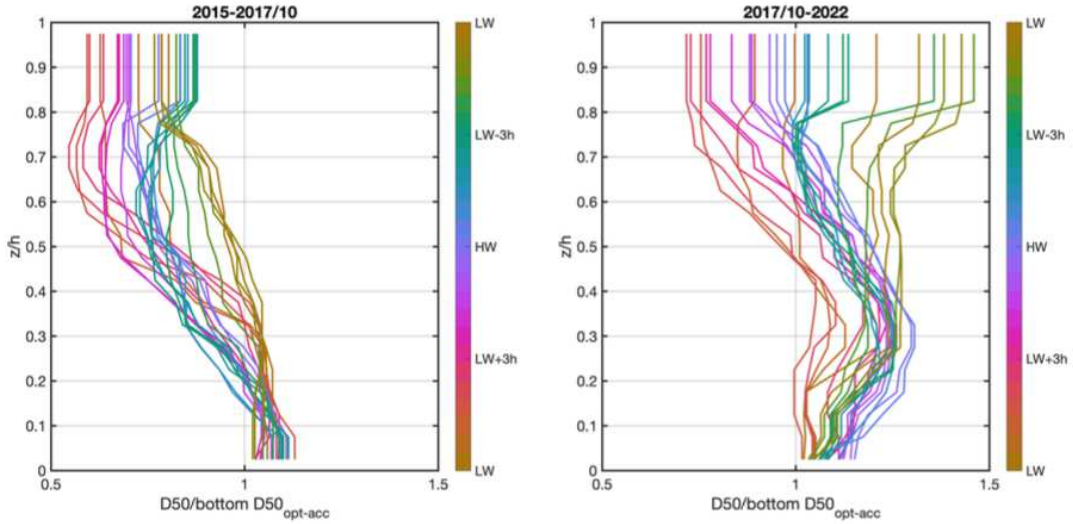

Figure 23: Optimal D50 extrapolation along the water column based on bottom $D50_{opt\text{-}acc}$ calculated from bottom SPMC for 2015-2017/10 (left) and 2017/10-2022 (right).

Annexe 2

(a)

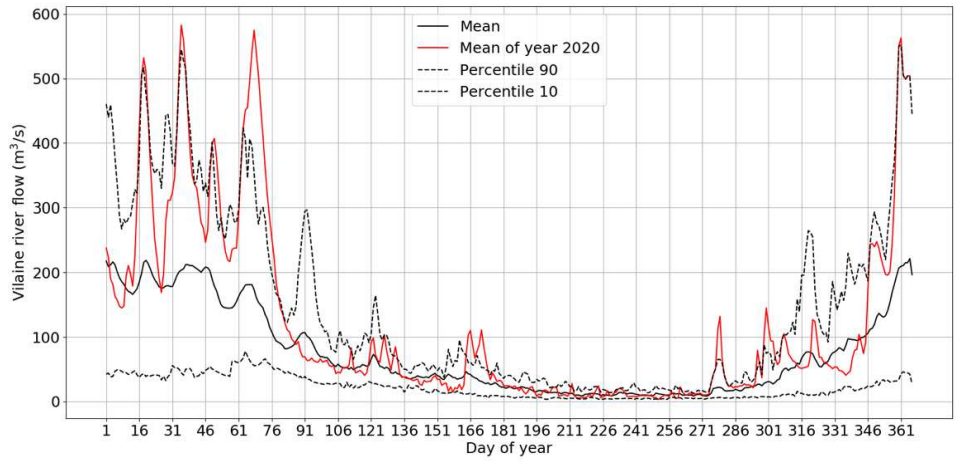
Mean
Mean of year 2020
Percentile 90
Percentile 10
Vilaine river flow (m³/s)
Day of year

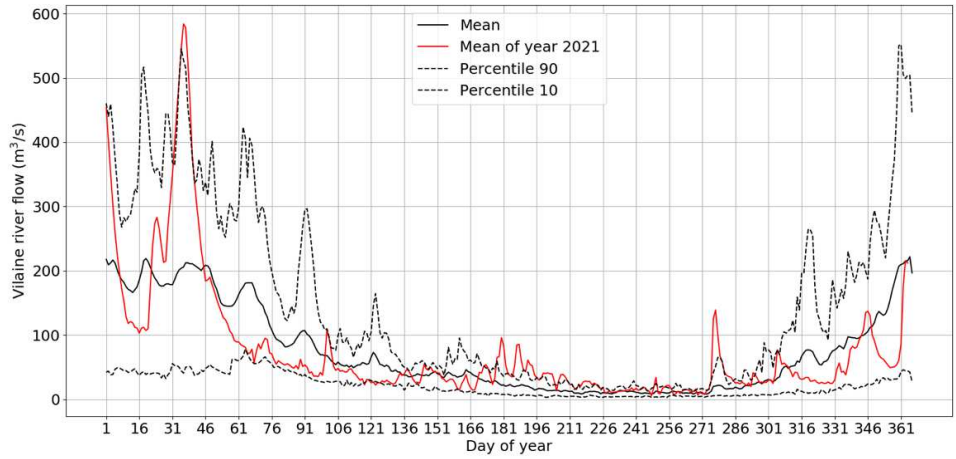
Mean
Mean of year 2021
Percentile 90
Percentile 10
Vilaine river flow (m³/s)
Day of year

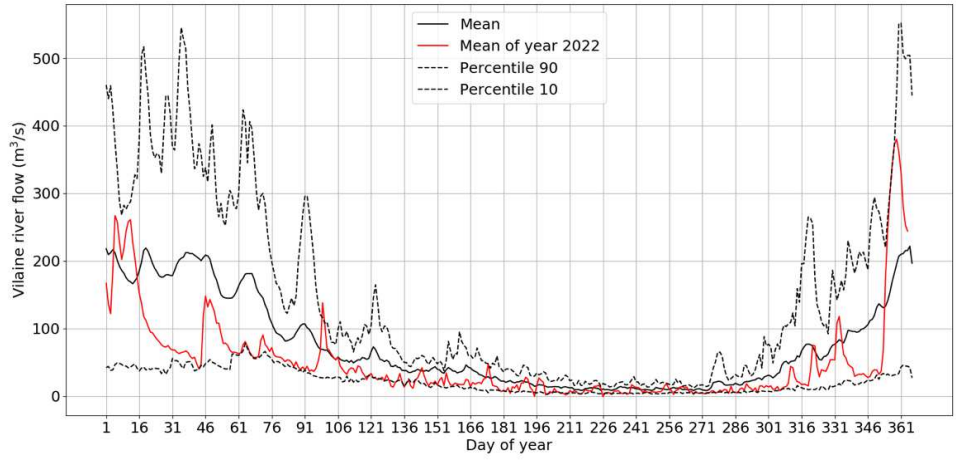
Mean
Mean of year 2022
Percentile 90
Percentile 10
Vilaine river flow (m³/s)
Day of year

(b)

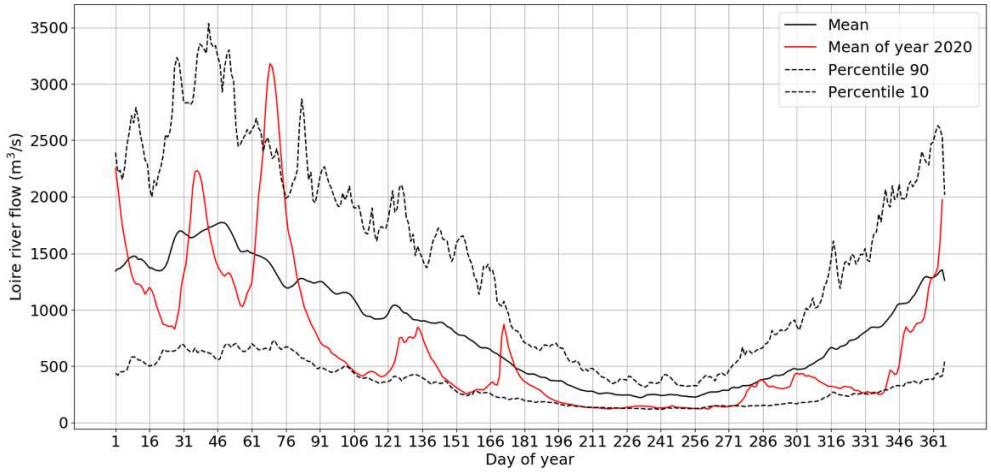

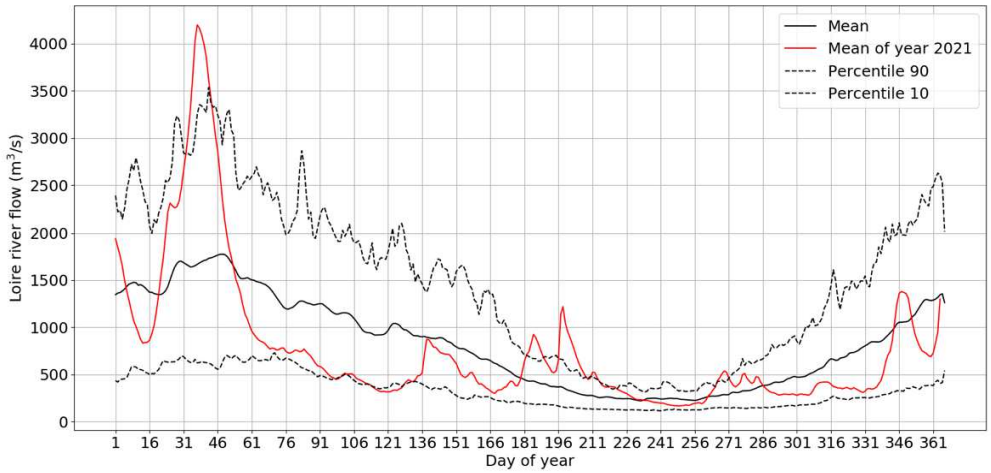

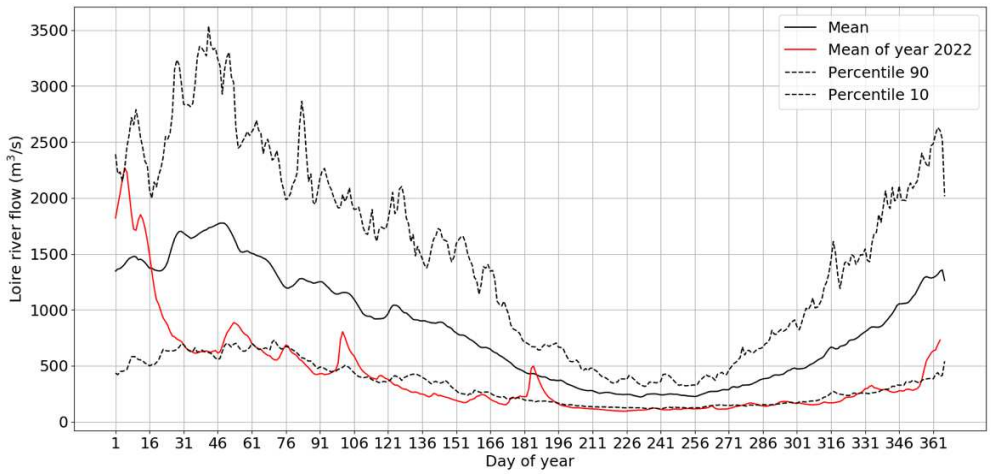

Illustrations du débit de (a) la Vilaine et (b) la Loire pour les années 2020, 2021 et 2022 avec la moyenne sur les trois années (trait noir plein), la moyenne de l'année considérée (trait rouge plein) et le percentile 10 et 90 sur les trois années (trait pointillé noir).

COLLEGE SCIENCES DOCTORAL DE LA MER BRETAGNE ET DU LITTORAL

UBO Université de Bretagne Occidentale

Titre : Vers la **C**ompréhension des réponses de l'environnement c**Ô**tier aux évènements e**XT**rêmes dans un contexte de changement **CLIM**atique (**COXTCLIM**)

Mots clés : Évènements extrêmes, Changement climatique, Environnement côtier.

Résumé : Le changement global est associé à des évolutions dans la dynamique des évènements extrêmes dans l'océan. Ces extrêmes qui affectent l'environnement et nos sociétés de façon dramatique sont amenés à s'intensifier, à devenir plus fréquents voir à durer plus longtemps et sur des zones de plus en plus grandes.

L'océan côtier est particulièrement impacté par ces extrêmes mais de nombreux questionnements restent ouverts. A travers l'exploration des vagues marines de chaleur et de froid, les dessalures extrêmes, les panaches sédimentaires et les efflorescences algales, j'ai pu identifier, définir et caractériser les évènements extrêmes le long des côtes françaises grâce à un réseau de bouées *in situ* haute fréquence. Afin de détailler au mieux ces évènements extrêmes et comprendre les processus auxquels ils sont associés des modèles numériques et des images satellites ont aussi été analysés.

Les forçages extrêmes comme les extrêmes environnementaux dans l'océan côtier français montrent une intensification de ces phénomènes cette dernière décennie. Certains extrêmes suivent les tendances globales quand d'autres sont contraient localement. La compréhension de la dynamique des évènements extrêmes ouvre des perspectives pour la définition de nouveaux indicateurs pour une meilleure gestion des environnements côtiers.

Title : Towards understanding coastal environment responses to extreme events in a context of climate change (**COXTCLIM**)

Keywords : Extreme events, Climate change, Coastal environment.

Abstract : Global change is associated with changes in the dynamics of extreme events in the ocean. These extremes, which dramatically affect the environment and our societies, are set to intensify, become more frequent and even last longer, over ever larger areas.

The coastal ocean is particularly affected by these extremes but many questions remain open. Through the exploration of marine heat waves and cold spells, extreme low salinity events, sediment plumes and algal blooms, I have been able to identify, define and characterize extreme events on the French coast thanks to a network of high-frequency *in situ* buoys. In order to better detail these extreme events and understand the processes with which they are associated numerical models and satellite images were also analyzed

Extreme forcing and environmental extremes in the French coastal ocean show an intensification of these phenomena over the last decade. Some extremes follow global trends, while others are forced locally. Understanding the dynamics of extreme events opens up the possibility of defining new indicators for better management of coastal environments.